ISSSD 2016

XVI INTERNATIONAL SYMPOSIUM ON SOLID STATE DOSIMETRY

Host

Mesoamerican Centre for Theoretical Physics

Proccedings
Vol. 3

Tuxtla Gutiérrez, Chiapas. México
September 24 to 28, 2016

Organizing Committee

ISSSD 2016

Juan Azorín Nieto

President

Rebeca Sosa Fonseca, Lydia Paredes Gutiérrez

Silvia Hidalgo Tobon, Erika P Azorín Vega

Juan Carlos Azorín Vega, Eugenio Torijano Cabrera

Epifanio Cruz Zaragoza, Pedro R. González Martínez

Teodoro Rivera Montalvo, Hector Rene Vega-Carrillo

ISSSD 2016

International Scientific Committee

ISSSD 2016

In-extenso papers

Volume 3

MCNPx Computational Estimation of the Calibration Factor of an *In Vivo* Counter for ^{18}F-FDG Activity Incorporated in the Brain

Bruno Melo Mendes[1,2], Telma Cristina Ferreira Fonseca[1], Kátia Duarte Vital[1]
Teógenes Augusto da Silva[1], Tarcísio Passos Ribeiro de Campos[2]

[1] Centro de Desenvolvimento da Tecnologia Nuclear (CDTN/CNEN)
Av. Presidente Antônio Carlos, 6.627. CEP 31270-901, Belo Horizonte-MG, Brasil. bmm@cdtn.br

[2] Departamento de Engenharia Nuclear – DEN; Programa de Pós-graduação em Ciências e Técnicas Nucleares; Universidade Federal de Minas Gerais - UFMG
Av. Presidente Antônio Carlos, 6.627. CEP 31270-901 Belo Horizonte - MG, Brasil

Abstract

In previous work, the computational modeling of the CDTN *in vivo* counter for estimation of ^{18}F-FDG activity incorporated into workers brains was validated. Here, we studied the Calibration Factor (CF) for seven distinct voxelized computational phantoms including the reference models from ICRP 110. Computational simulations were also carried out to study the effect of increasing the distance between the detector and the brain up to 100 cm. The degree of correlation among geometric and anatomical parameters of the computational models and the calibration factors were also evaluated. The morphological diversity of the computational phantoms resulted CF variations greater than 38% (39.8 ± 0.2 to 64.6 ± 0.5 Bq.CPS^{-1}). Despite the variations, CF has been reduced by the increasing distance, although the remarkable decrease in counting efficiency makes prohibitive this geometry. These findings suggest that head anatomic parameters can be used to improve CF estimation.

Keywords: Internal Dosimetry; MCNPx; Calibration Factor, ^{18}F-FDG.

1.- INTRODUCTION

Fludeoxyglucose F 18 (^{18}F-FDG) remains as the PET radiopharmaceuticals most used worldwide despite presenting some limitations [Gulyás and Halldin, 2012; Treglia *et al.,* 2014]. The demand for this radiotracer has expanded in the last decade. The number of ^{18}F-FDG doses produced annually in our institute increased more than 500% in 2010-2015 period. Scientific interest in ^{18}F-FDG also continues to raise. The use of the words "PET AND FDG" in MEDLINE/PubMed site demonstrates a rising number of papers year after year: 410 studies in 2000; 1350 in 2010; and 2230 in 2015 [PubMed, 2016].

The number of workers involved in the production and the clinical use of ^{18}F-FDG tends to increase, following the demand, as well as the risk of internal contamination. Fluorine-18 has a short half-life: 109.8 minutes [NNDC, 2016]. Thus, in most cases, it is not possible to detect radiation a day after contamination. Quantification of the incorporated activity and the estimation of the committed effective dose in such cases arise challenging, but is required to compose the cumulative occupational dose history.

In previous works, our group has developed a methodology for monitoring of staff members exposed to ^{18}F-FDG [Oliveira *et al.,* 2009; Oliveira *et al.,* 2013]. A real plastic head simulator (SiCab) with its brain volume filled with a positron emitter solution (^{22}Na/H_2O) was used to determine a calibration factor (CF) for converting counts per second (CPS) in activity (Bq). Recently a MCNPx computational model for this system was validated [Mendes *et al*., 2016].

Computer modeling has been successfully employed in the evaluation and the optimization of counting geometries (CG) and *in vivo* monitoring systems [Fonseca *et al.,* 2014a; Fonseca *et al.,* 2014b]. It is important to know the factors that have influence in determining the incorporated activity for a certain counting geometry and the uncertainties inherent to the monitoring system. In this work seven anthropomorphic computational phantoms, including ICRP voxelized reference adult phantoms (ICRP, 2009), were used to calculate the calibration factors and to study its variations. Computer simulations were

performed in order to evaluate the effect of the distance variation between the detector and the head model, called the head-detector distance (HDD), on the CF value. The degree of correlation among geometric and anatomical parameters of the computational models and the calibration factors were also studied.

2.- MATERIALS AND METHODS

2.1.- CF variation for seven phantoms and HDD influence

Seven voxelized phantoms representing adult male and female have been adapted to run on MCNPx. The reference models, RCP-AM and RCP-AF, were provided in ICRP 110 publication [ICRP, 2009]. Data files containing Katja and VisHum phantoms segmentation were kindly provided by the German Research Center for Environmental Health – GSF [GSF, 2016; Petoussi-Henss *et al.*, 2002; Zankl *et al.,* 1988]. The Voxel_Man phantom created by Zubal et al. was obtained on the web [IPAG, 2016; Zubal *et al.,* 1994]. C^{++} programs were developed *in house* for formatting the computational model data according to MCNPx input format. The phantom VW was segmented by our group from the data of the female model provided by the Visible Human Project [NLM, 2016]. VW_r was obtained by 10% linear reduction in VW model voxels dimensions. Table 1 shows the main characteristics of these phantoms.

The elemental composition and density data of computational model tissues were based on different publications, as can be identified in Table 1. ICRP 110 [2009], ICRU 46 [1992], ICRP 89 [2002] and the data from Cristy and Eckerman [1987] work were used for the MCNPx material definition according to the voxel model.

A positron source uniformly distributed in the brain volume of the model was simulated. The fluorine-18 positrons have an average energy of 249.8 keV. Energy versus probability table for ^{18}F positron emissions was provided by the DECDATA® software [ICRP, 2007].

Table 1 – Summary of some features of the seven computational phantoms.

Computational Phantom	Gender	Height (cm)	Weight (kg)	Matrix (columns x rows x slices)	Voxel Dimensions (column width x row depth x slice height)	Tissue Data
RCP-AM	Male	176	73	299 x 137 x 346	2.137 x 2.137 x 8.0 mm^3	ICRP 110 [2009]
RCP-AF	Female	163	60	254 x 127 x 220	1.775 x 1.775 x 4.84 mm^3	ICRP 110 [2009]
Katja	Female	163	62	299 x 150 x 348	1.775 x 1.775 x 4.84 mm^3	ICRP 110 [2009]
VisHum	Male	180	103	512 x 512 x 250	0.91 x 0.94 x 5.0 mm^3	ICRP 110 [2009]
Voxel_Man	Male	178	70	128 x 128 x 246	4.0 x 4.0 x 4.0 mm^3	Cristy and Eckerman [1987]
VW	Female	165	98	114 x 65 x 346	5.0 x 5.0 x 5.0 mm^3	ICRU 46 [1992] ICRP 89 [2002]
VW_r	Female	149	71	114 x 65 x 346	4.5 x 4.5 x 4.5 mm^3	ICRU 46 [1992] ICRP 89 [2002]

The sensible volume of a 3"x3" NaI(Tl) detector was modeled. The dimensions and material densities were provided by the equipment manual [CANBERRA, 2009]. The detector was placed tangentially at the top of the computater model's head. It was visually centered in x and y axis in relation to the brain, as can be seen in Figure 1. In order to assess the influence of the HDD variation in CF calculations, the detector was positioned at distances of 0 cm (HDD_0), 10 cm (HDD_{10}), 50 cm (HDD_{50}) and 100 cm (HDD_{100}) away from the head.

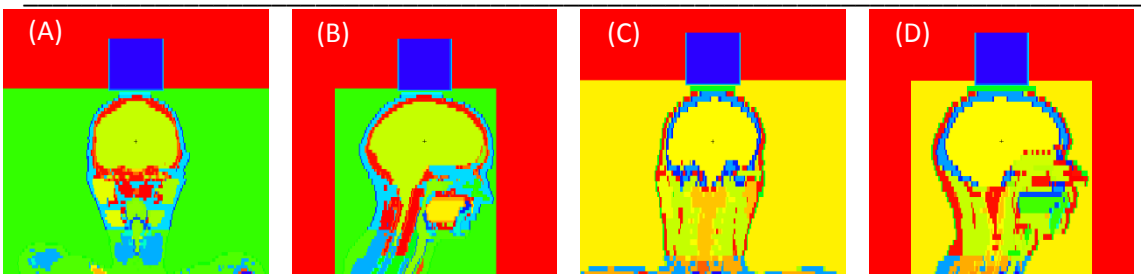

Figure 1 – MCNPx plot images showing NaI(Tl) detector positioning (HDD_0) for RCP_AF (A, B) and RCP_AM (C, D) ICRP reference adult voxelized phantoms.

The F8:p tally was used to assess the energy distribution of the photon pulses occurring in the sensitive volume of Nal(Tl) detector. Secondary particle transport was taken into account. The pulses were counted in energy bins incremented by 1 keV (0-700 keV). Energy indexing algorithm ITS was enabled (DBCN 17j 1) since such algorithm is considered more accurate than the "default" when using MCNPx electron transport [Reynaert *et al.*, 2002]. The calibration factor ($Bq.CPS^{-1}$) is calculated according to equation 1.

$$CF = 0.9673 \times (PPPos)^{-1} \quad (1)$$

where 0.9673 is the number of positrons emitted per ^{18}F decay [ICRP, 2007], PPPos is the number of 511 keV photon pulses in the sensitive volume of NaI(Tl) detector by positron emitted from the source.

The number of particles stories followed (NPS) was set so that the relative errors of the calculated calibration factor not exceed 1%, as a first estimate. NPS varies from 1E06 to 1.6E08.

The percentage difference between the minimum and the maximum calibration factor ($DCF_{Min-Max}$) was calculated for each head-detector distance simulated according to the following equation:

$$DCF_{Min\text{-}Max}\ (\%) = ((CFmin - CFmax)\ .\ CFmax^{-1}) \times 100 \qquad (2)$$

where, for a given HDD, CF_{min} is the minimum calibration factor and CF_{max} is the maximum calibration factor. The mean value, standard deviation and relative error of calibration factors were also calculated for each tested HDD.

2.2.- Correlation between CF and anatomical and geometric parameters

The identification of anatomical model parameters that are correlated with the calibration factors is desirable. Corrections on CF calculations can be applied so that more appropriate values for a given Occupationally Exposed Worker (OEW) can be used in the estimation of ^{18}F-FDG activity incorporated into his brain.

A group subdivision was performed among the evaluated anatomical and geometric parameters. Group 1 includes parameters that can only be measured by more complex imaging techniques such as MRI and CT: i) Average distance between brain voxels and the detector - AD_{BVD}; ii) Distance between brain and detector gravity centers - D_{BDGC}; iii) Minimum distance between the brain and detector - MD_{BD}; and iv) Brain Volume - BV. Group 2 includes the parameters that can be measured with simple tools like a tape-measure, or methodologies as images from video cameras installed near the counting system: i) Distance between the parallel planes of the detector surface (detector window) and auditory canals - D_{DSAC}; ii) Ear to ear distance – EED, i.e. the distance between one ear and the other passing over the top of the head; iii) Mean detector-head angle - MHDA; iv) Forehead to nape distance – FHND, i.e. the distance between the forehead and neck passing over the top of the head; iv) Head perimeter at the top of auricle insertion - HPTAI.

An in house C ++ program was created to calculate the average distance between the voxels of the brain and the detector center, the distance between the detector and brain gravity centers and the brain volume for each computational model. The other parameters were measured in the phantom images using the software ImageJ®. The MHDA was

calculated as the average of the angles between the head and the detector window measured in the sagittal and coronal planes. Figure 2 illustrates how some of these parameters were measured.

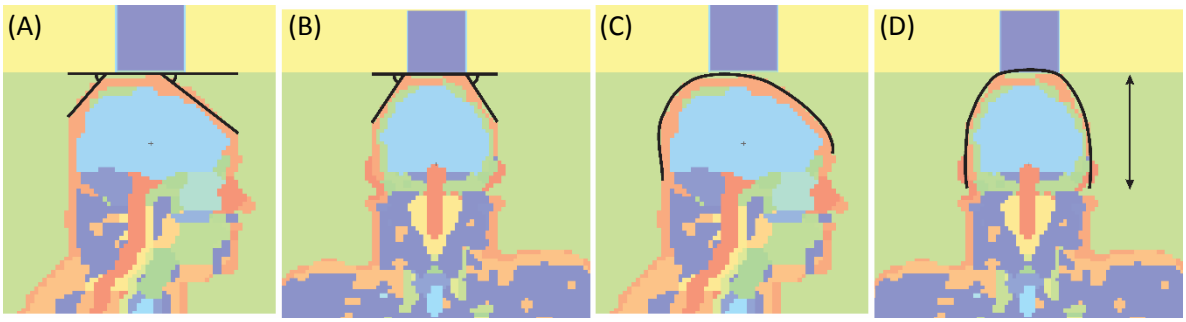

Figure 2 – Some of the Group 2 variables measured in the model. (A, B) – Detector-head angle – MHDA. (C) – Forehead to nape distance – FHND. (D) – Ear to ear distance – EED – and Distance between the parallel planes of detector surface and auditory canals – D_{DSAC} – (arrow).

Pearson test was the statistical method chose to evaluate the correlation between anatomic and geometric parameters of the models and their calibration factors. The Pearson correlation defines if there is a linear relationship between two variables. Software Minitab® was used to calculate the correlation coefficient (r) between variables and the calculated CF.

When the variable involve distance between the source and detector, the square of the variance was used in the correlation test. This was done because the intensity of radiation decreases with the square of the distance, and the Pearson test evaluates whether the correlation between the variables is linear. The degree of correlation between anatomic parameters of the models and CF was evaluated only for HDD_0, as that condition matches to the counting geometry currently used in OEW monitoring.

Scatter plot graphics of CF and some of group 1 a group 2 geometrical and anatomical parameters were presented in order to illustrate the degree of correlation among these variables.

3.- RESULTS

3.1.- CF variation for seven phantoms and HDD influence

The CF relative errors were equal or less than 1% in all cases simulated. Table 2 shows the calibration factors obtained for the seven different phantoms, considering the predetermined set of the head-detector distances.

The Voxel_Man phantom showed the lowest CF values for all HDD distances. The largest calibration factors were found to the VW model. ICRP reference phantoms showed intermediate CF values.

The CF values presented largest variations in the smallest head-detector distance (HDD_0). Both values of the relative error (RE) and the percentage difference between the minimum and the maximum calibration factor ($DCF_{Min-Max}$) confirm this fact. These parameters showed decreasing values with increasing HDD. Therefore, this reduction is followed by the increase of the calibration factor, as can be seen in Table 2.

Table 2 – Calibration Factor values from MCNPx simulations with seven different voxelized human phantoms. Four head-detector distances were modeled.

Computacional Phantoms	D = 0 cm		D = 10 cm		D = 50 cm		D = 100 cm	
	CF (Bq.Cps^{-1})	SD (Bq.Cps^{-1})	CF (Bq.Cps^{-1})	SD (Bq.Cps^{-1})	CF (Bq.Cps^{-1})	SD (Bq.Cps^{-1})	CF (Bq.Cps^{-1})	SD (Bq.Cps^{-1})
RCP_AF	50.3	0.1	179	1	1513	13	5004	39
RCP_AM	58.3	0.2	216	1	1670	15	5464	44
Katja	50.4	0.3	180	2	1518	13	5005	39
Voxel_Man	39.8	0.2	149	1	1342	11	4512	33
VW	64.6	0.5	217	2	1725	16	5715	34
VW_r	50.7	0.3	184	1	1556	14	5211	43
VisHum	50.4	0.2	178	2	1482	13	4992	39
CF_{mean}	52	8	186	24	1544	126	5129	386
RE (%)[a]	14.8		12.7		8.2		7.5	
$DCF_{Min-Max}$ (%)[b]	-38.4		-31.3		-22.2		-21.0	

[a] – RE (%) – Relative error = (SD . (CF_{mean}^{-1})).100
[b] - $DCF_{Min-Max}$ – Difference between CF_{max} and CF_{min} = ((CF_{min} – CF_{max}) . CF_{max}^{-1}).100

The detection efficiency (ε) ($CPS.Bq^{-1}$) is the inverse of CF ($Bq.CPS^{-1}$). Thus, it is noted that when the detector is positioned 100 cm from head, the system efficiency is about one hundred times smaller than when it was positioned at HDD_0. It can be also noted that $DCF_{Min-Max}$ and RE showed practically no differences for HDD_{50} and HDD_{100}.

3.2.- Correlation between CF and anatomical and geometric parameters

Table 3 shows the results of correlation between some model anatomical and geometric parameters of the models and their calibration factors obtained for HDD_0 (Table 2).

Table 3 – Group 1 and Group 2 model anatomical and geometric parameters measured for the computational phantoms and their Pearson correlation coefficient.

	Group 1 - variables				Group 2 - variables				
Computational Phantoms	**Squared AD_{BVD}**	**Squared D_{BDGC}**	**BV**	**Squared MD_{BD}**	**Squared D_{DSAC}**	**EED**	**MDHA**	**FHND**	**HPTAI**
	(cm^2)	**(cm^2)**	**(cm^2)**	**(cm^3)**	**(cm^2)**	**(cm)**	**(°)**	**(cm)**	**(cm)**
Voxel_Man	**140**	**113**	**1171**	**1,17**	**107**	**31,0**	**44,7**	**31,5**	**64,2**
RCP_AF	**164**	**142**	**1238**	**3,50**	**146**	**33,1**	**47,2**	**36,3**	**58,8**
VisHum	**168**	**145**	**1353**	**3,96**	**180**	**35,5**	**52,9**	**36,6**	**63,2**
Katja	**164**	**142**	**1238**	**3,50**	**156**	**33,5**	**48,1**	**36,4**	**58,7**
VW_r	**163**	**142**	**1135**	**3,17**	**179**	**36,3**	**49,1**	**32,6**	**57,1**
RCP_AM	**174**	**150**	**1381**	**4,00**	**190**	**36,9**	**58,1**	**35,9**	**63,2**
VW	**191**	**165**	**1556**	**4,08**	**231**	**39,9**	**51,1**	**35,8**	**63,4**
Pearson Correlation Factor (r)	**0,981**	**0,962**	**0,841**	**0,825**	**0,949**	**0,933**	**0,663**	**0,571**	**0,111**
P-Value	**< 0,001**	**< 0,001**	**0,018**	**0,022**	**0,001**	**0,002**	**0,104**	**0,180**	**0,813**

AD_{BVD} – Average distance between brain voxels and the detector; D_{BDGC} – Distance between centers of gravity of the brain and detector; MD_{BD} – Minimum distance between brain and detector; BV – Brain volume; D_{DSAC} - Distance between the parallel planes of detector surface and auditory canals; EED – Ear to ear distance; MDHA – Mean detector-head angle; FHND – Forehead to nape distance; HPTAI – Head perimeter at the top of the auricle insertion.

The square of the mean distance between the brain voxels (source) and the center of the detector - AD_{BVD}, presented the best correlation index with CF (0.981) among the Group 1

parameters. At Group 1, the square of the distance between centers of gravity of the brain and detector (D_{BDGC}) also showed high correlation with CF. Correlation factors lower than 0.9 were found for both the brain volume and the square of the minimum distance between brain and detector. Figure 3 shows the scatter plot graphics of CF and squared AD_{BVD} and squared D_{BDGC} parameters.

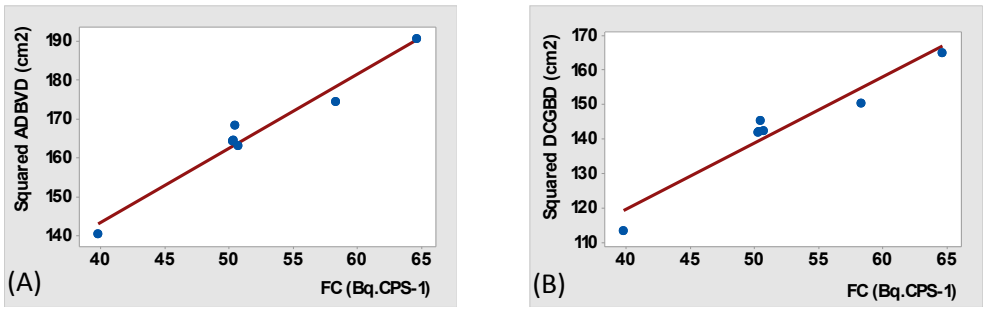

Figure 3 - Scatter plot of CF and squared AD_{BVD} (A) and squared D_{BDGC} parameters (B)

Two of the anatomical parameters of Group 2, that can be measured with simple techniques, presented a Pearson correlation coefficient with the CF values above 0.9: the square of the distance between the parallel planes of the detector surface and auditory canals - DDSAC and the ear to ear distance - EED. The other parameters showed a correlation coefficient below 0.7. Figure 4 shows the scatter plot graphics of CF and squared D_{DSAC} and EED parameters.

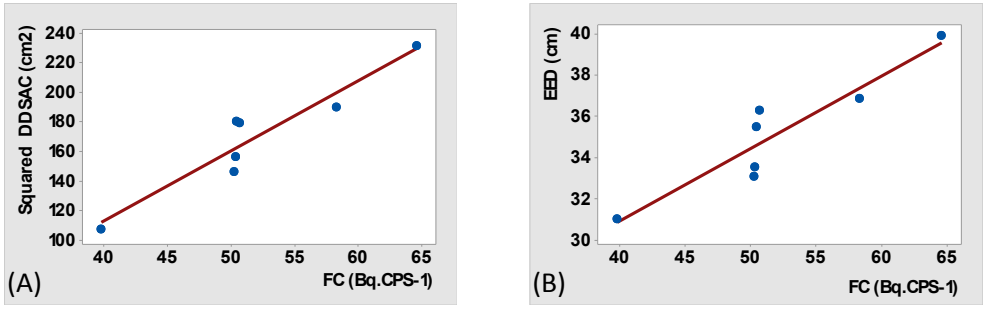

Figure 4 - Scatter plot graphics of CF and squared D_{DSAC} (A) and EED parameters (B)

4.- DISCUSSION

4.1.- CF variation for seven phantoms and HDD influence

The NaI(Tl) detector was positioned in contact with the head (HDD_0) in the established counting geometry for the determination of the ^{18}F-FDG activity incorporated in OEWs involved in the radiopharmaceutical production. In this condition, the deviation percentage between the minimum and maximum CF values ($DCF_{Min-Max}$) was -38.4%. The relative error (ER) was 14.7%, considering the averaged CF obtained for the seven phantoms and its standard deviation. Such values can be considered acceptable for radiation protection purposes. However, it should be kept in mind that the number of models studied was small (seven) and it may represent only a sample of the human population variability.

Moving away the detector from the head reduces $DCF_{Min-Max}$ and ER of -38.4% and 14.7% (HDD_0) to -21.0% and 7.5% (HDD_{100}), respectively. However, an associated reduction in the detection efficiency was observed. The calibration factor for HDD_0 was about 100 times smaller than for HDD_{100}. Usually, *in vivo* internal contamination monitoring is intended to detect even negligible incorporated activities. Thus the counting geometry with better efficiency (HDD_0) must be maintained. On the other hand, when high levels of contamination occur, increasing the distance between the head and the detector could be useful. In addition to a smaller variation of CF values, a reduction in the dead time of the system is also expected. It was observed that $DCF_{Min-Max}$ and ER values for HDD_{50} were practically de same as for HDD_{100}. Therefore HDD greater than 50 cm should not be used.

4.2.- Correlation between anatomical and geometric variables and CF

Group 1 anatomical and geometric parameters, those that can be measured by complex imaging techniques such as MRI and CT, showed a correlation coefficient (r) superior than 0.8. A_{DBVD}, D_{BDGC} are closely associated with the brain shape. These parameters showed the best correlation with CF. The brain volume (BV) had an intermediate correlation with CF within this group, being less than 0.9. In this work MD_{BD} presented the worst

correlation coefficient among Group 1 parameters. The distance between detector-brain (MD_{BD}) depends on the thickness of the tissue layers surrounding the brain (skin, muscle and bone, mainly). Given the low correlation coefficient between MD_{BD} and CF, it is observed that the variation in the composition and thickness of the tissues surrounding the brain of the studied models seems not to be the main factor in influencing CF values.

The results for the present counting geometries and for 511keV-photon source point out to the fact that the shape of the brain has greater influence on the calibration factor than the brain volume or the thickness and composition of tissue layers between the brain and the detector. This statement should be considered with caution, since it is based on a small sample of the population. However, could present important implications, especially for the physical model construction. In these cases, special attention should be given to the brain shape.

The use of complex imaging techniques like MRI to obtain personalized calibration factors is a suitable possibility that may bring good CF estimative. However, its practicability and cost-effectiveness are questionable. Its indication should be limited to situations in which the calculation of the incorporated activity must be performed with great accuracy. Perhaps it can be justified for accidents with high activity uptake. In such cases, a more accurate calculation of the committed effective dose can result in better decisions in the treatment managing of the contaminated person.

The model anatomical and geometric parameters that can be measured with simple techniques showed a wide variation in the degree of correlation with CF (0.949 to 0.111). The MDHA, FHND and HPTAI parameters cannot be considered as good options for estimation of the personalized calibration factors since they have a low correlation coefficient with CF. On the other hand D_{DSAC} square and EED present (r) values exceeding 0.9. D_{DSAC} can be measured in video images from cameras installed in the counting system. A simple apparatus can also be developed to make the D_{DSAC} measurement directly in the person. The distance between the ears can be easily measured with a plastic measuring tape. Also, simulations with a larger number of phantoms must be performed to confirm the

correlation between these variables and CF. If proven, the personalization of CF values may be obtained with a simple technique for all monitored individuals.

5.- CONCLUSIONS

Considering the counting geometric parameter (HDD_0) defined for the ^{18}F-FDG internal contamination monitoring evaluated on the set of seven computational models, one can expect a similar variation of 38% or more on the individual calibration factors among the occupational exposure works.

The deviations of the CF values can be reduced, increasing the distance between the head and the detector which is the brain morphological parameters of the models. Beyond 50 cm the variation reduction is very low. This methodology should only be adopted in cases of severe contamination, since the detection efficiency drop considerably as the head-detector distance increase.

The AD_{BVD} and D_{BDGC} anatomical and geometric parameters of the models were correlated with CF significantly. This indicates that the brain shape has great influence on the calibration factor calculations. MRI images can be used to measure this parameter, thus personalized calibration factors can be generated. However the high cost of this imaging technique limits its use only to situations where greater accuracy in incorporating activity calculation is required.

Among the anatomical parameters that can be measured easily, D_{DSAC} and EED showed good correlation with CF for the studied phantoms. If such statement can be confirmed in studies with a larger number of computational phantoms, personalized calibration factors can be achieved for all monitored individuals with relative simplicity.

Acknowledgments

We would like to thank the Laboratório de Metrologia de Nêutrons of the Instituto de Radioproteção e Dosimetria (IRD/CNEN) for consenting the use of high-performance cluster for the calculations. This work is part of the project MCTI INCT Radiation Metrology in Medicine and is also supported by the following Brazilian institutions: Fundação de Amparo à Pesquisa de Minas Gerais (FAPEMIG – Projeto Universal), and Conselho Nacional de Desenvolvimento Científico e Tecnológico (CNPq-REBRAT-SUS).

REFERENCES

CANBERRA. Canberra Industries, Inc. MODEL 802 – SCINTILLATION DETECTORS. United States of America (2009).

Cristy M; Eckerman K F. (1987). *Specific Absorbed Fractions of Energy at Various Ages from Internal Photon Sources – I.Methods*. Oak Ridge National Laboratory, Oak Ridge, Tennessee, USA.

Fonseca T C F; Bogaerts R; Hunt J; Vanhavere F. (2014a). *A methodology to develop computational phantoms with adjustable posture for WBC calibration*. Physics in Medicine and Biology, **59(22)**: 6811-6825.

Fonseca T C F; Bogaerts R; Lebacq A L, Mihailescu C L; Vanhavere F. (2014b). *Study of the Counting Efficiency of a WBC Setup by Using a Computational 3D Human Body Library in Sitting Position Based on Polygonal Mesh Surfaces*. Health Physics, **106(4)**: 484-493.

GSF - German Research Center for Environmental Health. Helmholtz Zentrum München. Helmholtz Zentrum München. AMSD Research Unit Medical Radiation Physics and Diagnostics. (2016). http://www.helmholtz-muenchen.de/amsd/service/scientific-services/index.html. (accessed September 05 2016).

Gulyás B; Halldin C. (2012). *New PET radiopharmaceuticals beyond FDG for brain tumor imaging*. The Quarterly Journal on Nuclear Medicine and Molecular Imaging, **56**: 173-190.

ICRP Publication 89. (2002). *Basic Anatomical and Physiological Data for Use in Radiological Protection: Reference Values*. Annals of ICRP, **32(3-4)**: 1-277.

ICRP Publication 107. (2007) *Nuclear Decay Data for Dosimetric Calculations*. Annals of ICRP, **38(3)**: 1-96.

ICRP Publication 110. (2009). *Adult Reference Computational Phantoms*. Annals of ICRP, **39(2)**: 1-166.

ICRU Report 46. PHOTON, ELECTRON, PROTON AND NEUTRON INTERACTION DATA FOR BODY TISSUES. Bethesda, United States of America (1992).

Mendes B M; Fonseca T C F; Vital K D; Paiva F G; Santana P C; Silva T A; Campos T P R. (2016). *Validação da Modelagem Computacional do Fantoma de Cabeça do Laboratório de Dosimetria Interna – LDI/CDTN para Monitoração da Contaminação Interna.* SENCIR - Terceira Semana de Engenharia Nuclear e Ciências das Radiações, Belo Horizonte, Brazil, October 4-6, **n/a**.

National Library of Medicine (NLM). (2016). The Visible Human Project. https://www.nlm.nih.gov/research/visible/visible_human.html. (accessed September 05 2016).

National Nuclear Data Center (NNDC). (2016). ENSDF Decay Data in the MIRD (Medical Internal Radiation Dose) Format for 18F. http://www.nndc.bnl.gov/useroutput/18f_mird.html (accessed September 05 2016).

Oliveira C M; Dantas A L; Dantas B M. (2009) *A methodology to evaluate occupational internal exposure to fluorine-18*. Cellular and Molecular Biology (Noisy-le-Grand, France), **55(3)**: 29-33.

Oliveira C M; Lima F F; Oliveira M L; Silva T V; Dantas A L; Dantas B M; Alonso T C; Silva T A. (2013) *Evaluation of a technique for in vivo internal monitoring of ^{18}F within a Brazilian laboratory network*. Radiation Protection Dosimetry, **153(1)**: 100.105.

Petoussi-Henss N; Zankl M; Fill U; Regulla D. (2002). *The GSF family of voxel phantoms*. Radiation Protection Dosimetry, **47**: 89-106.

PubMed. (2016) National Center for Biotechnology Information (NCBI), National Library of Medicine (NLM), National Institutes of Health (NIH). http://www.ncbi.nlm.nih.gov/pubmed/?term=fdg+and+pet (accessed September 05 2016).

Reynaert N, Palmans H, Thierens H, Jeraj R. (2002). *Parameter dependence of the MCNP electron transport in determining dose distributions*. Medical Physics, **29(10)**: 2446-2454.

Treglia G; Sadeghi R; Del Sole A; Giovanella L. (2014). *Diagnostic performance of PET/CT with tracers other than F-18-FDG in oncology: an evidence-based review*. Clinical and Translational Oncology. **16**: 770–775.

IPAG. (2016). Yale University School of Medicine. Image Processing and Analysis Group -IPAG. The Zubal Phantom – Voxel based anthropomorphic phantoms. http://noodle.med.yale.edu/zubal/data.htm. (accessed September 05 2016).

Zankl M; Veit R; Williams G; Schneider K; Fende H; Petoussi N; Drexler G. (1988). *The construction of computer tomographic phantoms and their application in radiology and radiation protection*. Radiation Protection Dosimetry, **27**: 153-164.

Zubal I G; Harrell C R; Smith E O; Rattner Z; Gindi G R; Hoffer P B. (1994). *Computerized Three-dimensional Segmented Human Anatomy*. Medical Physics, **21(2)**: 299-302

Dose profile study in head CT scans using radiochromic films

Alvaro Mauricio Ladino Gómez[1*] and Arnaldo Prata Mourão[1,2]

[1] Department of Nuclear Engineering, Federal University of Minas Gerais,
Av. Antônio Carlos 6627, CEP: 31270-90, Pampulha, Belo Horizonte, MG, Brazil
amlgphys@gmail.com

[2] Biomedical Engineering Center, Federal Center for Technological Education of Minas Gerais,
Av. Amazonas, 5253 - Sala 113. CEP: 30421-169, Nova Suíça, Belo Horizonte, MG, Brazil
apratabhz@gmail.com

Abstract

Diagnostic images of Computed Tomography generate higher doses than other methods of diagnostic radiology using X-ray beam attenuation. Clinical applications of CT have been increased by technological advances, what leads to a wide variety of scanner in the in Brazilian technological pool. It has been difficult to implement dose reduction strategies because of the lack of proper guidance on computed tomography examinations. However, CT scanners allow adjusting acquisition parameter according to the patient's physical profile and diagnostic application for which the scan is intended. The knowledge of the dose distribution is important because changes in image acquisition parameters may provide dose reduction. In this study, it was used a cylindrical head phantom in PMMA with 5 openings, what allows dose measurement in 5 regions. In a GE CT scanner, DISCOVERY model of 64 channels, the central slice of the head phantom was irradiated and the absorbed doses were measured using a pencil ionization chamber. Radiochromic film strips were placed in the peripheral and in the central region of the head phantom and was performed a scan of 10 cm in the phantom central region. The scan was performed using the head scanning protocol of the radiobiology service, with a voltage of 120 kV. After scanning, the radiochromic film strips were digitalized and their digital images were used to have the dose longitudinal profiles. The dose values recorded have variation in a range of 18,66 to 23,57 mGy. In the results it was compared the dose index values obtained by the pencil chamber measurement to the dose longitudinal profiles recorded by the film strips.

Keywords: dosimetry, computed tomography, medical images.

1.- INTRODUCTION

Health professionals are helped by diagnostic images to detect different diseases. Image acquisition protocols should be based on research to maintain or improve the image quality and reduce risks due to the use of ionizing radiation. For this reason, evaluation of the patient's mass and volume needs to be observed, the analysis of the optical density, the dose measurement and contrast are some factors to be considered to optimize the parameters for image acquisition with diagnostic quality [Dalmazo et al., 2010; Dance 2014].

It may be difficult to detect small variations in the body internal structures due to inherent artifacts of medical images. It is necessary to get a contrast between the surrounding structures and the structure wanted to be observed. In practice this means that this structure must have a X-ray beam absorption different from the others neighboring structures [Almeida 2008; Calzado and Geleijns 2010].

The use of computerized systems and digital images leads the process of diagnostic to another level of quality, significantly increasing its diagnostic applications. Thus, this kind of technology brings new challenges related to the image acquisition that demand an assessment to minimize the risk-benefit [Andisco et al,. 2014; Rodrigues et al., 2009].

Computed Tomography (CT) had its first applications in the decade of 1970s and over the years has become one of the most important methods of diagnostic imaging, significantly improving the quality of medical services. CT images allow observing low contrast structures such as soft tissues, unlike radiographies. CT scans are radiological tests responsible for the greatest contribution to the population dose [Augusto 2009].

2.- MATERIALS AND METHODS

Experiments were performed in a GE CT scanner; model DISCOVERY with 64 channels using a head phantom. This phantom has a cylindrical shape with 16 cm in diameter and 15 cm in length, made in polymethyl methacrylate (PMMA). The phantom has five openings, one central and four peripherals lagged each other 90°. The peripheral openings have their center located 1cm from the edge. The openings have dimensions of 1.27 cm in diameter and 15 cm in length. For the positioning of the phantom in the gantry isocenter the peripheral openings were aligned similarly with them positions 3, 6, 9 and 12 hours of an analog clock. The phantom positioning is observed in the Figure 1.

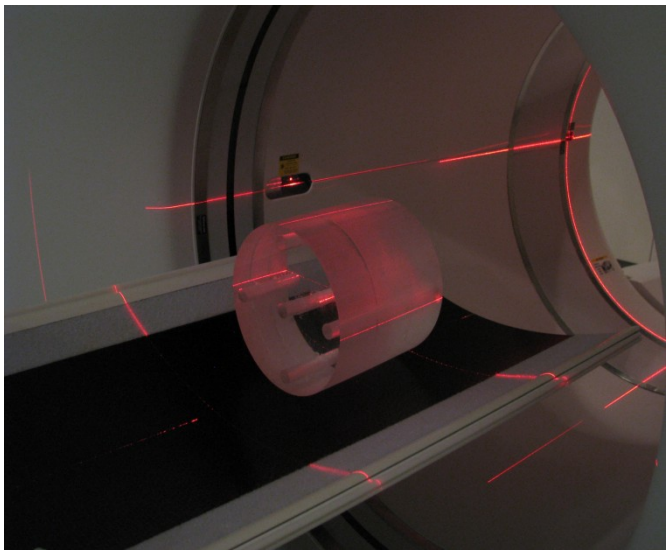

Figure 1. - Positioning of the head phantom in the gantry.

The absorbed dose measurements were made with an ionization chamber RADCAL®, Model ACCU-GOLD2. The central slice of the phantom was successively irradiated with the pencil chamber placed into the phantom. The pencil chamber was placed alternatively in each positon while the others positions were filled with cylindrical PMMA rods with 1.27 mm in diameter and 15 cm in length. For each chamber placement it has got five measurements.

A Radiochromic film sheet, model GAFCHROMIC XR-QA2A®, was used for the longitudinal dose profile records. Strips were cut in sizes of 0.5 x 12.5 cm^2 and identified, then, they were placed into special cylindrical rods made in PMMA with 1.27 mm in diamenter and 15 cm in length. The PMMA rods, charged with the film strips, were placed into the five phantom openings. The irradiation of the film strips was done with a helical CT scan.

Radiochrimic films exhibit a darkening proportional to the amount of deposited energy when exposed to ionizing radiation. The film used was developed as a tool for quality control of ionizing radiation beams and it is not sensitive to visible light. This film is recommended for record doses in a range of 0.1 to 20 cGy for X-ray beams generated by voltages in the range of 20 to 200 kV. In the Figure 2 it is possible observe the contrast of the color intensity between an irradiated strip *a* and a non-irradiated strip *b* (Background). Scanned images of the film strips were obtained for observing the color intensity variation generated by exposure [Ashland Inc. 2015].

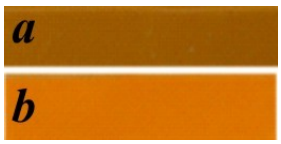

Figure 2. - Radiochromic film strips, irradiated (*a*) and background (*b*).

Digital image of the film strip was performed with a Hewlett Packard scanner, model Scanjet G4050 in a reflexive mode and with a 300 ppi resolution. Digital images were saved in .jpg format. The obtained images were worked with the imageJ software and processed using the tool split colors RBG (red, blue and green). Only the color red has been used to observe the color intensity variation in greyscale. The color red was chosen because it has the greater response variation. The intensity values obtained from the irradiated strips were subtracted from the intensity value recorded in a non-irradiated strip.

The protocols used to irradiate the central slice to do measurements with the pencil chamber and to scan 10 cm of the central region of the phantom to irradiate the film strips are shown in the Table 1.

Table 1.- Irradiation parameters.

Detector	Technique	Voltage (kV)	Charge (mA.s)	Tickness beam (mm)	Length (cm)	pitch
Pencil Chamber	axial	120	100	10	-	-
Film strips	helical	120	100	40	10	0,984

3.- RESULTS

The CT dose index values ($CTDI_{100}$) and standard deviation (SD) obtained with the pencil chamber measurements are presented in the Table 2. The recorded values variation is in a range of 18,66 to 23.57 mGy to the central slice irradiation. The minimum recorded value is in the central position and the maximum in the 12 position.

Table 2: Measures of $CTDI_{100}$ (mGy).

Position	3	6	9	12	Central
	20.80	19.30	20.31	22.63	18.73
	20.79	19.36	20.40	22.65	18.73
Measures	20.83	19.37	20.33	23.57	18.72
	20.82	19.55	20.33	22.67	18.70
	20.80	19.45	20.31	22.74	18.66
Average	20.80	19.40	20.33	22.85	18.71
SD	0.02	0.10	0.04	0.40	0.03

The average dose values were obtained through measures with ionization chamber, whereas the pitch used in CT scan for the film strips irradiation, was used to perform the calibration of the film strips and convert the color intensity values, in greyscale, to Absorbed Dose in mGy [NIST 2016].

Longitudinal profile curves of absorbed dose were obtained from the digital images of the film strips. The table 3 presents the absorbed dose values reported by the ionization chamber corrected by the pitch with the intensity color values of the film strip darkening. They were used to obtain the calibration factors for each one of the five measured points.

Based on $CTDI_{100}$ values measured in the central and phantom peripheral openings, it was possible to calculate the weighted dose index ($CTDI_w$), and the volumetric dose index $CTDI_{vol}$, given by equation 1 and 2 [Wambersie 2008]. The values obtained were of 20.13 and 20.46 mGy, respectively.

$$CTDI_w = \frac{1}{3} CTDI_{100,C} + \frac{2}{3} CTDI_{100,P} \quad (1)$$

$$CTDI_{vol} = \frac{CTDI_w}{pitch} \quad (2)$$

Table 3: Absorbed dose values, darkening of films and calibration factors.

Position	Absorbed Dose (mGy)	Color Intensity (greyscale)	Calibration Factor (mGy/greyscale)
3	21.14	66.95	0.315
6	19.72	64.76	0.304
9	20.67	67.57	0.305
12	23.22	69.68	0.333
Central	19.02	64.02	0.297

In the Figure 3 longitudinal dose profile curves recorded by the film strips in the five positions are shown. These curves obtained have a similar behavior, in which the maximum dose values happen in the central region. Recorded dose values are lower in the central position and grow in sequentially positions 6, 3, 9 and 12.

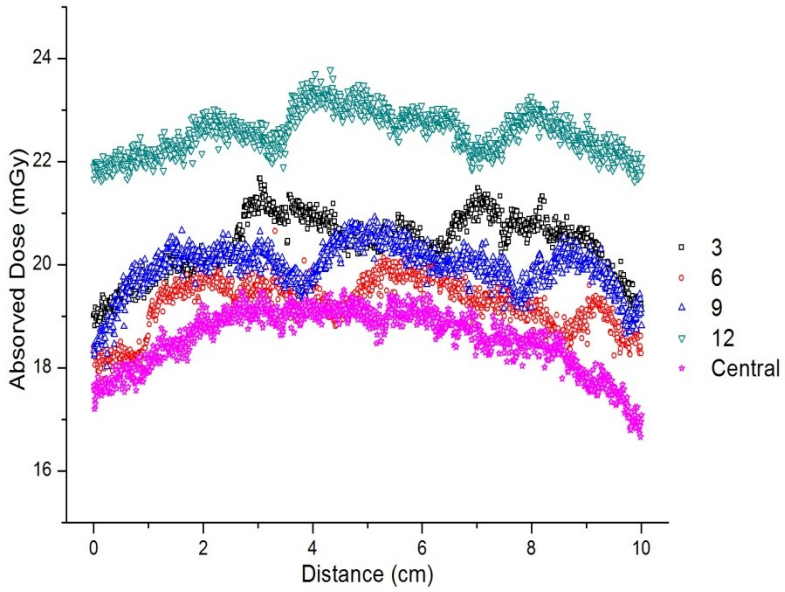

Figure 3.- Dose profile curves.

The Fig. 4 presents a bar graph with the average dose values recorded by film strips.

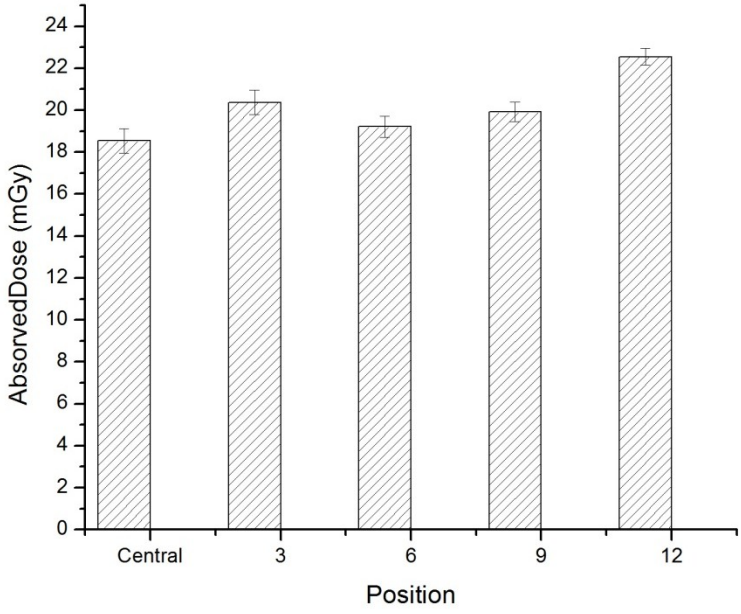

Figure 4.- Average absorbed dose obtained by the film strips.

4.- DISCUSSIONS

Recorded values in the 6 position are the lowest among the records in peripheral positions, due to the attenuation of the X-ray beam promoted by the table in the incidence infero-superior. This behavior was observed by the measuring performed with the pencil chamber, the minimum dose value recorded happens in the central position and the maximum in the 12 position.

In the dose profile graph it is possible to observe that the 12 position received the greatest amount of radiation since in that position it experiences less attenuation of the X-rays beam, while the opposite occurs in the position 6, since this point is more closer to the table where the phantom is placed.

All the Dose profile curves present the higher dose values in the central region and lower ones in the extremities, demonstrating the greater influence of scattered radiation in the dose composition of the central slice. The dose profile curve in the central position has a continuous behavior because this position has a constant distance from the X- ray beam focus during all the time. On other hand, peripheral curves present two valleys separated by 4 cm, because that is the beam thickness. These valleys happen when the X-ray beam is the farthest distance from the point of measurement. Thus, the valleys are lagged a ninety-degree angle, as the peripheral positions of measurements.

4.- CONCLUSIONS

Absorbed dose records by the radiochromic film strips for each position of measurement in the head phantom were similar to the values obtained by the pencil ionization chamber. Film strips may be used as a reliable tool in the analysis of absorbed dose, in the search for optimizing the acquisition protocols for head CT scans.

The longitudinal dose profile curves recorded by film strips present information of the dose distribution inside the phantom. The radiochromic films provided detailed information about the absorbed dose along the longitudinal axis.

Absorbed dose values found in the processing of film strips are slightly higher than the values obtained by ionization chamber by reason of the pitch value of 0.984. The volumetric dose index value obtained with the data recorded by the pencil ionization chamber is close to the value indicated by the helical scanning equipment report.

Acknowledgments

The authors are thankful to CAPES, FAPEMIG & CNPq for their support in this study, we also thanks the technical and specialized professionals in the handling equipment and the Federal University of Minas Gerais UFMG.

REFERENCES

Almeida M. (2008). *Avaliação da Qualidade de Imagem e do Índice Volumétrico de Kerma Ar em Tomografia Computadorizada (C_{vol}) em Recife*. Dissertação (Mestrado)-Universidade Federal de Pernambuco. Programa de Pós-graduação em Tecnologias Energéticas e Nucleares. Recife, Brazil

Andisco D; Blanco S, Buzzi A E. (2014). *Dosimetry in Computed Tomography*. Revista Argentina de Radiología; 78(3): 156-160. Buenos Aires, Argentina.

Ashland Inc. [online] *Gafchromic™ XR film. Gafchromic™ Rdiology Films*, <http://www.ashland.com/products/gafchromic-radiology-films>. [Reviewed on December 2015].

Augusto F M. (2009). *Estudo da Qualidade da Imagem e Índices de Dose em tomografia Computadorizada*. Dissertação (Mestrado)-UFRJ/ COPPE/ Programa de Engenharia Nuclear. Rio de Janeiro, Brazil.

Calzado A; Geleijns J. (2010). *Computed Tomography. Evolution, technical principles and applications.* Revista de Física Médica; 11(3): 163-180. Spain

Dance, DR. et al. *Diagnostic radiology physics: A handbook for teachers and students*. American Association of Physicists in Medicine. (2014).709p.

NIST. [online]. *National Information Security and Technology News*. <http://www.nist.org/>. [Reviewed on January 2016].

Rodrigues D; Barbosa S; Ghilardi T, et al. (2009) *Quality control and dosimetry in computed tomography units.* Colégio Brasileiro de Radiologia e Diagnostico por Imagem Mai/Jun;42(3): 171-177. Brazil

Wambersie, A. (2008) *Radiation Quantities and Units, Dose to Patient, and Image Quality in Computed Tomography (CT).* European Commission. 18-19.

Angular Dependence on the Records of Dose in Radiochromic Films Strips

Kamila Cristina Costa[1], Thessa Cristina Alonso[2,4]
Paulo Márcio Campo de Oliveira[3], Arnaldo Prata Mourão[1,4]

[1] Biomedical Engineering Center, Federal Center for Technological Education of Minas Gerais,
Av. Amazonas, 5253 - Sala 113. CEP: 30421-169, Nova Suíça, Belo Horizonte, MG, Brazil
kamilacosta1995@gmail.com

[2] Development Center of Nuclear Technology, CNEN
Av. Antônio Carlos 6627, CEP: 31270-90, Pampulha, Belo Horizonte, MG, Brazil
alonso@cdtn.com

[3] Department of Anatomy and Imaging, Federal University of Minas Gerais,
Av. Prof. Alfredo Balena, 190 CEP: 30130-100, Belo Horizonte, MG, Brazil
paulomarcio2000@gmail.com

[4] Department of Nuclear Engineering, Federal University of Minas Gerais,
Av. Antônio Carlos 6627, CEP: 31270-90, Pampulha, Belo Horizonte, MG, Brazil
apratabhz@gmail.com

Abstract

Radiological images have relevant information both for the diagnostic results as to treatment decisions. Then, the diagnostic quality of image that allows a proper analysis should be achieved with the lowest possible deposition of dose in a patient. CT scans produce sectional images that allow the observation of internal structures of the human body without overlap. As in conventional radiology, the contrast which allows obtaining CT images results from the difference in X-ray beam absorption, according to the characteristics of each tissue. The increased of the beam absorption by a tissue means that it appears brighter in the image. In CT scanners, X-ray tube rotates around the patient, and this rotation results in a cross-sectional image of the body. From a sectional image series is possible to obtain a 3D image that can be viewed from different angles. Among the methods of dose measurement is the use of radiochomic films, which record the energy deposition by darkening its emulsion. The radiochromic films show little sensitivity to visible light and respond better to exposure to ionizing radiation. In this work, strips of the radiochromic film GAFCHROMIC XR-QA2 were irradiated at different angular positions for radiation quality RQT8, defining a beam of X-rays generated from a voltage of 100 kV. The response of radiochromic films depending on the doses was assessed through digital images obtained by HP Scanjet G4050 scanner. Digital images were analyzed using ImageJ software, which allowed obtaining numerical

values corresponding to the intensity of darkening for each film. The aim of this study is to evaluate the dose deposition in radiochromic film according to the angular variation in order how is affected the record. So, to examine the use of film strips to record doses in Computed Tomography tests.

Keywords: *dosimetry; radiochromic film; angular dependence.*

1.- INTRODUCTION

Computed tomography (CT) unlike the conventional diagnostic methods, can observe internal structures of the human body producing sectional images of the human body, without overlapping tissues. In CT, an X-ray tube rotates around the patient irradiating a thin tissue slice, and this rotation allows generating a cross section image of the irradiated slice. This way, from a sectional image series is possible to obtain a 3D image that can be viewed from different angles. As in conventional radiology, contrast which allows obtaining CT images results from the difference in X-ray beam absorption, according to the characteristics of each tissue. The increased of the X-ray beam absorption by a tissue means that it appears brighter in the image [Mourão 2015].

Despite the evolution of CT scanners, the increase in the number of survey information was not followed by significant reduction in radiation dose received by the patient. CT examination generates a much higher dose to the patient when compared to other radiological tests, also based on X-ray technology. An addition CT tests with greater exposures produce better images [Mourão 2009; Dance et al 2014].

Radiochromic films are a dose measurement methods commonly used for quality control. They have a polymeric structure in an emulsion layer which darkens as it receives a certain amount of radiation. A greater the amount of radiation reaching the film means it will be darker. [Rampado et al. 2006].

The aim of this study is to evaluate the angular dependence to the dose deposition in radiochromic film strips in order to use them in experiments to record absorved dose in CT tests. In CT tests the X-ray beam incidence varies throughout the patient irradiation process and therefore, the use of radiochromic film in CT tests should considerate this characteristic. The X-ray beam incidence angle can interfere in the process of dose measurements with film strips.

2.- MATERIALS AND METHODS

In this work, we used the film GAFCHROMIC® XR-QA2, specific to radiology applications. This film has high sensitivity to ionizing radiations with doses in the range from 1.0 to 200 mGy and it can work with X-ray beams generated from voltages between 20 kV and 200 kV, for this, it is indicated for dose deposition analysis involving X-ray beams [Alnawaf et al. 2010; Silva et al. 2010; Ashland Inc. 2016].

Radiochromic films are basically made up of three layers: coating, emulsion and base. These films allow viewing of changing colors with a high contrast due to yellow polyester coating. However, the coating does not affect spectral absorption properties in the red region, which is the main region of interest for analysis in reflected mode by scanners. Figure 1 shows the separation of a film strip into layers.

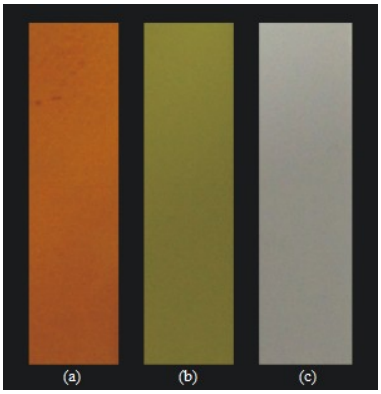

Figure 1 - Radiochromic film layers: yellow transparent coating (a), green emulsion (b) and white base (c).

The degree of color intensity recorded by the film allows the correlation with the absorbed dose. Figure 2 shows filmstrips irradiated with different absorbed dose values.

Figure 2 – Intensity color variation degree by irradiation, reference strip and irradiated strips irradiated with increasing doses from the left.

The process of preparation and irradiation of the films was carried out following three steps: preparing film strips, film strips irradiations and data collection.

The film strips are produced by cutting a radiochromic film sheet GAFCHROMIC® XR-QA2. It was cut into six film strips of 0.5 x 5.0 cm^2. Then they have been identified to be irradiated by an X-ray beam generated by a voltage of 100 kV. For the irradiation of the film strips they were prepared on a Styrofoam support, which is a material with light absorption, preventing the scattered radiation generation. The films were positioned on the support in order to adapt them to the angular positions of X-ray beam incidence for angles of 0°, 45°, 90°, 135°, 180° and 270.

Film strip support was placed 2.0 m far from the X-ray beam focus and the strips received an air kerma of 19.63 mGy. The X-ray beam was produced by industrial equipment *Pantak Seifert*, Model HS ISOVOLT 320 of constant potential. The machine operates in the range of 5 to 320 kV, with a current ranging from 0.1 to 45 mA, power dissipation at maximum anode 2240 W and can be operated continuously varying only the power of energy dissipation according to the focus that is being used: the thick focus with the size of 3.6 mm and fine of 1.9 mm. The machine is very stable and operates under conditions in which the standard deviation of the intensity of X-ray beam does not exceed 0.3% of the measurements. Figure 3 shows the setup used in the film strip exposition.

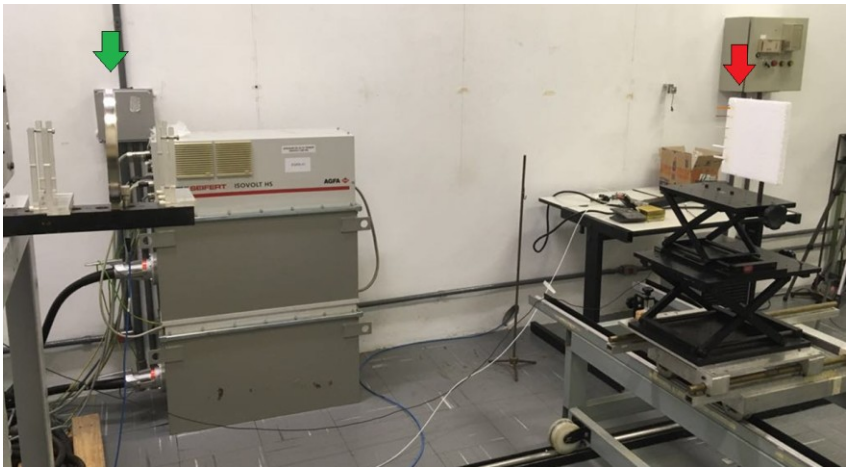

Figure 3 - Setup for irradiation film strips (green and red arrows indicate the position of X-ray tube and film strips).

After irradiation, digital images of radiochromic film strips were obtained, with a resolution of 300 ppi, using an HP Scanjet G4050 scanner. The digital images were processed using ImageJ software, in order to evaluate the responses of intensity color of the strips, according to the angular variation. This software allowed the split of RGB colors, and only the color red data was used.

In the image obtained for the change in the red color it was carried out the color inversion in greyscale and there were obtained numerical values corresponding to the darkening intensity for each one of the five strips exposed. One strip was not irradiated and its record in greyscale was subtracted from the other values of the irradiated strips. The intensity value recorded in the not-irradiated film strip, for the red color in the greyscale, was 37.77.

3.- RESULTS

With the numerical values obtained from scanned images of film strips the change in the intensity color value was obtained in greyscale. For every strip it has been obtained an average intensity value and a standard deviation. Table 1 correlates the average value in greyscale with the angular position for each film strip. This table also shows the variation of each grayscale value compared to the value of the 0° film strip. This strip was considered as the reference in which the X-ray beam incident is perpendicular to the emulsion layer passing first by the yellow transparent coating.

In subdivisions of film layers, the emulsion is deposited on the base and the emulsion has a protection coating. The base of GAFCHROMIC® XR-QA2 is a little more radiopaque than the yellow transparent coat

Table 1.- Intensity values recorded in greyscale correlated with the angular position of the film strip.

Angular Position	Intensity greyscale	SD	Variation (%)
0°	72.16	0.56	-
45°	71.67	0.66	-0.68
90°	59.25	0.70	-17.90
135°	70.13	0.48	-2.20
180°	71.33	0.61	-1.15
270°	57.22	0.56	-20.70

Figure 4 shows radiography of the base layer (a) and yellow coat (b). Therefore, when irradiation is done, the X-ray beam should preferably pass through the transparent cover first. So, it means that the beam is minimally filtered before interacting with the emulsion layer.

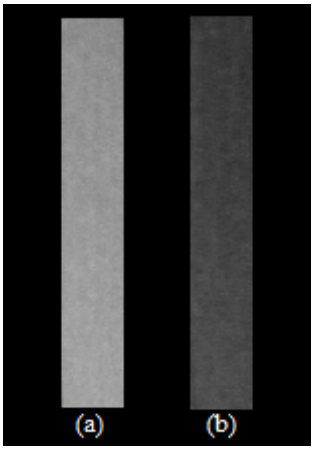

Figure 4: X-ray of the radiochromic film layers, white base (a) transparent coating (b).

4.- DISCUSSION

The maximum intensity value recorded occurs in the strip with an X-ray incidence angle of 0°, directly irradiated. For the strips placed in 45°, 135° and 180° the records were a bit smaller than the intensity value recorded by the film strip in 0°. For the film strips in 90° and 270° the recorded values presented the greater difference.

The strips in 45° and 135° have nearest records. However the darkening for the angle 135° is smaller than the incident to position 45°. When the beam enters by the base layer there is bit more absorption before it reaches the emulsion layer, because transparent coating layer is less radiopaque then the base.

As the strip 180° has the opposite position to the reference, its darkening was slightly lower, as the base received the beam directly and this came less intense to the emulsion layer. Records for the strips 90° and 270° showed the greatest variations in relation to the reference because the beam incidence was parallel to layers of these strips, as occurred perpendicular to the strip layers 0°.

5.- CONCLUSIONS

From the observed results, it was concluded that absorbed dose by the patient's tissues in CT scans does not occur homogeneously due to the body heterogeneities, position on the table of the CT scanner and the rotation of X-ray tube around the patient.

Calibration of radiochromic film developed for use in diagnostic radiology must be taken into account that the incidence angle of the X-ray beam may interfere in the darkening response of the film.

Thus, calibration using a reference beam for CT scans that uses only the direct beam incidence on the coating layer may not meet the necessary characteristics for dose measurements directly in CT scans, unless with the use of a correction factor. When using phantom in CT tests, film strips are placed parallel to the longitudinal axis of the table. In this case, the X-ray beam hits the film strips with angles ranging from 0 to 360^{o}.

Acknowledgments

Acknowledgements to support provided by CAPES, FAPEMIG and CDTN/CNEN. This work is part of the project INCT Metrology of Radiation in Medicine.

REFERENCES

Alnawaf H, Tsang C, Butson MJ, Yu PKN. (2010). *Absorption spectra response of XRQA radiochromic film to x-ray radiation*. Radiation Measurements **45**: 129-132.

Ashland Inc. [online] *Gafchromic™ XR film. Gafchromic™ Radiology Films*, <http://www.ashland.com/products/gafchromic-radiology-films>. [Reviewed on May 2016].

Dance, DR. et al. *Diagnostic radiology physics.* (2014). A handbook for teachers and students. American Association of Physicists in Medicine. 709p.

Mourão AP, Oliveria FA. *Fundamentos de Radiologia e Imagens.* São Paulo, Difusão Editora (First edition, 2009).

Mourão AP. *Tomografia Computadorizada: tecnologias e aplicações.* São Paulo, Difusão Editora. Rio de Janeiro, Editora Senac (Second edition, 2015).

Rampado O, Garelli E, Deagostini S, Ropolo R. (2006). *Dose and energy dependence of response of Gafchromic® XR-QA film for kilovoltage x-ray beam.* Physics in Medicine and Biology **51**: 2871-2881.

Silva MSR, Khoury HJ, Borrás C, Cassola VF, Ginori JL. (2010). *Calibração do filme radiocrômico GAFCHROMIC XR-RV2 para radiologia.* Revista Brasileira de Física Médica **4(2)**: 45-48.

Dosimetric Study on Head CT Scans Using Adult and Newborn Phantoms

Giovanni Antônio Paiva de Oliveira[1,2] and Arnaldo Prata Mourão[1,3]

[1] Department of Nuclear Engineering, Federal University of Minas Gerais,
Av. Antônio Carlos 6627, CEP: 31270-90, Pampulha, Belo Horizonte, MG, Brazil

[2] Department of Anatomy and Imaging, Federal University of Minas Gerais,
Av. Prof. Alfredo Balena, 190 CEP: 30130-100, Belo Horizonte, MG, Brazil
giovanni_paiva@hotmail.com

[3] Biomedical Engineering Center, Federal Center for Technological Education of Minas Gerais,
Av. Amazonas, 5253 - Sala 113. CEP: 30421-169, Nova Suíça, Belo Horizonte, MG, Brazil
apratabhz@gmail.com

Abstract

Computed Tomography is the radiodiagnostic method that most contributes to the dose deposition in population. Therefore, the dose reductions used in these tests are very important, especially for pediatric patients who have a life expectancy greater than the rest of the population. This study purpose to compare the doses generated from newborns compared to adult patients in head Computed Tomography scans. Two head phantoms in a cylindrical shape made in PMMA were used, one to adult and another to newborn patient dimensions. The pediatric routine scan protocol from a radiological service was used for the Computed Tomography scans. They were performed in General Electric Computed Tomography scanner, Bright Speed model with 4 channels. The absorbed dose measurements were performed with a pencil chamber placed into both phantoms. The newborn head phantom was developed in order to compare the amount of absorbed dose by the phantoms when it is used the same acquisition protocol. The dose found for newborn phantom was 29.9% higher than the adult phantom.

Keywords: Dosimetry, Computed Tomography, Medical Images.

1.- INTRODUCTION

Computed Tomography (CT) is diagnostic radiology method a known since 1972, and since then it had an exponential improvement in its technological performance and a remarkable growth in its clinical use. The use of helical scans associated with multidetectors arc allowed to reduce the acquisition time of the CT tests and to improve the image quality leading to a more reliable study [Ribeiro and Pereira 2012].

The radiation used in CT tests can cause damages to human cells and can lead to tumor development. An international radiation protection standard was created in order to minimize the danger of the radiation for occupational and public exposure. The radiological protection standard applies to the principle of justification and optimization as well as the dose or risk limitation. The standard control is to achieve by local and individual monitoring, including a trustful instrumentation, measurements and their interpretation [Alonso 2009].

CT is the diagnostic radiology method which most contributes to dose deposition in population, and and for this reason the reduction of doses used in these tests become very important, especially for pediatric patients. [Alonso 2009].

Several countries have already implemented into their legislation the need to check the doses received by patients who undergo radiological tests through defined measurements and related parameters. The Brazilian legislation defines limites only by MSAD (multiple scan average dose) in a typical adult patient as a parameter of quality control of the CT scans. The values are a maximum limit of 50 mGy to the head , 35 mGy to the lumbar spine and 25 mGy to the abdomen . [Brazil 1998].

To make sure that such low radiation levels are reasonably applicable in the CT tests, the optimization and justification principles must be considered, as the cumulative dose increases each time the patient undergoes a CT scan [McNitt-Gray 2002].

There are several factors that have a direct impact on the cumulative dose, such as the radiation beam spectrum, the current and voltage supply of the X-ray tube, the tube time rotation, the beam thickness, the scanning length, the shape of the cut section, the pitch and the distance from the beam focus to the gantry isocenter [Alonso 2009].

The factors that directly influence the image quality may not have a direct impact on the radiation dose, such as the reconstructive filters. Choices of different parameters in CT protocols o can change the dose in patient [Oliveira 2011].

2.- MATERIALS AND METHODS

2.1.- Ionization Chamber:

The studies to observe the absorbed dose variation of an adult and a newborn (NB) head phantom were performed in the General Electric CT scanner, Bright Speed model with 4 channels using a pencil chamber

.

The pencil ionization chamber connected to the electrometer is used in dosimetry of X-ray beams in CT scanners. In this study it was used a Unfors Ray Safe system composed by a pencil ionization chamber and a electrometer. Fig. 1 shows the pencil ionization chamber and the electrometer used in the measurements.

Figure 1.- Pencil ionization chamber and electrometer UNFORS Ray Safe.

2.2.- Phantoms

The adult and newborn (NB) head phantoms have a cylinder shape with 16 cm and 11 cm in diameter, respectively. Both phantoms have a length of 15 cm and are made in PMMA. The newborn head phantom was built based on the measurements of head circumference of 34.54 cm, which corresponds to 42 weeks or 14 days of life for a male newborn and 44 weeks or 28 days of life for a female newborn [Villar et al. 2015]. The head phantoms have five openings, one central and four peripherals lagged by 90 degrees. The peripheral openings have the center 10 mm from the edge of the phantom. Figure 2 shows a frontal view of the newborn and adult head phantoms, and the draw in Figure 3 shows their dimensions.

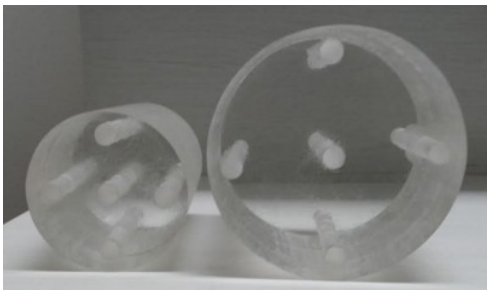

Figure 2.- newborn and adult head phantoms.

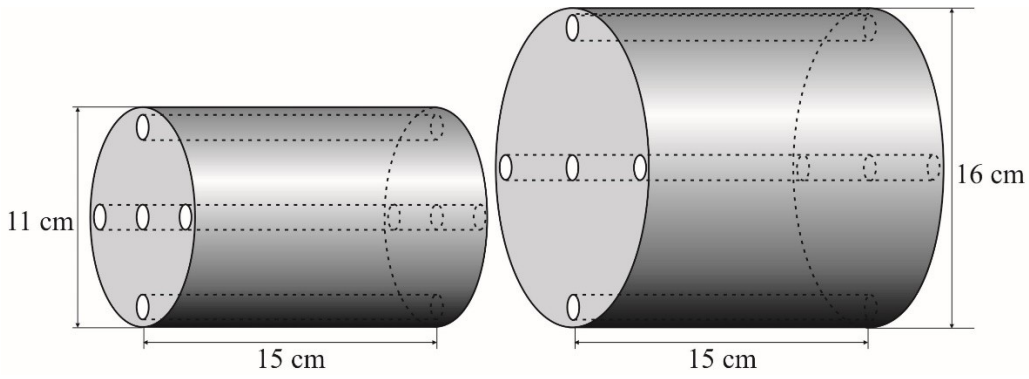

Figure 3.- Dimensions of the newborn and adult head phantoms.

The openings of the phantoms are filled with PMMA rods that need to be removed one by one for the pencil chamber placement in order to measure the absorbed dose in the five positions. The phantoms were placed in the gantry isocenter and the peripheral openings were identified as the hours of an analog clock: 3, 6, 9, 12. Fig. 4 shows the adult head phantom placed in the gantry isocenter and the pencil chamber into the opening12.

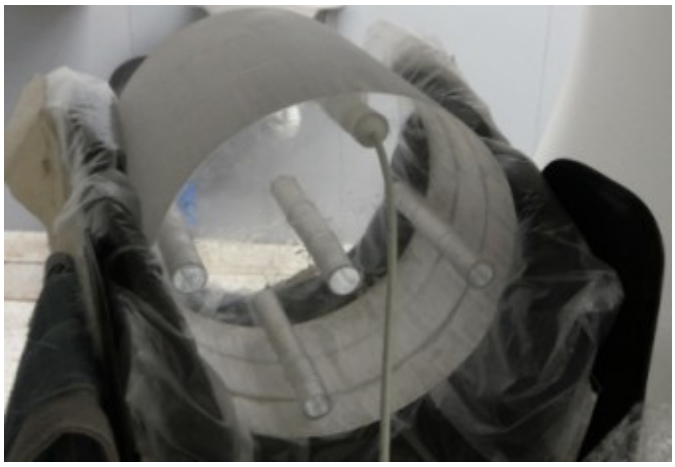

Figure 4.- Adult head phantom placed in the gantry isocenter.

2.3.- Measurements

The central slice was successively irradiated in axial mode, and the measurements were done five times in each position using a pencil ionization chamber. The gantry was in the angle position of 0 degrees and the phantom in the isocenter on a static table during the central slice irradiation.

When the pencil chamber was placed into an opening the others were filled with PMMA rods. The pencil chamber was placed alternating with each opening of the adult phantom and then alternating with each opening of the newborn phantom. The parameters used in central slice irradiation are presented in Tab. 1.

Table 1.- Central slice acquisition protocol

Technique	Voltage (kV)	Charge (mA.s)	Thickness beam (mm)
axial	120	100	10

3.- RESULTS

The results of CT air kerma index $C_{K,PMMA,100}$ measured with the pencil ionization chamber allows obtain an average value and a standard deviation (SD) for each measurement position in each head phantom. These values are presented in the Table 2 for the adult phantom and in the Table 3 for the NB phantom.

Table 2.- $C_{K,PMMA,100}$ values for adult and NB phantoms.

POSITION	Adult		NB	
	$C_{K,PMMA,100}$ (mGy)	SD	$C_{K,PMMA,100}$ (mGy)	SD
3	24,03	0,08	30,36	0,09
6	22,63	0,03	29,06	0,04
9	22,66	0,15	29,42	0,06
12	23,85	0,13	30,64	0,04
Central	22,80	0,04	30,40	0,02

Fig. 5 allows compare the variation of $C_{K,PMMA,100}$ in each position of the adult and NB phantom.

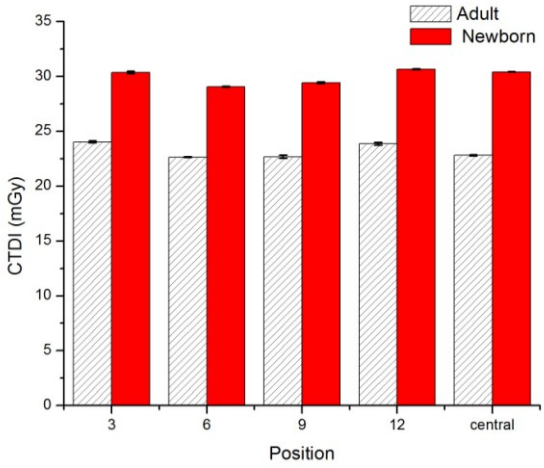

Figure 5.- $C_{K,PMMA,w}$ values in newborn and adult head phantom.

The values of weighted CT air kerma ($C_{K,PMMA,w}$) are used to show the average dose in a single slice. It is calculated using the $C_{K,PMMA,100}$ average value from the central position and the mean of average value of $C_{K,PMMA,100}$ TDI_{100} measured in peripheral points (3, 6, 9 and 12), according with equation 1 [WAMBERSIE 2005]. The $C_{K,PMMA,w}$ values obtained are shown in the Table 3.

$$C_{K,PMMA,w} = \frac{1}{3} C_{K,PMMA,100,C} + \frac{2}{3} C_{k,PMMA,100,P} \quad (1)$$

Table 3. - Valores de $C_{K,PMMA,w}$

Phantom	**$C_{K,PMMA,w}$ (mGy)**
Adult	23,13
Newborn	*30,05*

4.- DISCUSSIONS

The $C_{K,PMMA,100}$ values shown in table 2 are similar in all positions of the both phantoms. Considering the lower dose value the highest dose value is 6.19% higher for the adult phantom and 5,43% for the NB phantom. In all the positions of the NB phantom the $C_{K,PMMA,100}$ is higher than the values obtained in the adult phantom. They are varying from 26, 34% higher in the position 3, just 33,33% higher in the central position.

Considering the $C_{K,PMMA,w}$ values obtained the NB phantom receives a dose just 29,92% higher than the adult phantom. This indicates an average index of overdose in the NB phantom.

5.- CONCLUSION

The results comparing the phantom doses showed that for the same protocol of scan the newborn phantom receives a higher radiation dose when it is compared with the adult phantom. Considering the cut section variation studied, from 11 cm to 16 cm in diameter, The dose in small sections is higher. That's important to think about studies for optimizations of the head acquisition protocol for pediatric patients because these patients presents the higher variation in head circumferences and they have a longer life expectancy.

Acknowledgments:

The authors are thankful to CAPES, FAPEMIG & CNPq for their support in this study.

REFERENCES

Alonso, T.C. "Study Of The Ct Peripheral Dose Variation In A Head Phantom,", INAC, Rio de Janeiro, RJ, Brazil, September 27 to October 2, 2009.

BRAZIL. Radiological Protection Guidelines in Radiology Medical and Odontológico. 1998, p. 59.

ICRP, "ICRP 103: The 2007 Recommendations of the International Commission on Radiological Protection", Ann. ICRP, vol. 37, p. 330 (2007).

McNitt-Gray, M. F. "AAPM/RSNA Physics Tutorial for Residents: Topics in CT. Radiation dose in CT", Radiographics, vol. 22, no. 6, pp. 1541–1553 (2002).

Oliveira, B. B. "Perfil De Dose Em Varreduras De Tórax Por Tomografia Computadorizada", 2011, Dissertação apresentada ao Curso de Pós-Graduação em Ciência e Tecnologia das Radiações, Minerais e Materiais,CDTN, Minas Gerais, Brasil.

Ribeiro, L. P. and R. P. Pereira, "Estudo da dose nos exames de tomografia computadorizada abdominal em um equipamento de 6 cortes *", *Radiol. Bras.*, vol. 45, no. 5, pp. 326–333, (2012).

Villar, J. et al., "Postnatal growth standards for preterm infants: the Preterm Postnatal Follow-up Study of the Intergrowth-21st Project", The Lancet Global Health,vol.3(11), pp.681-691 (2015).

WAMBERSIE, A. THE INTERNATIONAL COMMISSION ON RADIATION UNITS AND MEASUREMENTS. Journal of the ICRU, v. 5, n. 2, p. ii–iii, 1 dez. 2005. Available at: <http://jicru.oxfordjournals.org/cgi/doi/10.1093/jicru/ndi017>.

Evaluation of Mammographic X-ray Beams Using a Phosphor Plate

Mabel Bustos Flores[1], Arnaldo Prata Mourão[1, 2]

[1] Departamento de Engenharia Nuclear, Universidade Federal de Minas Gerais, Belo Horizonte, Brazil, mbustos@ufmg.br

[2] Centro de Engenharia Biomédica, Centro Federal de Educação Tecnológica de Minas Gerais, Belo Horizonte, Brazil, apratabhz@gmail.com

Abstract

Currently, breast cancer is the second type of cancer more with higher overall incidence recorded in 2015, more than 57,000 new cases according to the National Cancer Institute of Brazil. Mammography is now one of the imaging techniques most widely used worldwide for the early diagnosis of breast cancer. The computed radiography (CR) plates are used to obtain digital radiographies, and are widely used for digital mammogram production. This study aims to evaluate the variation response in the exposure of a CR plate in a mammography unit. For this study a mammography device model Graph AF Mammo, made by VMI and a CR plate, model Regius, were used for mammography. Experiments were made with two X-ray beams of 20 and 25 kV. Successive exposures of the CR plate were made in a time range time from 0.5 to 2.5 s., to obtain unprocessed images .raw and subsequently make the measurement of time, air kerma and air kerma rate using a Ray Safe Xi meter. Five measurements for each exposure time were performed and the images were analyzed using the ImageJ software. A matrix of 21 x 21 pixels was selected in the central region of each image to obtain the intensity value, in grey scale, for each exposure time. From these data, a correlation of the degree of darkening was made with time and the air kerma. The behavior of the curves corresponding to the intensity average values of central pixels in relation to the exposure time and air kerma are similar for both voltages, showing an initially linear behavior and then a plate saturation region, whichever occurs first at the greatest value of the applied voltage.

Keywords: Mammography; Computed Radiography; X Radiation.

1.- INTRODUCTION

According to the International Agency for Research on Cancer, among cancers that affect women, breast cancer is the high rate of incidence and mortality over 25 % and 15 % of cases, respectively. It is estimated that more than 1.67 million women were diagnosed with the disease and more than 521,000 deaths in 2012. The National Institute of Cancer of Brazil estimates 57,000 new cases for this year.

The high incidence of this disease requires the development of quality assurance programs in mammography services and criteria for assessing the quality of mammographic images, testing specific performance in order to obtain an accurate and early diagnosis of Cancer [IAEA 2006].

Mammography is a radiographic technique optimized for the breast exam and is a highly effective means of breast cancer detection at an early stage [Dance *et al.*, 2014]. The success of mammography for screening depends on the production of high quality images with appropriate doses. The production of such images is a complex and difficult task due to the breast anatomical structure [Mawdsley *et al.*, 2011; INC 2012].

Mammographic images can be analog or digital. Conventional radiography uses a chassis with radiographic films and intensifier screen, and digital radiography can be subdivided between computed radiography (CR) and direct radiography (DR) [Oliveira *et al.*, 2014; Oliveira 2011]. The challenges in creating a digital mammography system with improved performance are mainly related to the X-ray detector and the digitizer unit [Dance *et al.*, 2014].

The CR systems use a photostimulable phosphor plate into a cassette. CR image acquisition is a two stage process. In the first stage is performed the exposure of the CR plate and in the second stage is performed the reading of information contained in the cassette with the digitizer unit [NHS 2006].

When the CR plate is exposed to an X-ray beam, photostimulable materials absorb part of this beam and emit electrons of its crystalline structure [Mawdsley *et al.*, 2011]. Some of these electrons lose some of their energy by interaction with other electrons in the crystalline structure and others are trapped at higher energy levels, which remain stable for some time, creating a latent image [Mawdsley *et al.*, 2011; Dance *et al.*, 2014]. The number of trapped electrons is proportional to the amount of incident radiation on the photostimulable material [Oliveira 2011].

For reading the CR plate, it is introduced in the digitizer unit and with a thin laser stimulation electrons return to their ground state, causing light emission which is converted into a proportional electrical signal, from which the image is formed [Mawdsley *et al.*, 2011; Blanco *et al.*, 2014]. Generally, a logarithmic transformation is applied to the signal during this stage [Blanco *et al.*, 2014].

In computed radiography, the digital mammography image quality is determined by a set of parameters that need to be carefully selected before the image acquisition: voltage applied to the X-ray tube, anode-filter combination and exposure time of the acquisition system [Jakubiak 2013]. The objective of this work was to evaluate mammographic X-ray beams using a phosphor plate varying the parameters of voltage and exposure time.

2.- MATERIALS AND METHODS

The VMI mammographic equipment, model Graph Mammo AF, show in Figure 1, having a rotating anode and combination of anode/filter Molybdenum, was used to evaluate the mammographic CR plate, size 18 x 24 cm^2, model Regius RP6M110 manufactured by Konica Minolta, shown in Figure 2a .

Figure 1.- VMI mammography device.

Figure 2.- Mammographic CR plate (a). RaySafe Xi (b).

The behavior of the CR plate was studied by the acquisition of unprocessed images using two supply voltages of 20 and 25 kV, keeping the electrical current constant of 70 mA for both voltages and the distance from the focus to the detector of 53.3 cm, without the use of the compression plate.

The unprocessed images, in *.raw* pattern, were obtained by successive exposures of the CR plate, varying the exposure time in a range of 0.5 to 2.5 s for both X- ray beams. Five images were obtained for each voltage and time exposition. The CR plate has a size of 236.95 mm by 176.75 mm (5416 x 4040 pixels) with the pixel size of 43.85 µm. The intensity values in CR images, in greyscale, can have a range of 4,096 numeric values, where zero is the white color and 4,095 is the black.

Subsequently, using the same exposure techniques were realized 5 measurements of air kerma, kerma rate and exposure time for each exposure, using the RaySafe Xi meter shown

in Figure 2b. The solid state detector used for the measurement was placed in the center of the CR plate.

From the images obtained was realized the analysis of the intensity variation in greyscale, corresponding to the darkening of the CR plate in the central region of the image, and then in the total image area. These analyses were performed using ImageJ software, where an area of 21 x 21 pixels was selected in the central region of each image to obtain the intensity average value corresponding to the darkening to each beam and exposure time.

Finally, two images were selected with the same exposure time and different voltages and it was made the selection of the total area of the image to evaluate the variation in image darkening degree in relation to air kerma.

3.- RESULTS

From these data obtained concerning the darkening of the CR plate as a function of exposure time, air kerma and air kerma rate were calculated average values for both voltages. After that, was made the correlation of the image darkening degree in the greyscale with the exposition time was made to get through curve fitting the time for which the plate begins to saturate. For the 20 kV beam the CR plate saturates at 10.7 s, while for the 25 kV beam it saturates at 3.7 s, shown in the graphic of Fig. 3 and 4, respectively.

Additionally, was made the correlation of the image darkening degree in greyscale with the air kerma for both voltages, shown in the Figures 5 and 6.

Finally, two selected images obtained for each X-ray beam in linear response region were used to show the darkening variation in the CR plate area from the maximum and minimum darkening values with relation to air kerma incident in the plate, obtaining 3D graphics

shown in the Figures 7 and 8. The darkening area presented a variation of 65.61% below the maximum value of the degree of darkening for the 20 kV beam, and 62.66% to the 25 kV beam.

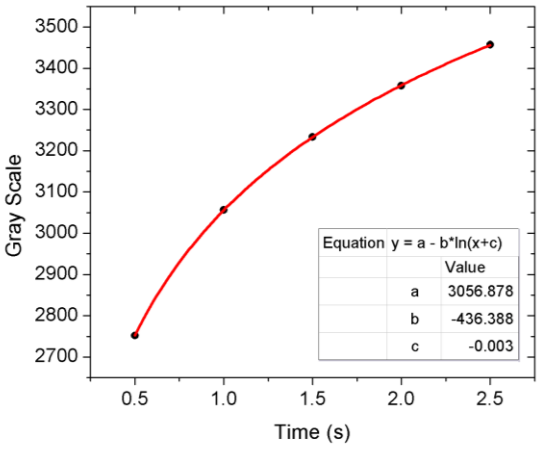

Figure 3.- Response curve of the CR plate corresponding to 20 kV beam.

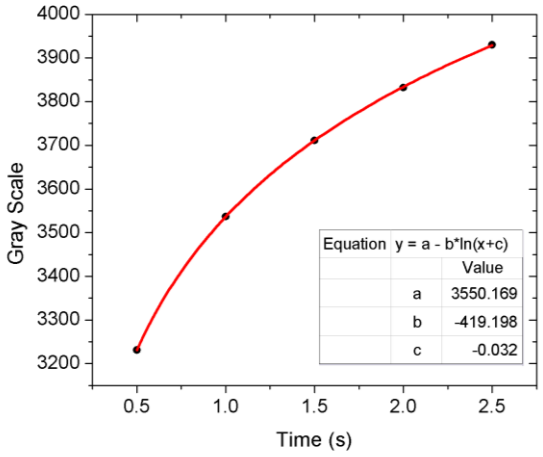

Figure 4.- Response curve of the CR plate corresponding to 25 kV beam.

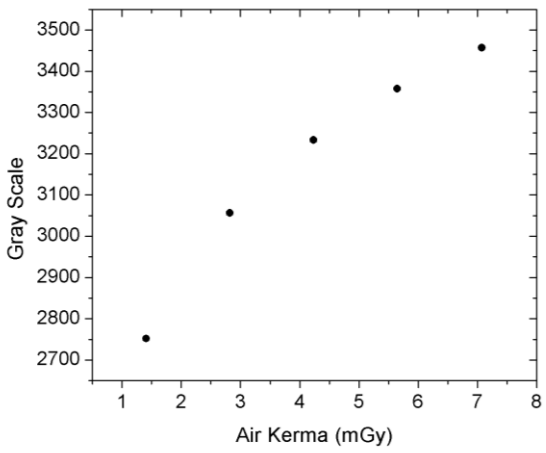

Figure 5.- Correlation of image darkening degree with air kerma for 20 kV beam.

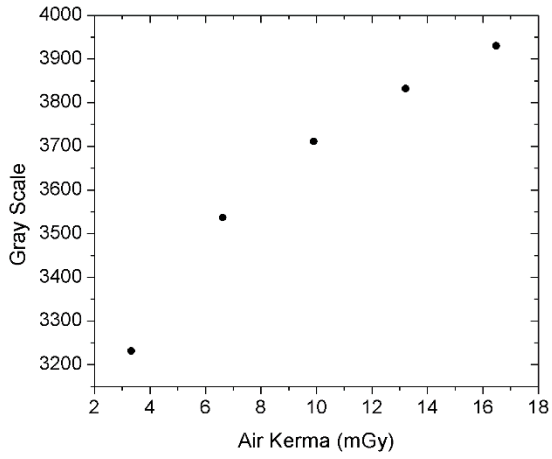

Figure 6.- Correlation of the image darkening degree with air kerma for 25 kV beam.

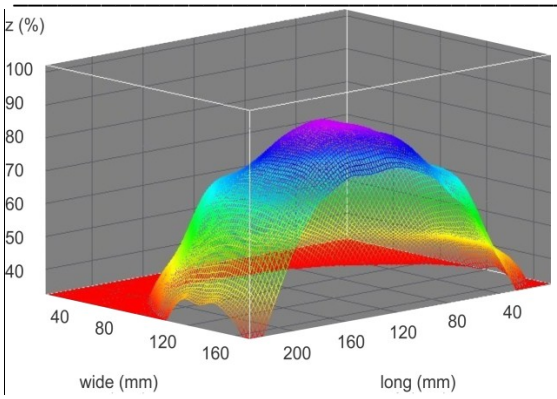

Figure 7.- The Percentage of intensity variation in the CR plate area for 20 kV beam and exposure time 2.0 s.

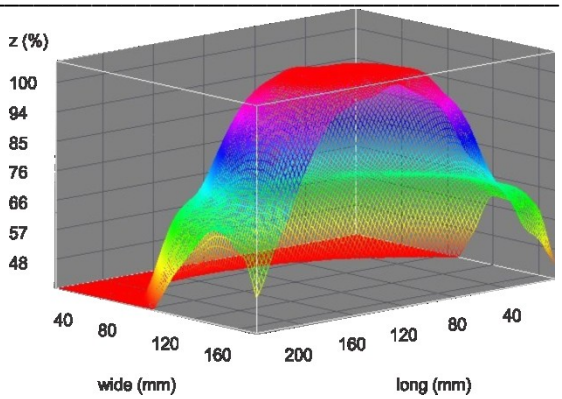

Figure 8.- The percentage of intensity variation in the CR plate area for 25 kV beam and exposure time 2.0 s.

4.- DISCUSSION

The correlations made on the darkening degree of the CR plate relative to the exposure time and air kerma show similar behavior for both beams of 20 and 25 kV. The results demonstrate that, according to the degree of darkening of the CR plate, this presents a linear behavior initially and then a saturation region. According to curve fitting made, it is presented first to the curve corresponding to the higher value of applied voltage. Similar behavior occurs in the correlation of the darkening degree with air kerma.

The behavior of the percent variation of the darkening degree recorded by the CR plate for the voltage of 20 kV presented a minimum value 65.61% below the maximum value. This means that if the maximum air kerma rate measured for that image is 5.65 $mGy.s^{-1}$, the minimum air kerma rate is 3.71 $mGy.s^{-1}$. The region where the maximum value of air kerma is recorded is in the central part of the CR plate nearest to the chest position, and the lowest value was registered in the most distant region of the patient chest.

The behavior of the percentage variation of air kerma recorded by the CR plate for 25 kV, showed less variation, this varies 62.66% below the maximum value, this means that if the value of the maximum air kerma rate is 13.21 $mGy.s^{-1}$, the minimum value is 8.28 $mGy.s^{-1}$. Additionally, it was observed that the air kerma rate remains constant independently the variation of exposure time.

5.- CONCLUSIONS

Knowledge of the saturation characteristics of the CR plate relative to exposure times, air kerma and air kerma rate allows the selection of parameters more suited to work with these voltages without approaching the saturation region of the CR plate, which would minimize underexposed problems hindering the quality of diagnostic image and help provide adequate dose to the patient. It is important to ensure that efforts to reduce patient doses do not also reduce doses to the image receptor to such an extent that the image quality is degraded to an unacceptable level.

The behavior of the darkening degree variation in the CR plate, evidences that the input signal could cause interference if the plate size is not appropriate, especially when it is used for large breasts.

Acknowledgments

The authors are grateful for the support to the Coordenação de Aperfeiçoamento de Pessoal de Nível Superior (CAPES), the Fundação de Amparo à Pesquisa do Estado de Minas Gerais (FAPEMIG), and the Conselho Nacional de Desenvolvimento Científico e Tecnológico (CNPq).

REFERENCES

Blanco, S., Andisco, D. Di Risio, C. Buzzi, A. E. La digitalización de equipos de mamografía: elementos fundamentales a tener en cuenta para beneficiarnos de la tecnología. Revista Argentina De Radiología, Elsevier España, v. 78[4], 2014:236-239 p.

Dance, D. R. Chistofides, S. Maidment, A. D. A. McLean I. D. Ng, K. H. Diagnostic radiology physics. INTERNATIONAL ATOMIC ENERGY AGENCY. Vienna, 2014: 682p. ISBN 978–92–0–131010–1.

INSTITUTO NACIONAL DEL CÁNCER. PROGRAMA DE CONTROL DE CÁNCER DE MAMA (PCCM)-Manual Operativo para el uso de Mamografía en Tamizaje. Argentina, 2012: 82 p.

INTERNATIONAL ATOMIC ENERGY AGENCY [IAEA]. Control de Calidad en Mamografía: Protocolo elaborado en el marco de dos proyectos regionales ARCAL/OIEA. Viena: OIEA, 2006, 138p.

Jakubiak, R. R. Gamba, H. R. Neves, E. B. Peixoto, J. E. Image quality, threshold contrast and mean glandular dose in CR mammography. IOP Publishing. Physics in Medicine. Biology, v.58, 2013:6565–6583 p.

Mawdsley, G.E. Bloomquist, A.K. Yaffe, M.J. Digital Mammography Quality Control for the Mammographic Physicist. Toronto: Ontario Breast Screening Program. November, 2011: 166p.

NHS Cancer Screening Programmes. Commissioning and routine testing of full field digital mammography systems. NHSBSP Equipment Report 0604. September 2006. Version 2. Guildford, UK: 58 p.

Oliveira, B. B. Oliveira, M. A. Paixão, L. Teixeira, M. H. A. Nogueira, M. S. Dosimetry and image quality assesment in a direct radiaography system. Radiologia Brasileira, SP, v. 6, n. 47, 2014: 361–367p.

Oliveira, M. A. Avaliação da dose glandular e qualidade da imagem de pacientes submetidas a mamografias com processamento de imagem digital (Disertação-Mestrado). CENTRO DE DESENVOLVIMENTO DA TECNOLOGIA NUCLEAR. Programa de Pós-Graduação em Ciência e Tecnologia das Radiações, Minerais e Materiais. Belo Horizonte, 2011: 93 p

Evaluation of the Image Quality of Chest CT Scans: A Phantom Study

Priscilla Inglid Martins Naves[1,*] and Arnaldo Prata Mourão[1,2]

[1] Biomedical Engineering Center, Federal Center for Technological Education of Minas Gerais, Av. Amazonas, 5253 - Sala 113. CEP: 30421-169, Nova Suíça, Belo Horizonte, MG, Brazil
priscillainglid@gmail.com

[2] Department of Nuclear Engineering, Federal University of Minas Gerais, Av. Antônio Carlos 6627, CEP: 31270-90, Pampulha, Belo Horizonte, MG, Brazil
apratabhz@gmail.com

Abstract

Computed tomography (CT) is considered one of the most important methods of medical imaging employed nowadays, due to its non-invasiveness and the high quality of the images it is able to generate. However, the diagnostic radiation dose received by an individual over the year often exceeds the dose received on account of background radiation. Therefore, it is important to know and to control the dose distribution in the a patient by varying the image acquisition parameters. The aim of this study is to evaluate the variation of the image quality of chest CT scans performed by two phantoms. In this paper, a cylindrical Polymethyl Methacrylate (PMMA) chest phantom was used and a second PMMA phantom has been developed with the same volume but an oblong shape, based on the actual dimensions of a male human thorax, in the axillary region. Ten-centimeter scans of the central area of each phantom were performed by a 16-channel Toshiba CT scanner, model Alexion. The scanning protocol employed was the radiology service protocol for chest scans. The noise survey was conducted within the image of the center slice, in five regions: one central and four peripheral areas close to the edge of the object (anterior, posterior, left and right). The recorded values showed that the oblong phantom, with a shape that is more similar to the actual human chest, has a considerably smaller noise, especially in the anterior, posterior and central regions.

Keywords: Computed tomography, chest phantom, image quality, dose reduction.

1.- INTRODUCTION

The advent of computed tomography (CT) in the decade of 1970 marked the beginning of new possibilities for radiology studies. The main reason is that CT allows visualization of internal structures of the human body through anatomical cuts, without intervention. Thus, the image generation of structures not accessible such as the brain, became possible. This medical imaging method has had a great technological advance since its inception, using technologies increasingly complex and better, which allows its use in almost every medical specialties [Mourão, 2007].

The most recent CT scanners have helical technology with multi-detectors (MDCT) which are able to do scans of a complete-volume in less than 5 seconds. In addition to that, the improvement in the image reconstruction process and in the post-processing software has contributed to the generation of images with increasingly higher quality [Pina, et al. 2009]. Even though, among the medical imaging methods that use ionizing radiation, CT scan is the procedure that results in the highest dose in patient [Brenner & Hall, 2007; Dance et al. 2014]

Although the risk associated with radiological examination is considered small when compared to the risk due to natural radiation, any additional risk, even if minimal, is unacceptable if there is no benefit to the patient. For this reason, it is necessary to understand the relationship between the dose distribution, the image acquisition parameters and the final quality, in order to get useful images for diagnosis and a level of radiation exposure as low as possible [Silva, 2014]. Nowadays, the variability of procedures and technical protocols used in CT scans has been a prominent discussion topic among the medical and scientific community, and some quality standards and Dose Reference Levels (DRL) have been defined [Borém, Figueiredo, & Silveira, 2013].

However, further researches to provide optimization of the acquisition protocols used in CT scans remain to be conducted. In this regard, the PMMA phantoms are often used in cranial and chest CT scans, for instance, as they present absorption and spreading characteristics similar to those regions [Dalmazo et al. 2010]. The results produced are consistent and

enable the necessary studies to evaluate, analyze and make the current protocols more adequate, aiming at decreasing the radiation dose received by the patient and maintaining the image diagnostic quality [Goldman 2007].

The objective of this study is to evaluate the influence of the shape of two chest phantoms (cylindrical and oblong) in the image noise level of images generated in a CT scanner.

2.- MATERIALS AND METHODS

In this work, experimental measurements were obtained from two PMMA chest phantoms. These objects are frequently used to simulate CT scans, since the patients should not be used in experiments with ionizing radiations. Cylindrical phantoms are used in tests of head and chest, generating good results for the head, for example, due to the similarity between the shapes. A second object with an oblong shape was developed based on the actual dimensions of the axillary region of a male adult chest. This object has the same flat surface area, width and volume of the cylindrical phantom and a shape more similar to that of the human chest. Thus, the only variable between them is the shape.

Figures 1 and 2 show the dimensions of the cylindrical and oblong phantoms, respectively.

Figures 3 show the cylindrical and the oblong phantoms, placed at the isocenter of the CT scanner gantry.

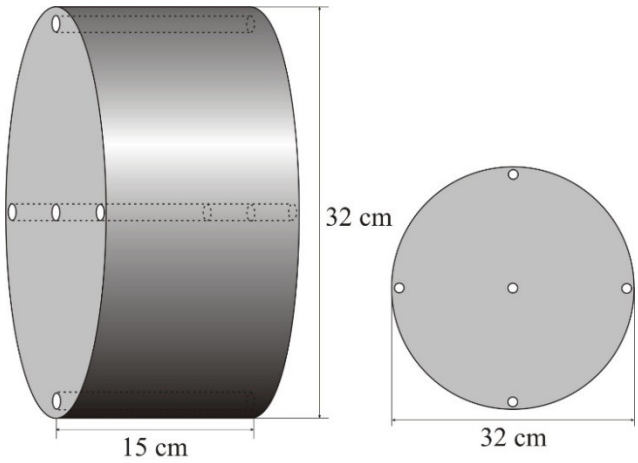

Figure 1.- Dimensions of the cylindrical chest phantom.

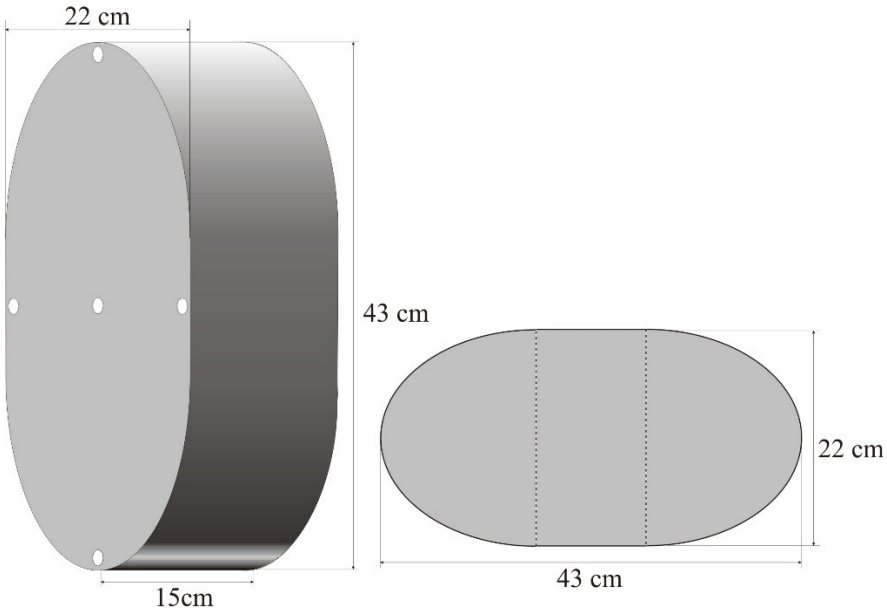

Figure 2.- Dimensions of the oblong chest phantom.

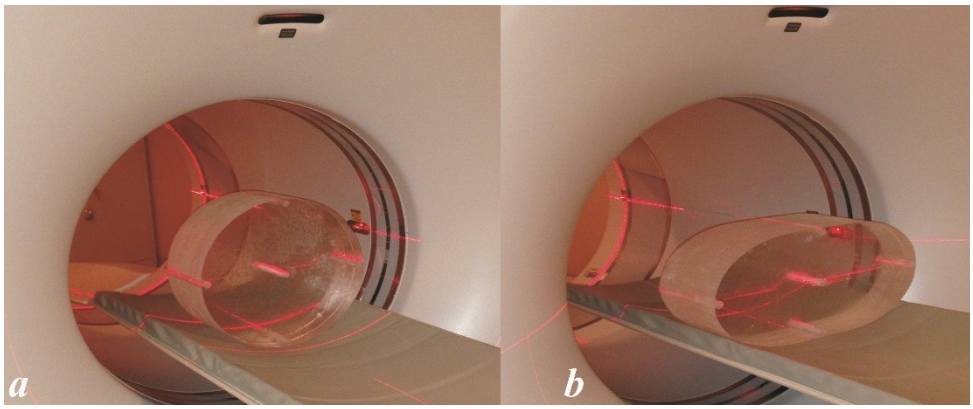

Figure 3.- Positioning of Chest PMMA phantoms, cylindrical *a* and oblong *b*.

Scans were carried out in a Toshiba CT scanner, model Allexion with 16 channel . Table 1 shows the acquisition protocol parameters that were used for the image generation.

Table 1.- Protocol of chest scan.

Parameter	Value
Voltage (kV)	120
Current (mA)	200
Tube rotation time (s)	0.8
Charge (mA.s)	196
Beam tickness (mm)	8
Pitch	1.4

The chest phantoms have five openings one central and four peripherals, where it is possible to place metering devices in order to perform the dose evaluation. However, the purpose of this paper is to evaluate the influence of the phantom shape on the quality of the generated image, through the analysis of the noise level. The openings were filled with PMMA rods, in order to produce a uniform volume phantom.

The analysis and assessment of the acquired image quality has been made with the medical image software *RadiAnt.* It is used for image observation in DICOM format. Five points of interest were selected, four of them near to the edge of the object and one in the central region. As in a clock hours, the peripheral points were identified as 3, 6, 9 and 12, and the central point as C, considering its frontal position inside the gantry.

Figures 4 show the axial images of the central slice of cylindrical and oblong phantoms, where the points of interest are identified.

The central image of the scan was selected for this study because it is the slice that receives the largest dose portion, due to scattered radiation coming from the adjacent slices. In each of the measurement points, the average value in Hounsfield scale ($HU_{average}$) and the standard deviation (SD) for a constant-area region of interest (ROI) were obtained.

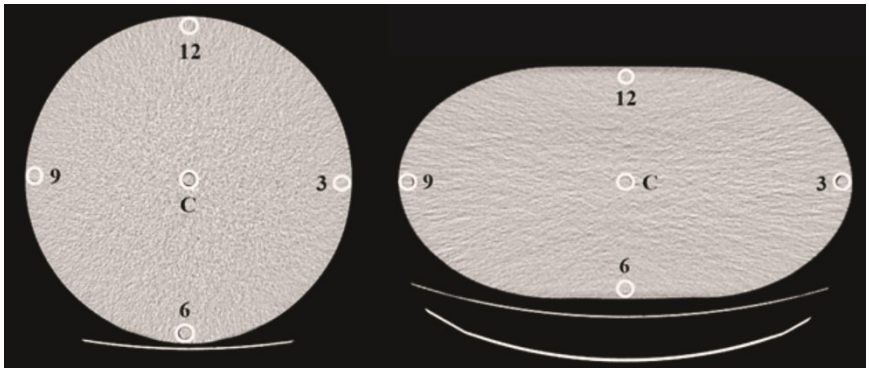

Figure 4.- Axial image of the central slice of the cylindrical and oblong phantoms, with the measurement points.

So, it became possible to calculate the noise in each point, using the Equation 1.

$$Noise = \left(\frac{SD}{HU_{average} - HU_{air}} \right) \times 100\% \quad (1)$$

3.- RESULTS

Table 2 presents the values in Hounsfield Units (HU) and the standard deviations (SD) obtained in the chosen ROI. The area of the ROI used was 0.6 cm² and it has approximately 110 pixels.

Table 2.- HU values in the ROI.

Position	Cylindrical		Oblong	
	Average (HU)	SD	Average (HU)	SD
C	125.47	32.47	124.38	124.38
3	122.10	21.48	120.11	19.49
6	128.25	28.50	129.83	23.37
9	129.36	23.91	117.12	20.02
12	134.41	28.04	124.17	26.34

From the acquired data and considering that -1000 HU is the minimum value in the Hounsfield scale and the value for the air ($HU_{air} = -1000$), noise values in each point were calculated and they are shown in Table 3.

Table 3.- Noise in the cylindrical and oblong phantoms.

Point	Noise (%)	
	Cylindrical	Oblong
C	2.89	1.73
3	1.91	2.09
6	2.53	1.77
9	2.12	2.36
12	2.47	1.62
Average	2.47	1.77
SD	0.38	0.30

4.- DISCUSSION

From the noise values shown in Table 2, it is possible to observe that the cylindrical phantom presents higher values than the oblong, about 39.54% higher in average. That is mainly due to the increase in the HU value at the central point of the cylindrical phantom, due to the beam hardening that hits this point that is always filtered by the same PMMA thickness, regardless of the incidence angle of the X-ray beam. In the oblong phantom, the shorter axis, composed of the points 6, 12 and C, presents higher HU values than the horizontal axis. For both phantoms, the highest HU value occurs in the point 6, because of the X-ray beam filtration by the table.

Figure 7 shows some details of the central portion of both phantoms. As it can be seen, the noise in the oblong phantom is noticeably lower than in the cylindrical one. Noise values were calculated at each point and are presented in Table 3. The noise values in the points 3 and 9 for both objects are very similar. As for the shorter axis, including the central point, the noise is considerably higher in the cylindrical phantom.

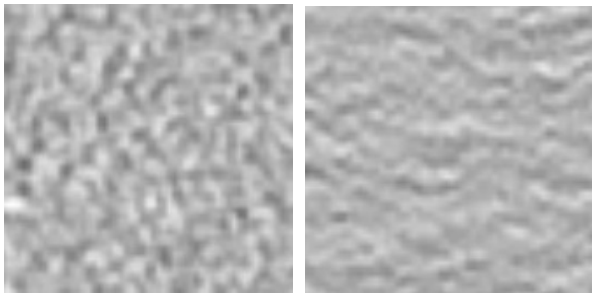

(a) (*b*)

Figure 7: Detail of the noise near the central point in the images of the cylindrical phantom *(a)* and of the oblong phantom *(b)*.

5.- CONCLUSIONS

The development of an imaging phantom with a shape is more similar to the human chest results in values closer to the ones found on actual patient's chest exams. On this paper, it was noted that, for the same acquisition protocol, noise level is noticeably lower in the oblong phantom. That difference is related only to the shape of the object, as both studied phantoms have the same volume and, for that reason, it might be interpreted as a consequence of the image reconstruction process.

The acquisition parameters are directly associated with image quality and with the absorbed dose by patient, and acquisitions that deposit higher doses tend to result in a lower image noise. Therefore, protocols used currently in chest scans can be revised in order to decrease dose emitted to the patient during the exam without magnification of image noise, avoiding diagnostic data losses.

Acknowledgments

The research reported in this paper has been supported by FAPEMIG, CNPq and CAPES.

REFERENCES

Borém LMA, Figueiredo MFS, Silveira MF, Rodrigues Neto JF. (2013). *O conhecimento dos médicos da atenção primária à saúde e da urgência sobre os exames de imagem.* Radiol Bras. Nov/Dez;46(6):341–345.

Brenner DJ, Hall EJ. (2007). *Computed Tomography — An Increasing Source of Radiation Exposure.* The New England Journal of Medicine 357:2277-84.

Dalmazo J, Elias JJ, Brocchi MAC, Costa PR, Azevedo-Marques PM. (2010). *Otimização da dose em exames de rotina em tomografia computadorizada: estudo de viabilidade em um hospital universitário.* Radiol Bras. 43(4):241–248.

Dance, DR. et al. *Diagnostic radiology physics:* A handbook for teachers and students. American Association of Physicists in Medicine. (2014).709p.

Goldman LW. (2007). *Principles of CT: Radiation Dose and Image Quality*. J. Nucl. Med. Technol.; 35:213-225.

Mourão AP. *Tomografia Computadorizada, Tecnologia e Aplicações*. São Caetano do Sul, Difusão. (Second edition, 2007).

Pina DR, Duarte SB, Ghilardi TN, Morceli J, Carbi EDO, Souza RTF, Costa AN, Ribeiro SM. (2009) *Controle de qualidade e dosimetria em equipamentos de tomografia computadorizada*. Radiol Bras. 42(3):171–177.

Silva, RACD. (2014). *Tomografia Computadorizada: Análise e optimização das práticas na realização de exames em adultos e pediátricos. Análise do nível de adequação às recomedações internacionais*. Universidade Católica Portuguesa. Porto, Portugal

Dosimetric Study in Chest Computed Tomography Scans of Adult and Pediatric Phantoms

Wadia Namen Aburjaile[1], Gislene Guedes[2] and Arnaldo Prata Mourão[1,2]

[1] Department of Nuclear Engineering, Federal University of Minas Gerais,
Av. Antônio Carlos 6627, CEP: 31270-90, Pampulha, Belo Horizonte, MG, Brazil
wadia.namen@gmail.com

[2] Biomedical Engineering Center, Federal Center for Technological Education of Minas Gerais,
Av. Amazonas, 5253 - Sala 113. CEP: 30421-169, Nova Suíça, Belo Horizonte, MG, Brazil
gislenebhz@gmail.com apratabhz@gmail.com

Abstract

The Computed Tomography scan is a radiological technique that permits an evaluation of the patient internal structures. In the last ten years, this technique has had a high growth due to clinical cases of medical emergencies, cancer and pediatric trauma. Widespread of this technique has a significant increase in the patient dose. The risk associated with the radiological examination can be considered very low compared to the natural risk. However, any additional risk, no matter how small, is unacceptable if it does not benefit the patient. To be aware of the dose distribution is important when the objective is to vary the acquisition parameters aiming a dose reduction. The aim of this study is develop a pediatric chest phantom to evaluate the dose variation in CT scans. In this work, a cylindrical adult chest phantom made in polymethyl methacrylate was used and a second chest phantom was developed, based on dimensions of in eight year old patient in oblong shape. The two simulators have 5 openings, one is central and four are peripheral lagged by 90º, which allow positioning a pencil chamber aiming an observation of the dose in 5 regions. In a GE CT scanner, Discovery model and 64 channels, the central slice of both simulators were irradiated successively to obtain dose measurements using a pencil chamber. The irradiation of the central slice was conducted using the service protocol. The registered dose values showed that the pediatric phantom had higher doses especially in the anterior, posterior and central regions. The results also enabled a comparison among the index dose values obtained from the measurements with the pencil chamber.

Keywords: Dosimetry; Computed Tomography; Medical Images.

1.- INTRODUCTION

Computed Tomography (CT) tests are increasingly required in diagnostic process image. Currently, most equipment used for CT scans has multi-detector arc, also known as multi-slice CT scanner. There is a steady increase in demand for CT scans in pediatric patients, mainly as a result of high rates of traumatic injuries caused by car accidents, bicycle falls, blunt trauma, head trauma, as well as a significant increase in the incidence of childhood cancers where these images are normally used in the diagnostic process.

The actual protocols used in radiological services routine are based on adult patients and predetermined by manufacturers, without considering the differences in volume and mass of the anatomical structure studied in pediatric patients [Booni 2007; Dance et al. 2014].

Despite allowing the use of four different supply voltage levels in the X-ray tube, the vast majority of CT scans is performed with the voltage value of 120 kV. Since the image produced by the CT scanner shows an axial section, for the diagnosis of any organ it is necessary the acquisition of a sequence of cross-sectional images that allow the observation of the whole structure of this organ. Thus, the produced images representing axial sections, beginning on organ base to its apex, as if the organ were sliced continuously [Burgener 2001].

CT scanners installed in diagnostic services have great technological variations, such as data acquisition times or protocols used to obtain images, which depend on the available technology. Therefore, images produced with the same diagnostic objective can generate different absorbed doses in patient. This may be due to technological difference of CT scanners or acquisition protocols used. Radiation doses deposited in patients are directly associated to deleterious effects prompted by ionizing radiation, such as the occurrence of cataract and tumors [ICRP 2002].

No matter whether it is in diagnostic radiology or radiotherapy processes, it is very important to know the dose deposited in human tissues. The dose deposited in a pediatric

patient is directly related to the energy stored during the ionizing radiation exposition. This parameter is used to reference the possible future effects caused in the exposed population, such as the occurrence of cancers. CT scan is the diagnostic method which more deposits dose in patients [Li et al. 2007].

Phantoms are used in irradiation processes to measure the energy deposition in organs and to observe how the dose distribution happens in an irradiated volume, in a similar way to the human body. In this work, an adult chest standard phantom was used, and a second phantom was developed with the proportions of an 8-year-old pediatric chest taking into account the axillary region. The pediatric chest phantom was built with measures of the thoracic perimeter percentile to the age of 8.

2.- MATERIALS AND METHODS

Experiments were made to compare the absorbed doses of the pediatric chest phantom with the adult standard chest phantom, and they were performed in a GE CT scanner, Discovery model with 64 channels. A pencil ionization chamber was used together with an electrometer to realize measurements of Computed Tomography Dose Index [AAPM 2010].

2.1.- Phantoms

The adult chest phantom is a cylinder with 32 cm in diameter and the chest pediatric phantom was developed in an oblong shape with a cut area of 14 cm x 29 cm, representing measures of an 8-year-old pediatric patient in the axillary region. Both phantoms have 15 cm in length and are made in polymethyl methacrylate (PMMA).

The oblong pediatric chest phantom was built in the percentile measures of the thoracic perimeter to the age of 8, in the axillary region. Both chest phantoms have five openings with 1.27 cm in diameter; one is central and four peripherals lagged by 90°. The center of peripheral openings is 1 cm from the phantom edge. Figure 1 presents the shape of the developed pediatric chest phantom and its dimensions.

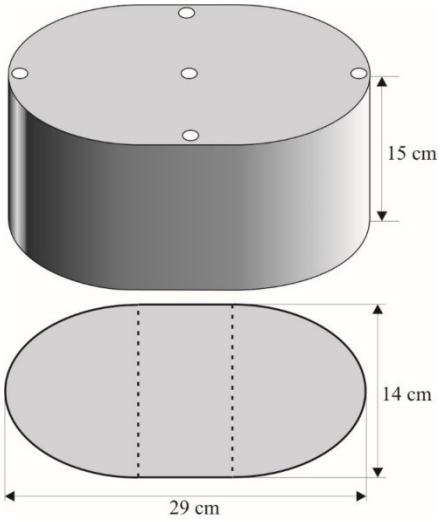

Figure 1.- Pediatric chest phantom.

The phantoms' openings are filled with PMMA rods and they should be removed one by one to place the pencil chamber aiming the dose measurements in the five positions. The objects were placed in the gantry isocenter and the peripheral openings were used to aid the placement. The central opening was identified with C and the peripherals were identified how 3, 6, 9, and 12 according to the hours of an analog clock. Fig. 2 shows the pediatric chest simulator placed in the gantry isocenter.

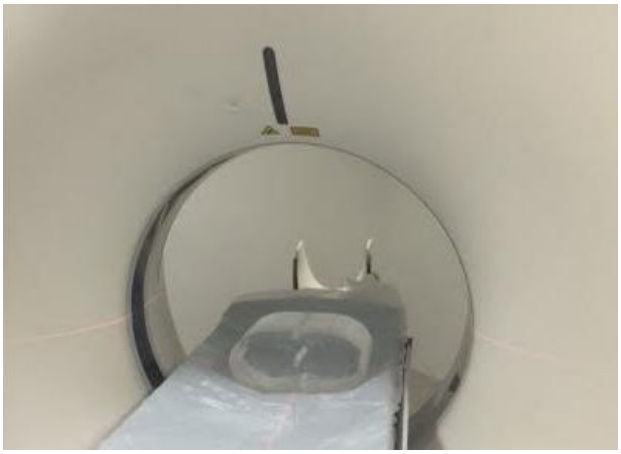

Figure 2.- Pediatric chest phantom placed in the gantry isocenter.

2.2.- Measurements

Absorbed dose measurements were carried out using a pencil chamber with the chest scan protocol used in radiology service routine. They were registered with the gantry in 0^{o} tilt and with the simulators placed in the gantry isocenter. The pencil chamber was placed alternately in the adult chest phantom openings and subsequently in the pediatric ones. Measures were done in the Computerized Tomography Dose Index ($CTDI_{100}$) [EC 2004].

Successive irradiations of the central slice were executed in axial mode with the pencil chamber placed in the phantoms' openings. Five measurements were carried out to each positioning of the chamber. Central slice irradiations were executed in both phantoms, in axial mode, with a voltage of 120 kV and a charge of 100 mA.s in the X-ray tube, rotation time of 0,5 s. The thickness beam had 10 mm.

3.- RESULTS

All obtained results in the measurements were multiplied by the conversion factor Air-PMMA. $CTDI_{100}$ average values with standard deviations (SD) obtained with the central slice irradiation are shown on Tables 1 to adult and pediatric chest phantoms.

Table 1.- $CTDI_{100}$ values to Adult and pediatric phantoms.

Position	Adult		Pediatric	
	$CTDI_{100}$ (mGy)	SD	$CTDI_{100}$ (mGy)	SD
3	11,90	0,33	13,92	0,04
6	10,50	0,03	17,26	0,20
9	11,93	0,04	14,01	0,04
12	12,52	0,34	19,12	0,10
Central	5,73	0,02	14,34	0,06

The graphic shown in the Fig. 3 allows a comparison between the dose index ($CTDI_{100}$) obtained by the measurements with the pencil chamber in the five points of interest of the adult and pediatric phantoms.

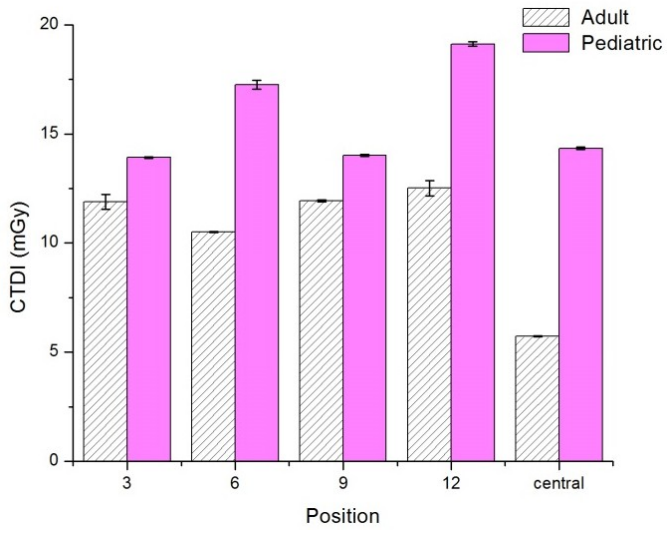

Figure 3.- Dose Index values ($CTDI_{100}$) in adult and pediatric phantoms.

Based on $CTDI_{100}$ values measured in the central and peripheral openings of the phantoms, it was possible to calculate the weighted dose index ($CTDI_w$), given by equation 1, where $CTDI_{100,C}$ is the average value measured in the central opening and $CTDI_{100,P}$ is the mean of the average values in the peripheral openings.

$$CTDI_w = \frac{1}{3} CTDI_{100,C} + \frac{2}{3} CTDI_{100,P} \quad (1)$$

$CTDI_w$ values indicate the average dose of a single tomographic slice irradiation [ICRP 2000]. While $CTDI_W$ generates a dose value from central and peripheral doses in the same plan, perpendicular to a patient longitudinal axis, $CTDI_{vol}$ considers the longitudinal axis scan (Z-axis) from the acquisition and it is defined by equation 2 [APPM 2010]. The pitch value to the chest scan protocol used in the acquisition in helical mode is 0,984. $CTDI_w$ and $CTDI_{vol}$ values obtained to the adult and pediatric chest phantoms are shown on Table 3.

$$CTDI_{vol} = \frac{CTDI_w}{pitch} \quad (2)$$

Table 2.- $CTDI_w$ and $CTDI_{vol}$ values.

Object	$CTDI_w$ (mGy)	$CTDI_{vol}$ (mGy)
Adult	9,72	9,88
Pediatric	15,50	15,75

4.- DISCUSSION

Observing the dose index values $CTDI_{100}$ of the adult chest simulator there is a need to remark the proximity of the peripheral registered doses, having the lowest dose occurring in point 6 and the highest one in the point 12. This characteristic happens due to the beam's contribution in the dose deposition during the infero-superior incidence, when the beam is filtered by the table in which the object is placed. Since the filtered beam is more attenuated, its contribution is smaller and this effect is more observed in point 6 where the incidence contribution is bigger while the reverse situation occurs in point 12.

The central region dose is practically half value of the peripheral dose, showing that the beam which reaches the central region is always filtered by the same PMMA thickness regardless of the beam incidence angle. X-ray beam absorption by PMMA promotes a considerably attenuation due to the cylindrical adult chest simulator thickness.

Recorded doses in all points of the pediatric phantom were higher than the ones recorded in the adult one. Peripheral doses in the smallest object axis, points 6 to 12, are higher than the ones of the major axis, 3 to 9. Differently from the adult object, the recorded dose in central region presents a value which is close to the peripheral doses of the major axis.

Comparing the weighted dose index ($CTDI_w$) to both phantoms, the dose received by the pediatric patient is around 59.47% higher than the one received by the adult. However, comparing the measured dose in the central position of the pediatric phantom, it is about 150.26% higher than the adult in the same position.

5.- CONCLUSIONS

The measured doses enabled an observation of how dose distribution varies with the thickness variation and shape of the phantom. The pediatric phantom showed that patients with lower volumes receive higher doses than those ones received by the adult patients, when the same scanning protocol is used.

Doses in the central position of the chest and mediastinum region were proportionally higher in the oblong object that has a similar shape to the format of the chest in axillary region [Kleinman 2010]. This characteristic remarks that doses in patients in this region are frequently superior to the ones estimated with the cylindrical simulator, since the human chest has an anteroposterior axis which is smaller than the lateral one.

Acknowledgments

This work was supported by the FAPEMIG and CNPq. Also, the Molecular Imaging Center of UFMG is acknowledged for producing the images.

REFERENCES

American Association of Physicists in Medice (2010). *Comprehensive Methodology for the Evaluation of Radiation Dose in X-Ray Computed Tomography* (Report #111). College Park, MD. (implemented by TG-200).

Boone JM. *The trouble with $CTDI_{100}$*. Med Phys. 2007; 34(4):1364-1371.

Burgener F; Kormano M. *Differential Diagnosis in Computed Tomography*. CINAMON, Jay. Marconi multislice spiral CT principles & applications, Atlanta, 2001. 61p.

Dance, DR. et al. *Diagnostic radiology physics:* A handbook for teachers and students. American Association of Physicists in Medicine. (2014).709p.

European Commission. European Guidelines on quality criteria for computed tomography. EUR 16262 EN. Luxemburgo: Office for Official Publications of the European Communities; 2004.

ICRP. *Diagnostic reference levels in medical imaging: review and additional advice*. ICRP Publication, Oxford:Pergamon Press, UK. 2002. 14p.

ICRP. *Managing patient dose in computed tomography*. ICRP Publication 87. Annals of the ICRP 30 (4), Oxford:Pergamon Press, UK. 2000.

Kleinman PL et al. *Patient size measured on CT images as a function of age at a tertiary care children's hospital*. AJR Am J Roentgenol. 2010; 194(6):1611-1619, Thieme, 2a. edição, 2012;

Li, J et al. *Automatic patient centering for MDCT: effect on radiation dose*. American Journal of Roentgenology 188.2 (2007): 547-552.

Study of CT Head Scans Using Different Voltages: Image Quality Evaluation

Iara Pacheco de Freitas Correa[1], Thessa Cristina Alonso[2]
Priscila Santana[3], Arnaldo Prata Mourão[1,4]

[1] Biomedical Engineering Center, Federal Center for Technological Education of Minas Gerais,
Av. Amazonas, 5253 - Sala 113. CEP: 30421-169, Nova Suíça, Belo Horizonte, MG, Brazil
iarapfcorrea@gmail.com

[2] Development Center of Nuclear Technology, CNEN
Av. Antônio Carlos 6627, CEP: 31270-90, Pampulha, Belo Horizonte, MG, Brazil
alonso@cdtn.com

[3] Department of Anatomy and Imaging, Federal University of Minas Gerais,
Av. Prof. Alfredo Balena, 190 CEP: 30130-100, Belo Horizonte, MG, Brazil
pridili@gmail.com

[4] Department of Nuclear Engineering, Federal University of Minas Gerais,
Av. Antônio Carlos 6627, CEP: 31270-90, Pampulha, Belo Horizonte, MG, Brazil
apratabhz@gmail.com

Abstract

Computed tomography (CT) was introduced to medical practice in 1972. It generates images recognized by high diagnostic potential. CT allows investigation of structures in the human body inaccessible by conventional image dmethods, replacing invasive methods in many cases. Noise is a kind of variation of brightness observed on CT images, and it is inherent to this method. The magnitude of the noise is determined by the standard deviation of CT numbers of a region of interest (ROI) in a homogeneous material. The aim of this study is to analyze the noise in head CT images generated by different acquisition protocols using four voltage values. Five different scans were performed using a female Alderson phantom and their images were analyzed with the RadiAnt software. With the average HU values and standard deviation of each scan, the values of noise were calculated in some ROI. The obtained noise values were compared and it was observed that the 140 kV voltage promotes the in the lower noise in the image, resulting in better image quality. The results also show that the parameters, such as voltage and current, can be adjusted so that the noise can be decreased. Thus, acquisition protocols may be adapted to produce images with diagnostic quality and lower doses in patient.

Keywords: *Computed Tomography, medical images, noise.*

1.- INTRODUCTION

A computed tomography (CT) system consists, basically, in an X-ray tube that rotates around the patient emitting radiation. A detector set positioned on the opposite side of the X-ray tube captures photons passing through the patient without interacting, and a reconstruction algorithm, composed by sequence of mathematical instructions, converts the signals measured in different angles of incidence of the X-ray beam by detectors in an axial image [Garib et al. 2007; Goldiman 2007].

The image obtained is shown as a matrix in which each pixel is associated with a numerical value, called CT number. This number is expressed in Housfield units (HU) and it is related to the average linear coefficient of attenuation volume element (voxel) belonging to the irradiated slice that is being irradiated and is represented by a pixel in the image [Mourão 2015; Dance 2014].

Generated images in a CT test have some advantages over radiographies, such as the ability to distinguish structures of organs and tissues with minor differences in density, in particular soft tissue. CT images have not geometric distortion and the image represents a cross section without anatomical structure superimposition.

Quality of the CT image is influenced by the parameter of the acquisition protocol that is related too with the patient dose. There are parameters related to the reconstruction and image display, and the clinical characteristics (patient size, patient cooperation in relation to the movement and contrast medium administration procedure) that affect the image quality but not affect the patient dose. The acquisition protocol of a scan should always be adjusted so that the image had at tem same time diagnostic quality and reduced artifacts and noise [De Pina 2009].

Noise is an index related to the graininess observed on CT image, how lower is the noise more homogeneous is the representation of the structure. It is a result of the quantum nature of X-ray photons, and the reconstruction image process generates a local static fluctuation

in CT numbers, in a region representative of homogeneous material. Noise magnitude is determined by standard deviation of the CT numbers on the region of interest (ROI) in a homogeneous material. The predominant source of noise is the fluctuation of the number of X-ray photons detected. Therefore, it depends on the detector efficiency and the flow of photons that reaches the detector.

There are others factors that may influence noise value, such as the tube voltage, cathode-anode current, beam filter, slice thickness, body volume and composition of the region under study and the reconstruction algorithm. The aim of this study is to analyze the noise in head CT scans generated by different acquisition protocols [Mourão 2015, Hoffman 2011].

2.- MATERIALS AND METHODS

Scans were performed in a General Electric CT scanner, Discovey model with 64 channels. Five head CT scans were performed using a female phantom Alderson Rando®. This phantom is composed of a human skeleton covered by a material physically and chemically similar to the soft tissues of an adult human body. The body trunk is divided in axial slices of 2.5 cm thick. Figure 1 shows the phantom with the head positioned in the gantry isocenter.

Figure 1.- Alderson Rando phantom positioned in the CT scanner.

Scans were done for a distance of 125 mm starting on the head top, Pitch 0.531, Table Speed 10.62 $m.s^{-1}$, tube rotation time of 0.5 s, X-ray beam thickness of 20 mm and reconstruction of the image of 3.75 mm. The acquisition parameters variables for each scan are shown in Table 1. In the table they are also given the CT Dose Index values estimated by the scanner software, CTDIvol and DLP.

Tomographic image analysis was performed using the RadiAnt software, a viewer of medical images in DICOM format. For each scan protocol, three ROIs were selected in three different images, in the top, middle and base of the head scan. The ROI size has about 100 pixels. Figure 2 shows three axial images (top, middle and base) extracted from head CT scan with the ROI positions, anterior (A), central (C) and posterior (P) .

Table 1.- Variable parameters of acquisition protocols.

Scan	Voltage (kV)	Current (mA)	CTDIvol (mGy)	DLP (mGy.cm)
1	120	150,00	26,07	433,47
2	120	101,00*	17,08	288,98
3	100	125,40*	13,65	226,92
4	80	193,72*	12,11	201,44
5	140	101,00*	24,14	401,47

* automatic mA, average value.

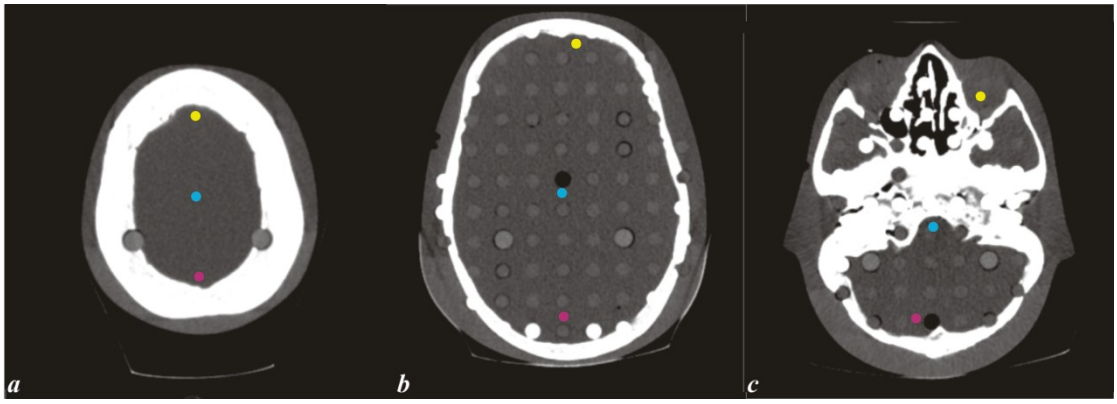

Figure 2 – head axial images, top (a), middle (b) and base (c).

For each analyzed image (top, middle and base) in the scan, there were obtained three average values in HU and their standard deviation (SD). With these data, noise was calculated using the equation (1).

$$Noise = \left(\frac{SD}{HU_{average} - HU_{air}}\right).100\% \quad (1)$$

Where $HU_{average}$ is the average number of CT ROI in Housfield scale and HU_{air} is the CT number of the air (-1000).

Noise value is given by the SD divided by the ROI CT number subtracted the air CT number, because the lowest Hounsfield scale value is the air and its value is not zero, it is -1000 HU. So, the size of the ROI measure starts in -1000. This value must be subtracted so that it has a zero reference for the lowest recorded value. The final value of the noise is given in percent.

3.- RESULTS

The calculated noise values for the studied scans are shown in the Tables 2, 3 and 4, corresponding to the top, middle and base images, respectively.

Table 2.- Percentage noise values in the top image.

Scan	Position			Average	SD
	A	C	P		
1	0.67	0.67	0.65	0.66	0.01
2	0.93	0.89	0.82	0.88	0.06
3	1.05	1.13	1.02	1.07	0.06
4	1.24	0.95	1.06	1.08	0.15
5	0.76	0.70	0.81	0.76	0.06

Table 3.- Percentage noise values in the middle image.

Scan	Position			Average	SD
	A	C	P		
1	1.06	0.80	0.73	0.86	0.17
2	1.10	1.12	0.95	1.06	0.09
3	0.97	1.15	1.23	1.12	0.13
4	1.56	2.29	1.39	1.75	0.48
5	1.07	0.92	0.53	0.84	0.28

Table 4.- Percentage noise values in the base image.

Scan	Position			Average	SD
	A	C	P		
1	0.71	1.03	1.16	0.97	0.23
2	0.99	1.52	1.16	1.22	0.27
3	1.23	1.67	1.44	1.45	0.22
4	1.39	2.17	1.30	1.62	0.48
5	0.53	1.27	1.08	0.96	0.38

Table 5 shows the average noise and the standard deviation for each scan using the values shown in the Tables 2, 3 and 4. These values were used to do the graph presented in the Figure 3.

Table 5.- General percentage noise values.

Scan	Image			Average	SD
	Top	Middle	Base		
1	0.66	0.86	0.97	0.83	0.16
2	0.88	1.06	1.22	1.05	0.17
3	1.07	1.12	1.45	1.21	0.21
4	1.08	1.75	1.62	1.48	0.36
5	0.76	0.84	0.96	0.85	0.10

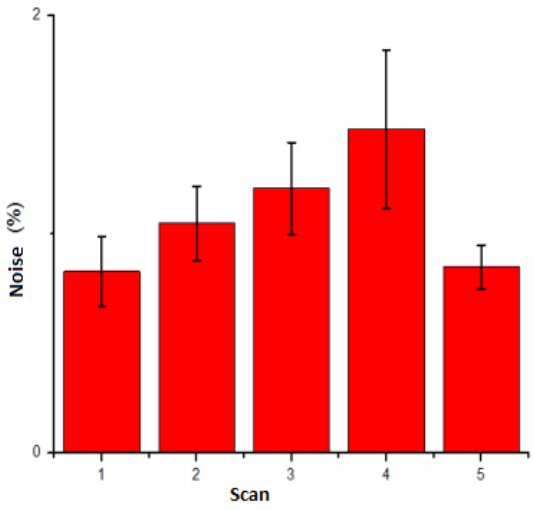

Figure 3.- Graphical comparison of noise percentage.

4.- DISCUSSION

By the analyses of the noise in performed scans it is observed that the top images have a lower noise values than the middle and the base in all scans. Probably this has been caused by the small head diameter in this region.

The use of automatic adjust made increase the noise values, compared with the first scan in which it was used a fixed current, but in general the percentage noise value is low in all the scans, varying from 0.83 to 1.48%, and the images have a good diagnostic quality. However, considering the scans 2, 3, 4 and 5, independent of the observed image (top, middle or base), the higher voltage value applied in the tube generated the lower noise value.

The use of automatic current in the scan 2 (120 kV) promoted a reduction of about 36.67% in the current value. This reduction in current promoted a proportional reduction of dose, according to the dose estimation given by the scanner software.

This behavior is in agreement with the expected since the number of photons that reach the detector will be greater at more penetrating beams and for this reason the voltage 140kV promoted the lowest noise value for use in automatic mode. The greatest variation of noise was found for the scanning with 80 kV (1.48%) and with this scan the patient dose would be the lower. The dose reduction estimated by the scanner software is about 53.55% compared to the fixed current scan, used how routinely used in the Radiology Service.

5.- CONCLUSIONS

The obtained noise values were compared and it was observed that the 140 kV voltage promoted the slightest noise in the image, resulting in the best image quality. The results also showed that the parameters, such as voltage and current, may be adjusted, so that the noise can be decreased. Thus, it is possible to get images with diagnostic quality and lower doses in patient by adapting acquisition protocols.

It should also be appreciated that the dose received by the patient will also be larger, so that the parameters must be adjusted to obtain a final image with a low noise and a smaller dose deposition to minimize the increased probability of injuries to the patient.

Acknowledgments

Acknowledgements to support provided by CNPq, FAPEMIG, The Molecular Imaging Center of UFMG for the generation of images and Prof. Arnaldo Prata Mourão for guidance throughout the work.

REFERENCES

Dance, DR. et al. *Diagnostic radiology physics:* A handbook for teachers and students. American Association of Physicists in Medicine. (2014).709p.

DePina DR; Duarte SB, Netto TG; Morceli J; Carbi EDO; DeSouza RTF; Ribeiro SM. (2009). Controle de qualidade e dosimetria em equipamentos de tomografia computadorizada. *Radiologia Brasileira*, *42*(3).

Garib DG; Raymundo Jr R; Raymundo MV; Raymundo DV; Ferreira SN. (2007). Tomografia computadorizada de feixe cônico entendendo este novo método de diagnóstico por imagem com promissora aplicabilidade na Ortodontia. *R Dental Press Ortodon Ortop Facial*, *12*(2), 139-56

Goldman LW. (2007). Principles of CT: radiation dose and image quality. *Journal of nuclear medicine technology*, *35*(4), 213-225

Hoffmann E. Estudo de Parâmetros Físicos Envolvidos com a Qualidade da Imagem em Tomografia Computadorizada de Feixe Cônico. *Revista da Graduação* 4.1 (2011).

Mourão AP. (2015). Tomografia computadorizada: tecnologias e aplicações. *Difusão. São Caetano do Sul, Brasil*.

Medición de Dosis en Tiroides en Pacientes Sometidos a Ortopantografía Digital Utilizando Dosímetros de Estimulación Óptica

Jesús Gerardo Gutiérrez Marquez[1, 2], Lourdes Yatzil Avalos Piña[3]
Alberto López Valencia[1] Teodoro Rivera Montalvo[1]

[1] Centro de Investigación en Ciencia Aplicada y Tecnologías Avanzadas.
Calzada Legaría No. 694 Col. Irrigación.
Delegación Miguel Hidalgo, Ciudad de México, México

[2] Departamento de Física Médica, Hospital de Oncología Centro Médico Nacional Siglo ,XXI.
Av. Cuauhtémoc No. 330, Col. Doctores.
Delegación Cuauhtémoc, Ciudad de México, México.

[3] Facultad de Odontologia, UNAM.

E-mail: jggm25@yahoo.com.mx
poker_2343@hotmail.com

Resumen

El presente trabajo estudia la dosis equivalente a tiroides en 300 pacientes sometidos a estudios de ortopantografía digital para fines odontologícos utilizando dosímetros de estimulación óptica (OSL) como dosímetros in-vivo con la finalidad de comprobar si esta se encuentra dentro de parámetros aceptables para prevenir riesgos estocásticos y evaluar los posibles riesgos provocados por la técnica utilizada para este tipo de estudio (66 kv, 5 mA, 14.1 s). Se utilizaron 3 dosímetros OSL por paciente, los cuales fueron colocados por el medico sobre la piel que se encuentra por encima de la glándula tiroides (utilizando referencias anatómicas y palpación) la información de los pacientes fue dividida por talla de cuello y sexo encontrando un ligero aumento en la dosis equivalente en pacientes femeninas y pacientes de talla pequeña, siendo la combinación femenina/ talla pequeña el grupo que se encuentra sometido a mayor dosis, los resultados obtenidos fueron comparados con estudios similares realizados en maniquíes antropomorfos con dosímetros TLD obteniendo menores resultados. La dosis equivalente encontrada si bien se encuentra por debajo del umbral daño estocástico debe de ser motorizada con fines de protección radiológica y registro.

Palabras clave: OSL, radiodiagnóstico, dosimetría, protección radiológica, ortopantografía digital.

1. - INTRODUCCIÓN

En la práctica odontológica el uso de equipos de ortopantografía digital es considerado como necesario para el diagnóstico y posterior tratamiento de ciertos problemas dentales en los cuales el uso de placas radiográficas es considerado insuficiente, una correcta gestión y uso de tal herramienta es necesaria para asegurarse que las dosis impartida por el dispositivo se encuentran dentro de márgenes aceptables que permitan reducir el riesgo de posibles efectos adversos asociados a su uso, el principal órgano en riesgo en la zona donde se realizan este tipo de procedimientos es la glándula tiroides que es el órgano mas cercano a la región a irradiar y sera el órgano a evaluar, por tal motivo proponemos el uso dosímetros OSL para el monitoreo de las dosis equivalente a superficie sobre la zona donde se encuentra el órgano en cuestión.

Los dosímetros OSL pueden ser utilizados en el monitoreo de dosis ambiental, dosimetría personal y dosimetría in-vivo dentro de los centros de radio diagnóstico, en este trabajo se realizo el monitoreo de 300 pacientes de ambos sexos entre los 18 y 40 años de edad sometidos a un estudio de ortopantografía digital con una técnica estándar (66 kv, 5 mA, 14.1 s).

2. - MATERIALES Y METODOS

La curva de calibración utilizada para la lectura de los dosímetros OSL fue construida con un grupo de dosímetros irradiados con un tubo de rayos X con una capa hemi-reductora de 2.9 mm de aluminio, 80 kV facilitados por la compañía Landauer con un certificado de calibración vigente, la obtención de las lecturas fue realizada con una unidad lectora microStar de Launder Inc. El ortopantógrafo digital utilizado fue un "Instrumentarium OP200D" en el cual se programó una técnica común para todos los pacientes 66 kv, 5 mA, 14.1 s (valores que utiliza para todos sus pacientes el centro donde se realizó el estudio).

El medico coloco 3 dosímetros en cada paciente cuidando su correcta posición por medio de palpación y referencias anatómicas fijando un dosímetros al frente y los dos restantes uno del lado derecho y otro del lado izquierdo, una vez irradiados los dosímetros eran leídos y posteriormente des-estimulados para su re-uso, Se utilizó una totalidad de 100 dosímetros OSL para analizar 300 pacientes.

3. – RESULTADOS.

La dosis equivalente promedio para los pacientes se muestran en las siguientes tablas.

Tabla no.1 resultados pacientes masculinos.

Paciente masculino talla grande.			
Posición de dosímetro	Derecha	Media	izquierda
Promedio de dosis (μSv)	30	25	29
Paciente masculino talla media.			
Posición de dosímetro	Derecha	Media	izquierda
Promedio de dosis (μSv)	32	27	31
Paciente masculino talla pequeña.			
Posición de dosímetro	Derecha	Media	izquierda
Promedio de dosis (μSv)	36	35	32
Pacientes masculinos			
Promedio de dosis (μSv)	3 dosímetros	Dosis máxima	Dosis mínima
Talla grande	31	36	27
Talla media	28	34	22
Talla pequeña	35	40	27

Tabla 2. Resultados pacientes femeninos.

Paciente femenino talla grande.			
Posición de dosímetro	Derecha	Media	izquierda
Promedio de dosis (μSv)	38	33	39
Paciente femenino talla media.			
Posición de dosímetro	Derecha	Media	izquierda
Promedio de dosis (μSv)	50	42	50
Paciente femenino talla pequeña.			
Posición de dosímetro	Derecha	Media	izquierda
Promedio de dosis (μSv)	57	43	53

Pacientes femeninos			
Promedio de dosis (μSv)	3 dosímetros	Dosis máxima	Dosis mínima
Talla grande	37	43	32
Talla media	48	55	40
Talla pequeña	51	59	41

Tabla 3. Comparación y resultados finales.

	Promedio masculino	Promedio femenino	Promedio total
Dosis (μSv)	32	46	39
Comparación con bibliografía			
Este trabajo (66 kV, 5 mA, 14.1 s)		Ludlow et al (66 kV, 16 mA, 14.1 s)	Gavala et al (66 kV, 8 mA, 18 s)
(μSv)	39	50	88

4. – DISCUSIÓN.

El sistema OSL demostró ser practico para este tipo de dosimetría su portabilidad fue especialmente útil en este trabajo y su presentación permitió su colocación en el paciente de manera práctica y no invasiva , los resultados obtenidos fueron mas bajos que los de la literatura lo anterior es debido por la diferencia en la calidad del haz de los tubos utilizados (diferentes marcas y capas hemi-reductoras) y en los mAs usados, (esta medida esta relacionada directamente con la dosis) en nuestro estudio fueron programados 70.5 mAs en Ludlow et al 225.6 mAs y en Gavala et 188 mAs no obstante , es necesario el uso de esta tecnología en radiodiagnóstico para comprobar su uso en dosimetría in-vivo.

5. – CONCLUSIONES.

En los resultados mostrados en las tablas anteriores es posible observar claramente que en el caso de pacientes femeninos y pacientes de talla pequeña existe un aumento palpable en la dosis equivalente a la que se ve expuesto el paciente lo anterior puede ser atribuido al diámetro del cuello y aunque estas dosis son menores a la dosis necesaria para generar un daño estocástico es importante registrarlas y optimizarlas, para tal efecto se propone utilizar una técnica con menor corriente de tubo, para el caso de realizar un estudio en mujeres y/o pacientes de talla pequeña y realizar protocolos con técnicas especificas para las diferentes morfologías de los pacientes.

REFERENCIAS.

EDUARDO G. YUKIHARA, STEPHEN W. S. MCKEEVER, "OPTICALLY STIMULATED LUMINESCENCE: FUNDAMENTALS AND APPLICATIONS", JOHN WILEY AND SONS, INC. (1ST EDITION 2011).

C. A. Perks, C. Yahnke and M. Million, "Medical dosimetry using Optically Stimulated Luminescence dots and microStar readers", 12th International Congress of the International Radiation Protection Association.

E G Yukihara and S W S McKeever, "Optically stimulated luminescence (OSL) dosimetry in medicine", Physics in Medicine and Biology, 53(20), 351-379 (2008).

Paul A. Jursinic, "Characterization of optically stimulated luminescent dosimeters, OSLDs, for clinical dosimetric measurements", Med. Phys. 34(12), 4594-4604 (2007).

Ludlow JB, Davies-Ludlow LE, Brooks SL, Dosimetry of two extraoral direct digital devices: Orthopos plus DS panoramic unit, dentomaxillofac radiol. 2003 julio; 32(4) :229-34.

Gavala sophia, Radiation dose reduction in direct digital panoramic radiography, European journal of radiology. Mayo 2008 71(1):42-8.

The influence of an extrapolation chamber over the low energy X-ray beam radiation field

Marcus Tadeu Tanuri de Figueiredo[1], Teógenes Augusto da Silva[1]

[1] Development Center of Nuclear Technology, CDTN/CNEN, Av.Pres. Antônio Carlos, 6.627 - Campus UFMG, CEP 31270-901 - Caixa Postal 941, CEP 30161-970
Belo Horizonte, Minas Gerais Brazil mttf@cdtn.br

Abstract

The extrapolation chambers are detectors whose sensitive volume can be modified by changing the distance between the electrodes and has been widely used for beta particles primary measurement system. In this work, was performed a PTW 23392 extrapolation chamber Monte Carlo simulation, by mean the MCNPX code. Although the sensitive volume of an extrapolation chamber can be reduced to very small size, their packaging is large enough to modify the radiation field and change the absorbed dose measurements values. Experiments were performed to calculate correction factors for this purpose. The validation of the Monte Carlo model was done by comparing the spectra obtained with a CdTe detector according to the ISO 4037 criteria. Agreements smaller than 5% for half value layers, 10% for spectral resolution and 1% for mean energy, were found. It was verified that the correction factors are dependent of the X-ray beam quality.

Keywords: Extrapolation chamber**;** Monte Carlo simulation**;** CdTe spectrometry**;** low energy

1. - INTRODUCTION

According to the principles of radiation protection, practices involving ionizing radiation should be planned and executed so that the values of individual doses, the number of people exposed and the likelihood of accidental exposures are as low as reasonably achievable.[1] To this end, it is necessary that in the course of radiation dosimetry, reliable dosimeters must be used. The International Organization for Standardization (ISO), in order to promote the standardization and international metrology consistency established sets of X-ray beams of reference, filtered and fluorescence for calibration and dosimeters tests, whose implementation in metrology laboratories must meet specific technical requirements.[2] National laboratories, including the Nuclear Technology Development Center / Dosimeters Calibration Laboratory (LCD / CDTN) implanted reference beams of filtered X-rays ISO 4037. By the other hand, the lack of traceable detectors prevented the attainment of some implanted beams dosimetry.

However, cavitary chambers can be made of air equivalent material and, with proper choice of its walls thickness could be used for primary measurements; provided that it is possible the application of Bragg-Gray principle. [3] One conditions of the Bragg-Gray principle is that the detector presence does not affect the electron fluency. Although the sensitive volume of an extrapolation chamber can be reduced to very small size, their packaging is large enough to modify the radiation field and change the absorbed dose measurements values and so, it is no possible the applying of Bragg-Gray principle without corrections factors.

In this paper the LCD / CDTN irradiation system consisting of the X-ray equipment model ISOVOLT HS 320, manufactured by Pantak Seifert,[4] and the extrapolation chamber PTW 23392[5] were simulated, by the Monte Carlo method, using the MCNPX code [3]. An extrapolation chamber is a cavitary-chamber whose sensitive volume can be adjusted by the electrodes distance adjusts.[7]

Were introduced in the simulation environment the additional filtration for ISO L low energy X-ray quality. A second simulation was performed in the same environment but without the extrapolation chamber. The validation of the Monte Carlo model was done by comparing the spectra obtained with a CdTe detector according to the ISO 4037 criteria.[2]

The aim of this paper is to evaluate the influence of the presence of a PTW 23392 extrapolation chamber on low energy radiation fields and calculate correction factors.

2.- MATERIALS AND METHODS

2.1 The Simulation of the Irradiation Room

In this study, to simulate the irradiation room of dosimeters calibration laboratory (LCD/CDTN) was used the MCNPX code that is able to simulate the spread of both, photons and electrons, in the energy range of interest. The MCNPX is a tool in large use for dose calculation and shielding. Has been constantly updated and has a huge user community.

The constant flow of e-mail between users led good documentation. The MCNPX code instructions, through command lines, divided three main parts: surface card, cells card, and material card. On the surface card are defined the geometry of the cells, in turn, will be filled by the materials defined in material card. The command *tally* refers to the quantity is being studied and should be positioned in the cell of interest. The radiation source may be defined in various ways, depending on the problem.

The geometry of this specific system was described by cells, which are defined by surfaces filled with materials whose data is available. In this paper, the geometry of the simulation project was built by macrobodies, especially the right circular cylinder (RCC), to the PTW 23392 extrapolation chamber and rectangular parallelepiped (RPP) to the X-ray tube shielding box and to the characterization filters. The geometry contemplated only the relevant objects of irradiation room, mainly the PTW 23392 extrapolation chamber, in accordance with the chamber instruction manual [5] and additional information [8].

Figure 1 shows the PTW 23392 extrapolation chamber cross section view.

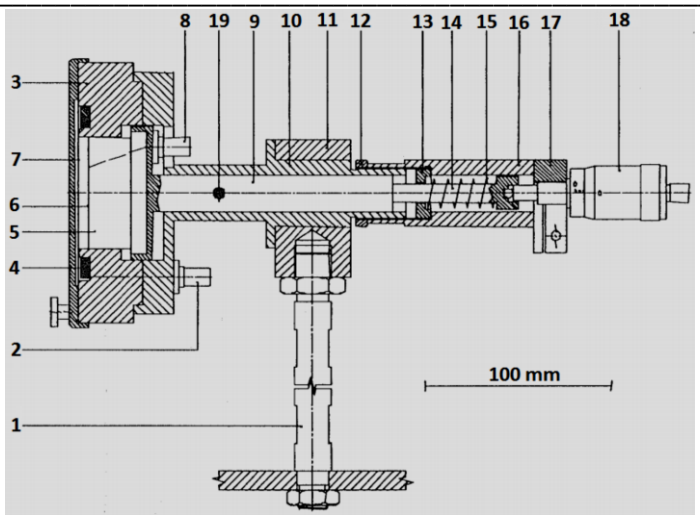

Figure 1 PTW 23392 extrapolation chamber cross-section; 1 support ; 2 bias terminal ; 3 encapsulation ; 4 tension ring ; 5 acrylic block ; 6 graphitized surface; 7 entry sheet; 8 terminal collector ; 9 sliding rod ; 10 central guide ; 11 adjuster ; 12 nut ; 13 screw ring ; 14 pin , 15 Spring ; 16 Tube; 17 bracket , 18 micrometer ; 19 piston clamping screw. (Source : PTW 2002)

A simplified front of PTW 23392 extrapolation chamber was used for modeling; figure 2 shows a PTW 23392 not scaled diagram view.

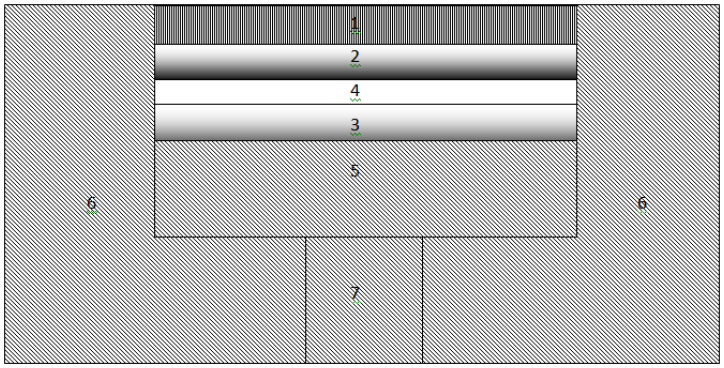

Figure 2 Relevant parts of the extrapolation chambers: 1- Polyethylene terephthalate (entrance foil) 2- Graphite Coated surface 3- Graphite coated surface 4– Extrapolation chamber sensitive volume 5- Rear electrode 6- Polymethylmethacrylate (acrylic) encapsulation. 7- Stem sliding adjustment

Were included in the simulating environment the X-ray shield box and the additional filters for the reproduction of the low energy ISO X-ray beams, series L, both built by rectangular parallelepipeds (RPP).[9] The X-ray beams pulse height spectra of the LCD / CDTN irradiation system up to 30 kV was measured by mean the CdTe spectrometry system,

without any additional filtration. These normalized spectra were used to provide the energy histogram to define the source specifications (SDEF). It was chosen a point isotropic source with a histogram of energy, but collimated into the cone of direction, where particles are confined to a directional cone, whose angle was calculated to fit exactly the diameter of the irradiation system shutter.

In low-energy radiation systems, the interaction of photons with the layer of atmospheric air between source and detector is relevant, and so therefore it is necessary to carefully examine the atmospheric air composition that may change with climatic conditions. In this study it was considered dry air as a gas mixture that compiles the ratio showed at table 1[10]

Table 1 Atmospheric Dry Air Composition

Nitrogen	Oxygen	Argon	Carbon
78.4437 %,	21.0750%,	0. 4671%	0.0151%

By the other hand, the amount of water vapor in the atmospheric air depends on the climatic parameters: temperature, atmospheric pressure and relative humidity and was determined based on the LCD climate conditions, measured during the experimental performance, which they were: temperature 21.3ºC atmospheric pressure 91.92kPa and relative humidity 72.7%. It was determined the saturation pressure for the above temperature, by Tetens formula. The definition of the climate conditions on the LCD / CDTN, allowed to calculate the water vapor fraction in the atmospheric air and hence the fraction of each of the main elements of the mixture.

To evaluate the influence of the presence of an extrapolation chamber on a radiation field would be necessary to carry out dosimetric quantities measures, with the ionization chamber and in her absence. The ratio of results would be used as correction factor. Of course this is not a feasible experiment, except by means of computer simulation. In this simulation project it was choosen the Tally +f6 that matches to deposition energy by mass unit. Results for N and L low energy series, in both cases, were compared.

2.2 The Spectra Measurements

The simulating project of the irradiation system was constructed from the probabilities of each energy, consists of X-rays beams, specific for each tube voltage value. These probabilities were experimentally obtained by normalizing the measured spectra. In this study, the spectrum measurements were carried out at the shortest distance possible- 25 cm, between the focus and detector - in order to avoid, or reduce, the influence of air layer, whose relevance is greater at low energy. Distance limitations are mainly due the low counts rates allowed by Amptek spectrometric system.[11] The spectra, obtained in tabular form, were normalized and used in the source specification (SDEF) and presented in graphical form for purposes of comparison results.

2.3 The Validation of MCNPX Project

There are no, universally established, criteria for validation of computer simulations. In this study were used the ISO 4037 criteria for characteristics x-ray beam implanting. The ISO 4037-1, *X and gamma reference radiation for calibrating dosemeters and doserate meters and for Determining Their response as a function of photon,* determines that an X-ray beam of reference, ISO 4037, can be considered implanted in an irradiation system, since measured characterization parameters, agrees within limits of the specific ISO values, for each quality. The defined parameters are: half-value layers, spectral resolution and mean energy.[2] In this work the measured spectra and the simulation spectra respectively, were used to calculate the parameters mean energy and spectral resolution. By the other hand, the half-value layer in both case, were determined through the use of absorbers for various thicknesses. Results were compared.

3.-RESULTS AND DISCUSSIONS

Table 2 shows the distribution of components of atmospheric air within the aforementioned parameters.

Table 2 Composition of Atmospheric Air in Average Climatic Conditions

Element	Nitrogen	Oxygen	Argon	Hydrogen	Carbon
(%)	75.799	20.716	0.451	1,132	0,0144

The proportions shows in table 2 were used in the material card description. Were observed a reduction, in terms of density, comparing with dry air, by the introduction of water vapor. In fact, the other climatic parameters, atmospheric pressure and temperature are not relevant in this case, since, in the laboratories, the percentage variations in, Kelvin temperature and atmospheric pressure, are minimal, however the relative humidity can change dramatically.

Moreover the results showed that even for a large variation, in relative humidity, the composition of atmospheric air remained essentially the same and produced no significant changes in terms of the photon interaction, but it is necessary to study their contribution as a source of uncertainty.

The measurements of low-energy X-ray spectra, without additional filtration, served primarily to provide the histograms of the sources description. On the other hand, measures of the filtered beams L10, L20 and L30 spectra, with the detector positioned at the standard distance, allowed model validation, giving the results of correction factors improved reliability.

Figures 3, 4, 5, 6 and 7 shows the normalized spectra of the aforementioned reference radiation.

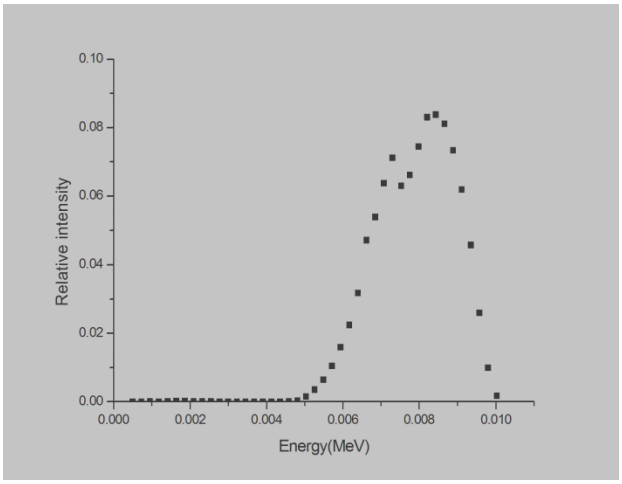

Figure 3 Measured and normalized spectrum of 10 kV beam with7mm Be filtration

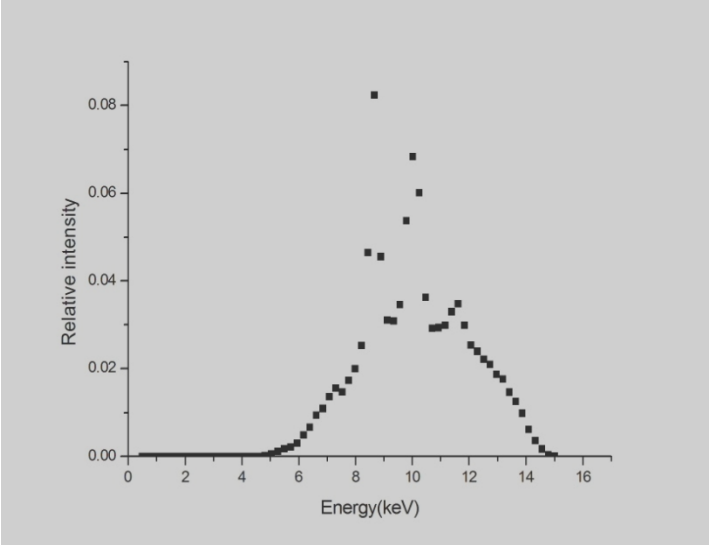

Figure 4 *Measured and normalized spectrum of 15 kV beam with7mm Be filtration*

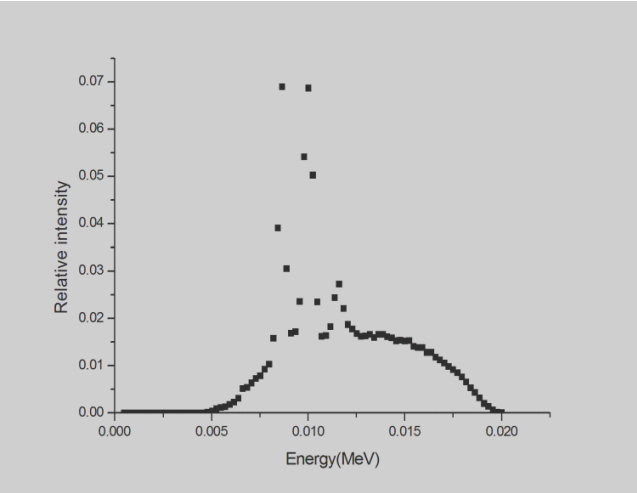

Figure 5 Measured and normalized spectrum of 20 kV beam with7mm Be filtration

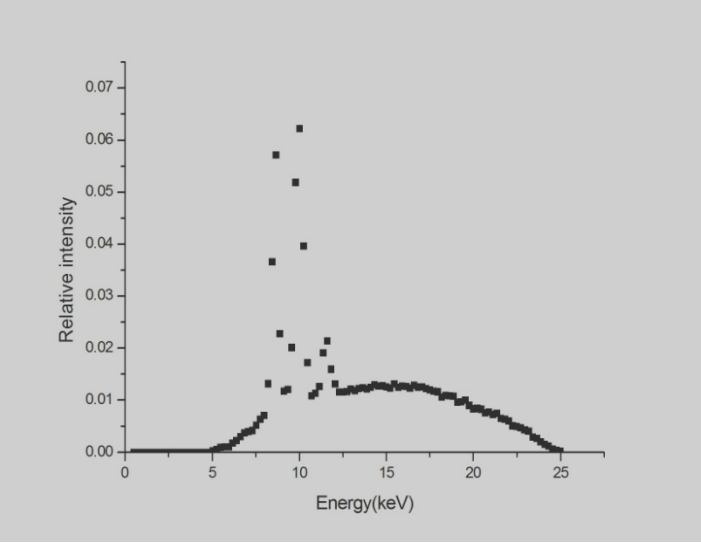

Figure 6 Measured and normalized spectrum of 25 kV beam with7mm Be filtration

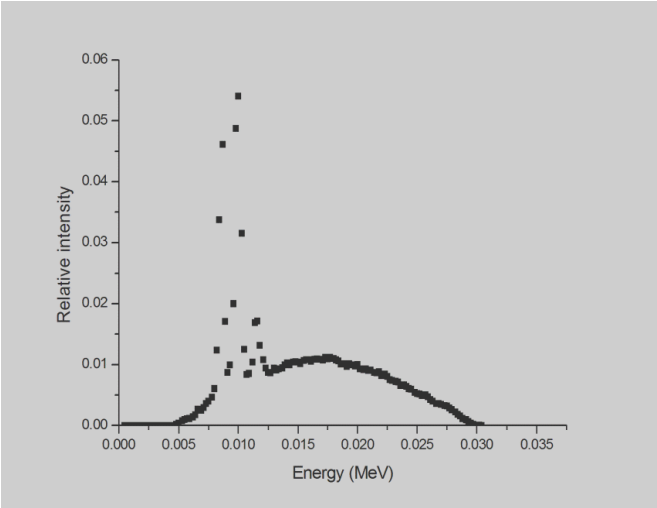

Figure 7 Measured and normalized spectrum of 30 kV beam with7mm Be filtration

Figures 8 and 9 show the simulated and the measured spectra of the ISO L30 X- ray beam.

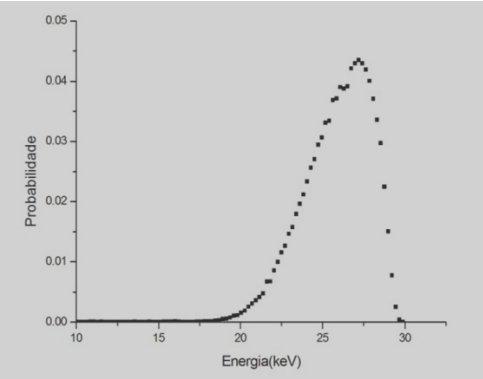

Figure 8 L 30 measured spectra

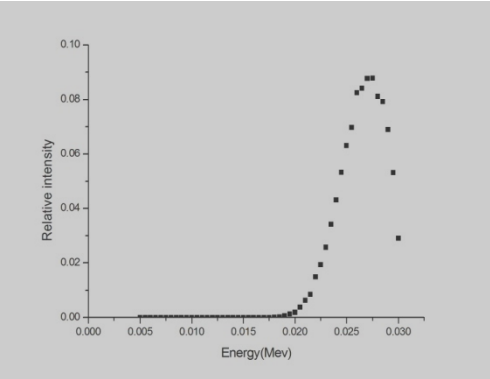

Figure 9 L 30 MCNPX simulated spectra

Table 5 shows the characterization parameters: half-value layer, spectral resolution and mean energy, obtained by analysis of measure and simulated spectra and through complementary experiment.

Table 3 comparing values of the measured L 30 ISO characterization parameters and obtained by simulation MCNPX

ISO Quality	half- Value layer(mmAl)		mean energy (keV)		spectral resolution	
	Experimental	MCNPX	Experimental	MCNPX	Experimental	MCNPX
L 30	1.45	1.51	26.42	26.31	24.03	21.71

Compared to the values of the parameters of the implementation procedure, here was an increase in half value layer of 4.1% a reduction in mean energy 0.5% and a9.6% reduction of the spectral resolution This limits fall within the deployment criteria of ISO 4037 reference X-ray beam.

The correction factors for the presence effect of the extrapolation chamber, over the radiation fields, were calculated comparing the absorbed dose values, observed in the cell that corresponds to the extrapolation chamber sensitive volume, in both cases, ie, with the extrapolation chamber and in it absence.

Table 4 correction factors of the presence of extrapolation chamber of the radiation field at low energies obtained by MCNP simulation

	Dose (Mev/g.N)							
	L 10	L 20	L 30	N10	N15	N20	N25	N30
Absence	9.993E-06	5.806 E-06	4.237 E-07	6.22E-05	5.59E-05	5.03E-05	1.93E-05	8.01E-06
Presence	9.792E-06	5.312 E-06	3.317E-07	5.95E-05	5.02E-05	4.41E-05	1.85E-05	7.32E-06
Correction factor	1.022	1.094	1.277	1.044	1.115	1.140	1.046	1.093

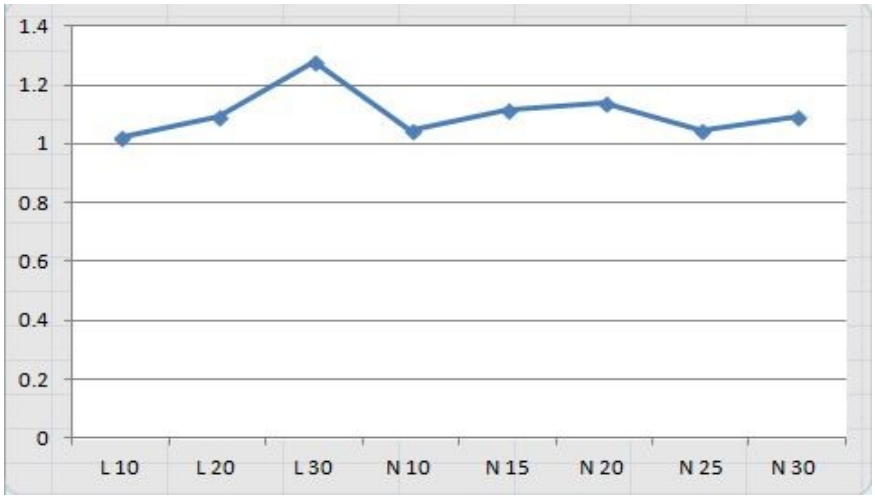

Figure 10 correction factors of the presence of extrapolation chamber of the radiation field at low energies obtained by MCNP simulation

4.-CONCLUSIONS

The results obtained in the validation procedures indicated that the model was designed properly and they were consistent with experimental results. By the other hand, the focus of the issue is to obtain a single correction factor that could calculate all the modifying action of the extrapolation chamber over the radiation field. The clear dependence of the correction factors, with the radiation quality, indicates that the correction factors are to be calculated individually for each reference X-ray beam, implanted on the irradiation system.

ACKNOWLEDGMENTS

This work was supported by INCT Radiation Metrology in Medicine.

We would like to thank the Laboratório de Metrologia de Nêutrons of the Instituto de Radioproteção e Dosimetria (IRD/CNEN) for consenting the use of high-performance cluster for the calculations

Marcus Tadeu Tanuri de Figueiredo is thankful to CNEN for his doctorate fellowship

REFERENCES

[1]INTERNATIONAL ATOMIC ENERGY AGENCY. Calibration of radiation protection monitoring instruments.: Vienna: IAEA 2000. 153 p. (Safety reports series, 16).

[2]ISO, International Organization for Standardization .1996. *ISO 4037. X and gamma reference radiation for calibrating dosemeters and dose rate meters and for determining their response as a function of photon energy. Geneva:* International Organization for Standardization 1996

[3] Knoll, G F. *Radiation detection and measurement***.** New York John Wiley & sons, 1979. 816

[4] AGFA NDT PANTAK SEIFERT GMBH AGFA NDT PANTAK SEIFERT GMBH & CO.KG. Higly Stabilized Industrial X-Ray Equipment ISOVOLT 320: Operating Instructions. 2003

[5] Briesmeister, J.F., 2000. MCNP™—*A general Monte Carlo N-particle Transport Code*, Version 4C. Los Alamos National Laboratory Report LA-13709-M.

[6]PTW-Freiburg, 2002. Instruction Manual Extrapolation Chamber according to Böhm Type 23392 Freiburg Germany : s.n. 2002

[7] INTERNATIONAL COMMISSION ON RADIATION UNITS AND MEASUREMENTS. **Radiation quantities and units**. Bethesda, MD: ICRU, 1980. (ICRU, 33).

[8]Reynaldo, SR Benavente, JA and Da Silva, TA 2013 *Characterization of an extrapolation chamber as a primary standard dosimeter for beta dosimetry.* Scientia Plena 2013 vol 9 pp 081002-6

[9] Shultis, J. K. Faw,R. E. Dept *MCNP primer*, Shultis, J. K. Faw,R. E. Dept. of Mechanical and nuclear engineering Kansas State University- Manhattan,2004

[10] NIST, National Institute of Standards and Technology, Available from <http://www.nist.gov >

[11] AMPTEK, X-Ray & Gamma Ray Detector, XR-100T-CdTe [Internet]. Bedford MA, [cited 2014 Oct 6]. Available from: 〈http://www.amptek.com/xr100cdt.html.

Determinación de dosis absorbida en cristalino y glándula tiroides con protocolos de irradiación aplicados en equipos de ortopantomografía para panorámica dental

Awer Andres Muñoz Ardila[1], Modesto Antonio Sosa Aquino[2], Juan Carlos Azorín Vega[2], Miguel Ángel Vallejo Hernández[2], Lina Marcela Ramírez Arbeláez[1]

[1] Grupo de Investigación e Innovación Biomédica, Instituto Tecnológico Metropolitano, Medellín, Colombia.

[2] Departamento de Física, Universidad de Guanajuato, León, Guanajuato, México.

Resumen

Las radiaciones ionizantes son de gran utilidad en el ámbito médico para el uso diagnóstico de diferentes patologías. Actualmente existen diferentes tecnologías para diagnóstico con imágenes que utilizan Rayos X convencional, tomografía computada, mastografía, angiografía, panorámica dental, entre otros. No obstante, cabe destacar que la exposición a radiaciones de este tipo de exámenes diagnósticos se ha incrementado considerablemente en los últimos años debido a que los exámenes radiológicos no siempre se llevan a cabo en función de las necesidades clínicas reales de cada paciente, incrementando el riesgo de adquirir cáncer. En esta investigación se midió dosis absorbida en cristalino y glándula tiroides con la ayuda de dosímetros TLD100 ubicados en un fantoma de PMMA adaptado para equipos de ortopantomografía (Panorámica dental) en 5 Hospitales; utilizando los parámetros pre configurados para adulto normal para la irradiación; Se utilizó un Equipo Harshaw 3500 para la lectura de los dosímetros obteniéndose así el valor de 1.324 ± SD 0.01 mGy para cristalino y 1.044 ± SD 0.03 mGy valores los cuales se pretenden validar bajo otras condiciones y protocolos.

Palabras clave: Ortopantomografía, TLD100, Termoluminiscencia, dosis absorbida, Tiroides, Cristalino.

1.- INTRODUCCIÓN

Las radiaciones ionizantes son de gran utilidad en el ámbito médico para el uso en el diagnóstico de diferentes afecciones que se presentan diariamente, sin embargo el Consejo Nacional de Protección y Medición de la Radiación (NCRP, por sus siglas en inglés) según sus reportes anuales, indica que la exposición durante dichos exámenes ha aumentado considerablemente en diferentes órganos debido a que los exámenes radiológicos no están siendo en función de las necesidades clínica de cada paciente [Bolus ,N. 2009].

Actualmente existen diferentes tecnologías para diagnóstico con imágenes que utilizan rayos x, tales como: la Radiología Convencional que consiste en un amplio espectro de técnicas de imagen, los cuales forman una imagen al interactuar con las diferentes densidades y espesores de los tejidos del cuerpo humano [Srivastava *et al*,2006]; la tomografía, la mastografía, la angiografía, la ortopantomografía, entre otros.

Los equipos de ortopantomografía se utilizan para ayudar ya sea al odontólogo, al cirujano plástico o médicos especialistas en general a determinar malformidades congénitas, daños dentales (cavidades), enfermedades periodontales (encías), abscesos o crecimientos anormales, tales como tumores o quistes, además de también mostrar la ubicación y condición de los dientes impactados o los dientes que se encuentran aún bajo la encía, etc [Pandolfo y Mazziotti, 2013].

Así entonces, el uso frecuente de estas tecnologías conlleva a evaluar los diferentes riesgos o efectos de acuerdo a la dosis suministrada para realizar el radiodiagnóstico. En esta rama existen estudios que se han encargado de compilar información integral de dosis absorbida en los procedimientos de panorámica dental en comparación con otras técnicas de diagnóstico odontológico [van Aken & van der Linden, 1966]. Actualmente, las investigaciones tienden a centrarse en la evaluación de la exposición a la radiación de órganos específicos tales como la glándula tiroides, la parótida, los ojos, entre otros. [Moundi et al., 2013].

Los efectos radiobiológicos relacionados con los equipos de panorámica dental son un factor de riesgo para órganos tales como la tiroides y el cristalino; teniendo la posibilidad de ser causante de cáncer tiroideo [Wakeford R, 2004. Sarne D, 1996] y cataratas radio inducidas por la distribución de la dosis en las estructuras oculares. [Lesperance M, 2014]. Los factores de riesgo pueden ser determinados con ayuda de dosimetría termoluminiscente a través de la dosis absorbida, por lo que debemos ser capaces de estimar con esta magnitud el daño producido por la radiación en un órgano que ha sido irradiado por un tipo específico de radiación [Andisco, Blanco, & Buzzi, 2014].

1.1.- BASES TEÓRICAS

La interacción de radiación con la materia implica la transferencia de energía de la radiación con la materia con la que interacciona. "La radiación puede interaccionar directamente con el núcleo del átomo, con los electrones orbitales o con ambos. La probabilidad de que ocurra un determinado mecanismo de interacción y, por lo tanto, el poder de penetración de los diversos tipos de radiación, depende del tipo y energía de la radiación como de la naturaleza de la materia con la que interacciona. En general se producirá ionización y excitación de los átomos del absorbedor" [Azorín Nieto & Azorín Vega, 2010].

Los efectos de la radiación sobre la materia se pueden manifestar mediante tres mecanismos principales: ionización, excitación y disociación. La radiación ionizante o de alta energía es aquella radiación capaz de producir iones al quitar o agregar un electrón a un átomo donde irradia y puede ser clasificada en electromagnética (fotones) y corpuscular según su naturaleza. Cuatro son los mecanismos de interacción de la radiación electromagnética (fotones) con la materia que son significativos: efecto fotoeléctrico, efecto Comptom, producción de pares y dispersión coherente o de Rayleigh.

Para efectos de la medición de la radiación se utilizan ciertos sólidos que tienen la propiedad de emitir luz después de ser previamente irradiados si se eleva su temperatura a un valor suficiente por debajo de su temperatura de incandescencia y este fenómeno es relevante en la medición de radiación ionizante ya que la luz emitida es proporcional a la dosis absorbida [Azorín Nieto, 1993]. La dosis absorbida es una medida de la cantidad de energía de una radiación ionizante depositada en una masa. Formalmente, la dosis absorbida en un punto es definida según la ICRU como $D = \frac{\Delta\varepsilon}{\Delta\, m}$ donde $\Delta\varepsilon$ es la energía media transferida por la radiación a una masa Δ m [Gillette & Alpen, 1998]. El objetivo de éste trabajo fue determinar la dosis absorbida en cristalino y glándula tiroides con protocolos de irradiación utilizados en equipos de ortopantomografía para panorámica dental.

2.- MATERIALES Y MÉTODOS

2.1 Diseño del Fantoma

El diseño del fantoma se realiza de acuerdo a un muestreo antropométrico, donde una vez conocidos los valores estándar de la morfología evaluada (15x20x15), se procede a desarrollarlo con materiales de acrílico tipo PMMA donde se tiene en cuenta las características anatómicas de las partes a simular (espesor) [Golikov VY, Nikitin VV,1989].

2.2 Selección del Lote Dosimétrico

Para efectos de evaluación de dosis absorbida en algún órgano se utilizan cristales de LiF:Mg,Ti denominado TLD100 con un número atómico efectivo 8,2; ya que por su naturaleza atómica (Z) poseen similaridades con los tejidos biológicos humanos [Azorín Nieto, 1993]

2.3 Protocolo de borrado y elaboración de la curva de calibración

Para el protocolo de borrado se utilizan 18 pastillas de TLD100 los cuales son colocados en un crisol. Éste se introduce en una mufla marca TERLAB precalentada a 240 °C mientras alcanza los 400 °C para el proceso de borrado y así obtener una mayor reproducibilidad de los resultados. Así entonces se colocan los dosímetros durante 1 hora a 400 °C, tiempo en el cual el aumento de la temperatura ayuda a liberar todas las trampas energéticas del material termoluminiscente y así eliminar información parasita que pudiese crear datos no repetibles. Seguidamente se deja enfriar la plancheta y una vez este un poco más al ambiente se introducen nuevamente los dosímetros a la mufla durante 2 horas a una temperatura de 100 °C para obtener un borrado aún más fino [Azorín Nieto, 1993].

Los dosímetros han sido calibrados con una fuente de rayos X odontológico, a una energía de 90 keV y una distancia de 50 cm del tubo; se colocan de a 2 pastillas dentro de un porta dosímetro. El método de calibración elegido para los dosímetros TLD100 es el de sustitución [Loaiza Calderon & Alvarez Romero, 2006], el cual consiste en a) Calibrar un punto del campo de radiación en términos de la rapidez de Dw, usando para cada energía el protocolo correspondiente, cámaras de ionización patrón secundario o fuentes radioactivas de referencia (Rx periapical para éste caso). b) Colocar en el mismo punto de calibración los dosímetros TLD100 e irradiarlo para varias Dw, de manera independiente de acuerdo al rango de la curva de calibración, controlando el tiempo de irradiación. c) construir la curva de calibración: Intensidad de respuesta vs dosis (Fig. 1).

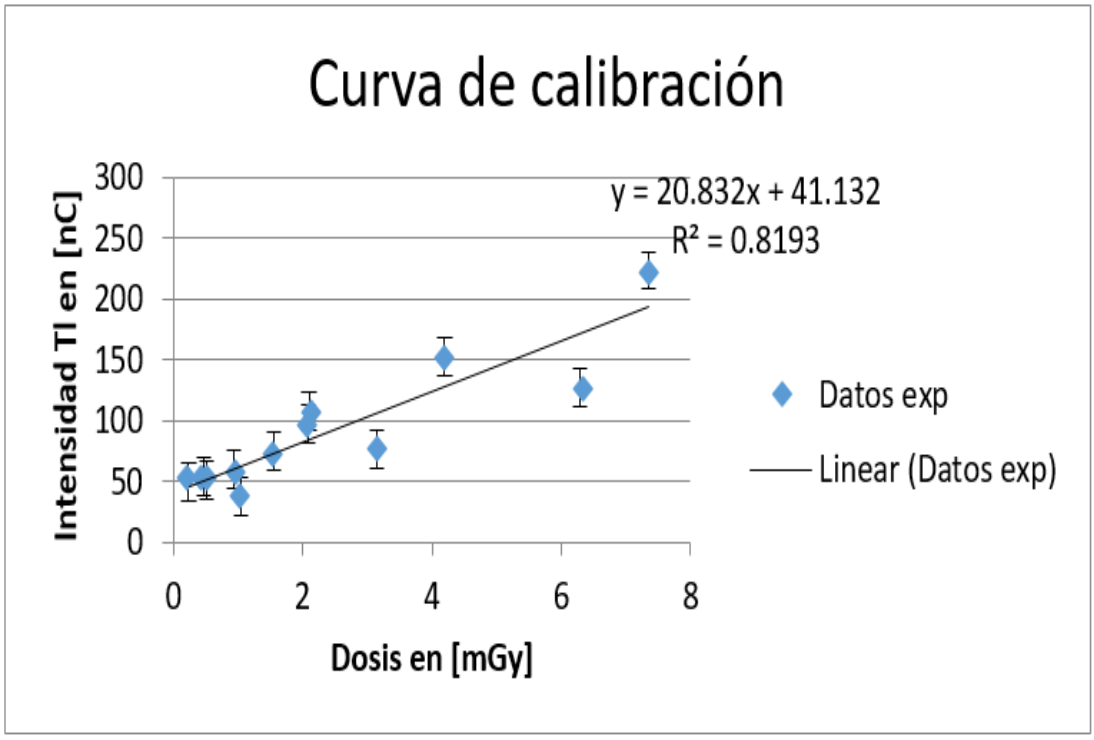

Figura 1. Respuesta Termoluminiscente del TLD100 en función de la dosis.

2.4 Evaluación de protocolos de irradiación en ortopantomógrafos

De acuerdo a los equipos disponibles para realizar las irradiaciones, se ha consultado con los diferentes técnicos cuáles son sus parámetros más utilizados para obtener su imagen panorámica según su equipo y los datos médicos del paciente. Por lo que se ha encontrado que lo más común es obtener la imagen panorámica a 70kVp, 12 mA, 15s para un adulto normal. Adicionalmente, Se dispone a colocar una porta dosímetro con 2 unidades de TLD-100 por cada órgano a evaluar. Es ésta investigación se utilizaron 6 dosímetros por irradiación (4 para cristalino, 2 para tiroides) tres irradiaciones por equipo en un total de 5 equipos de ortopantomografía (Fig.2).

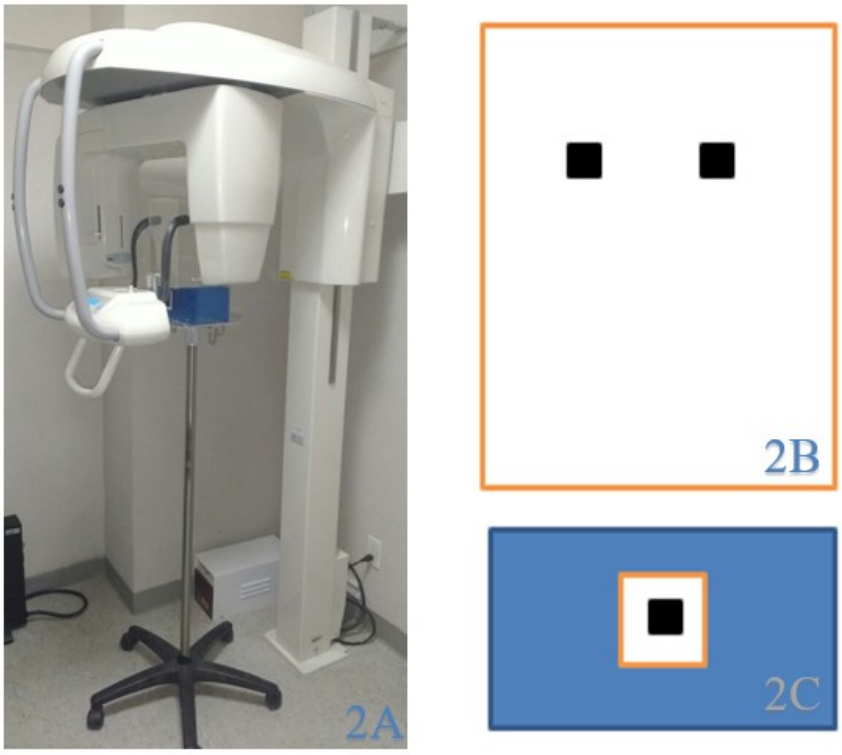

Figura 2 (A, B, C). Arreglo dosimétrico para ortopantomografía con fantoma

FIG.2A Ubicación y ajuste del fantoma al equipo: Se retira posicionador de maxilar inferior, se colocan los posicionadores de cráneo, se realiza un ajuste a cero de la posición del equipo. FIG 2B Descripción gráfica de la ubicación de los dosímetros (Puntos negros) para el muestreo en cristalino y glándula tiroides FIG 2C.

2.5 Configuración del arreglo experimental para Lecturas de TLD

Para la configuración del arreglo experimental para lecturas de TL existen diferentes maneras de realizar las pruebas de lectura las cuales dependen de las condiciones que se requieran en el estudio; Para éste caso se realizan en un cuarto casi oscuro para evitar que radiaciones incidentes de otro intervalo de energías desajusten las trampas anteriormente desequilibradas del material utilizado. se obtiene lectura de luz de referencia.

La lectura de dosímetros se realiza entonces con ayuda del equipo Harshaw modelo 3500 el cual digitaliza sus resultados a través del software win rem. EL procedimiento a ocupar consiste en configurar el protocolo TTP (Time Temperature Profile Setup) configurando la temperatura de precalentado (Preheat) con 50 °C por 20 s; después se realiza una configuración de la rampa de precalentamiento (Temperature Rate) de 10 °C por cada segundo y también se ingresa una temperatura máxima de calentamiento a 300 °C.

3.- RESULTADOS Y DISCUSIÓN

Analizando las lecturas obtenidas de los dosímetros irradiados representando el cristalino, el promedio de dosis (mGy) absorbida por el equipo Kodak 8000C Digital fue de 1.37 ± SD 0.01 (mGy), Sirona Orthopos 1.24 ± SD 0.01 (mGy), Panoramic Corporation 1.47 ± SD 0.01 (mGy), Carestream CS9300 1.36 ± SD 0.01 (mGy), OP300 Maxio 1.18 ± SD 0.01 (mGy), obteniendo un promedio de dosis de 1.324 ± SD 0.01 (mGy), que se puede observar en la Tabla 1.

El análisis de las lecturas de los dosímetros irradiados representando la glándula tiroidea (Tabla 2) demuestra que la dosis absorbida fue en promedio de 1.044 ± SD 0.03 (mGy). Para el equipo kodak 8000C Digital su dosis fue de 0.82 ± SD 0.03 (mGy), Sirona Orthopos 1.07 ± SD 0.03 (mGy), Panoramic Corporation 1.15 ± SD 0.03 (mGy), Carestream CS9300 1.31 ± SD 0.03 (mGy), OP300 Maxio 0.87 ± SD 0.03 (mGy).

Dosis Cristalino	
Equipo de Ortopantomografía	**Dosis (mGy)**
Kodak 8000C Digital	1.37 ± SD 0.01
Sirona Orthopos	1.24 ± SD 0.01
Panoramic Corporation	1.47 ± SD 0.01
Carestream CS 9300	1.36 ± SD 0.01
OP300 Maxio	1.18 ± SD 0.01
Promedio de Dosis	1.324 ± SD 0.01

Tabla 1. Dosis en Cristalino

Dosis Glándula Tiroides	
Ortopantomógrafos	**Dosis (mGy)**
Kodak 8000C Digital	0.82 ± SD 0.03
Sirona Orthopos	1.07 ± SD 0.03
Panoramic Corporation	1.15 ± SD 0.03
Carestream CS 9300	1.31 ± SD 0.03
OP300 Maxio	0.87 ± SD 0.03
Promedio de Dosis	1.044 ± SD 0.03

Tabla 2. Dosis en Tiroides

La tabla 1 muestra que la mayor dosis recibida en cristalino fue de 1.47 ± SD 0.01 (mGy) en el equipo Panoramic Corporation. Esta dosis comparada con la obtenida en otros

estudios anteriores de 0.12 mGy ±0.068 en cristalino (Moudi, E. et Al.2013) varia tal vez por los protocolos de irradiación utilizados, el equipo, las condiciones y el tipo de dosímetro utilizado. La tabla 2 muestra que la mayor dosis en tiroides fue de 1.47 mGy ± SD 0.03 en el equipo Carestream CS9300 en comparación con la obtenida de 0.15 mGy ±0.06 las probables razones de esta contravención son las condiciones y técnica usada.

5.- CONCLUSIONES

El objetivo de evaluar la dosis absorbida en cristalino y glándula tiroides fue logrado con el uso de dosímetros TLD100 adaptados a un fantoma, siendo ésta una técnica reproducible y confiable. Sin embargo, el procedimiento para medir la exposición a la radiación de los pacientes en radiografía panorámica dental con dosímetros termoluminiscentes requiere ser evaluado in situ con el paciente ya que los resultados con el fantoma no se evidencia diferencias relevantes a las dosis límite establecidas por la ICRP (Statement on Tissue Reactions,2011).

Se midió dosis absorbida en cristalino y glándula tiroides en un fantoma de PMMA adaptado para equipos de ortopantomografía en 5 hospitales obteniéndose el valor en mGy de 1.324 ± SD 0.01 en cristalino y 1.044 ± SD 0.03 en tiroides con dosímetros TLD100 calibrados con una fuente de rayos X odontológico tipo periapical. Los valores encontrados están por encima de los valores encontrados en la literatura; las posibles explicaciones para esto son la utilización de diferentes parámetros, los tipos de equipo, las condiciones, la fuente de calibración, el fantoma usado, entre otros.

Para validar los resultados encontrados se realizarán nuevas mediciones en diferentes condiciones y probando con otras fuentes de calibración como Cs-137, Co-60, Rayos X convencional, entre otros. Buscando de este modo el protocolo adecuado y seguro en la medición de estas mismas dosis en México para pacientes debido a la poca frecuencia de estos estudios en ortopantomografía en el país.

Agradecimientos

Se Agradece la colaboración de I.B. Lizbeth Piña en la revisión; A las unidades HRAEB, HAL, HAP, ESDOM, CEDIMEX por permitir realizar las irradiaciones.

REFERENCIAS

Andisco, D., Blanco, S., & Buzzi, A. (2014). Dosimetría en radiología. Revista Argentina De Radiología, 78(2), 114-117. http://dx.doi.org/10.1016/j.rard.2014.06.010

Azorín Nieto, J. & Azorín Vega, J. (2010). Protección radiológica. México, D.F.: Universidad Autónoma Metropolitana.

Azorín Nieto, J. (1993). Estudio de las propiedades termoluminiscentes y ópticas de los principales materiales dosimétricos (Doctorado en Ciencias). Autónoma Metropolitana - Iztapalapa.

Bolus N. (2009). Reporte 160. Programa de Tecnología en Medicina Nuclear.

Charles, M. (2007). ICRP Publication 103: Recommendations of the ICRP. Radiation Protection Dosimetry, 129(4), pp.500-507.

Gillette, E. & Alpen, E. (1998). Radiation Biophysics. Radiation Research, 149(5), 529.

Golikov VY, Nikitin VV. Estimation of the mean organ doses and the effective dose equivalent from Rando phantom measurements. Health Phys 1989; 56:111—5

Lesperance M, Martinov M, Thomson R. (2014). Monte Carlo dosimetry for 103Pd, 125I, and 131Cs ocular brachytherapy with various plaque models using an eye phantom. Med Phys. 41(3):031706.

Loaiza Calderon, S. & Alvarez Romero, J. (2006). Calibración de polvo TLD-100 para energías de 60Co, 137Cs, 192Ir y RX de 250, 50 kVp en dosis absorbida en agua con fines de control de calidad dosimétrico para braquiterapia de alta tasa de dosis. Revista Mexicana De Física, 52(5), 413–421.

Moudi, E., Hadian, H., Monfared, A., Haghanifar, S., Deilam, G., & Bahemmat, N. (2013). Assessment of radiation exposure of eyes, parotid and thyroid gland during panoramic radiography. World Journal of Medicine And Medical Science Research, 1(3), 044 - 050.

Pandolfo I, Mazziotti S. (2013). Orthopantomograpgy [monograph on the Internet]. Milán: Springer-Verlag Italia; Disponible en http://link.springer.com/book/10.1007%2F978-88-470-5289-5

Sarne DSchneider A. (1996). External Radiation and Thyroid Neoplasia. Endocrinology and Metabolism Clinics of North America.25(1):181-195.

Srivastava S, Unni T, Pandarkar S, Mahajan K, Suthar R. (2006). Radiografía Convencional [Conventional Radiograpy]. Issue 285. 174-180.

Van Aken, J. & van der Linden, L. (1966). The integral absorbed dose in conventional and panoramic complete-mouth examinations. Oral Surgery, Oral Medicine, Oral Pathology, 22(5), 603-616. http://dx.doi.org/10.1016/0030-4220(66)90164-2

Wakeford R. (2004). The cancer epidemiology of radiation. Oncogene; 23(38):6404-6428.

Dosis absorbida en el feto de una paciente embarazada cuando se administra I^{131} (yoduro)/Tc^{99m} (pertecnetato) durante estudios tiroideos

Marcial Vásquez Arteaga[1, 2], Víctor Murillo Caballero[1], Juan Arbayza Fructuoso[1]
Paulino Sánchez Sandoval[1], Carlos Cabrera Salvatierra[1]

[1]Nuclear Physics Laboratory; National University of Trujillo (UNT), Trujillo, Perú,
marvva@hotmail.com

[2]Cesar Vallejo Private University (UCV), Av. Larco, Cuadra 17, Trujillo, Perú,
stick_2091@hotmail.com

Abstract

Se estima la dosis de radiación absorbida en el feto de una mujer gestante durante sus estudios tiroideos, a través del análisis de la biocinética de radiofármacos que contiene I^{131} (yoduro) o Tc^{99m} (pertecnetato). Se usa el formalismo MIRD, y su representación Cristy- Eckerman. Los resultados indican:

La dosis absorbida por el feto de una mujer de 3,6 y 9 meses de gestación debido a las emisiones del Tc^{99m} es menor a la obtenida por el I^{131}; representan el 34.7% ,6% y 3.5% de la dosis generado por el yoduro.

La auto dosis en el feto de una mujer gestante se deben fundamentalmente al depósito local de energía de las emisiones beta y gamma del I^{131} siendo mayor al reportado por las emisiones gamma y electrones de conversión del Tc^{99m}.para los fetos de 6 y 9 meses.

La dosis incorporada al feto debido a los órganos de los tejidos maternos, que hacen parte de la biocinética, se deben básicamente a la emisión de sus fotones gamma y corresponden a 38.50% /60.52% en fetos de 3 meses ,64.71% /12.43% en fetos de 6 meses, y 69.79% /10.97% en fetos de 9 meses para los radiofármacos Tc^{99m} (pertecnetato) /I^{131} (yoduro),

Los órganos de la biocinética que contribuyen a la dosis del feto se deben fundamentalmente a la vejiga, seguido del resto, e intestino delgado (fetos de 3 meses); del resto, seguido del intestino delgado y vejiga (fetos de 6 meses);de la vejiga, seguido del intestino delgado y estomago (fetos de 9 meses) cuando se usan el I^{131} ; mientras que para el Tc^{99m} contribuyen la vejiga y resto (fetos de 3 meses); de la placenta, seguido del resto y vejiga (fetos de 6 y 9 meses) .

Keywords: Feto, MIRD Dosimetry, Pertecnetato, yoduro

1.- INTRODUCCIÓN

El estimado de dosis absorbida por el feto de una mujer gestante durante estudios tiroides, puede ser realizado a través del análisis de la biocinética de radiofármacos, que contengan Tc^{99m} (pertecnetato) y I^{131} (yoduro)

1.1 Bases Teóricas

Para estimar la dosis absorbida por el feto de una mujer gestante, debido a las contribuciones dosimétricas de los órganos de la biocinética, fueron utilizados el formalismo MIRD y la representación de Cristy-Eckerman para dichos órganos. Medical Internal Radiation Dosimetry considera las ecuaciones [Asociación Argentina de Biología y Medicina Nuclear, 2013]:

$$\frac{D_{fotones}(feto)}{A_0} = \sum_{i=1} \left[\sum_k \Delta_k \, \Phi_k \, (feto \leftarrow i) \right] \tau_i \qquad rad / \mu Ci$$

$$\frac{D_{particle}(feto \leftarrow feto)}{A_0} = [\bar{E}_{particle} \frac{\tau_{feto}}{m_{feto}} \,] x 2,13 \qquad rad / \mu Ci$$

$\tau_{TB} = tiempo\ de\ residencia\ del\ cuerpo\ total$

$m_{TB} = masa\ total\ del\ cuerpo$

2.- MATERIALES Y MÉTODOS

Las fracciones absorbidas, Φ_k (feto ← i) g-1, de los "i" órganos analizados (tiroides, estomago, intestino delgado, feto, vejiga y el tejido restante, para el radiofármaco I^{131}; tiroides, estomago, LLI,ULI, feto, vejiga y el tejido restante, para el Tc^{99m} que corresponden a las energías de los fotones "k" del Tc^{99m} y del I^{131} que fueron obtenidos de ORNL/TM-12907, [M.G.Stabin ,E:E: Watson 1995] . Los tiempos de residencia de los mencionados radiofármacos, en cada órgano de la biocinética, dados en las tablas 1, fueron obtenidas de la página web [HPS, 1997].

Tabla 1. Tiempos de Residencia para Órganos de la biocinética del I^{131} y Tc^{99m} (horas) [HPS, 1997]

RFM	Tiroides	Estómago	Intestino delgado	Feto (3 meses)	Feto (6 meses)	Feto (9 meses)	Vejiga	Resto del cuerpo
I-131	6.10E+01	1.33	1.5	8.20E-02	2.21E+00	4.71E+00	1.92	6.40

RFM	Tiroides	Estómago	LLI	ULI	Feto	Vejiga	Placenta	Resto del cuerpo
Tc-99m	3.80E-02	3.03E-01	4.90E-01	7.90E-01	3.34E-01	7.95E-01	9.5E-01	5.02

$\Delta_k = 2{,}13\ n_k\ E_k \quad (\frac{rad-gm}{\mu Ci-hr})$, representa la energía media de los "k" fotones emitidos en el decaimiento del Tc99m, dados en Tabla 3, fueron obtenidas de página web [HPS, 2013].

Tabla 2. Data nuclear para fotones emitidos (MeV) del Tc^{99m} y I^{131}más significativas

RFM	Fotones	E_k (Me V)	n_k/des	$\Delta_k = 2{,}13\ n_k\ E_k$ $(\frac{rad-gm}{\mu Ci-hr})$
I^{131}	Radiación Gamma	0,080	0,026	0,0044
		0,284	0,06	0,0363
		0,364	0,817	0,6334
		0,637	0,0717	0,097
		0,723	0,0177	0,027
	Radiación Característica	0,0295	0,0138	0,00088
		0,0298	0,0256	0,0016
		0,0336	0,009	0,0006
Tc^{99m}	Radiación Gamma	0,1405	0,8906	0,2665
		0,1426	0,0002	0,0001
	Radiación Característica	0,0183	0,021	0,0008
		0,0184	0,040	0,0016
		0,0206	0,012	0,0005

$\bar{E}_{particle}$(MeV/des), representa la energía media de partículas emitidas por el Tc^{99m}, es decir, representa a los electrones que aparecen en los procesos de decaimiento, por captura

y electrones Auger; están dadas en la Tabla 4 y fueron tomados de página Web [HPS, 2013]

Tabla 3. Data nuclear para partículas emitidas (MeV) del Tc^{99m} más significativas [HPS, 2013].

RFM	**Partículas**	**E_k (MeV)**	**n_k/des**	$n_k E_k$ (MeV/des)	$\bar{E}_{particle} = \sum n_k E_k$ (MeV/des)
Tc^{99m}	Electrones de conversión	0,1195	0,088	0,01052	0,01446
		0,1216	0,0055	0,00067	
		0,1375	0,0107	0,0015	
		0,1396	0,0017	0,00024	
		0,1400	0,0019	0,00026	
		0,1404	0,0004	0,00006	
		0,1421	0,0003	0,00004	
		0,0016	0,746	0,0012	
	Electrones Auger	0,0022	0,102	0,00022	0,00054
		0,0155	0,0207	0,00032	

Tabla 4. Data nuclear para partículas emitidas (MeV) del I^{131} más significativas [HPS, 2013].

RFM	Partículas	E_k (MeV)	n_k /des	$n_k E_k$ (MeV/des)	$\bar{E}_{particle} = \sum n_k E_k$ (MeV/des)
I^{131}	Radiación Beta	0,0694	0,021	0,00145	0,1818
		0,0966	0,073	0,007	
		0,1916	0,899	0,1722	
		0,283	0,0048	0,00135	
	Electrones de Conversión	0,0456	0,0354	0,0016	0,0083
		0,359	0,0025	0,00089	
		0,3299	0,0155	0,0051	
		0,2497	0,003	0,00075	
	Electrones Auger	0,0034	0,051	0,00017	0,000147
		0,0246	0,006	0,000147	

Valores de masa del feto, así como del resto de órganos de la biocinética, fueron obtenidos de pag 41 , ORNL/TM-12907, [M.G.Stabin ,E:E: Watson 1995]

Tabla 5. Valores de masas (g) de la tiroides y feto de una mujer embarazada, en la representación Cristy –Eckerman [M.G.Stabin ,E:E: Watson 1995]

Fantoma	Mujer Adulta (no gestante)	3 meses Mujer gestante	6 meses Mujer gestante	9 meses Mujer gestante
	Masas (g) de órganos			
Feto	-	458	1.640	2.960
Tiroides	17	17	17	17

Utilizando el esquema MIRD y la representación de Cristy-Eckerman para fetos de una madre gestante de 3, 6, y 9 meses, el estudio consiste en demostrar si las contribuciones dosimétricas de órganos que son parte de la biocinética del Tc^{99m} (pertecnetato), y del I^{131}, son significativas en el estimado de la dosis absorbida durante estudios tiroideos en la madre gestante .

3.- RESULTADOS

Tabla 6. Dosis de radiación en feto de 03 meses, representación Cristy-Eckerman, Formalismo MIRD (mGy / MBq)

RFM	Emisiones	$\frac{D}{A_o}(feto \leftarrow feto)$	$\frac{D}{A_o}(feto \leftarrow i)^*$	Sub-total	Total (mGy/MBq)
Tc^{99m} (pertecnetato)	Fotones gamma	0.0062(29.10%)	0.0082 (38.50%)	0.0150 (70.42%)	0.0213
	(p) Radiación característica	0.0006(2.82%)			
	Electrón Conversión.	0.0061 (28.60%)	-	0.0063 (29.58%)	
	Electrón Auger.	0.00023 (1.07%)			
I^{131} (Yoduro)	Fotones gamma	0.0045 (7.34%)	0.0371 (60.52%)	0.0417 (68.03%)	0.0613
	(p) Radiación característica	0.00007(0.114%)			
	Emisores Beta	0.0187 (30.51%)	-	0.0196 (31.97%)	
	Electrón Conversión	0.0009(1.47%)			
	Electrón Auger	0.00002(0.033%)			

. (*) i = todas las fuentes excepto el feto.

Tabla 7.- Dosis de radiación en feto de 06 meses, representación Cristy- Eckerman , formalismo MIRD (mGy / MBq)

RFM	Emisiones	$\frac{D}{A_o}(feto \leftarrow feto)$	$\frac{D}{A_o}(feto \leftarrow i)^*$	Sub-total	Total (mGy/MBq)
Tc^{99m} (pertecnetato)	Fotones gamma	0. 0028(20.58%)	0.0088 (64.71%)	0.0118 (86.76 %)	0.0136
	(p) Radiación característica	0.00016(1.18%)			
	Electrón Conversión.	0.0017 (12.5%)	-	0.00176 (12.94%)	
	Electrón Auger.	0.000064(0.471%)			

I^{131} (Yoduro)	Fotones gamma	0.0507 (22.34%)	0.0282 (12.43%)	0.0796 (35.08%)	0.2269
	(p) Radiación característica	0. 0007(0.31%)			
	Emisores Beta	0.1408(62.05%)	-	0.1473 (64.92 %)	
	Electrón Conversión	0.0064(2.82%)			
	Electrón Auger	0. 0001(0.044%)			

(*) i = todas las fuentes excepto el feto.

Tabla 8.- Dosis de radiación en feto de 09 meses, representación Cristy- Eckerman , formalismo MIRD (mGy / MBq)

RFM	**Emisiones**	$\frac{D}{A_o}(feto \leftarrow feto)$	$\frac{D}{A_o}(feto \leftarrow i)^*$	**Sub-total**	**Total (mGy/MBq)**
Tc^{99m} (pertecnetato)	Fotones gamma	0. 00189(19.68%)	0.0067 (69.79%)	0.0086 (89.58 %)	0.0096
	(p) Radiación característica	0.00004(0.42%)			
	Electrón Conversión.	0.00093 (9.79%)	-	0.00096 (10.00%)	
	Electrón Auger.	0.00004(0.36%)			
I^{131} (Yoduro)	Fotones gamma	0.072 (25.99%)	0.0304 (10.97%)	0.103 (37.18%)	0.277
	(p) Radiación característica	0. 0009(0.325%)			
	Emisores Beta	0.1663(60.04%)	-	0.174 (62.82%)	
	Electrón Conversión	0.0076(2.74%)			
	Electrón Auger	0. 00013(0.05%)			

*Excepto la vejiga.

Tabla 9.- Principales contribuciones dosimétricas debido a los órganos de la biocinética, representación Cristy- Eckerman, formalismo MIRD (mGy / MBq)

RFM	Tc^{99m} (pertecnetato)			I^{131} (Yoduro)		
Tiempo	**3 meses**	**6 meses**	**9 meses**	**3 meses**	**6 meses**	**9 meses**
Dosis						
$\frac{D}{A_o}(feto \leftarrow vej.)$	3.206E-03 (15%)	1.284E-03 (9.4%)	1.211E-03 (12.60%)	2.068E-02 (34.26%)	7.841E-03 (3.46%)	2.068E-02 (7.6%)
$\frac{D}{A_o}(riñ \leftarrow RB)$	2.227E-03 (10.47%)	1.902E-03 (13.97%)	1.518E-03 (17.45%)	2.501E-03 (4.08%)	8.527E-03 (3.75 %)	
$\frac{D}{A_o}(feto \leftarrow ULI)$	1.515E-03 (6.24%)	1.330E-03 (9.78%)	7.686E-04 (8.0%)			
$\frac{D}{A_o}(feto \leftarrow placent)$		3.320E-03 (24.26%)	2.536E-03 (26%)			
$\frac{D}{A_o}(feto \leftarrow stom.)$				1.347E-03 (2.20%)		2.171E-03 (0.79%)
$\frac{D}{A_o}(feto \leftarrow id.)$				1.099E-02 (17.94%)	7.995E-03 (3.52%)	3.332E-03 (1.19%)

4.- DISCUSIÓN

De las tablas N° 6, 7, 8 y 9 observamos:

La dosis total absorbida por el feto de una mujer gestante debido a las emisiones de Tc^{99m} / I^{131}; están dadas por 0,0213mGy.MBq^{-1} / 0.0613 mGy.MBq^{-1} (fetos de 03 meses); 0,0136mGy.MBq^{-1} / 0.2269 mGy.MBq^{-1} (fetos de 06 meses) y 0,0096mGy.MBq^{-1} / 0.277 mGy.MBq^{-1}(fetos de 09 meses). Se observa que la dosis debido al Tc^{99m} es menor a la obtenida por el I^{131} representando el 34.7% , 6% y 3.5% de la dosis generado por el yoduro.

Corresponde el 61.5% /39.48%; 35.29% /87.57% y 30.21% /89.03% al valor de la auto dosis del feto de la mujer gestante de 03, 06 y 09 meses respectivamente. El depósito local de su energía debido a las emisiones beta y gamma del I^{131} es mayor al reportado por las emisiones gamma y electrones de conversión del Tc^{99m} para los fetos de 6 y 9 meses.

La dosis incorporada al feto debido a los órganos de los tejidos maternos, que hacen parte de la biocinética, se deben básicamente a la emisión de sus fotones gamma y corresponden al 38.50% /60.52% en fetos de 3 meses ,64.71% /12.43% en fetos de 6 meses, y 69.79% /10.97% en fetos de 9 meses para los radiofármacos Tc^{99m} (pertecnetato) /I^{131} (yoduro),

Los órganos de la biocinética que contribuyen a la dosis del feto se deben fundamentalmente a la vejiga, seguido del resto, e intestino delgado (fetos de 3 meses); del resto , seguido del intestino delgado y vejiga (fetos de 6 meses); de la vejiga, seguido del intestino delgado y estomago (fetos de 9 meses) cuando se usa el I^{131}; mientras que para el Tc^{99m} contribuyen la vejiga y del resto (fetos de 3 meses);de la placenta, seguido del resto y vejiga (fetos de 6 y 9 meses). Los porcentajes de cada uno de ellos se registran en tabla 9.

Las contribuciones dosimétricas de dichos órganos se deben mayormente a los fotones gamma emitidos por los radiofármacos que a sus rayos x- característicos.

Los resultados de dosis absorbida obtenidos en el feto de una mujer gestante, son consistentes con los publicados en Tables of Radiation Absorbed Dose to The Embryo/Fetus from Radiopharmaceuticals [HPS, 1997].

Dependiendo del tipo de radiofármaco usado y su biocinética, corresponderá la significancia de sus contribuciones en el estimado de dosis absorbidas por los riñones [Vásquez M. et al, 2015].

5.- CONCLUSIONES

Utilizando la metodología MIRD y la representación Cristy-Eckerman para el feto de una mujer gestante, se demuestra que, durante estudios tiroideos de una mujer gestante, las contribuciones dosimétricas de órganos, que hacen parte de la biocinética del Tc^{99m} (pertecnetato) y I^{131} (yoduro), son muy significativas en el estimado de la dosis absorbida por el paciente.

REFERENCIAS

Asociación Argentina de Biología y Medicina Nuclear (2013). Dosis de radiación recibida por los pacientes tras la administración de radiofármacos. <Aabymn.org.ar/archivos/dosisradiacion.pdf >

M.G.Stabin, E:E: Watson (1995). Physical models and dose factors for use in internal dose assessment, Oak Ridge, TN: ORNL/TM-12907

Health Physics Society (1999).Tables of Radiation Absorbed Dose to the Embryo/fetus fromRadiopharmaceuticals,<www.orau.org/ptp/PTP%20Library/library/ptp/.../mso212.PDF>

Health Physics Society (2013). Kinetic Models Used as the Basic for the Dose Estimates, < http://hps.org/publicinformation/radardecaydata.cfm. >

Quimby, E., Feitelberg, S., Gross, W. (1970). Radiactive Nuclides in Medicine and Biology.Third edition. Lea & F. Philadelphia: 2332-236

Vásquez, M, Díaz, E., Castillo, C. *et.al*.,(2015)"Evaluacion de la dosis absorbida durante estudios de la función renal debido al I-123 / I-131 (Hippuran) and In-111 (DPTA)", Braz. J.Rad. Sci. 3(2).

A 222 Energy Bins Response Matrix for a ^{6}LiI Scintillator BSS system

Marco A. S. Lacerda[1], Hector Rene Vega-Carrillo[2], Roberto Méndez-Villafañe[3] Alfredo Lorente-Fillol[4], Sviatoslav Ibañez-Fernandez[4], Eduardo Gallego-Diaz[4]

[1]Laboratório de Calibração de Dosímetros, Centro de Desenvolvimento da Tecnologia Nuclear, CDTN/CNEN, Av. Presidente Antonio Carlos, 6627, 31270-901, Belo Horizonte, Brazil, masl@cdtn.br

[2]Unidad Academica de Estudios Nucleares, Universidad Autónoma de Zacatecas, UAZ, Apdo. Postal 336, 98000, Zacatecas, Zac, Mexico

[3]Laboratorio de Patrones Neutrónicos, Centro de Investigaciones Energéticas, Medioambientales y Tecnológicas, CIEMAT, Av. Complutense, 22, 28040, Madrid, España

[4]Departamento de Ingenieria Nuclear
Universidad Politécnica de Madrid, UPM, 28006, Madrid, España,

Abstract

A new response matrix was calculated for a Bonner Sphere Spectrometer (BSS) with a ^{6}LiI(Eu) scintillator. We utilized the Monte Carlo N-Particle radiation transport code MCNPX, version 2.7.0, with ENDF/B-VII.0 nuclear data library to calculate the responses for 6 spheres and the bare detector, for energies varying from 9.441E(-10) MeV to 105.9 MeV, with 20 equal-log(E)-width bins per energy decade, totalizing 222 energy groups. A BSS, like the modeled in this work, was utilized to measure the neutron spectrum generated by the ^{241}AmBe source of the Universidad Politécnica de Madrid (UPM). From the count rates obtained with this BSS system we unfolded neutron spectrum utilizing the BUNKIUT code for 31 energy bins (UTA4 response matrix) and the MAXED code with the new calculated response functions. We compared spectra obtained with these BSS system / unfold codes with that obtained from measurements performed with a BSS system constituted of 12 spheres with a spherical ^{3}He SP9 counter (Centronic Ltd., UK) and MAXED code with the system-specific response functions (BSS-CIEMAT). A relatively good agreement was observed between our response matrix and that calculated by other authors. In general,

we observed an improvement in the agreement as the energy increases. However, higher discrepancies were observed for energies close to 1E(-8) MeV and, mainly, for energies above 20 MeV. These discrepancies were mainly attributed to the differences in cross-section libraries employed. The ambient dose equivalent (H*(10)) calculated with the ^{6}LiI-MAXED showed a good agreement with values measured with the neutron area monitor Berthold LB 6411 and within 12% the value obtained with another BSS system (BSS-CIEMAT). The response matrix calculated in this work can be utilized together with the MAXED code to generate neutron spectra with a good energy resolution up to 20 MeV. Some additional tests are being done to validate this response matrix and improve the results for energies higher than 20 MeV.

Keywords: Monte Carlo, Neutron Spectrometry, Bonner sphere neutron spectrometer.

1.- INTRODUCTION

Neutron spectrometry is important for complete characterization of the radiation field in workplaces. From the neutron fluence spectrum, it is possible to determine the radiation protection quantities (absorbed dose in the body, D_T, and effective dose, E) or operational quantities (dose equivalent personal Hp(d) and ambient dose equivalent H*(10)). Bonner multisphere spectrometry systems, more commonly known as Bonner Spectrometers Systems (BSS), are normally used for neutron spectrometry studies. BSS have the advantage of an almost isotropic response, covering a wide energy range from thermal to GeV [Bramblett *et al.*, 1960; Awschalow and Sanna 1985; Thomas and Alevra 2002; McDonald *et al.*, 2002].

BSS consist of a thermal neutron detector surrounded by a set of moderating polyethylene spheres of varying thickness. There is a response function for each detector/moderator, defined as the reading per unit fluence, as function of neutron energy. The response function is normally calculated using Monte Carlo (MC) codes and validated with measurements performed in standardized monoenergetic neutron fields [McDonald *et al.,* 2002; Mazrou *et al.*, 2010].

From the response functions, a response matrix (R) with "m × n" values are created, where "m" represents the matrix rows or the number of detector/moderating spheres and "n" stands for the total number of energy bins considered. The Response matrix (R) and BSS readings (M), assumed contained in a vector of "n" elements, are utilized to obtain the spectral information, Φ, also assumed contained in a vector with "n" elements. Then, a set of "m" linear equations can be written as showed in Equation 1.

$$M = R \cdot \Phi \qquad (1)$$

Neutron spectrum is derived by applying an inverse process, called unfolding procedure, that is a typical few-channel unfolding, since the number of individual measurements, "m", is significantly smaller than the number of energy bins, "n". There are some unfolding procedures utilized to provide a mathematical solution with an acceptable physical meaning for this under-determined problem. Linear and non-linear least-squares adjustments, the Bayesian theory, the principle of maximum entropy, Monte Carlo and approaches based on Artificial intelligence technology are the methods used for unfolding [Matzke 2002]. Many computerized BSS unfolding codes have been developed using the methods previously described, such as BON94, BUNKI / BUNKIUT, MAXED, FRUIT, BUMS, NSDUAZ and NSDann [Lowry *et al.*, 1984; Sweezy *et. al.*, 2002; Reginatto *et al.,* 2002; Bedogni *et al.,* 2007; Sannikov 1994; Vega-Carrillo *et al.,* 2012; Martinez-Blanco *et al.*, 2009].

The accuracy of the spectral neutron fluence derived by any unfolding procedure using experimental readings of the BSS is limited by the accuracy of the appropriate response matrix. There are some published response functions available for BSS with ^{6}LiI detectors [Sanna 1973; Hertel and Davidson 1985; Mares and Schraube 1994; Vega-Carrillo *et al.,* 2008; Mazrou *et al.,* 2010], ^{3}He proportional counters [Mares *et al.,* 1991; Aroua *et al.,* 1992; Wiegel and Alevra 2002] and passive detectors [Bedogni *et al.*, 2008; Garny *et al.*, 2009; Vega-Carrillo *et al.*, 1999].

In this paper we utilized the Monte Carlo N-Particle radiation transport code MCNPX [Pelowitz 2011] to calculate the response functions of a Bonner Sphere Spectrometer (BSS) with a ^{6}LiI(Eu) scintillator. Then, a BSS, like the modeled in this work, was utilized to measure the total neutron spectrum generated by the ^{241}AmBe source of the Universidad Politécnica de Madrid (UPM). This spectrum was compared with that obtained with a BSS system with a ^{3}He proportional counter.

2.- MATERIALS AND METHODS

We utilized the Monte Carlo N-Particle radiation transport code MCNPX, version 2.7.0, with ENDF/B-VII.0 nuclear data library, to calculate the response functions of a Bonner Sphere Spectrometer (BSS) with a ^{6}LiI(Eu) scintillator. We designed a realistic model of the cylindrical detector (0.4 cm x 0.4 ∅ cm) with its metallic cask, the light pipes and the polyethylene spheres. MC calculations were performed for the following sphere diameters, in inches: BALL 2 (2"), BALL 3 (3"), BALL 5 (5"), BALL 8 (8"), BALL 10 (10") and BALL 12 (12"). We also performed simulations with the bare detector, without a polyethylene sphere, BALL 0. Responses were calculated for all spheres and the bare detector for energies varying from 9.441E(-10) MeV to 105.9 MeV, with 20 equal-log(E)-width bins per energy decade, totalizing 222 energy groups. The number total of input files were 7 x 222 = 1554. Two Python programs were developed to aid rapid creation of input files for each sphere / energy bin and rapid extraction of the responses from output files.

Atomic composition and physical data were taken from Seltzer and Berger [1982]. We used S(α,β) cross section tables for polyethylene (density = 0.95 g.cm^{-3}) to take into account the chemical binding and crystalline effects on thermal neutron scattering at room temperatures [Pelowitz 2011]. For the scintillator crystal we adopted a density of 3.494 g.cm^{-3} and the following mass fractions: 4.36E(-2), 1.8E(-1) and 9.546E(-1) for ^{6}Li, ^{7}Li and ^{127}I, respectively.

To ensure a uniform irradiation of the spheres, we assumed monoenergetic neutron sources like disks with the same diameters as the spheres. These disks were centered on and perpendicular to the axis of the detector. The environment between the source and the BSS system was treated as void. The response was defined as the number of ^{6}Li(n, t)^{4}He reactions occurring within the scintillator, per each neutron incident neutron fluence

normalized to one starting particle. We utilized the Equation 2, in MCNPX, to obtain the response, R.

$$R = \Phi \cdot a_S \cdot n_{6Li} \cdot V_{\text{det}} \cdot \sigma(n,t) \qquad (2)$$

Where,

Φ : particle fluence, in cm^{-2}, given by the tally 4, in MCNPX output;

a_S : area of the neutron source, in cm^2;

n_{6Li} : number density, in (1E24 . cm^{-3});

V_{det} : sensitive detector volume, in cm^3;

$\sigma(n,t)$: ^{6}Li(n, t)^{4}He cross section, in barn. Reaction number MT=105 in MCNPX input.

The MCNPX was implemented to run under UNIX operating system on the EULER supercomputer, a high performance cluster (HPC) of CIEMAT, composed of 256 blades, 2x Intel Xeon 5450 Quad Core 3.0 GHz processors (2048 cores total). Between 8 and 16 processors were used to parallel processing/simulation of the inputs. The number of histories necessary to obtain uncertainties less than 3%, varied for each sphere / energy bin, from 1E6 to 3E8. The only variance reduction technique we utilized consisted of subdividing the spheres in a series of concentric shells, weighting the cells with different neutron importance. The closer the neutrons approach the counter volume, the higher is the importance.

A BSS system manufactured by the Ludlum Measurements, like the modeled in this work, was utilized to measure the neutron spectrum generated by the ^{241}AmBe source of the Universidad Politécnica de Madrid (UPM). This source has an activity of 111 ± 10% GBq and a nominal strength of $6.64 \cdot 10^6\ s^{-1}$ on February 5, 1969.

Measurements were performed at 115 cm from the source, on the calibration bench, as showed in the Figure 1. From the count rates obtained with this BSS system (BSS-^{6}LiI), we unfolded the total neutron spectrum (Φ_{tot}). Data were unfolded utilizing: (a) the BUNKIUT code [Lowry *et al.*, 1984] with the SPUNIT algorithm and UTA4 response matrix (31 energy bins) and; (b) MAXED computer code, from the UMG 3.3 package [Reginatto *et al.* 2004], with the new calculated response functions. We also compared spectra obtained with these BSS system / unfold codes with those obtained from measurements performed with a BSS system constituted of 12 spheres with a spherical ^{3}He SP9 counter (Centronic Ltd., UK). For this BSS system (BSS-^{3}He), MAXED computer code from the UMG 3.3 package was also utilized with the system-specific response functions (CIEMAT-BSS), determined in the Physikalisch-Technische Bundesanstalt (PTB) (Braunschweig, Germany).

The initial guess spectrum utilized in all cases was that obtained with Monte Carlo calculations, from a previous model of the irradiation facility [Vega-Carrillo *et al.* 2012]. The neutron energy spectra were folded with fluence-to-ambient dose equivalent conversion coefficients, in pSv.cm^{2}, from the ICRP 74 [ICRP 1996].

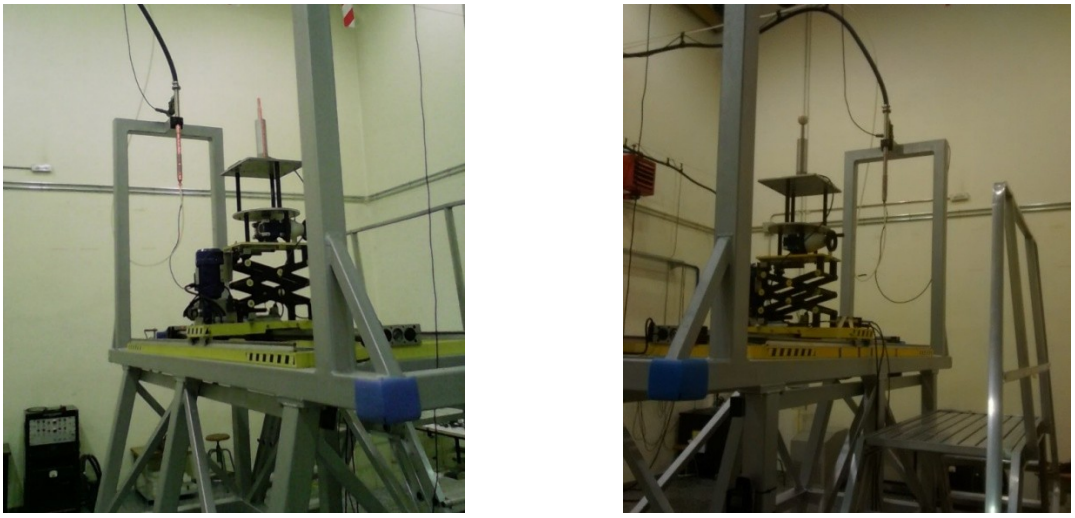

Figure 1. BSS-^{6}LiI on the calibration bench (bare detector and 2 inch sphere (BALL 2).

3.- RESULTS

Figure 2 present MCNPX calculated response matrix for all spheres. Figures 3 to 9 show a comparison of the response function for each sphere, calculated in this work, and data published by Vega-Carrillo *et al.*, [2008] and Mares and Schraube [1994a] for the same model of BSS system. Additional data provided by Mares and Schraube [1994b], with the inclusion of more energy bins, are also showed in these graphs.

Figure 10 shows the total neutron lethargy spectrum unfolded from the count rate data obtained with the BSS-^{6}LiI system, utilizing the BUNKIUT code for 31 energy bins. Figure 11 shows the total neutron lethargy spectrum unfolded from the same count rate data, utilizing the MAXED computer code from the UMG 3.3 package, with the new calculated response functions, for 222 energy bins.

Figure 12 shows the Total Neutron Lethargy spectrum unfolded from the count rates obtained with the BSS-^{3}He system utilizing the MAXED computer code from the UMG 3.3 package, with the specific response functions (CIEMAT-BSS), for 222 energy bins.

Table 1 shows a comparison of the quantities: total fluence and fluence components (thermal, epithermal and fast), ambient dose equivalent (H*(10)) and average energy, for the measurements performed with the BSS-^{6}LiI and BSS-^{3}He, and unfolded utilizing the BUNKIUT code for 31 energy bins and MAXED for 222 energy bins. For the BUNKIUT code is also showed the error in fitting process. This software does not provide the uncertainties for the quantities mentioned. We have also to emphasize that the H*(10) showed in the table for the BUNKIUT code is not that provided by the software. We calculated H*(10) folding the neutron energy spectrum (provided by the software) with the fluence-to-ambient dose equivalent conversion coefficients, in pSv.cm^{2}, from the ICRP 74 [ICRP 1996].

For the MAXED code, the uncertainties in the total fluence and H*(10) are those provided by the software IQU_FC33, from the UMG 3.3 package. IQU_FC33 considers variations in the measured data and in the default spectrum and uses standard methods to do sensitivity analysis and uncertainty propagation [Reginatto *et al.* 2004]. Energy ranges considered for the fluence components are: below 0.5 eV for thermal neutrons, between 0.5 eV and 0.1 MeV for epithermal, and above 0.1 MeV for fast neutrons.

Figure 13 shows a comparison of the Total Neutron Lethargy spectra measured with the BSS-^{6}LiI and BSS-^{3}He and unfolded utilizing the BUNKIUT code for 31 energy bins and MAXED for 222 energy bins.

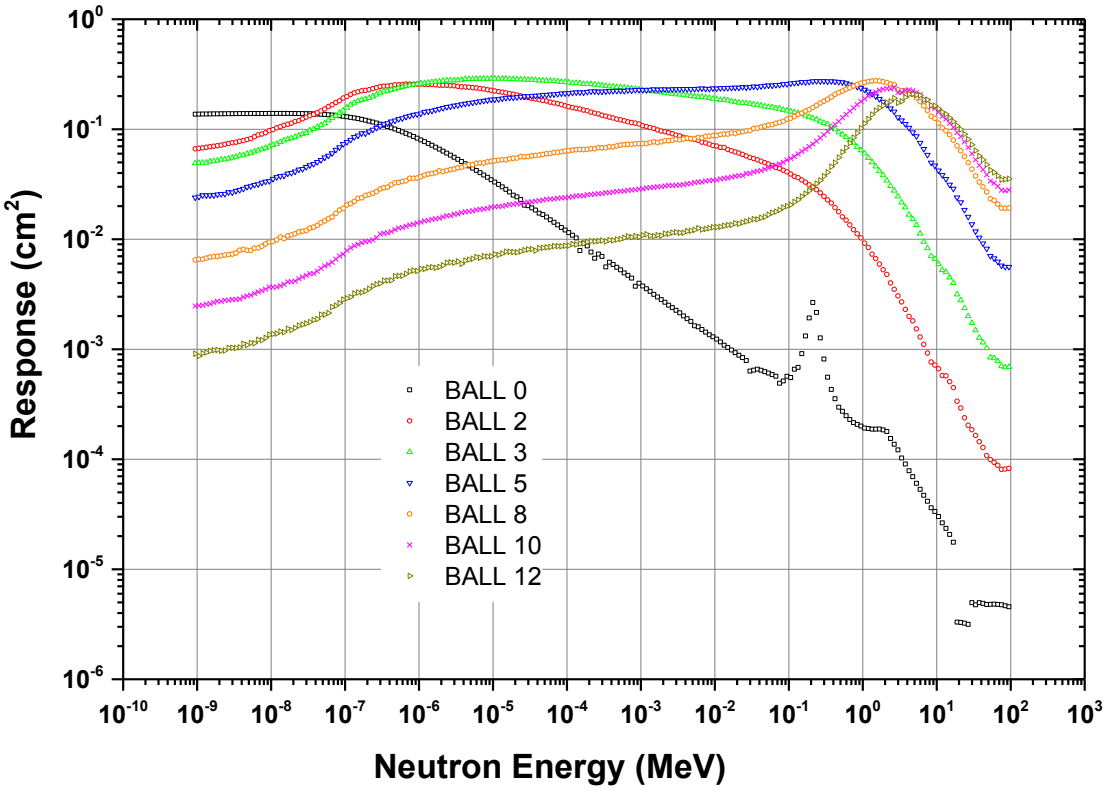

Figure 2. MCNPX calculated response matrix for the BSS-^{6}LiI.

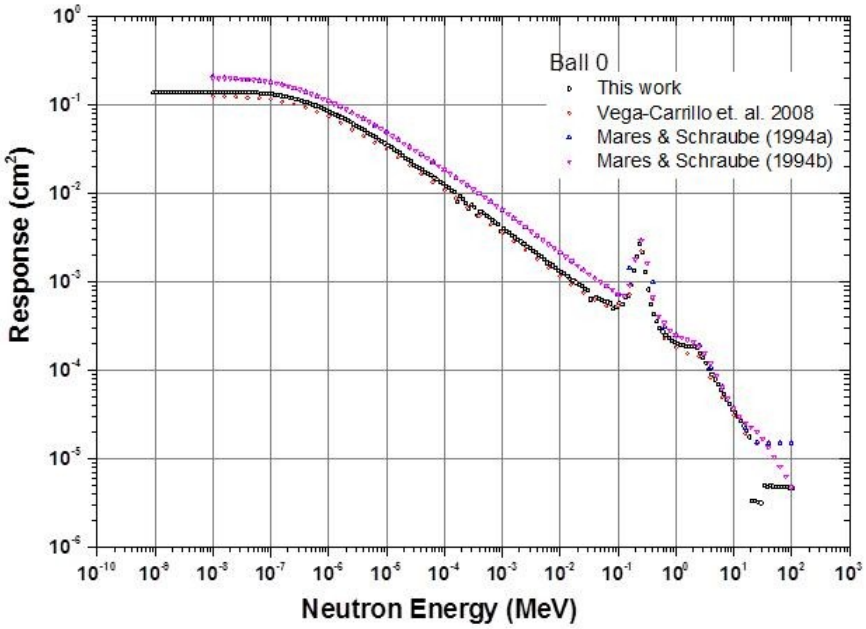

Figure 3. Comparison of the response function for the bare detector (BALL 0), calculated in this work, and other published data.

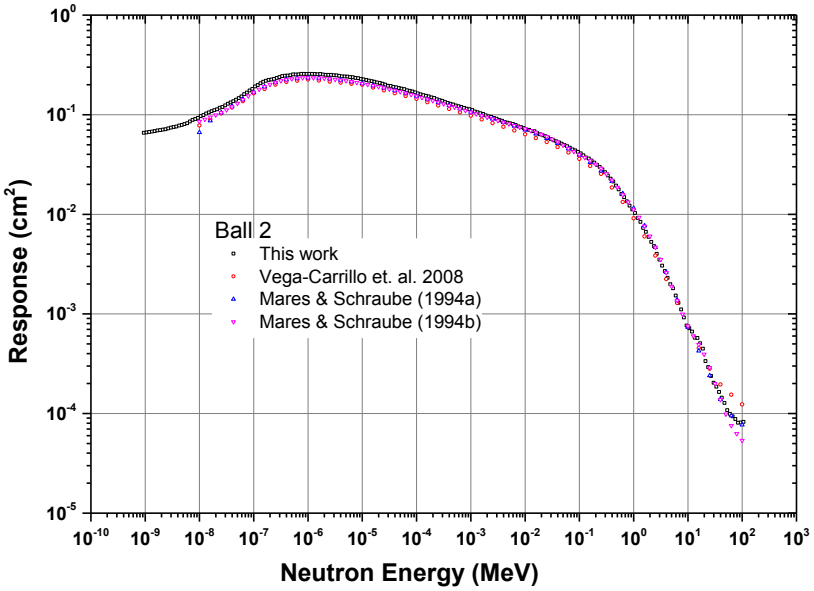

Figure 4. Comparison of the response function for detector with the 2 inch sphere (BALL 2), calculated in this work, and other published data.

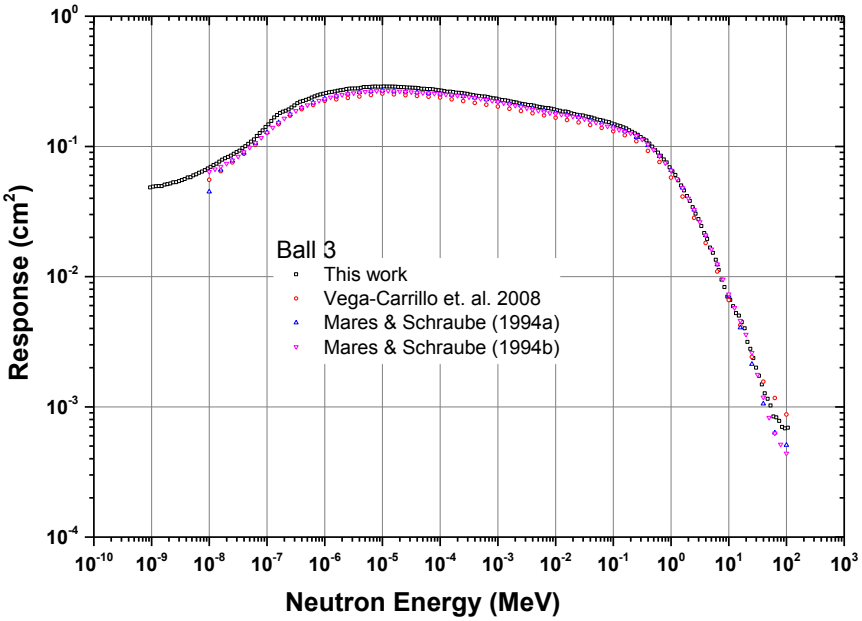

Figure 5. Comparison of the response function for detector with the 3 inch sphere (BALL 3), calculated in this work, and other published data.

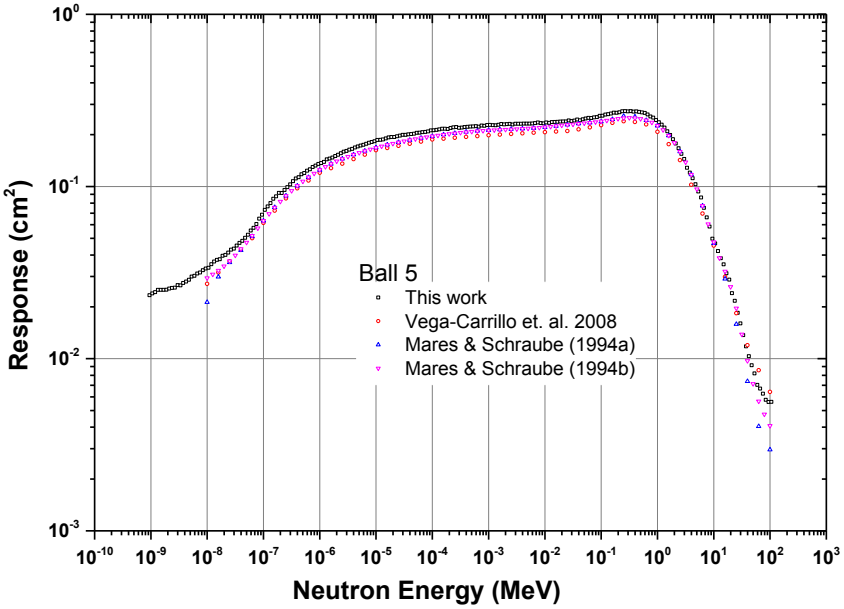

Figure 6. Comparison of the response function for detector with the 5 inch sphere (BALL 5), calculated in this work, and other published data.

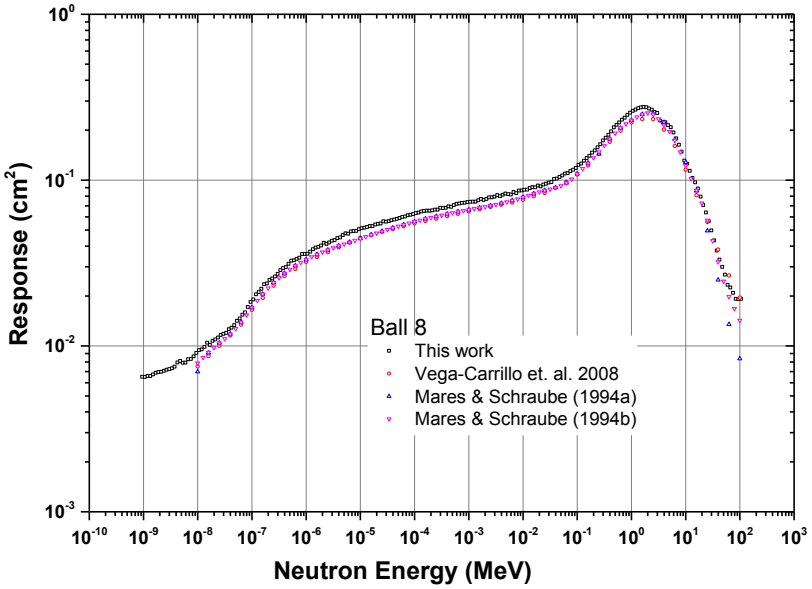

Figure 7. Comparison of the response function for detector with the 8 inch sphere (BALL 8), calculated in this work, and other published data.

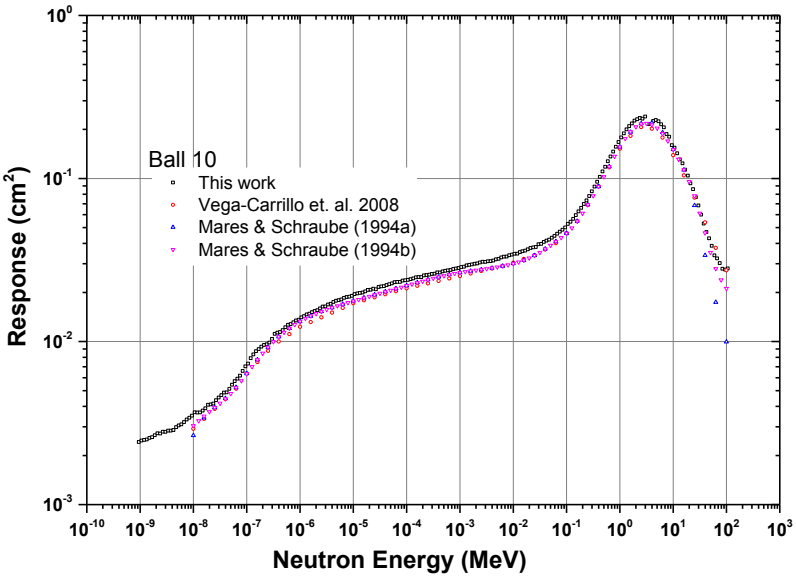

Figure 8. Comparison of the response function for detector with the 10 inch sphere (BALL 10), calculated in this work, and other published data.

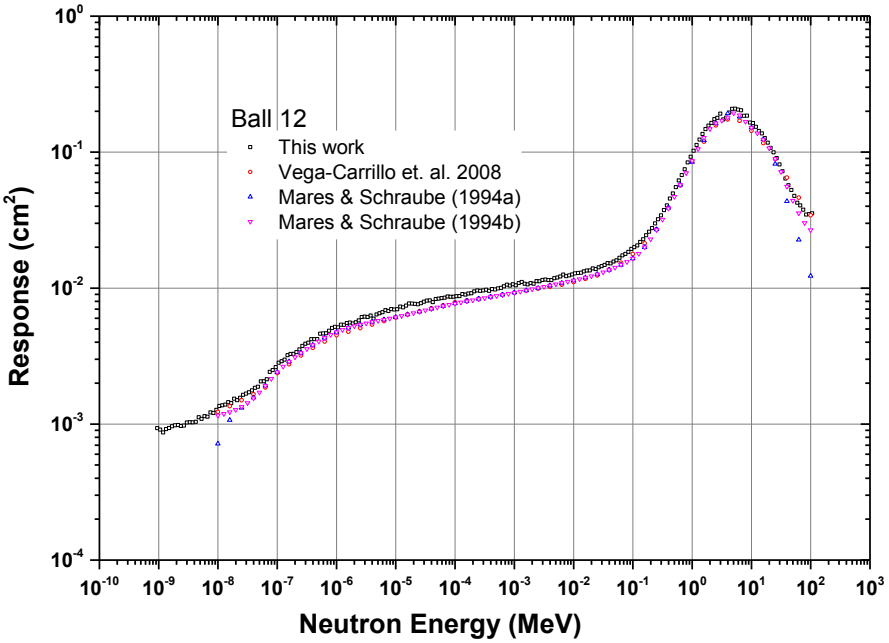

Figure 9. Comparison of the response function for detector with the 12 inch sphere (BALL 12), calculated in this work, and other published data.

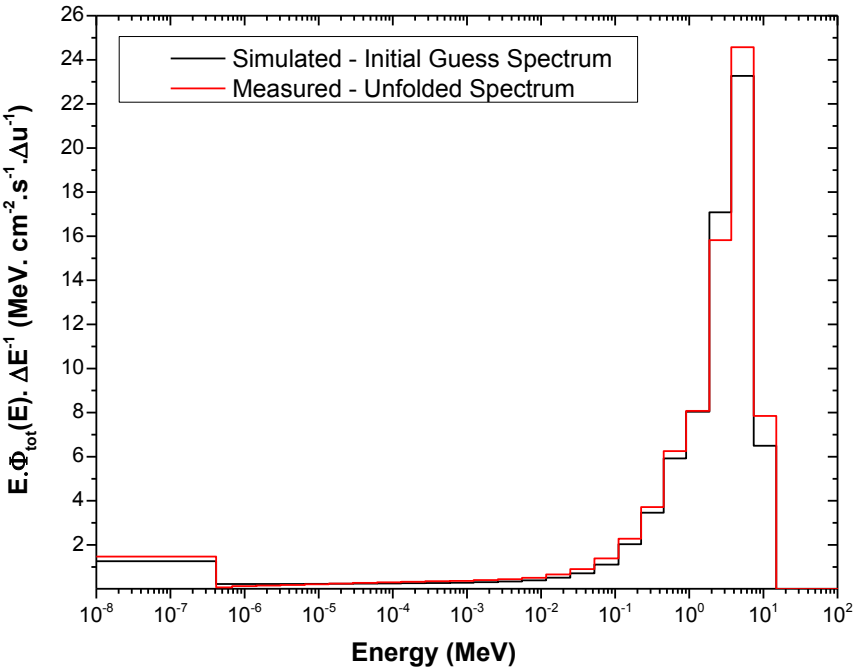

Figure 10. Total Neutron Lethargy Spectrum for the ^{241}AmBe source of the UPM, at 115 cm, measured with the BSS-^{6}LiI system and unfolded with the BUNKIUT code for 31 energy bins.

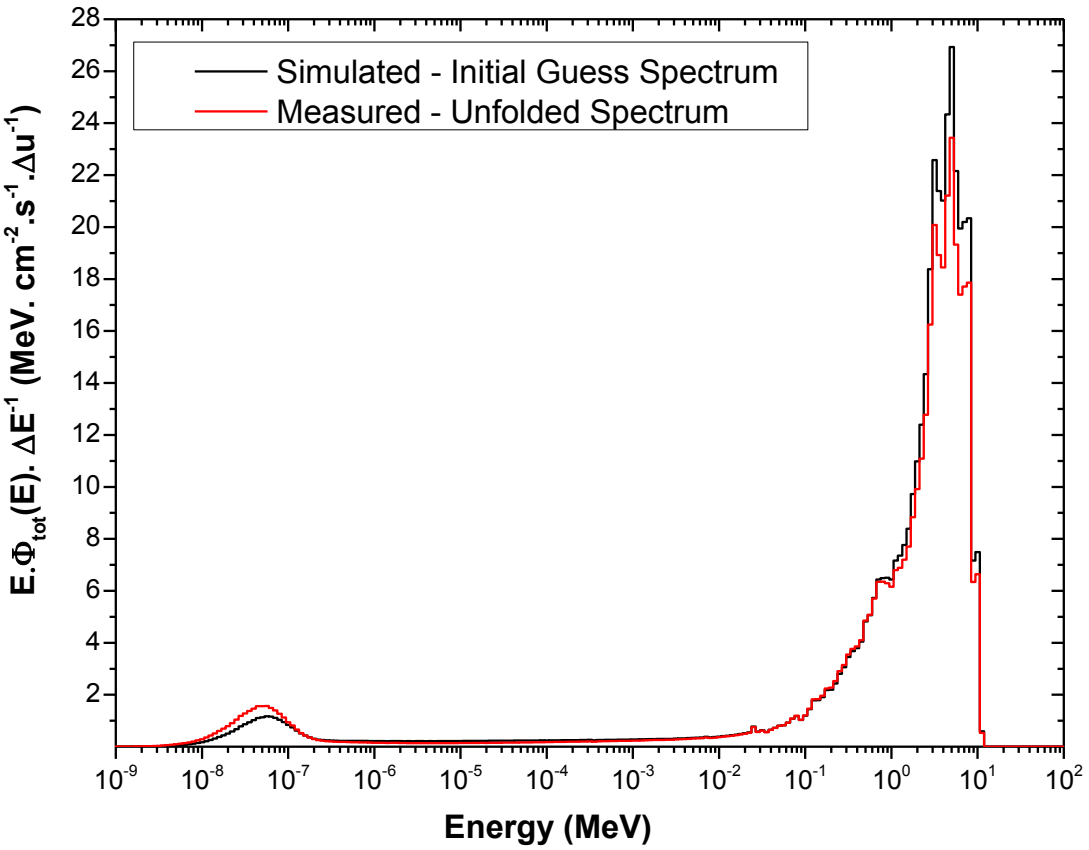

Figure 11. Total Neutron Lethargy Spectrum for the ^{241}AmBe source of the UPM, at 115 cm, measured with the BSS-^{6}LiI system and unfolded with the MAXED computer code from the UMG 3.3 package, with the new calculated response functions (for 222 energy bins).

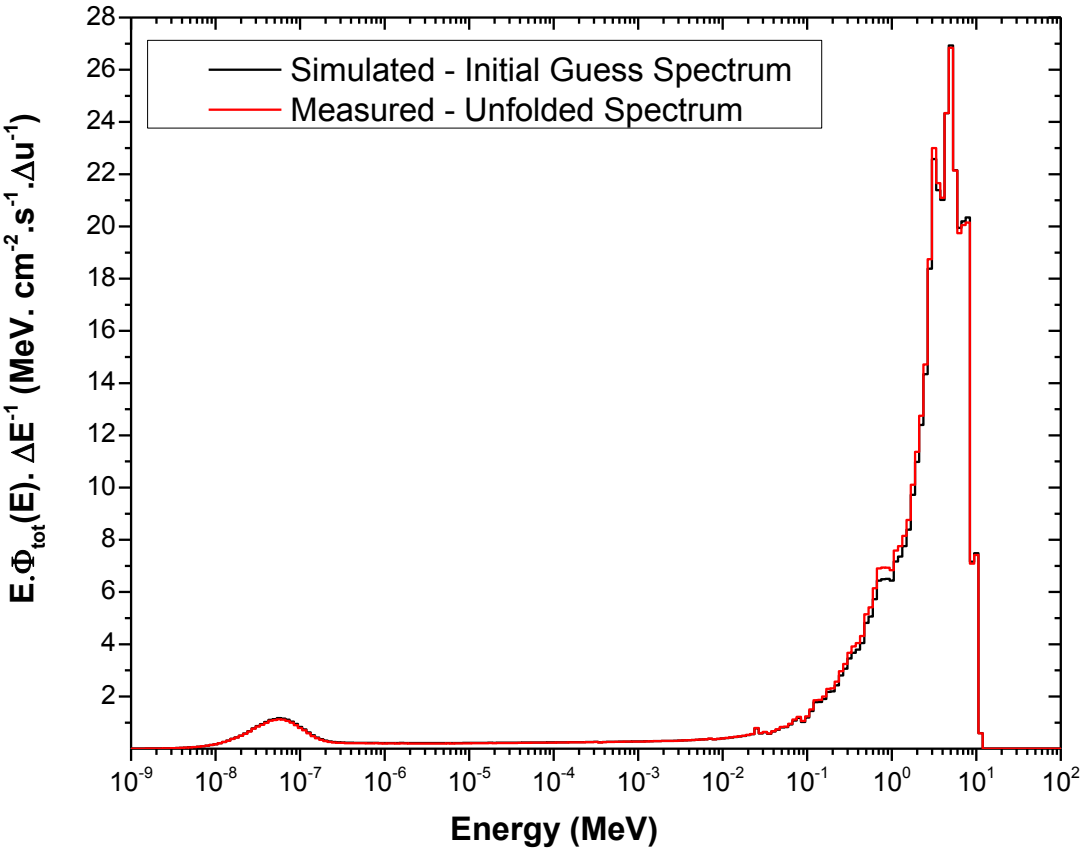

Figure 12. Neutron Lethargy Spectrum for the ^{241}AmBe source of the UPM, at 115 cm, measured with the BSS-^{3}He system and unfolded with the MAXED computer code from the UMG 3.3 package, with the specific response functions (CIEMAT-BSS) for 222 energy bins.

Table 1. Comparison of the quantities: total fluence and fluence components (thermal, epithermal and fast), ambient dose equivalent rate (H*(10)) and average energy for the measurements performed with the BSS-^{6}LiI and BSS-^{3}He and unfolded utilizing the BUNKIUT code for 31 energy bins and MAXED for 222 energy bins.

	BSS-^{6}LiI	BSS-^{6}LiI	BSS-^{3}He
	BUNKIUT	**MAXED**	**MAXED**
Total Fluence rate ($cm^{-2}.s^{-1}$)	53.7	47.1 ± 0.43%	51.4 ± 0.27%
$\Phi_{thermal}$ (%)	5.3	6.7	4.5
$\Phi_{epithermal}$ (%)	9.2	7.3	7.7
Φ_{fast} (%)	85.5	86.0	87.8
H*(10) (µSv/h)	65.9	57.4 ± 0.56%	64.2 ± 0.31%
Average Energy (MeV)	3.6	3.4	3.5
Error of the fit(%)	0.32	-	-

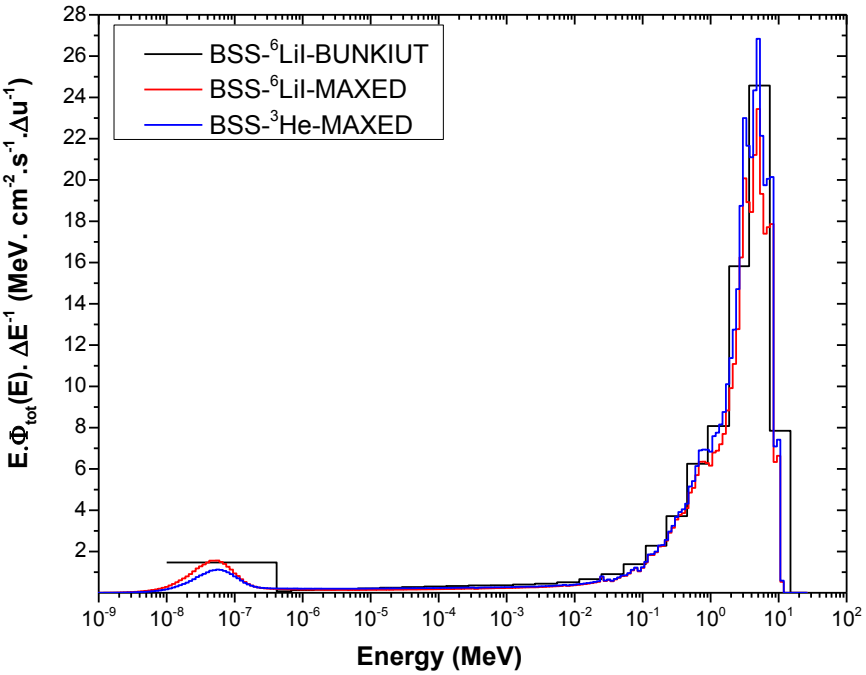

Figure 13. Comparison of the Total Neutron Lethargy spectrum measured with the BSS-^{6}LiI and BSS-^{3}He and unfolded utilizing the BUNKIUT code for 31 energy bins and UMG for 222 energy bins.

4.- DISCUSSION

Figure 2 shows the response functions for all spheres presented an agreement in shape with other available in literature [Mares and Schraube 1994a; Vega-Carrillo *et al.* 2008; Decker *et al.* 2015]. The bare detector (BALL 0) presented a shape close to the shape of the $^{6}Li(n,t)^{4}He$ cross section. For the BALL 8 to BALL 12 the responses increase slowly with the neutron energy reaching a maximum value close to 1.7 MeV, 2.4 MeV and 3 MeV, respectively, presenting an accentuated decreasing after that. For the BALL 5 the same behavior is noticed. However, the maximum occurs at about 270 keV. BALL 2 and BALL 3 present an increasing in the responses only up to 1.1E(-5) and 1.1E(-6) MeV, respectively. After that, the responses also decrease in a faster manner.

Figures 3 to 9 shows a comparison among between our data and other published elsewhere, for the same detector model. Only BALL 0 did not present a good agreement with Mares and Schraube [1994a,b] for thermal and epithermal energies. This can be attributed not only to the differences in cross-section libraries, but also, to the differences in irradiation setup. Mares and Schraube [1994a,b] calculated the responses for the bare detector, considering a lateral irradiation of the detector, different of the condition simulated in our work.

We can notice a relatively good agreement for BALLS 2 to 12 for energies below 20 MeV. For these spheres, our simulations generally overestimate the responses for energies below 20 MeV. We can also see that there is, in general, an improvement in the agreement as the energy increase. For the BALLS 2 to 12, a higher discrepancy starts to occur for energies close to 1E(-8) MeV. However, the authors mentioned, did not perform simulations for energies lower than 1E(-8) MeV. The disagreement can become worst in this energy range and below 1E(-8), if an extrapolation of responses behavior is done with the data published by these authors.

For energies above 20 MeV, our data present significant differences with data of Mares and Schraube [1994a,b] for all spheres. Indeed, for the BALL 0, an anomalous behavior is

noticed. We can observe a rapid decreasing followed by an almost constant response. These observations can also be attributed to the differences in cross-section libraries. As the ENDF/B-VII.0 nuclear data library does not have available data for energies higher than 20 MeV, MCNPX utilizes a constant cross section equal to the value at 20 MeV. This adopted value is supposed to be much higher than the real cross section values for energies between 20 MeV and 105.9 MeV. Another point to study is the influence of other nuclear reactions occurring on Lithium (^{6}Li and ^{7}Li) for energies higher than 4 MeV, what we did not take into account in our simulations.

Figure 10 and 11 shows the total neutron lethargy spectra unfolded from the count rate data obtained with a BSS-^{6}LiI system, like the modeled in this work. Both spectra exhibited an expected shape for an ^{241}AmBe source in a vault room with the characteristics of the UPM. Spectrum unfolded with the BUNKIUT code for 31 energy bins exhibited a shape very similar to the initial guess spectrum utilized in the unfolding process and is slightly offset up at all energy range. Already, the spectrum unfolded with the MAXED code and the new response matrix, even exhibiting a shape very similar to the simulated guess spectrum, is offset up in the thermal region and shifted down for energies higher than 2 MeV.

Figure 12 shows the spectrum unfolded from the count rates obtained with the BSS-^{3}He system utilizing the MAXED code and CIEMAT-BSS response matrix. In this case, the unfolded spectrum shape very well with the simulated guess spectrum. A comparison of the three spectra is presented in the Figure 13, showing a relatively good agreement at all energy ranges, taking into account the poor energy resolution of the spectrum unfolded with the original BUNKIUT code (with 31 energy bins).

Table 1 shows that spectrum unfolded with MAXED and the new response matrix (^{6}LiI-MAXED) presents a smaller value of total fluence, equivalent dose (H*(10)) and average energy. We can also observe a higher fraction of thermal neutrons ($\Phi_{thermal}$), respectively 26% and 49% higher than the same fraction observed for BSS-^{6}LiI-BUNKIUT and BSS-^{3}He-MAXED. The fraction of epithermal neutrons is very close to that observed for BSS-^{3}He (within about 5%). Spectrum unfolded with the BUNKIUT code presented a greater

value of H*(10), about 14% higher than the value calculated with the new response matrix and very close (< 3%) to that obtained from BSS-^{3}He. Value obtained with the BSS-^{3}He was very close to that obtained from MC calculations, 63.5 μSv/h. On the other hand, H*(10) obtained with ^{6}LiI-MAXED agreed better with measurements performed with a calibrated neutron area monitor BERTHOLD LB6411, 60.5 μSv/h.

5.- CONCLUSIONS

A new response matrix was calculated for a Bonner Sphere Spectrometer (BSS) with a ^{6}LiI(Eu) scintillator. Responses were calculated for 6 spheres and the bare detector, for energies varying from 9.441E(-10) MeV to 105.9 MeV, with 20 equal-log(E)-width bins per energy decade, totalizing 222 energy groups. These response functions were inserted in the response input file of the MAXED code and utilized to unfold the total neutron spectra generated by the ^{241}AmBe source of the Universidad Politécnica de Madrid (UPM).

A relatively good agreement was observed between our response matrix and that calculated by other authors. In general, we observed an improvement in the agreement as the energy increases. However, higher discrepancies were observed for energies close to 1E(-8) MeV and, mainly, for energies above 20 MeV. These discrepancies can be mainly attributed to the differences in cross-section libraries employed. However, we need to evaluate the influence of other nuclear reactions occurring on Lithium (^{6}Li and ^{7}Li) for energies higher than 4 MeV, what we did not take into account in our simulations.

Spectrum unfolded with MAXED and the new response matrix (^{6}LiI-MAXED) presented a smaller value of total fluence, equivalent dose (H*(10)) and average energy. However, the ambient dose equivalent (H*(10)) calculated with the ^{6}LiI-MAXED showed a good agreement with values measured with the neutron area monitor Berthold LB 6411 and within 12% the value obtained with another BSS system (^{3}He-BSS).

The response matrix calculated in this work can be utilized together with the MAXED code to generate neutron spectra with a good energy resolution up to 20 MeV. Some additional tests are being done to validate this response matrix and improve the results for energies higher than 20 MeV.

Acknowledgments

M.A.S. Lacerda is grateful to CNPq (Brazilian National Council for Scientific and Technological Development) for a postdoctoral fellowship (Proc. 233341/2014-5). M.A.S. Lacerda is also grateful to financial support provided by CNPq (MCTI/CNPq/Universal Proc. 449199/2014-2) and FAPEMIG (Research Support Foundation of Minas Gerais State, Brazil) (PPM-00208-15).

REFERENCES

Aroua A; Grecscu M; Lanfranchi M; Lerch P; Prête S; Valley JF. (1992). *Evaluation and test of the response matrix of a multisphere neutron spectrometer in a wide energy range. Part II: Simulation*. Nuclear Instruments and Methods **A321**, 305-311.

Awschalow M; Sanna RS. (1985). *Applications of Bonner detectors in neutron field dosimetry*. Radiation Protection Dosimetry **10**: 89-101.

Bedogni R; Esposito A; Gentile A; Angelone M; Gualdrini G. (2008). *Determination and validation of a response matrix for a passive Bonner Sphere Spectrometer based on gold foils*. Radiation Measurements **43**:1104-1107.

Bedogni R; Domingo C; Esposito A; Fernandez F. (2007). *FRUIT: an operational tool for multisphere neutron spectrometry in workplaces*. Nuclear Instruments and Methods in Physics Research A **580**: 1301-1309.

Bramblett RL; Ewing RI; Bonner TW. (1960). *A new type of neutron spectrometer*. Nuclear Instruments and Methods **9**: 1-12.

Decker AW; McHale SR; Shannon MP; Clinton JA; McClory JW. (2015). *Novel Bonner Sphere Spectrometer Response Functions Using MCNP6*. IEEE Transactions on Nuclear Science **62(4)**: 1-6.

Garny S; Mares V; Rühm W. (2009). *Response functions of a Bonner sphere spectrometer calculated with GEANT4*. Nucl. Instrum. Meth. Phys. Research A 604, p.612-617, 2009.

Hertel, N.E., Davidson, J.W. (1985). *The response of Bonner spheres to neutrons from termal energies to 17.3 MeV*. Nuclear Instruments and Methods in Physics Research A **238**: 509-516.

ICRP. (1996). International Commission on Radiological Protection. *Conversion coefficients for use in radiological protection against external radiation*. **ICRP Publication 74**, Ann. ICRP 26 (3-4).

Los Alamos National Laboratory. (2008). *MCNP-A General Monte Carlo N-Particle Transport Code, version 5*. X-5 Monte Carlo Team. **LA-UR-03-1987**.

Lowry KA; Johnson TL. (1984). *Modifications to recursion unfolding algorithms to and more appropriate neutron spectra*. Health Physics **47**: 587-593.

Mares V; Schraube G; Schraube H. (1991). *Calculated neutron response of a Bonner Sphere Spectrometer with ^{3}He counter*. Nuclear Instruments and Methods in Physics Research A **307**: 398-412.

Mares V; Schraube H. (1994a). *Evaluation of the Response Matrix of a Bonner Sphere Spectrometer with LiI detector from thermal energy to 100 MeV*. Nuclear Instruments and Methods in Physics Research A **337**: 461-473.

Mares V; Schraube H. (1994b). Personal communication.

Martinez-Blanco MR; Ortiz-Rodriguez JM; Vega-Carrillo HR. (2009). *NSDann, a LabVIEW tool for neutron spectrometry and dosimetry based on the RDANN methodology*. Proccedings of the Electronics, Robotics and Automotive Mechanics Conference, CERMA'09 131-136.

Matzke M. (2002). *Propagation of uncertainties in unfolding procedures*. Nuclear Instruments and Methods in Physics Research A **476**: 230-241.

Mazrou H; Idiri Z; Sidahmed T; Allab M. (2010). *MCNP5 evaluation of a response matrix of a Bonner Sphere Spectrometer with a high efficiency ^{6}LiI(Eu) detector from 0.01 eV to 20 MeV neutrons*. Journal of Radioanalytical and Nuclear Chemistry **284**: 253-263.

McDonald JC; Siebert BRL; Alberts WG. (2002). *Neutron spectrometry for radiation protection purposes*. Nuclear Instruments and Methods in Physics Research A **476**: 347-352.

Pelowitz DB. (2011). *MCNPX User's Manual, Version 2.7.0*. Los Alamos National Laboratory **Report LA-CP-11-00438**.

Reginatto M; Wiegel B; Zimbal A; Langner F. (2004). *The 'few-channel' unfolding programs in the UMG package: MXD_FC31 and IQU_FC31, and GRV_FC31, version 3.1*, Physikalisch-Technische Bundesanstalt (PTB).

Reginatto M; Goldhagen P; Neumann S. (2002). *Spectrum unfolding, sensitivity analysis and propagation of uncertainties with the maximum entropy deconvolution code MAXED*. Nuclear Instruments and Methods in Physics Research A **476**: 242-246.

Sanna RS. (1973). *Thirty-One Group Response Matrices for the Multisphere Neutron Spectrometer over the energy range thermal to 400 MeV*. USAEC, **Report HASL-267**.

Sannikov AV. (1994). *BON94 code for neutron spectra unfolding from Bonner spectrometer data*. CERN internal Report **CERN/TIS-RP/IR/94-16**.

Seltzer, SM; Berger MJ. (1982). *Evaluation of the collision stopping power of elements and compounds for electrons and positrons*. The International Journal of Applied Radiation and Isotopes 33: 1189-1218.

Thomas DJ; Alevra AV. (2002). *Bonner sphere spectrometers – a critical review*. Nuclear Instruments and Methods in Physics Research A **476**: 12-20.

Vega-Carrillo HR; Wehring BW; Veinot KG; Hertel NE. (1999). *Response matrix for a multisphere spectrometer using ^{6}LiF thermoluminescence dosemeter*. Radiation Protection Dosimetry **81**: 133-140.

Vega-Carrillo HR; Donaire I; Gallego E; Manzanares-Acuña E; Lorente A; Iñiguez MP; Martin-Martin A; Gutierrez-Villanueva JL. (2008). *Calculation of Response matrix of a BSS with ^{6}LiI scintillator*. Revista Mexicana de Física **54**: 57-62.

Vega-Carrillo HR; Gallego E; Lorente, A; Rubio IP; Méndez R. (2012). *Neutron features at the UPM neutronics hall*. Applied Radiation and Isotopes **70**: 1603-1607.

Wiegel B; Alevra AV. (2002). *NEMUS-The PTB Neutron Multisphere Spectrometer: Bonner spheres and more*. Nuclear Instruments and Methods in Physics Research A **476**: 36-41.

Medición de la Concentración de ^{222}Rn en Residencias y Lugares de Trabajo en la Ciudad de Riobamba

Coralía Cuadrado[1] & Javier Carrasco[*1]

[1] Facultad de Ciencias, Carrera de Biofísica, Escuela Superior Politécnica de Chimborazo, Riobamba, Ecuador, coralia_cuadrado@hotmail.com

[*1] Facultad de Ciencias, Carrera de Biofísica, Escuela Superior Politécnica de Chimborazo, Riobamba, Ecuador, wcarrasco@espoch.edu.ec

Abstract

El ^{222}Rn pertenece a la serie radiactiva natural del ^{238}U, decae emitiendo partículas alfa con un semiperiodo de desintegración de 3,82 días. Es un gas incoloro e inodoro resultando imperceptible para los seres humanos. Se ha demostrado que la exposición al radón en interiores puede producir cáncer de pulmón, incluso para los niveles de radón relativamente bajos que suelen existir en los edificios residenciales [Zeeb, Shannoun, & OMS, 2015]. Se realizaron mediciones de la concentración de radón en residencias, oficinas y laboratorios universitarios en la ciudad de Riobamba, caracterizando los lugares por los materiales de construcción, su antigüedad, tiempo de estancia entre otras variables. Se utilizó un detector electrónico marca Corentium, que da una lectura corta en 24 horas y extendida en 7 días. Utilizando el coeficiente de conversión a dosis de radón 0.017 mSv/y para 1 Bq/m^3, recomendado por el ICRP se estimaron las dosis anuales para cada lugar. Los datos obtenidos muestran que los rangos son aceptables y están dentro las recomendaciones de la OMS, encontrándose fuera de rango un laboratorio de docencia debido que cuenta con uranio natural para prácticas. Las mediciones son las primeras que se realizan en el país y pueden servir para fomentar investigaciones en este tipo a nivel local, nacional y regional.

Keywords: Radón; Dosis radiactiva ambiental; Radiación natural.

1.- INTRODUCCIÓN

El ^{222}Rn es un elemento radiactivo que decae emitiendo partículas alfa y posee una vida media de 3,8 días, su estado es gaseoso y es imperceptible a nuestros sentidos es decir es incoloro, inodoro e insípido. Este elemento se presenta de forma natural en nuestro entorno ya que se encuentra formando parte del suelo y de materiales de construcción, por lo cual puede ser inhalado por el ser humano causando graves daños en su organismo. Los estudios acerca de ^{222}Rn en viviendas comenzaron desde la investigación europea realizada sobre la calidad de aire en los interiores en el año de 1879, a partir de ese entonces se han generado varios estudios en Europa, Norteamérica y Asia. En 2005 la OMS (Organización Mundial de la Salud) crea un proyecto internacional del Radón, cuyo objetivo es reducir el impacto del ^{222}Rn en la salud y concienciar al público y autoridades sobre la prolongada exposición a este elemento.

Las altas concentraciones de este gas en lugares que poseen poca ventilación ha llegado a provocar una alta exposición a este elemento radiactivo, mientras mayor concentración y mayor tiempo de exposición exista mayores serán los daños en el organismo, siendo el segundo causante de cáncer al pulmón después del tabaco. Fumadores activos y pasivos expuestos a ^{222}Rn aumentan su probabilidad de cáncer al pulmón. Por la cual la ICRP 115 (Comisión Nacional de protección radiológica), establece como nivel de referencia para los hogares una concentración de 300 Bq/m^3 equivalente a una dosis anual efectiva de 17 mSv, mientras que la misma concentración de ^{222}Rn en edificios tendrá un equivalente a 8 mSv.

Las técnicas utilizadas para la medición del ^{222}Rn se basan en la interacción de radiación alfa, beta o gamma emitida por este radioisótopo o por sus radioisótopos hijos producidos en su proceso de decaimiento. Su medición se puede realizar por métodos como: centelleo líquido, adsorción en carbón activado [López, Canoba, & Nuclear, n.d.], detector de trazas para partículas alfa (ATD), cámaras de ionización electret (EICs), detectores electrets, monitores de radón, entre otros [World Health Organization, 2009].

El conocimiento actual de los riesgos de ^{222}Rn asociada a otros órganos además de los pulmones no justifica la selección de un coeficiente detrimento diferente del coeficiente de mortalidad por cáncer de pulmón ^{222}Rn inducida. Del ICRP Publicación 65 recomienda que las dosis de ^{222}Rn y su progenie se deben calcular utilizando una dosis convención de conversión basado en datos epidemiológicos. Ahora se llegó a la conclusión de que el ^{222}Rn y su progenie deben ser tratados de la misma forma que otros radionúclidos en el sistema de la ICRP de protección; es decir, dosis de ^{222}Rn y la progenie del ^{222}Rn deben calcularse utilizando biocinéticos la ICRP y modelos dosimétricos. La ICRP proporcionará coeficientes de dosis por unidad de exposición al ^{222}Rn y la progenie del ^{222}Rn para diferentes condiciones de referencia de la exposición doméstica y ocupacional, con factores de equilibrio y las características especificadas en aerosol.[Tirmarche et al., 2010]

La mayor exposición al ^{222}Rn suele producirse en residencias y lugares de trabajo. La concentración de ^{222}Rn depende de:

1. La cantidad de Uranio que contienen las rocas y el terreno del subsuelo.
2. Las vías que el ^{222}Rn encuentra para filtrarse en las viviendas.
3. La tasa de intercambio de aire entre el interior y el exterior, que depende del tipo de construcción, la ventilación del lugar y la estanqueidad del edificio.

Por lo general, el ^{222}Rn suele alcanzar concentraciones más elevadas en los sótanos, bodegas y otras zonas estructurales que están en contacto directo con el terreno. El ^{222}Rn se filtra en las casas a través de grietas en el piso o en la unión del piso con las paredes, espacios alrededor de las tuberías o cables, pequeños poros que presentan las paredes construidas con bloques de hormigón huecos, o por los sumideros y desagües [Piedecausa-García, Payá, Recio, & Barbudo, 2011].

Las concentraciones de ^{222}Rn pueden variar tanta entre construcciones adyacentes como entre secciones de la misma residencia o edificio, o incluso de un día para otro o de una hora para otra. La concentración de ^{222}Rn en las viviendas puede medirse de un modo

sencillo y económico. Debido a esas fluctuaciones, es preferible calcular la concentración media anual en el aire de interiores, midiendo las concentraciones de ^{222}Rn al menos durante tres meses. Ahora bien, las mediciones han de llevarse a cabo con arreglo a los protocolos nacionales, a fin de garantizar su uniformidad y su fiabilidad a la hora de tomar decisiones.[Darby, et al., 2005].

Entre uno de los factores que influyen en la concentración de ^{222}Rn es el material de construcción por lo que en la tabla 1 se indican los niveles de ^{222}Rn en diferentes materiales de construcción [Najam, Tawfiq, & Mahmood, 2013].

Tabla 1: Niveles de ^{222}Rn presente en materiales de construcción.

Material de construcción	**Concentración de ^{222}Rn**	**Nivel de exhalación de ^{222}Rn (Bq/m^{2}h)**
Cemento blanco	156.74	0.94
Yeso	165.5	1
Cemento	205.5	1.24
Ladrillo	166.55	1.01
Bloques de concreto	251.58	1.52
Piedra	121.95	0.72
Cerámica	174.12	1.05
Porcelana	270.04	1.63
Mármol negro	209.04	1.26
Cerámicas orgánicas	217.77	1.31
Granito rojo	383.3	2.3
Mármol Blanco	200.27	1.21
Adobe	35.28	0.24

Obtenida de: Najam, L. etl.al. 2013

2.- MÉTODOS Y MATERIALES

Se midió la concentración de ^{222}Rn en residencias y en lugares de trabajo en la ciudad de Riobamba. Esta ciudad se ubica en la región central de Ecuador a una altura media de 2 750 m.s.n.m., posee una población de 252 865 habitantes [INEC, 2013]. La temperatura media anual oscila los 13,7 ^{o}C, mientras que la velocidad media anual del viento es de 2.5 m/s [INAMHI, 2014]. Los lugares fueron escogidos de manera aleatoria dentro del área urbana. Durante los meses de junio, julio y agosto de 2016, se midieron 30 puntos, entre ellos 14 viviendas, 13 oficinas o lugares de atención al público y 3 laboratorios de docencia pertenecientes a la Escuela Superior Politécnica de Chimborazo.

Para medir la concentración de ^{222}Rn se utilizó el detector digital Corentium Home, el cual entrega una lectura corta en 24 horas y una extendida en 7 días. Este monitor se colocó en la primera planta de las residencias y lugares de trabajo, excepto en un laboratorio y una oficina que están ubicados en el segundo nivel de la edificación. Además de la medida de la concentración de radón se tomaron datos del tipo de material de la construcción, la ventilación y la edad de la edificación.

Los materiales de las construcciones comunes en la región son adobe, bloque y ladrillo combinados con madera y cemento. La ventilación se ha clasificado como Alta, Mediana y Poca, según el número de entradas de aire y la predisposición de los habitantes o usuarios a ventilarla las habitaciones. Para la edad de la edificación se ha categorizado con un valor de Antigua si tiene entre 51 y 100 años, Mediana edad si está entre los 16 y 50 años y Nueva si es menor a los 15 años. Para la estimación de la dosis anual recibida se utilizó el coeficiente de conversión a dosis de radón 0.017 mSv/año para 1 Bq/m^3, que supone 7000 horas al año dentro de la edificación, recomendado por el ICRP. En las residencias se ha considerado para el cálculo un tiempo de estadía promedio de 20 y 14 horas, asumiendo una persona que permanece en la vivienda y una que sale a trabajar fuera de la misma. En el caso de las oficinas y lugares de atención al público se ha considerado un tiempo de 8 y

4 horas, cinco días a la semana por 48 semanas laborables. Por último, el tiempo considerado en laboratorios de docencia es de 4 y 2 horas por semana, durante 8 meses.

3.- RESULTADOS

Los datos obtenidos de la concentración de radón y las características de las edificaciones se detallan en la **Tabla 2.** En las viviendas existen 3 que se clasifican como Antiguas, 8 como de Mediana edad y 3 Nuevas. De igual manera para los lugares de trabajo existen 2 Antiguas, 9 de Mediana edad y 2 Nuevas. Mientras que todos los laboratorios se encuentran categorizadas como de Mediana edad.

Tabla 2.- Caracterización de los lugares medidos

N°	Código	Planta	Material de construcción	Ventilación	Edad
			Residencias		
1	H-01	1	Adobe y piso de madera	Mediana	Antigua
2	H-02	1	Adobe y piso de madera	Poca	Antigua
3	H-03	1	Ladrillo y madera	Mediana	Nueva
4	H-04	1	Ladrillo y cemento	Mediana	Nueva
5	H-05	1	Bloque y cemento	Mediana	Mediana
6	H-06	1	Bloque y cemento	Poca	Mediana
7	H-07	1	Bloque y cemento, piso flotante	Mediana	Mediana
8	H-08	1	Bloque y cemento	Poca	Antigua
9	H-09	1	Bloque y cemento	Mucha	Nueva
10	H-10	1	Bloque y cemento	Mediana	Mediana
11	H-11	1	Bloque y cemento	Mediana	Mediana
12	H-12	1	Ladrillo y cemento	Poca	Mediana
13	H-13	1	Ladrillo y cemento	Poca	Mediana
14	H-14	1	Bloque y cemento	Poca	Mediana

Lugares de Trabajo					
15	O-01	2	Bloque y cemento	Poca	Mediana
16	O-02	1	Bloque y cemento	Mediana	Mediana
17	O-03	1	Ladrillo y cemento	Mediana	Antigua
18	O-04	1	Bloque y cemento	Poca	Mediana
19	O-05	1	Ladrillo y cemento	Mediana	Mediana
20	O-06	1	Bloque y cemento	Mediana	Nueva
21	O-07	1	Bloque y cemento	Mediana	Mediana
22	O-08	1	Bloque y cemento	Mediana	Antigua
23	O-09	1	Ladrillo y cemento	Mediana	Mediana
24	O-10	1	Ladrillo y cemento	Mediana	Nueva
25	O-11	1	Bloque y cemento	Mediana	Mediana
26	O-12	1	Ladrillo y cemento	Mediana	Mediana
27	O-13	1	Ladrillo y cemento	Poca	Mediana
Laboratorios					
28	L-01	1	Ladrillo y cemento	Poca	Mediana
29	L-02	2	Bloque y cemento	Mediana	Mediana
30	L-03	1	Ladrillo y cemento	Mediana	Mediana

La **Figura 1**. muestra la ubicación de estas edificaciones dentro del área urbana de la ciudad de Riobamba.

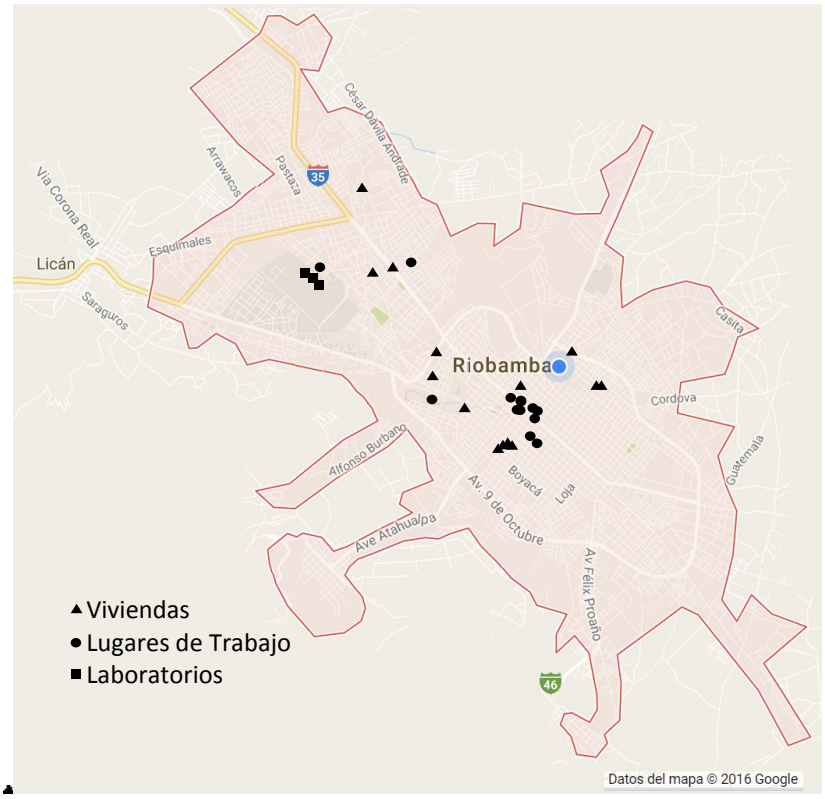

Figura 3.- Localización de los puntos medidos

Las **Tablas 3, 4** y **5** muestran la concentración de radón y la dosis anual recibida por partículas alfa, producto de la desintegración del radón radiactivo y que pueden ser inhaladas por los ocupantes de las edificaciones.

Tabla 3.- Concentración de ^{222}Rn y Dosis anual recibida en viviendas

Cód.	Concentración ^{222}Rn (Bq/m^3)	Concentración ^{222}Rn (pCi/L)	Dosis Efectiva Anual 20 h/día (mSv)*	Dosis Efectiva Anual 14 h/día (mSv)**
H-01	95	2,568	1,685	1,180
H-02	59	1,595	1,047	0,733
H-03	27	0,730	0,479	0,335
H-04	32	0,865	0,568	0,397
H-05	20	0,541	0,355	0,248
H-06	10	0,270	0,177	0,124
H-07	7	0,189	0,124	0,087

H-08	6	0,162	0,106	0,075
H-09	10	0,270	0,177	0,124
H-10	2	0,054	0,035	0,025
H-11	5	0,135	0,089	0,062
H-12	25	0,676	0,444	0,310
H-13	16	0,432	0,284	0,199
H-14	24	0,649	1,685	1,180

*Totalizando 7300 horas/año. ** Totalizando 5113 horas/año.

Tabla 4.- Concentración de ^{222}Rn y Dosis anual recibida en Lugares de trabajo

Cód.	Concentración ^{222}Rn (Bq/m^3)	Concentración ^{222}Rn (pCi/L)	Dosis Efectiva Anual 8 h/día (mSv)*	Dosis Efectiva Anual 4 h/día (mSv)**
O-01	16	0,432	0,075	0,037
O-02	18	0,486	0,084	0,042
O-03	10	0,270	0,047	0,023
O-04	119	3,216	0,557	0,278
O-05	95	2,568	0,445	0,222
O-06	16	0,432	0,075	0,037
O-07	35	0,946	0,164	0,082
O-08	21	0,568	0,098	0,049
O-09	23	0,622	0,108	0,054
O-10	32	0,865	0,150	0,075
O-11	15	0,405	0,070	0,035
O-12	26	0,703	0,122	0,061
O-13	10	0,270	0,047	0,023

*Totalizando 1927 horas/año. ** Totalizando 964 horas/año.

Tabla 5.- Concentración de ^{222}Rn en Laboratorios ESPOCH

Cód.	Concentración ^{222}Rn (Bq/m^3)	Concentración ^{222}Rn (pCi/L)	Dosis Efectiva Anual 4 h/día (Sv)*	Dosis Efectiva Anual 2 h/día (Sv)**
L-01	404	10,919	0,628	0,314
L-02	14	0,378	0,022	0,011
L-03	4	0,108	0,006	0,003

*Totalizando 640 horas/año. ** Totalizando 320 horas/año.

En la **Figura 2.** se agrupan las viviendas por su edad y de manera descendente en función a la concentración de radón en las mismas, se observa que las categorizadas como Antiguas H-01 y H-02 son las de mayor concentración de radón, la H-08 a pesar de ser una construcción de más de 50 años tiene una concentración muy baja. Las de Mediana edad varían desde los 2 a 25 Bq/m^3. Las viviendas menores a 15 años de construcción presentan niveles mayores a las viviendas de Mediana edad, excepto la H-09, que presenta un valor de 10 Bq/m^3.

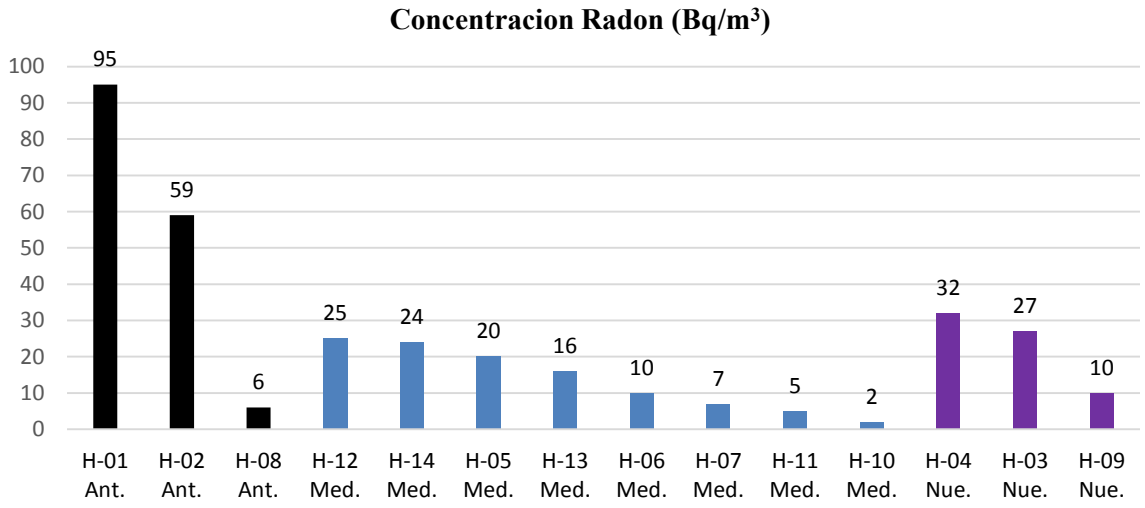

Figura 4- Concentración de Radón en Residencias

En la **Figura 3.** se muestra que O-04 y O-05 son los de mayor concentración de radón siendo estos lugares edificaciones de Mediana edad. Para la edificación Antiguas el nivel de concentración es bajo en comparación con las anteriores. Solo se ha registrado una edificación nueva la cual tiene una concentración de 32 Bq/m^3.

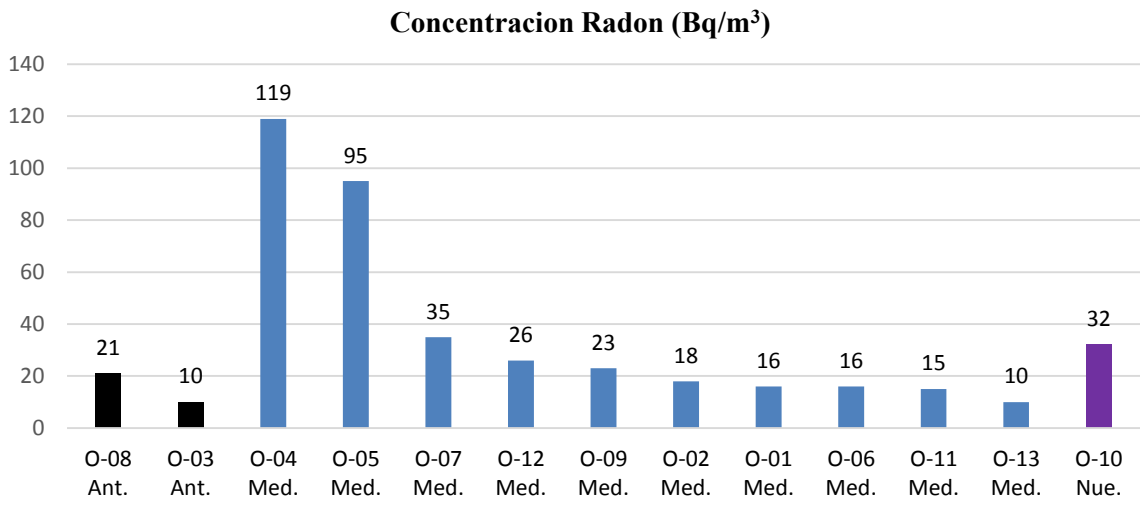

Figura 5.- Concentración de Radón en Lugares de Trabajo

Los tres laboratorios analizados se encuentran en instalaciones de entre 15 y 50 años, categorizadas como de Mediana edad, En la **Figura 4.** se observa que L-02 y L-03 se encuentran con niveles bajos de concentración. L-01 presenta el nivel más alto de los 30 lugares medidos, incluso supera la recomendación del ICRP de 300 Bq/m^3.

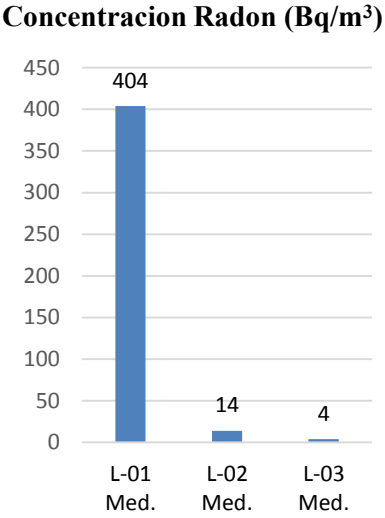

Figura 6.- Concentración de Radón en Laboratorios

4.- DISCUSIÓN

Dentro del grupo de viviendas, solo dos superan el 1 mSv/año, con 20 horas diarias de permanecía. Este tiempo podría parecer mucho, pero puede ser el caso de amas de casa, personas de tercera edad, enfermas o con discapacidades. Se puede considerar 14 horas diarias de permanencia para aquellas personas que realizan sus actividades fuera de casa, en este caso solo H-01 supera el 1 mSv/año. Las viviendas Antiguas H-01 y H-02, resultan ser las de mayor concentración de radón excepto la H-08, las dos primeras son de adobe y pisos de madera mientras que la última es de bloque con mampostería de cemento y piso flotante. Los niveles de exhalación son mayores en cemento que en el adobe **(Tabla 1.)**, entonces el radón puede provenir de los pisos de madera que no han sido sellados herméticamente, el piso flotante es hermético en comparación con pisos antiguos de madera. Las viviendas Nuevas H-04 y H-03 presentan mayor concentración de radón que las de Mediana edad, estas últimas pueden presentar reparaciones y mayores capas de pintura haciendo más herméticas las paredes y pisos.

En los lugares de trabajo, O-04 y O-05 presentan los mayores niveles de concentración de radón, siendo ambas edificaciones de Mediana edad, O-04 es una bodega con poca ventilación y O-05 una ferretería. Considerando un tiempo de 8 horas diarias se llega cercanamente a los 0,5 mSv/año en estos lugares de trabajo. Para las edificaciones Antiguas en este caso O-08 y O-03, el nivel de concentración resulta ser bajo. La única edificación Nueva O-10 presenta características similares de concentración que en las viviendas nuevas con 32 Bq/m^3. Los niveles de dosis recibida en general son aceptables.

El laboratorio L-01, presenta el más alto nivel de concentración de radón de las 30 mediciones, incluso sobre la recomendación del ICRP de 300 Bq/m^3, pero siendo un área de acceso restringido y de permanencia limitada no presenta riesgo para sus ocupantes, si se cumplen los principios de protección radiológica establecidos para la práctica. La dosis recibida será de 0.628 mSv/año si se trabajare 4 horas a la semana durante 8 meses. La

radiación alfa generada se debe a material radiactivo de origen natural utilizado para prácticas estudiantiles.

5.- CONCLUSIONES

Los resultados de las mediciones muestran que la concentración de radón radiactivo en residencias y lugares de trabajo en la ciudad de Riobamba, se encuentran por debajo de los niveles recomendados por la OMS. El Ecuador y varios de los países en la región no poseen normativas para el manejo y control de elementos radiactivos de origen natural, por lo debemos basarnos en normas internacionales. Al ser el radón la segunda causa de cáncer de pulmón, es importante que las autoridades atiendan esta problemática de la manera oportuna y adecuada, dando a conocer de qué se trata y las formas de mitigación.

La mayoría de las edificaciones estudiadas presentan valores muy bajos y cercanos a la concentración ambiental exterior que en la región oscila los 16 Bq/m^3. Los pisos antiguos no hermetizan correctamente el suelo en las edificaciones antiguas presentando mayores concentraciones, pero debajo de las recomendaciones internacionales. Una edificación de Mediana edad, puede tener más capas de pintura en las paredes y haber cambiado sus pisos antiguos por modernos y herméticos por lo que presenta menores concentraciones que una casa nueva.

Es importante cumplir con los protocolos de manejo de materiales radiactivos en centros de docencia e investigación, respetando los criterios de blindaje, distancia y tiempo de permanencia. Para el caso del laboratorio que supera el límite permisible, se debe crear un sistema de ventilación natural que procure alcanzar los 300 Bq/m^3 o menos, ya que la ventilación es muy limitada.

REFERENCIAS

Darby, S., Hill, D., Auvinen, A., Barros-Dios, J. M., Baysson, H., Bochicchio, F., … Doll, R. (2005). Radon in homes and risk of lung cancer: collaborative analysis of individual data from 13 European case-control studies. *BMJ (Clinical Research Ed.)*, *330*(7485), 223. http://doi.org/10.1136/bmj.38308.477650.63

INAMHI. (2012). Anuario Metereológico.

INEC. (2013). PROYECCIÓN DE LA POBLACIÓN ECUATORIANA, POR AÑOS CALENDARIO, SEGÚN CANTONES 2010-2020. Retrieved from http://www.ecuadorencifras.gob.ec/inec-presenta-sus-proyecciones-poblacionales-cantonales/

López, F., Canoba, A., & Nuclear, A. (n.d.). DETERMINACIÓN DE RADÓN POR ADSORCIÓN EN CARBÓN ACTIVADO Y MEDICIÓN POR CENTELLEO LÍQUIDO1. *Iaea.org*. Retrieved from http://www.iaea.org/inis/collection/NCLCollectionStore/_Public/29/057/29057126.pdf

Najam, L. A., Tawfiq, N. F., & Mahmood, R. H. (2013). Radon Concentration in Some Building Materials in Using CR-39 Track Detector. *International Journal of Physics*, *1*(3), 73–76. http://doi.org/10.12691/IJP-1-3-3

Piedecausa-García, B., Payá, S. C., Recio, M. A. M., & Barbudo, M. A. S. (2011). Radiactividad natural de los materiales de construcción. Aplicación al hormigón. Parte II. Radiación interna: el gas radón. *Cemento Hormigón*, (946), 34–50.

Tirmarche, M., Harrison, J. D., Laurier, D., Paquet, F., Blanchardon, E., Marsh, J. W., & International Commission on Radiological Protection. (2010). ICRP Publication 115. Lung cancer risk from radon and progeny and statement on radon. *Annals of the ICRP*, *40*(1), 1–64. http://doi.org/10.1016/j.icrp.2011.08.011

World Health Organization. (2009). *WHO Handbook on Indoor Radon*. *WHO Handbook on Indoor Radon: A Public Health Perspective*. World Health Organization. Retrieved from http://www.ncbi.nlm.nih.gov/pubmed/23762967

Zeeb, Ha., Shannoun, F., & OMS. (2015). *Manual de la OMS sobre Radón en interiores*. Ginebra. Retrieved from http://www.who.int/iris/handle/10665/161913#sthash.2WvJkXnR.dpuf

Determination of Spatial Resolution of Positron Emission Tomograph of Clear PET-XPAD3/CT System

H. Olaya Dávila[1], C. Morel[2], H. F. Castro[3], S. A. Martínez Ovalle[1,*]

[1]Grupo de Física Nuclear Aplicada y Simulación, Universidad Pedagógica y Tecnológica de Colombia, Tunja- Colombia

[2] ImXGam Group, Centre de Physique des Particules de Marseille, Marseille- France

[3] Physics Department, Universidad Nacional de Colombia, Bogotá D.C - Colombia

Abstract

Based on The National Electrical Manufacturers Association (NEMA), using the AMINE software to construction of sinograms and using a radioactive source ^{22}Na that emitting positrons were made calculations for determine spatial resolution of ring array system of phoswich detectors of positron emission tomograph included in the CLEAR PET-XPAD3/CT prototype for small animals made in the laboratories of CCPM and whose project is led by the research group ImXgam. The radioactive source ^{22}Na approximately 9 MBq of activity, with spherical shape and diameter of 0.57mm immersed in a plexiglas disc was located at the geometric center of tomographic system with a Field of View (FOV) of 35 mm in the axial and transverse directions. Displacements of radiactive source were performed on the three cartesian axes and was rebuilt a sinogram for each axis. The shape of sinogram allow describe the correct position and the maximum efficiency of each detector. Subsequently, was carried out a scanning in each one of three spatial axes taking an enough distance covering the dimensions of radioactive source, were recorded data for each one of phoswich detector crystals which are aligned in the axis of movement. The process was repeated for other axes and then was offsetting the radioactive source with respect to the FOV and were calculated FWHM (Full Width at Half Maximum) and FWTM (Full Width at Tenth Maximum) values and performing statistics of these values with parabolic fitting, the latter setting allows to obtain parameters of spatial resolution of system.

Keywords: *PET, Spatial resolution, Phoswich detectors.*

1. INTRODUCTION

Medical imaging is a speciality that employs different methods of imaging to diagnose and to treat diseases by visualization of tissues within the human body. Currently, the radiologist is using different technologies such as: X ray radiography, ultrasound, Computed Tomography (CT), nuclear medicine, Positron Emission Tomography (PET) [Luo et al., 2010] and Magnetic Resonance Imaging (MRI). The success of medical imaging is to achieve more accurate diagnostic improving image quality with higher spatial resolution, lower noise, lower cost, decrease side effects on health and to obtain images in real time [Badawi, 2015].

More particularly, these two techniques allow simultaneous analysis of the metabolic function of tissues and anatomical information, as the location, shape and size of the lesion. This is an important new tool to provide more accurate diagnoses of disorders that previously could not be detected early. More often, PET is used to obtain image of body's biochemistry by glucose metabolism, which may be present for instance when there is an abnormal growth of cells, such as a cancerous tumour; whereas CT may precisely locate the position of the lesion with respect to the patient anatomy.

Positron Emission Tomography is a technique that allows obtain information of metabolic function of tissues and anatomical information through metabolism of glucose or tyrosine, this technique is based on the coincidence detection of gamma rays emitted in antiparallel directions which are the result of positron annihilation with an electron. [Juweid & Cheson, 2006].

The location of injury, its contour and the spatial resolution of image depends strongly on detection system and amount of radioactive material used. The new generation of scintillation crystals pixelated allow a better quality and spatial resolution of the diagnostic image. Another important point is that new detectors have short response times that reduce unwanted matches. The main objective of this work is to determine the spatial resolution of ClearPET/XPAD3/CT system.

1.1.- Theoretical basis

Positron Emission Tomography (PET), is an equipment used in the field of nuclear medicine, where a patient or a living creature who has been previously administrated a small quantities of radioactive material through inhalation, injection or ingestion, which is metabolized in the interest organ or tissue. Afterwards, radioactive material disintegrates producing transitions in which a proton decays into a neutron, emitting a positron (positive beta particle) and a neutrino. The interaction between a neutrino and matter has no relevance, but the positron with energy of 1.022 MeV interacts with an electron in the medium and produces annihilation where two 511 keV gamma photons in antiparallel direction to each other and are responsible of the formation of the diagnostic image (Figure. 1).

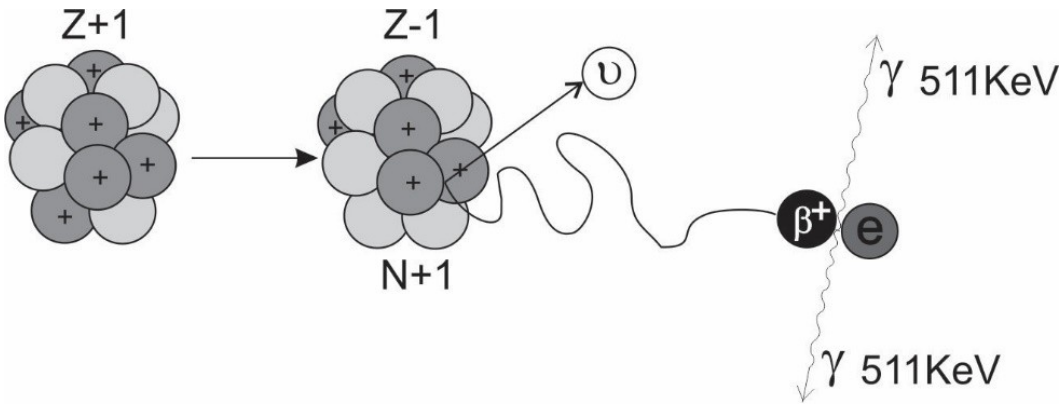

Figure 1. Annihilation and gamma photons production

The radioactive isotopes used in the PET are produced in a medical cyclotron, then taken to a radiochemistry laboratory, where they are combined with a chemical substance called tracer for latter administration. The mainly used radio-pharmaceuticals are shown in the Table 1:

Table 1. PET mainly used Isotopes [Kramer et al., 2008]

Isotope	Tracer	Physiological Process	Main Application
^{11}C	Methionine	Protein Synthesis	Oncology
^{11}C	Raclopride	D2 Receptor	Movement Disorder
^{13}N	Ammonia	Blood Perfusion	Myocardial Perfusion
^{15}O	Water/Dioxise	Blood Perfusion	Brain Activation
^{18}F	Fluorine Ion	Bone Metabolism	Oncology
^{18}F	Fluorine deoxyglucose	Glucose Metabolism	Oncology Neurology Cardiology

The acquisition of the image is based upon the external detection by coincidence of the two gamma rays and a valid annihilation event requires a coincidence in the order of 12 nanoseconds of difference between the opposite detectors in the ClearPET system. Each detector generates a pulse in the temporal space when it records a photon, these pulses are combined in a coincidence circuit and are considered a coincidence if both appear in a small window of time. See Figure 2.

The difference of time in the detection is known as a coincidence window and is given as, where t_2 and t_1 are the times of detection for each photon.

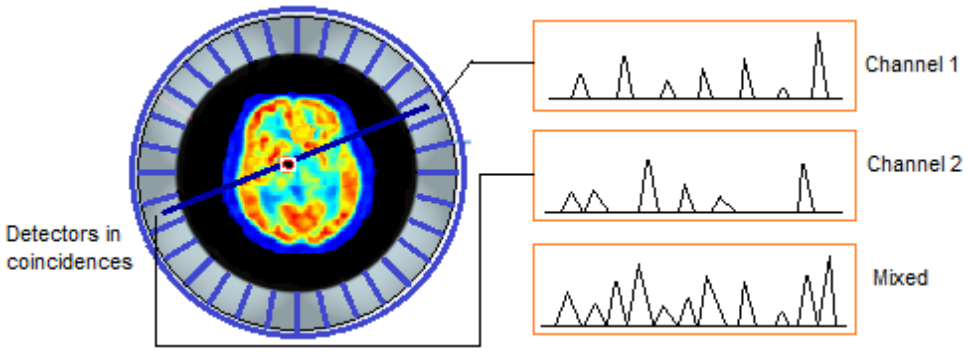

Figure 2. Coincidence of two opposite gamma photons. When a coincidence is achieved the amplitude of the pulses are added

The spatial resolution of a Positron Emission Tomograph represents its ability to distinguish between two points after image reconstruction. The measurement is performed by imaging point sources in a scattering medium. The objective of this procedure is to characterize the widths of the reconstructed image point spread functions (PSF) of a solid radioactive source of ^{22}Na. The width of the PSF is defined by its Full Width at Half Maximum Amplitude (FWHM) and its Full Width at Tenth Maximum Amplitude (FWTW), the above parameters define pixel size. Finally, the intrisic spatial resolution R_s of the PET is performed through Derenzo formula: [Hammonet, 2016].

$$R_s = a\sqrt{\frac{d^2}{2} + b^2 + r^2 + (0.0022D)^2} \quad (1)$$

Where **a** is an experimental factor result of the reconstruction method (which depends significantly on the filter used), **b** is the coding error of a block (0 when no link), **r** is the average trajectory of a positron, **d** is dimension of a pixel and **D** is diameter of the ring.

2.- MATERIALS AND METHODS

The ClearPET-XPAD/CT prototype for small animals was used for this work. The system is located at the ImXgam, CCPM laboratories in Marseille, France [Nicol, 2010]. A radioactive source ^{22}Na (0.542 MeV) and γ radiation (1.27 MeV) of approximately 9 MBq of activity, with spherical shape and diameter of 0.57mm immersed in a plexiglas disc was located at the geometric center of tomographic system with a Field of View (FOV) of 35 mm in the axial direction.

The radioactive source is located on a support which moves through an remote electromechanical system in axial, radial and tangential directions (3D). The geometric center of the disk with the source of ^{22}Na was fixed with a laser light and is fixed to the origin (0,0,0) of tomographic system and the software of data acquisition. Then was made a scanning with a length greater than the size of the disk for obtain data of intensity from the radioactive source with a Gaussian distribution. Subsequently, the source moves radially each 5mm until 25mm and was re-take the scanning data. For each scan was necessary to rebuild the sinogram to verify proper positioning. In total five samples were performed by each displacement and for each spatial axis due to the tomographics system contains three rings of scintillation detectors phoswich: (Lutetium Oxy-ortosilicate doped with cerium Lu_2SiO_5: Ce) and LUYAP (Lutetium Ortoaluminate de Yttrium doped with cerium $Lu_{0.7}Y_{0.3}AlO_3$:Ce). Finally, the whole process is repeated but placing the radioactive source at a distance of ¼ of the Field of View (FOV) of tomographic system [Dupont, 2014].

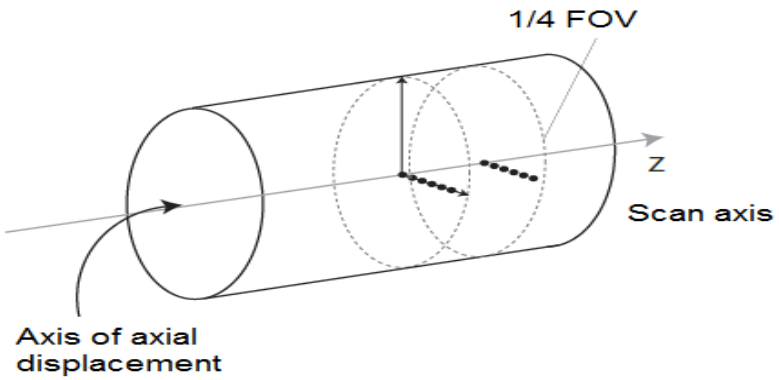

Figure 3. Scheme of positioning of ^{22}Na radioactive source. Each point represents the distance measured from the center of the axis (5, 10, 15, 20 and 25mm) [Hammonet, 2016].

3.- RESULTS

Each data collection was performed with times about 1 minute. In each scan were obtained 130 data on average. Then, was fitted to a Gaussian distribution, where the maximum height was found by performing a second adjustment with parabolic fit in the three largest intensity data. Finally, were calculated and recorded the FWTM and FWHM values for each measurement point. See Figure 4.

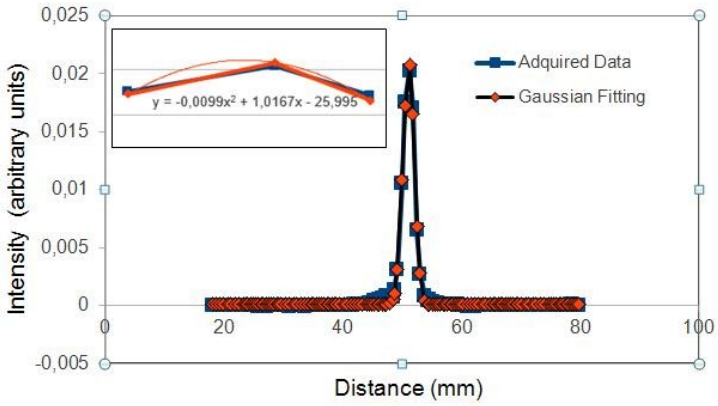

Figure 4. Spatial resolution. Adjustment of data acquired for the position (0,0,10) with a scan in the radial direction. In this case FWHM=2.243 mm and FWTM=4.124.

In the Table 2 are shown the FWHM and FWTM for each position of the ^{22}Na at differents distances for differents scanning directions.

Table 2. Spatial Resolution values calculated through parabolic fitting and weighted with those reported with Amine software. Reconstructed image pixel size (mm): 2.3; Slice thickness (mm): 0.575. At axial center.

	5mm		10mm		15mm		25mm	
	FWHM	FWTM	FWHM	FWTM	FWHM	FWTM	FWHM	FWTM
Radial	1.510	3.298	2.232	4.124	2.251	4.172	2.484	4.241
Tangential	2.331	4.334	2.557	4.747	2.578	4.793	2.850	4.869
Axial	1.692	3.261	1.754	3.584	1.968	3.554	2.247	4.072

	At ¼ axial FOV from center							
Radial	2.367	4.320	2.237	4.124	2.269	4.128	2.248	4.122
Tangential	2.550	4.690	2.588	4.747	2.566	4.716	2.601	4.768
Axial	1.833	3.588	1.996	3.664	2.035	3.756	2.535	4.648

In the Figures 5 and 6 are shown values of FWHM calculated from Gaussian analysis and parabolic fifting for each position and scanning directions. Position at axial center and at ¼ of field of view. The distances 0mm and 20 mm those are included into the figures.

In Table 3 are shown experimental values corresponding to the intrinsic spatial resolution of equation (1) and is included the pixel size calculated through the FWHM factors.

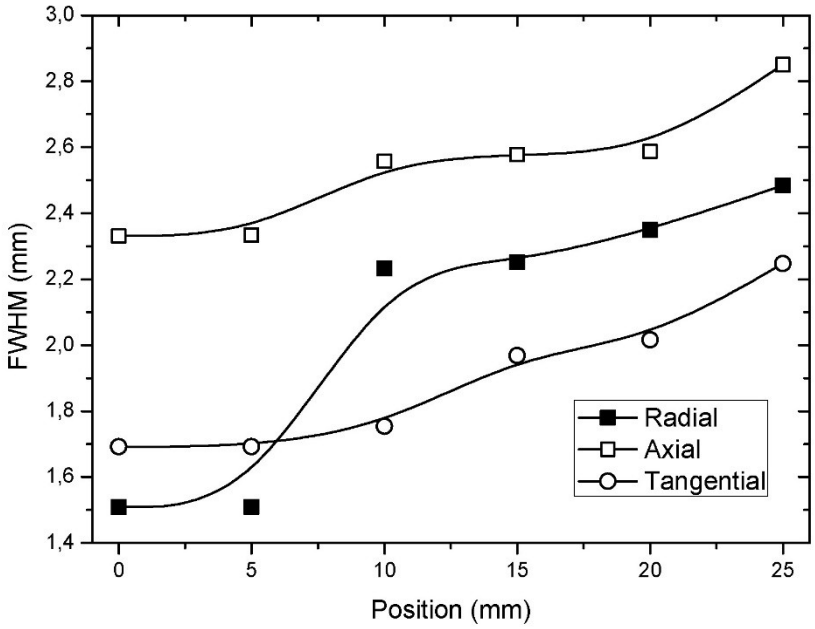

Figure 5. Spatial resolution at axial center

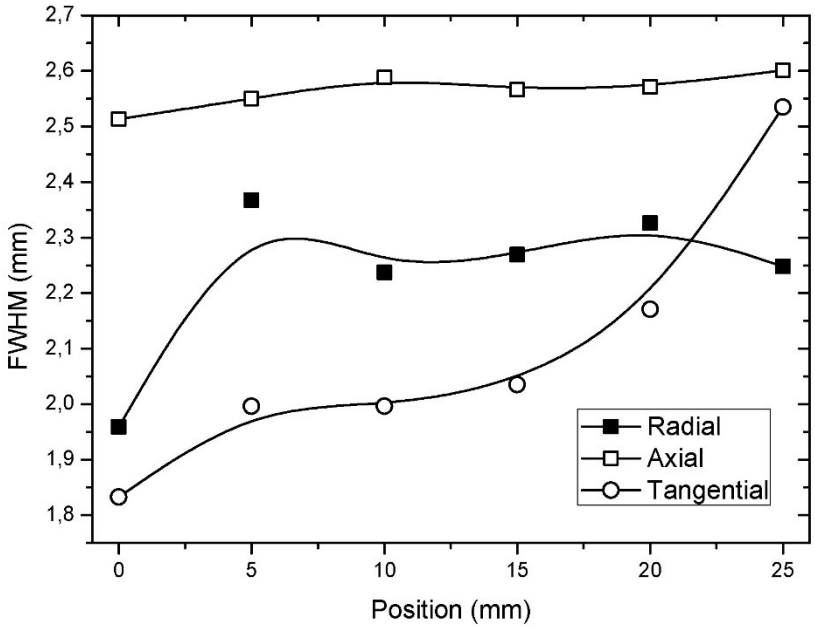

Figure 6. Spatial resolution at ¼ field of view (FOV)

Table 3. Parameters of intrinsic spatial resolution calculated and substituted in equation (1)

a = 1.2 mm	Value that is calculated in the software as a result of algorithm PET construction
b = 0	In the case of coupling a 1-1-crystal anode MaPMT
r□ 0.5 mm	That corresponding a full width at half maximum of the distribution of the mean path of positrons emitted before annihilation in water by a ^{22}Na source.
d = 2.3 mm	Dimension of a pixel
D = 137 mm	Is diameter of the ring of ClearPET system

The result of intrinsic spatial resolution of the system ClearPET-XPAD/CT is: R_s=2.07mm

4.- DISCUSSION

The methodology for obtaining the spatial resolution proposed in this paper is important to implement it within a framework of periodic quality control in PET, because the correct interpretation of diagnostic images metabolic depends on the quality of the image.

5.- CONCLUSIONS

The FWHM values and R_s factor that determining the spatial resolution of the ClearPET-XPAD/CT tomograph is correct relative to size of each pixel of phoswich detector and the diameter of the ring.

The methodology used in scanning of three spatial directions and the displacement of the radioactive source of ^{22}Na determine whether there is an abrupt change in FWHM or FWTM parameters whose origin could be the loss of efficiency of a pixel or a failure in phoswich module.

The spatial resolution will be higher in a positron emission tomograph applied in humans, because: the diameter of the ring is larger, the positron emitting isotopes such as ^{18}F have a longer mean free path than ^{22}Na and coupling signal usually is not obtained in a multi-anode photomultiplier tube (independent signals) like ClearPET.

Acknowledgments

Special thanks to CPPM, ImXgam group by cooperation in the development of this work.

REFERENCES

Badawi, R. (1999). Introduction to PET physics. Retrieved from University of Washington Division of Nuclear Medicine website: http://depts. washington. edu/nucmed/IRL.

Chantepie, B. (2008). Etude et réalisation d'une électronique rapide à bas bruit pour un détecteur de rayons X à pixels hybrides destiné à l'imagerie du petit animal (Doctoral dissertation, Université Aix Marseille II).

Dupont, M. (2014). Tomographie spectrale à comptage de photons: développement du prototype PIXSCAN et preuve de concept (Doctoral dissertation, Aix-Marseille).

Hammonet, M. (2016). Tomographie hybride simultanée TEP/TDM combinant détecteurs à pixels hybrides et modules phoswich à scintillateurs (Doctoral dissertation, Aix-Marseille Université).

Juweid, M. E., & Cheson, B. D. (2006). Positron-emission tomography and assessment of cancer therapy. New England Journal of Medicine, 354(5), 496-507.

Kramer, E. L., Ko, J. P., Mourtzikos, K., & Ponzo, F. (2008). Positron Emmission Tomography Computed Tomography: A Disease-Oriented Approach. Informa Healthcare.

Luo, W., Anashkin, E., & Matthews, C. G. (2010). Performance evaluation of a PEM scanner using the NEMA NU 4-2008 small animal PET standards. IEEE Transactions on Nuclear Science, 57(1), 94-103.

Nicol, S. (2010). Étude et construction d'un tomographe TEP/TDM pour petits animaux, combinant modules phoswich à scintillateurs et détecteur à pixels hybrides (Doctoral dissertation, Université de la Méditerranée-Aix-Marseille II).

Assessment of the Effectiveness of Attenuation of Leaded Aprons Through TLD Dosimetry and Monte Carlo Simulation Method

Hernán Olaya Dávila[1], José Antonio Díaz Merchán[1]
Héctor Rene Vega Carrillo[2], Segundo Agustín Martínez Ovalle[1,*]

[1]Grupo de Física Nuclear Aplicada y Simulación
Universidad Pedagógica y Tecnológica de Colombia
Tunja- Colombia

1 Unidad Académica de Estudios Nucleares de la
Universidad Autónoma de Zacatecas
C. Ciprés 10, Fracc. La Peñuela. 98068
Zacatecas, Zac. México

Abstract

Were performed experimental setups using an X-ray equipment continuous emission Pantak DXT-3000 and three types of leaded aprons with thickness of 0.25mm, 0.5mm and 0.75mm coated with Mylar Fiber coated Mylar on its surface. Apron was located at a distance of 2.5m with respect focus in order to cover a radiation field size of a meter in diameter. At the beam output were added aluminum filtration in order to reproduce qualities of narrow beams N40 ($E_{efective}$= 33keV), N80 ($E_{efective}$= 65 keV) and N100 ($E_{efective}$= 83 keV) according to the ISO standard 4037 (1-3). Each lead apron were fixed 10 TLD dosimeters over its surface, 5 dosimeters before and 5 dosimeters after with respect to X ray beam and were calibrated for Harshaw 4500 thermoluminiscent reader system order to assess the attenuation of each apron. Were performed dosimeters readings and were calculated the attenuation coefficients for each effective energy of X ray quality. In order to confirm the method of effective energy of ISO-4037 and evaluate effectiveness of lead aprons based on energy range for each medical practice was made a Monte Carlo Simulation using code GEANT4, calculating the fluence and absorbed dose in each one of the dosimeters Monte Carlo, then coefficients of linear attenuation were calculated and compared with the experimental data and reported by the National Institute of Standards and Technology (NIST).Finally, results are consistent between theoretical calculation and experimental measures. This work will serve to make assessments for other personalized leaded protections.

Keywords: TLD dosimeters, Monte Carlo, X rays, linear attenuation coefficients

1. INTRODUCTION

Leaded accessories of personal protection are fundamental in the medical radiodiagnostic, their objective is to reduce the radiation doses to occupationally exposed workers and in some cases in patients diagnosed in order to achieve the lowest possible level of radiation exposure As Low As Reasonably Achievable (ALARA) and allow it to make a process effective, reliable and safe [Kazempour et al., 2015].

Custom-made protections are manufactured commonly with material Pb of a low thickness and are used mainly in diagnostic radiology in all medical centers. Using simulation methods, there have been made many efforts in the design of protectors that, in addition to reducing the exposure to radiation for part of the POEs, to allow comfort in use, have long useful life and decrease the toxicity caused by Pb [Kazempour et al., 2015; Zehtabian et al., 2015].

Various studies, about the exposure to X-rays in different medical practices, have been made so far. Santos et. al., studied exposures of personnel occupationally exposed in interventional radiology using Monte Carlo simulation with MCNPX and Dummy anthropomorphic [Santos, 2015]. In this same line using Phantom RANDO, Shulze et. al., studied the effects of the dose in skin with and without the use of apron leaded to practices digital panoramic x-ray photography. They found significant increase in mammary region when not in use protective material [Schulze et al., 2016].

About this matter, it is considered that this type of protection is not well used in the countries of Latin America, that is to say, they are used incorrectly, in the sense that there is no awareness on the part of medical staff about the degree of importance that has its use from the point of view of radiation protection [Valentin, 2007].

Although, it is known that the leaded aprons are not in continuous use in the work of the occupationally exposed workers. In some hospital centers leaded aprons are not used due to the discomfort that its portability causes in the workers, and besides, because they are not

available on a particular site. The most common case happens in interventional radiology, when the medical staff does not use the protections listed below: leaded aprons, the protectors of the thyroid, the protective gonadal and glasses sinkers, because these ones will cause discomfort for the time that the practice of medical intervention lasts. However, conclusive studies confirm the importance of the use of protective devices of radiation routinely with a purpose to reduce the irradiation of sensitive structures such as the lens of the eye and thus, to decrease the probability of induction of Cataractogenesis [Seals et al., 2016].

There are several validation methods that allow to establish the reliability of the various devices used for protection of personnel to radiation. The most used are no doubt experimental measurements with thermoluminescent detectors (TLD). Hausler et. al., studied the dose received by 39 Medical Physics of 14 hospitals in Germany during procedures of interventional radiology. They conclude that if they are properly used, the protectors, the limits of annual doses, it is difficult to overcome [Hausler et al., 2009].

Although the use of the TLD is an excellent choice for demonstrating the effectiveness of leaded protectors, it is important to note that if experimental measurements could be substantiated with calculation of Monte Carlo, it is possible to get to design theoretical models that underpin any experiment [Kazempour et al., 2015; Zehtabian et al., 2015; Santos, 2015; Matyagin et al., 2016].

In this work, we used method Monte Carlo as a tool for the simulation with the code Geant4 [Agostinelli et al., 2003], to study the processes of interaction radiation field in protection accessories as customized leaded aprons, which are usually used in most medical centers. The purpose of the study is no other than to evaluate the degree of effectiveness of the apron leaded based to the thickness in lead and the effective power of broadcast proposed by the standard ISO 4037 [KSA, 2003].

1.1 Theoretical basis

When a mono energetic beam of electromagnetic radiation incident on a homogeneous material of density and thickness defined, the relative intensity subsequent to the processes of absorption and transmission are given by:

$$I = I_o\, e^{\mu\, x} \tag{1}$$

Where μ is the linear attenuation coefficient expressed in (cm^{-1}), x is the thickness of the material expressed in (cm). Implicitly, it has attenuation coefficient mass μ_m, given by the relationship:

$$\mu_m = \frac{\mu}{\rho} \tag{2}$$

Where ρ is the density of the material expressed in g/cm^3. In mono energetic bundles, for each kind of energy and material there corresponds a coefficient μ_m. In the case of poly energetic beams of X-rays for each spectrum there is an effective power which corresponds to an attenuation coefficient mass for a given material [Zehtabian et al., 2015].

The linear attenuation coefficient μ is directly related to the effective cross-section total interaction σ is defined as the probability of related interaction between a collision and the effective area expressed in barn (1 barn = 10^{-24} cm^2). The relationship between the linear attenuation coefficient and the effective cross-section is given by:

$$\frac{\mu}{\rho}=\frac{N_A}{A}\sigma \tag{3}$$

The main mechanisms of interaction of photons X of use in medical diagnosis with matter are the photoelectric effect and inelastic scattering of Compton. The effective cross-section of total attenuation is the resultant of the two effects above:

$$\sigma_{Total} = \sigma_{Photoelectric} + \sigma_{Compton} \tag{4}$$

2. MATERIALS AND METHODS

For the experimental study we used three types of leaded aprons of use in radiodiagnostics with thicknesses of 0.25 mm, 0.5 mm and 0.75 mm. Each apron leaded was located on a phantom anthropomorphic of Aldersson at a distance focus-surface of 2.5 m. We performed irradiations controlled from an equipment X-ray continuous emission Pantak DXT-3000 the Secondary Standard Dosimetry Laboratory in Bogota-Colombia. The radiation beams N-40 ($E_{efective}$ = 33 keV), N-80 ($E_{efective}$ = 65 keV) and N-100 ($E_{efective}$ = 83 keV) were reproduced using an ionization chamber plane parallel with calibration factors NDW for five (5) qualities of X-ray beams with HVL from 0.20 mm of Al to 1.5 mm of Cu. It was set, to the output of the beam of radiation, some leaks added in sheets of Al with thicknesses from 0.1 mm, in order to establish the first Half Value Layer (HVL) and the second Half Value Layer (2 HVL) that guarantees the uniformity of the radiation beam.

In each apron were put in 10 crystals of TLD-100 calibrated in a Harshaw 4500 reader for the gamma energy of Cs-137: 5 dosimeters on the outside of the apron and the other 5 with the same positions but behind the apron in order to evaluate the attenuation of the apron for each energy of x-rays. Previously, the dosimeters were subjected to an erase cycle on the Harshaw device.

The irradiation of the dosimeters was performed by using an arbitrary time of 5 minutes, because the objective of this work is to find relative values of the response of the dosimeters. They were later removed by the dosimeters of the apron and were read into the Harshaw devise along with two dosimeters that recorded the natural background. The same procedure with the other two leaded aprons was carried out. After obtaining the results of dose expressed in units of electrical charge (nC) tabulated the data by making difference between the groups of dosimeters and the conditions of quality of the radiation beam.

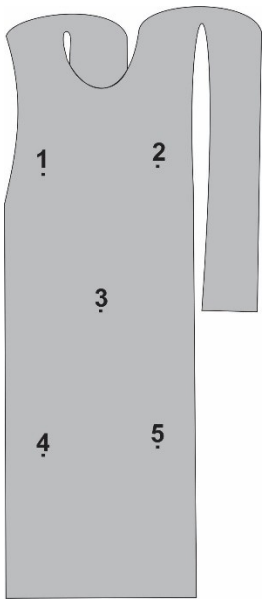

Figure 1. Geometry for the calculation is Monte Carlo with GEANT4 of the aprons, and detectors.

In the theoretical study the geometries of the detectors were constructed, the aprons, and their coating were placed on a phantom tissue ICRU see Figure 1. It simulates the aperture of the radiation beam by a cone located at the distance of irradiation used in the experiemntal measurement.

The focus of the tube where they originate X-rays was simulated as a beam monoenergético based on the effective power of the radiation beam (33 KeV, 65 KeV and 83 KeV).Were simulated $2 \cdot 10^9$ stories in each case using a cluster-parallelized. The code used in the calculation was GEANT4, we calculated the coefficients of linear attenuation of the leaded aprons and compared the simulation results with those obtained experimentally and those reported by the NIST for each of the energy efficient [Hubbell & Seltzer, 1995].

3. RESULTS AND DISCUSSION

According to the Standard ISO 4037 energy effective for each one of the qualities of X-rays used are: N-40 → 33 keV, N-80 → 65 keV y N-100 → 83 keV. These energies were used as a source term in the calculation of a Monte Carlo. To find the linear attenuation coefficient μ, it was calculated according to the equation of damping for a beam collimated:

$$\mu = -\frac{1}{x} ln\left(\frac{I}{I_o}\right) \tag{5}$$

Where I and I_o are the intensities or readings of the dosimeters in front of and behind of the apron, respectively, and the constant x corresponds to the thickness of the apron leaded. To all thicknesses of lead is added to 0.005 cm due to the coating on Mylar that has the apron leaded on both sides.

Apron 1: Table 1 shows the experimental results for the apron 1, has an average thickness of 0.25 mm to 5 dosimeters are located outside of the apron and 5 dosimeters located within the apron. This device is used especially in dental radiology.

Table 1. Data collected by crystals of TLD-100 in 10 points of the apron. The average reading of natural background radiation was 32 nC. Quality N-80 (65 keV), thickness 0.25 mm.

In front the apron I_o (nC)	Behind the apron I (nC)	Relationship (I/I_0)	Attenuation coefficient μ (cm^{-1})
225	51	0.226	59.48
246	57	0.231	58.61
235	54	0.229	58.96
241	55	0.228	59.13
230	60	0.261	53.72

The average value of the attenuation coefficient is 26.973 57.98 cm^{-1}. In the tables of the NIST for material Pb and the energy of photons of 0.083 MeV, the attenuation coefficient

mass total μ/ρ = 5.02 cm^2/g, thus the linear attenuation coefficient μ= 4.8 $cm^2/g \cdot 11.4\ g/cm^3$ = 57.57 cm^{-1}.

Apron 1: In Table 2 we show the experimental results for the apron 2, has an average thickness of 0.25 mm 5 dosimeters are located in front the apron and 5 dosimeters located behind the apron. This device is used especially in conventional radiology.

Table 2. Data collected by crystals of TLD-100 in 10 points of the apron. The average reading of natural background radiation was 32 nC. Quality N-100 (83 keV) thickness 0.25 mm

In front the apron I_o (nC)	Behind the apron I (nC)	Relationship (I/I_0)	Attenuation coefficient μ (cm^{-1})
355	178	0.501	27.613
360	181	0.502	27.504
327	172	0.525	25.698
371	183	0.493	28.268
362	190	0.524	25.784

The average value of the attenuation coefficient is 26.973 cm^{-1}. In the tables of the NIST for material Pb and the energy of photons of 0.083 MeV, the attenuation coefficient mass total μ/ρ = 2.419 cm^2/g,, thus the linear attenuation coefficient μ= 2.419 cm^2/g x 11.4 g/cm^3 = 27.576 cm^{-1}.

Apron 2: In Table 3 we show the experimental results for the apron 2, has an average thickness of 0.55 mm. 5 dosimeters are located in front the apron and 5 dosimeters located behind the apron. This device is used especially in conventional radiology.

The average value of the attenuation coefficient is of 23.995 cm^{-1}. In the tables of the NIST for material Pb and the energy of photons of 0.083 MeV, the attenuation coefficient mass total μ/ρ = 2.419 cm^2/g, thus the linear attenuation coefficient μ= 2.419 $cm^2/g \cdot 11.4\ g/cm^3$ = 27.576 cm^{-1}.

Table 3. Data collected by crystals of TLD-100 in 10 points of the apron. The average reading of natural background radiation was 32 nC. Quality N-100 (83 keV) thickness 0.55 mm

In front the apron I_o (nC)	Behind the apron I (nC)	Relationship (I/I_0)	Attenuation coefficient μ (cm^{-1})
354	94	0.265	24.109
362	94	0.259	24.515
329	96	0.291	22.394
375	97	0.258	24.585
363	95	0.261	24.373

Apron 3: In Table 4 we show the experimental results for the apron 3 has an average thickness of 0.75 mm to 5 dosimeters are located outside of the apron and 5 dosimeters located within the apron. This device is used especially in interventional radiology.

Table 4. Data collected by crystals of TLD-100 in 10 points of the apron. The average reading of natural background radiation was 32 nC. Quality N-100 (83 keV) thickness 0.75 mm

In front the apron I_o (nC)	Behind the apron I (nC)	Relationship (I/I_0)	Attenuation coefficient μ (cm^{-1})
354	48	0.135	26.641
362	50	0.138	26.394
329	background	0.097	31.070
375	45	0.120	28.270
363	40	0.110	29.409

The average value of the attenuation coefficient is 28.356 cm-1. In the tables of the NIST for the material Pb and the energy of photons of 0.083 MeV, the attenuation coefficient mass total μ/ρ = 2.419 cm^2/g, thus the linear attenuation coefficient μ= 2.419 cm^2/g ·11.4 g/cm^3 = 27.576 cm^{-1}.

In the following qualities was not possible to estimate the coefficients of the linear attenuation due to the readings on the dosimeters within the apron are of the order of the

natural background of radiation quality N-40 (33keV) thickness 0.55 mm, quality N-80 (65keV) thickness 0.55 cm, quality N-40 (33keV) thickness 0.75 mm and quality N-80 (65keV) thickness 0.75 mm

Table 5 shows the results obtained by the two methods and are compared with those reported by the NIST.

Tabla 5. Coeficientes de atenuación lineal. Measurement (Meas), NIST, Monte Carlo (MC)

	N-40			N-80			N-100		
Apron	Meas.	NIST	MC	Meas.	NIST	MC	Meas.	NIST	MC
0.25mm	269.15	291.06	268.35	57.980	57.570	56,369	26.973	27.576	27.449
0.55mm	background	291.06	background	background	57.570	45.70	23.995	27.576	21.153
0.75mm	background	291.06	background	background	57.570	45.654	28.356	27.576	22.809

4.- CONCLUSIONES

Effective energies of X rays narrow qualities (ISO-4037) that were reproduced experimentally in the Secondary Standard Dosimetry Laboratory corresponding with very good approach to monoenergetic values reported by the National Institute of Standards and Technology (NIST) based on the intercomparison of coefficients linear attenuation. Similarly, results obtained by simulation Monte Carlo method are generally consistent with the experimental data, except for lead aprons of 0.75mm and 0.5mm and effective energies of 33 keV and 65 keV due to attenuating more than 99% of radiation and are untrusted values of attenuation coefficients. The experiment reproduced in GEANT4 in this work is reliable to evaluate at the future any custom accessory shielding.

Experimental measurements and Monte Carlo calculations showed good agreement, which allows us to conclude that the values reported by the NIST for 0.55 and 0.75 mm for grades N-40 and N-80 requires review, because the Monte Carlo calculations have uncertainties < 1%, which ensures the reliability of the estimates.

REFERENCES

Agostinelli, S., Allison, J., Amako, K. A., Apostolakis, J., Araujo, H., Arce, P., ... & Behner, F. (2003). GEANT4—a simulation toolkit. Nuclear instruments and methods in physics research section A: Accelerators, Spectrometers, Detectors and Associated Equipment, 506(3), 250-303.

Häusler, U., Czarwinski, R., & Brix, G. (2009). Radiation exposure of medical staff from interventional x-ray procedures: a multicentre study. European radiology, 19(8), 2000-2008.

Hubbell, J. H., & Seltzer, S. M. (1995). Tables of X-ray mass attenuation coefficients and mass energy-absorption coefficients 1 keV to 20 MeV for elements Z= 1 to 92 and 48 additional substances of dosimetric interest (No. PB--95-220539/XAB; NISTIR--

5632). National Inst. of Standards and Technology-PL, Gaithersburg, MD (United States). Ionizing Radiation Div.

Kazempour, M., Saeedimoghadam, M., Shooli, F. S., & Shokrpour, N. (2015). Assessment of the Radiation Attenuation Properties of Several Lead Free Composites by Monte Carlo Simulation. Journal of biomedical physics & engineering, 5(2), 67.

Korean Standards Association. (2003). X and gamma reference radiation for calibrating dosemeters and doserate meters and for determining their response as a function of photon energy. Part, 1, 4037-1.

Matyagin, Y. V., & Collins, P. J. (2016). Effectiveness of abdominal shields in chest radiography: a Monte Carlo evaluation. The British Journal of Radiology, 89(1066), 20160465.

Santos, W. S., Neves, L. P., Perini, A. P., Belinato, W., Caldas, L. V., Carvalho, A. B., & Maia, A. F. (2015). Exposures in interventional radiology using Monte Carlo simulation coupled with virtual anthropomorphic phantoms. Physica Medica, 31(8), 929-933.

Schulze, R. K. W., Cremers, C., Karle, H., & de las Heras Gala, H. (2016). Skin entrance dose with and without lead apron in digital panoramic radiography for selected sensitive body regions. Clinical Oral Investigations, 1-7.

Seals, K. F., Lee, E. W., Cagnon, C. H., Al-Hakim, R. A., & Kee, S. T. (2016). Radiation-induced cataractogenesis: a critical literature review for the interventional radiologist. Cardiovascular and interventional radiology, 39(2), 151-160.

Valentin, J. (Ed.). (2007). The 2007 recommendations of the international commission on radiological protection (pp. 1-333). Oxford, UK: Elsevier.

Zehtabian, M., Piruzan, E., Molaiemanesh, Z., & Sina, S. (2015). Design of Light Multi-layered Shields for Use in Diagnostic Radiology and Nuclear Medicine via MCNP5 Monte Carlo Code. Iranian Journal of Medical Physics, 12(3), 223-228.

Estudio de radiosensibilidad en la germinación y crecimiento de la arveja *Pisum sativum L*, con semillas expuestas a radiación gamma

Janeth Ilguan[1], Victor Márquez[2], Javier Carrasco[1*],

[1] Facultad de Ciencias, Carrera de Biofísica, Escuela Superior Politécnica de Chimborazo, Riobamba, Ecuador, ilguanjanneth@gmail.com

[2] Facultad de Ciencias, Escuela de Física y Matemática, Escuela Superior Politécnica de Chimborazo, Riobamba, Ecuador, victore.marquezp@gmail.com

[1*] Facultad de Ciencias, Carrera de Biofísica, Escuela Superior Politécnica de Chimborazo, Riobamba, Ecuador, wcarrasco@espoch.edu.ec

Abstract

Se irradiaron semillas de *Pisum sativum L*, en un irradiador de ^{60}Co perteneciente a la Subsecretaria de Control y Aplicaciones Nucleares del Ecuador SCAN, la tasa de dosis al momento de la irradiación fue de 4.86 Gy/min. Las semillas fueron agrupadas en paquetes de 100 unidades y expuestas a dosis de 20, 40, 60, 80, 100, 120, 140, 160, 180 y 200 Gy. Se evaluó el número de germinaciones efectivas, los días para la germinación, el grosor del tallo principal, el número de ramificaciones y el tamaño de la planta. Para validar la experimentación se analizaron los datos estadísticamente por medio de pruebas de homogeneidad de varianzas, anova de un factor y análisis Scheffé a cada variable. El número de germinaciones efectivas se dio al 100% para 20 y 40 Gy luego decrece a mayor dosis llegando al 20 % a 200 Gy, siendo la media del testigo cercano al 90 %. Se evidenció una mayor estimulación en la germinación en el tratamiento a 20 Gy con una media de 5,0 días. Los tratamientos a dosis de 20, 40 y 60 Gy presentan un tamaño de planta mayor al testigo cuya media es de 68,30 cm. El número medio de ramificaciones del testigo es de 5.3 con una desviación típica de 0,675, resulta ser mayor en las dosis de 20 Gy y 40 Gy. En el estudio se concluye que se presentan mejores resultados al irradiar semillas *Pisum sativum L*, entre 20 y 60 Gy.

Keywords: Radón; Dosis radiactiva ambiental; Radiación natural.

1.- INTRODUCCIÓN

Las arvejas han crecido como una importante fuente de alimentación animal y humana por muchos siglos. Existen miles de variedades en todo el mundo. Se pueden clasificar en las siguientes categorías: de campo, que proporcionan forraje para alimentación animal, de mercado para el consumo humano en fresco, vining para el enlatado o congelación y secas en parte para el consumo humano, pero sobre todo para la alimentación animal (Cousin, 1997).

Actualmente se cultiva en las regiones templadas, en altas elevaciones, o durante las estaciones frías en las regiones cálidas de todo el mundo (Elzebroek & Wind, 2008). Los principales productores son China, India, Canadá, Rusia, Francia y los Estados Unidos (U.S. Department of Agriculture, 2012).

Los primeros experimentos con semillas expuestas a dosis relativamente bajas de radiación ionizante para estimular el crecimiento y el desarrollo se realizaron unos pocos años después del descubrimiento de los rayos X por Roentgen en 1895 (Zaka, Chenal, & Misset, 2004).

Existen varios informes sobre los efectos estimulantes que afectan el crecimiento de la planta cuando se hace uso de técnicas de irradiación con rayos radioactivos a bajas dosis como los realizados por Alarkon et al en 1987, Raghuvanshi en 1992, Charbaji y Nabulsi en 1999, Moussa 2006, Melki and Sallami en 2008 (Melki & Marouani, 2009). Tales exposiciones principalmente estimulan la germinación de las semillas, el crecimiento de plántulas, la floración, el tamaño de la planta y el rendimiento (Breslavets, 1946).

En Ecuador, existen dos irradiadores gamma de ^{60}Co, pertenecientes a la Escuela Politécnica Nacional EPN y a la Subsecretaria de Control y Aplicaciones Nucleares SCAN, estos han permitido desarrollar algunas investigaciones sobre la irradiación de muestras vegetales aplicados a la agricultura y a la agroindustria. Para esta investigación se utilizó semillas de arveja *Pisum sativum L*., variedad Esmeralda, que se caracterizan por tener una

flor blanca, y grano verde claro. El rendimiento en grano seco es de 1,640 kilos por hectárea y en grano tierno 2,436 kg (Instituto Nacional de Investigaciones Agropecuarias, 1997). En Ecuador desde hace muchos años, la arveja Esmeralda es utilizada en múltiples formas y fines como en vaina, grano tierno, enlatados, congelados y del grano seco entero o partido se hace harina, también se utiliza como abono verde.

2.- MATERIALES Y MÉTODOS

Para la experimentación se utilizaron semillas de arveja *Pisum sativum L.*, variedad Esmeralda INIAP 434. Las semillas fueron envasadas herméticamente en 11 paquetes con un contenido de 100 unidades cada uno. Las muestras a irradiar fueron trasportadas hacia la SCAN, el día 1 de febrero del 2016, la irradiación se realizó al día siguiente, utilizando un irradiador de ^{60}Co. Cada paquete fue irradiado respectivamente a 20, 40, 60, 80, 100, 120, 140, 160, 180, y 200 Gy. Durante todo el proceso se acompañó de una muestra de control, la cual no fue irradiada. La **Tabla 1.** muestra las características generales del irradiador gamma, con estos datos se determinó la dosis actual a la fecha de irradiación y el tiempo de irradiación para cada dosis requerida.

Tabla 6.- Características generales del Irradiador gamma de ^{60}Co JLSHEPARD MODEL

Actividad Inicial Ao	11500	Ci	Fecha A_o	1988-06-10
Tasa de Dosis $D_o(t)$	14,42	Gy/min	Fecha $D_o(t)$	2007-10-24
Semiperiodo $t_{1/2}$	5,2712	Años	Energía	1,17 MeV y 1,33 MeV

Fuente: Manual de Operación y en Caso de Emergencia del LSCD (Subsecretaría de Control y Aplicaciones Nucleares, 2014)

Las semillas fueron sembradas 5 días luego de la irradiación en la comunidad de San José de Sablog del cantón Guamote, provincia de Chimborazo en Ecuador. Se encuentra a una altitud de 3 050 m.s.n.m., posee una temperatura media anual de 12 °C, humedad relativa del 96,8%, nubosidad de 3,1 horas/día y precipitaciones promedio anuales de 681,3 mm. De octubre a mayo predomina el clima propio de invierno húmedo y frío y de junio a septiembre predomina el verano cálido, seco y ventoso.

Se realizó la preparación de terreno con anterioridad al día de sembrado, dejando el terreno mullido, desterronado y nivelado para asegurar la germinación de las semillas. Se formaron 11 parcelas separadas a 50 cm. La germinación empieza generalmente al final de la primera semana apareciendo el hipocótilo y la radícula, por lo que se revisó diariamente para datar el Número de Germinaciones Efectivas NGE y los Días para la Germinación

DG. En las plantas adultas se registró el Grosor del Tallo Principal GTP, el Número de Ramificaciones NR y el Tamaño de la Planta TP.

3.- RESULTADOS

La **Tabla 2.** muestra el número de germinaciones efectivas NGE, para cada tratamiento, se ha denominado T-00 a la muestra de control, que no ha sido irradiada pero que ha soportado todas las condiciones físicas en el transporte para la irradiación de las demás muestras.

Tabla 7.- Numero de germinaciones efectivas NGE

TRATAMIENTO	Dosis (Gy)	NGE
T-01	20	100
T-02	40	100
T-03	60	92
T-04	80	81
T-05	100	66
T-06	120	47
T-07	140	35
T-08	160	32
T-09	180	26
T-10	200	20
T-00	0	87

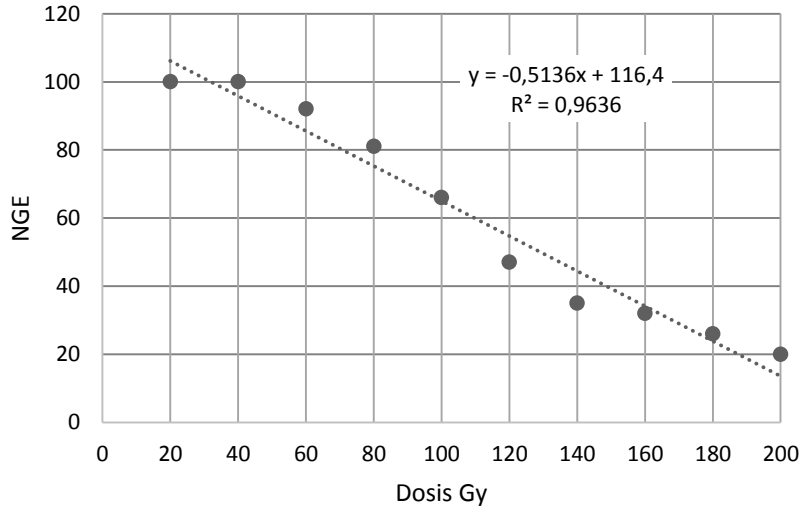

Figura 1. Número de germinaciones

Con los datos de NGE, obtenemos la Dosis Letal 50 DL_{50}, que representa la dosis a la cual el 50 % de las semillas no germinaron, para este caso obtenemos 129 Gy.

Variable: Días para la Germinación DG

No todas las semillas germinaron al mismo tiempo, **la Tabla 4**. muestra el tiempo promedio de los DG para cada tratamiento. Al igual que en todas las variables se realiza un análisis estadístico para confirmar si existe correlación entre la dosis aplicada y la variable estudiada.

Tabla 8.- Resumen del procesamiento de los casos

	Casos					
	Incluidos		Excluidos		Total	
	N	Porcentaje	N	Porcentaje	N	Porcentaje
DG * TRATAMIENTOS	110	100,0%	0	,0%	110	100,0%

Tabla 9.- Informe Estadístico

Días para la Germinación DG			
TRATAMIENTOS	Media	N	Desv. típ.
T-01	5,00	10	,667
T-02	5,60	10	,699
T-03	5,70	10	,675
T-04	5,60	10	,699
T-05	6,10	10	,738
T-06	5,80	10	,789
T-07	6,40	10	,699
T-08	6,70	10	,823
T-09	6,80	10	,789
T-10	6,70	10	,675
T-00	6,10	10	,876
Total	6,05	110	,892

Tabla 10.- Prueba de homogeneidad de varianzas

DG			
Estadístico de Levene	gl1	gl2	Sig.
,502	10	99	,885

Tabla 11.- Anova de un Factor

ANOVA DG					
	Suma de cuadrados	Gl	Media cuadrática	F	Sig.
Inter-grupos	32,273	10	3,227	5,862	,000
Intra-grupos	54,500	99	,551		
Total	86,773	109			

Tabla 12.- Análisis Scheffé[a] de la variable DG

Scheffé[a] DG				
TRATAMIENTOS		N	Subconjunto para alfa = 0.05	
			1	2
	T-01	10	5,00	
	T-02	10	5,60	5,60
	T-04	10	5,60	5,60
	T-03	10	5,70	5,70
	T-06	10	5,80	5,80
	T-05	10	6,10	6,10
	T-11	10	6,10	6,10
	T-07	10	6,40	6,40
	T-08	10		6,70
	T-10	10		6,70
	T-09	10		6,80
	Sig.		,074	,237
Se muestran las medias para los grupos en los subconjuntos homogéneos.				
a. Usa el tamaño muestral de la media armónica = 10,000.				

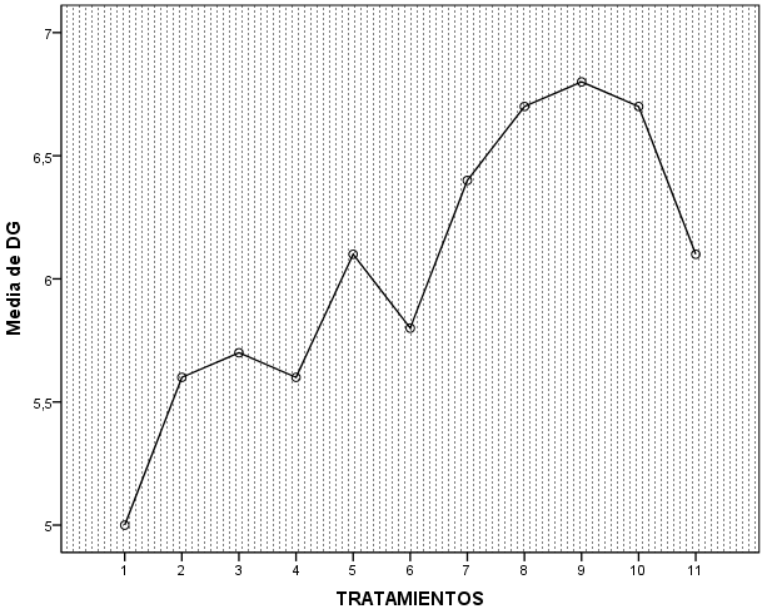

Figura 2. Días Para la Germinación

En el **Figura 2.**, se aprecia que la dosis radiactiva afecta el tiempo germinación de manera creciente. A dosis bajas la semilla, empieza a germinar desde los 4 días en adelante, mientras que a dosis altas la semilla germina en un tiempo de 6 hasta 7 días. La muestra de control germina en promedio a los 6 días.

Variable: Grosor del tallo principal GTP

Tabla 13. Informe Estadístico de la variable GTP

Descriptivos						
GTP (mm)						
T	N	Media	Desviación típica	Error típico	Intervalo de confianza para la media al 95%	
					Límite inferior	Límite superior
T-01	10	17,80	,919	,291	17,14	18,46
T-02	10	17,10	,738	,233	16,57	17,63
T-03	10	15,00	,816	,258	14,42	15,58
T-04	10	13,40	,516	,163	13,03	13,77
T-05	10	13,10	,876	,277	12,47	13,73
T-06	10	13,10	,738	,233	12,57	13,63
T-07	10	13,10	,568	,180	12,69	13,51
T-08	10	12,90	,738	,233	12,37	13,43
T-09	10	12,70	,675	,213	12,22	13,18
T-10	10	11,90	1,101	,348	11,11	12,69
T-11	10	14,50	,527	,167	14,12	14,88
Total	110	14,05	1,943	,185	13,69	14,42

Tabla 14. Prueba de homogeneidad de varianzas

GTP (mm)			
Estadístico de Levene	gl1	gl2	Sig.
1,518	10	99	,144

Tabla 15. Anova de un Factor

ANOVA GTP (mm)					
	Suma de cuadrados	Gl	Media cuadrática	F	Sig.
Inter-grupos	353,673	10	35,367	60,368	,000
Intra-grupos	58,000	99	,586		
Total	411,673	109			

Tabla 16. Análisis Scheffé de la variable GTP

Scheffé[a] G T P (mm)						
TRATAMIENTOS		N	Subconjunto para alfa = 0.05			
			1	2	3	4
	T-10	10	11,90			
	T-09	10	12,70			
	T-08	10	12,90			
	T-05	10	13,10	13,10		
	T-06	10	13,10	13,10		
	T-07	10	13,10	13,10		
	T-04	10	13,40	13,40		
	T-11	10		14,50	14,50	
	T-03	10			15,00	
	T-02	10				17,10
	T-01	10				17,80
	Sig.		,051	,098	,995	,935
Se muestran las medias para los grupos en los subconjuntos homogéneos.						
a. Usa el tamaño muestral de la media armónica = 10,000.						

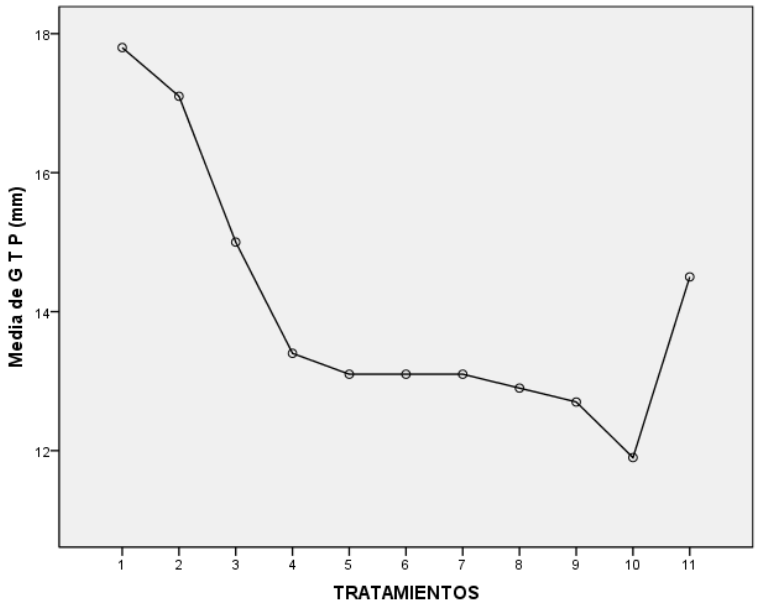

Figura 3. Grosor del tallo principal

De acuerdo a los datos obtenidos durante el trabajo experimental, en la **Figura 3.** se puede verificar la diferencia de GTP de la planta de arveja. A dosis altas el tallo de la arveja fue delgado y débil en comparación a las dosis bajas donde el tallo es más grueso. En la muestra de control GTP, es solo menor que los tratamientos T-01, T-02 y T-03.

Variable: Tamaño de la planta TP

Tabla 17. Informe estadístico de la variable TP

Descriptivos						
TP (cm)						
T	N	Media	Desviación típica	Error típico	Intervalo de confianza para la media al 95%	
					Límite inferior	Límite superior
T-01	10	112,40	2,271	,718	110,78	114,02
T-02	10	99,80	1,989	,629	98,38	101,22
T-03	10	80,00	4,082	1,291	77,08	82,92
T-04	10	68,50	3,375	1,067	66,09	70,91
T-05	10	58,10	2,283	,722	56,47	59,73
T-06	10	50,60	2,459	,777	48,84	52,36
T-07	10	48,00	2,582	,816	46,15	49,85
T-08	10	41,90	2,470	,781	40,13	43,67
T-09	10	34,50	,850	,269	33,89	35,11
T-10	10	30,30	1,567	,496	29,18	31,42
T-11	10	68,30	4,715	1,491	64,93	71,67

Descriptivos						
TP (cm)						
T	N	Media	Desviación típica	Error típico	Intervalo de confianza para la media al 95%	
					Límite inferior	Límite superior
T-01	10	112,40	2,271	,718	110,78	114,02
T-02	10	99,80	1,989	,629	98,38	101,22
T-03	10	80,00	4,082	1,291	77,08	82,92
T-04	10	68,50	3,375	1,067	66,09	70,91
T-05	10	58,10	2,283	,722	56,47	59,73
T-06	10	50,60	2,459	,777	48,84	52,36
T-07	10	48,00	2,582	,816	46,15	49,85
T-08	10	41,90	2,470	,781	40,13	43,67
T-09	10	34,50	,850	,269	33,89	35,11
T-10	10	30,30	1,567	,496	29,18	31,42
T-11	10	68,30	4,715	1,491	64,93	71,67
Total	110	62,95	25,250	2,407	58,17	67,72

Tabla 18. Prueba de homogeneidad de varianzas

TP (cm)			
Estadístico de Levene	gl1	gl2	Sig.
4,463	10	99	,000

Tabla 19. Anova de un factor

ANOVA TP (cm)					
	Suma de cuadrados	gl	Media cuadrática	F	Sig.
Inter-grupos	68714,273	10	6871,427	872,814	,000
Intra-grupos	779,400	99	7,873		
Total	69493,673	109			

Tabla 20. Análisis Scheffé[a] de la variable TP

Scheffé[a] TP (cm)										
TRATAMIENTOS		N	Subconjunto para alfa = 0.05							
			1	2	3	4	5	6	7	8
	T-10	10	30,30							
	T-09	10	34,50							
	T-08	10		41,90						
	T-07	10			48,00					
	T-06	10			50,60					
	T-05	10				58,10				
	T-11	10					68,30			
	T-04	10					68,50			
	T-03	10						80,00		
	T-02	10							99,80	
	T-01	10								112,40
	Sig.		,355	1,000	,929	1,000	1,000	1,000	1,000	1,000
Se muestran las medias para los grupos en los subconjuntos homogéneos.										
a. Usa el tamaño muestral de la media armónica = 10,000.										

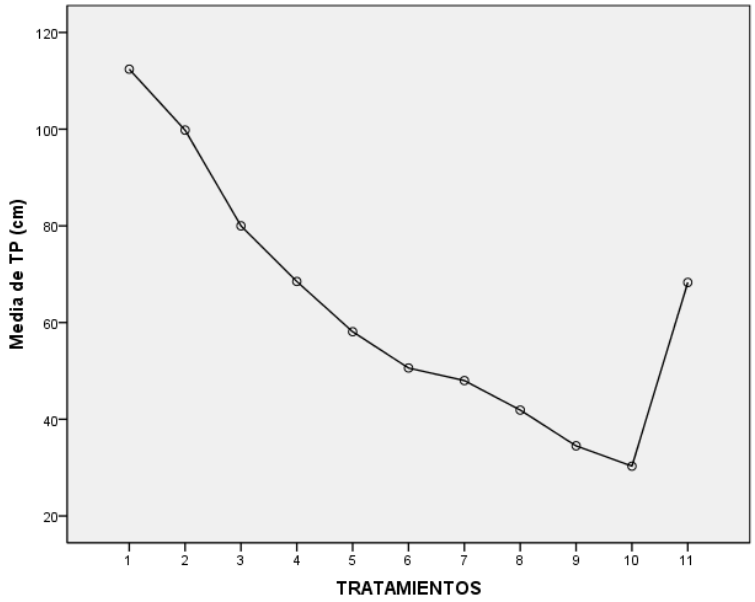

Figura 4. Tamaño de la planta

En la **Figura 4.** podemos observar que el tamaño de la planta decrece si la dosis aumenta casi de manera lineal. La muestra de control tiene una altura promedio de 68,30 cm

Variable: Número de ramificaciones NR

Tabla 21. Informe Estadístico de la variable NR

Descriptivos						
NR						
T	N	Media	Desviación típica	Error típico	Intervalo de confianza para la media al 95%	
					Límite inferior	Límite superior
T-01	10	7,30	,823	,260	6,71	7,89
T-02	10	5,80	,789	,249	5,24	6,36
T-03	10	5,00	,816	,258	4,42	5,58
T-04	10	4,60	,699	,221	4,10	5,10
T-05	10	4,60	,516	,163	4,23	4,97
T-06	10	4,50	,527	,167	4,12	4,88
T-07	10	4,20	,632	,200	3,75	4,65
T-08	10	3,70	,675	,213	3,22	4,18
T-09	10	3,20	,789	,249	2,64	3,76
T-10	10	3,10	,876	,277	2,47	3,73
T-11	10	5,30	,675	,213	4,82	5,78
Total	110	4,66	1,343	,128	4,41	4,92

Tabla 22. Prueba de homogeneidad de varianzas

NR			
Estadístico de Levene	gl1	gl2	Sig.
,543	10	99	,855

Tabla 23. Anova de un factor

ANOVA NR					
	Suma de cuadrados	Gl	Media cuadrática	F	Sig.
Inter-grupos	145,255	10	14,525	28,032	,000
Intra-grupos	51,300	99	,518		
Total	196,555	109			

Tabla 24. Análisis Scheffé[a] de la variable NR

Scheffé[a] NR								
TRATAMIENTOS		N	Subconjunto para alfa = 0.05					
			1	2	3	4	5	6
	10	10	3,10					
	9	10	3,20	3,20				
	8	10	3,70	3,70	3,70			
	7	10	4,20	4,20	4,20	4,20		
	6	10	4,50	4,50	4,50	4,50	4,50	
	4	10		4,60	4,60	4,60	4,60	
	5	10		4,60	4,60	4,60	4,60	
	3	10			5,00	5,00	5,00	
	11	10				5,30	5,30	
	2	10					5,80	
	1	10						7,30
	Sig.		,055	,055	,109	,322	,109	1,000
Se muestran las medias para los grupos en los subconjuntos homogéneos.								
a. Usa el tamaño muestral de la media armónica = 10,000.								

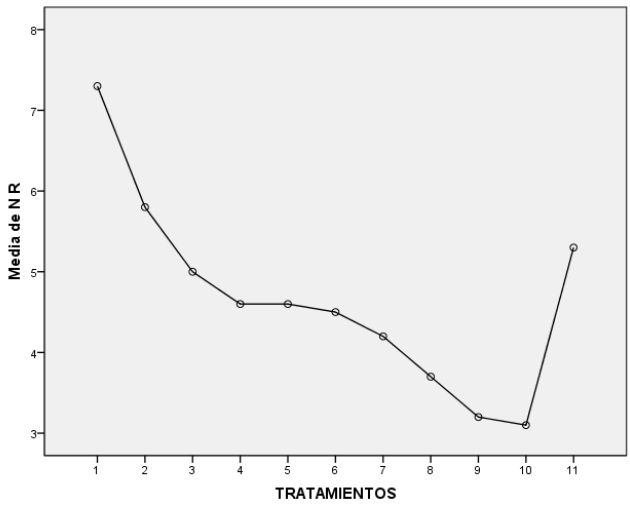

Figura 5. Numero de ramificaciones

El número de ramificaciones también es dependiente de la dosis con la que fueron irradiadas cada muestra, a dosis de 20 Gy, 40 Gy y 60 Gy la planta es más grande, por ende, tendrá más ramificaciones. Es así que el número de ramas va disminuyendo a mayor dosis.

4.- DISCUSIÓN

El número de germinaciones efectivas se dio al 100% para 20 Gy y 40 Gy luego decrece progresivamente hasta llegar a 20 % a una dosis de 200 Gy. El número de germinaciones promedio de la muestra de control es cercana al 90 %, existiendo una clara estimulación a las dosis mencionadas, las cuales además germinaron más pronto. La DL_{50} se encuentra a los 129 Gy, es decir a esta dosis la mitad de la población de semillas no germinará, inhibiéndose el proceso debido a los efectos de la radiación ionizante.

La media del tiempo de germinación de la muestra de control es de 6,10 días con una desviación típica de 0,876. Se evidencia mayor estimulación en la germinación en el tratamiento a 20 Gy con una media de 5,0 días, aumentando el tiempo de germinación de manera progresiva hasta los 180 Gy con una media 6,80 días, luego de esto se presenta una aparente disminución en el tiempo. T-05 a 100 Gy presenta iguales características que la muestra de control para esta variable.

Los tratamientos a dosis de 20 Gy, 40 Gy y 60 Gy presentan un tamaño de planta mayor a la muestra de control cuya media es de 68,30 cm con una desviación típica de 4,715 cm, para todos los demás tratamientos se presenta tamaños por debajo de la media de la muestra de control, el mayor tamaño fue de 112,40 cm a 20 Gy y el menor tamaño 30,30 cm a 200 Gy.

El número de ramificaciones de la muestra no irradiada es de 5.3 con una desviación típica de 0,675, resulta ser mayor en las dosis de 20 Gy y 40 Gy, luego de esto son inferiores, teniendo un promedio de 7.3 ramificaciones a 20 Gy y 3.10 ramificaciones a 200 Gy. Para el grosor del tallo principal se tiene un máximo de 17.80 mm a 20 Gy y un mínimo de 11,90 a 200 Gy, la media del testigo es de 14,50 mm resultando ser de mayor grosor las plantas expuestas a 20 Gy, 40 Gy y 60 Gy.

5.- CONCLUSIONES

La tasa de dosis radiactiva impartida a las semillas de arveja *Pisum Sativum L*. variedad Esmeralda, altera las características físicas y morfológicas tanto en la germinación de la semilla como en el crecimiento de la planta. Para las variables: número de germinaciones efectivas, días para la germinación, grosor del tallo principal, número de ramificaciones y tamaño de la planta se presentan mejores resultados al exponer las semillas entre los 20 y 60 Gy de radiación ionizante gamma.

REFERENCIAS

Breslavets, L. (1946). Plants and X-rays. *Acad Sci USSR Press*.

Cousin. (1997). Peas (Pisum sativum L.). *Field Crops Research*, 111-130.

Elzebroek, T., & Wind, K. (2008). *Guide to cultivated plants.* Oxfordshire, UK: CAB International.

Instituto Nacional de Investigaciones Agropecuarias. (1997). *Variedades de arveja.* Quito: INIAP.

Melki, M., & Marouani, A. (2009). Effects of gamma rays irradiation on seed germination and growth of hard wheat. *Environ Chem Lett*.

Subsecretaría de Control y Aplicaciones Nucleares. (2014). *Manual de operación y en caso de emergencias del LSCD.* Quito: SCAN.

U.S. Department of Agriculture. (2012). *Plant Guide Pea.* USDA.

Zaka, R., Chenal, C., & Misset, M. (2004). Effects of low doses of short-term gamma irradiation on growthand development through two generations of Pisum sativum. *Science of the Total Environment 320*, 121–129.

On the thermoluminescent Interactive Multiple-Trap System (IMTS) model: Is it a simple model?

M.I. Gil-Tolano[1,2], E. Cruz-Zaragoza[2,*], C. Furetta[2], L. Pérez Cruz[1,2], J. Roman-Lopez[3]

[1]Posgrado en Ciencias Químicas, Facultad de Química, Universidad Nacional Autónoma de México, Av. Universidad 3000, 04510 Ciudad de México, México

[2]Instituto de Ciencias Nucleares, Universidad Nacional Autónoma de México, A.P. 70-543, 04510 Ciudad de México, México
[*]Email: ecruz@nucleares.unam.mx

[3]CONACYT-Instituto de Ciencias Nucleares, Universidad Nacional Autónoma de México, A.P. 70-543, 04510 Ciudad de México, México

Abstract

In the thermally stimulated luminescence phenomenon, named thermoluminescence (TL), the electrons and holes generated by the radiation-matter interaction can be trapped by the metastable levels in the band gap of the solid. Following, the electron can be thermally releases into the conduction band and a radiatively recombination with hole close to the recombination center occurred and the glow curve is emitted. However, the complex mechanism of trapping and thermally releases occurred in the band gap of solid. Some models, such as; first, second, and general-order kinetics, have been well established to explain the behavior of the glow curves and their defects recombination mechanism. In this work, expressions for an Interactive Multiple-Trap System model (IMTS) was obtained assuming: a set of discrete electron traps (active traps AT), another set of thermally disconnected trap (TDT) and a recombination center (RC) too. A numerical analysis based on the Levenberg-Marquardt (LM) method in conjunction with an implicit Rosenbrock method was taken into account to simulate the glow curve. The numerical method was tested through synthetic TL glow curves for a wide range of trap parameters. The activation energy and kinetics order were determined using values from the General Order Kinetics (GOK) model as entry data to IMTS model. This model was tested using the experimental glow curves obtained from Ce or Eu –doped MgF_2(LiF) polycrystals samples. Results shown that the IMTS model can predict more accurately the behavior of the TL glow curves than those obtained by the GOK modified by Rasheedy and by the Mixed Order Kinetics model.

Keywords*:* thermoluminescence; multiple-trap model; GOK model; dosimeters; alkaline fluorides.

1.-INTRODUCTION

Thermoluminescence (TL) is a phenomenon exhibited by solids such as single crystals, polycrystalline materials, some amorphous and inorganic materials, that have been previously irradiated. The material with acceptable TL properties is named thermoluminescent dosimeter. Those materials which are based on alkali fluorides and on alkaline-earth fluorides, in particular, doped with rare earth ions are extensively used for dosimetry of ionizing radiation [Attix 1986; McKeever *et al*., 1995]. Several models and mathematical methods have been applied to obtain the trap parameters of an isolated TL glow peak [Furetta 2003; Yazici and Topaksu, 2003; Ogundare *et al.*, 2004; Rasheedy 2005; Favalli *et al*., 2006a; González *et al.*, 2006; Gómez-Ros *et al.*, 2006, Marcazzó *et al*., 2014]. Because the traps are generated by the presence of impurities or point defects such as vacancies or interstitials ions in the crystal, it is necessary find the energy level values that depend also on the kinds of impurities ions into the lattice material and their thermal treatment in order to develop an efficient dosimetric phosphor. However, mostly of the dosimetric phosphors shown their TL glow curves, acquired with a linear heating rate profile, shaped by several overlapping peaks. Very few methods exist for deconvolution of complex glow curves into their individual components; they are used to obtain information about the kinetics parameters for dosimetric purposes [Gómez-Ros *et al*., 2006; Kitis *et al*., 2006; Favalli *et al*., 2006b; Chen and Pagonis, 2011]. A widely accepted model for the deconvolution of TL glow curves is based on the one trap one-recombination center (OTOR) model [Chen and Pagonis, 2011]. In the OTOR model, each peak in the glow curve is a result of the flow of charge from the trap to the recombination center (RC) through the conduction band. In reality, once the trapped electrons were released into the conduction band due to thermal stimulation, they may be re-trapped by other traps. However, this model does not reflect the physical reality, because it excluded the interaction possibility of the electrons moving between traps through the conduction band or the valence band [Sakurai 2001]. In this work, the TL glow curves of MgF_2(LiF) polycrystals samples doped with Ce or Eu have been fitted by the proposed IMTS model using a numerical analysis based on the Levenberg-Marquardt (LM) with an implicit Rosenbrock methods. The use of a simplified model, that consider the traffic of electrons and holes, for deconvolution permit the optimization of computational procedure to obtain good results [Kadari *et al*., 2015; Marcazzó *et al.*, 2008; Chung *et al.,* 2012; Chung *et al.,* 2015; Sadek *et al.,* 2014]. This novel procedure for glow curves fitting takes into account the interaction among traps and the quasiequilibrium approximation (QE). The fit procedure can be employed for models having deep traps and several traps, the only restriction being that there is only one recombination center.

2.-RESULT

2.1.- Modelling of TL process

The model assumed in this paper is showing in Figure 1 and it is rather similar to several models given in the literature [Pagonis *et al*., 2006]. The model is based in a set of discrete electron traps (active traps AT), a set of thermally disconnected trap (TDT) and a recombination center (RC). For easy reference, Fig.1 shows in schematic form the levels transitions involved in the model.

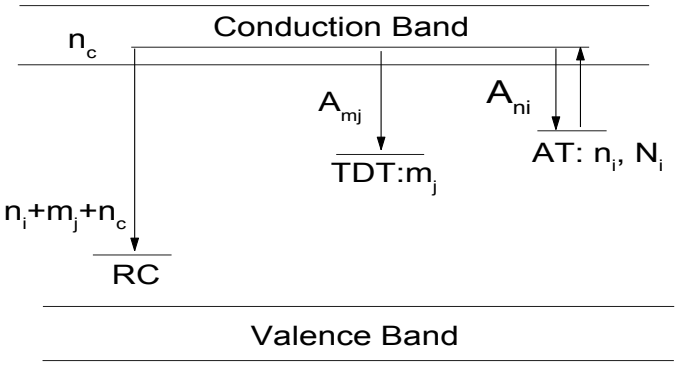

Figure 1: Scheme of the model considered in this work [Pagonis *et al*., 2006].

The starting point for understanding a TL glow curve comprising of several peaks could be to introduce a model involving different types of traps and recombination centers wherein the transitions are via the delocalized conduction band. The corresponding rate equations describing the traffic of electrons during excitation stage are as follows:

For $(i = 1, .., u)$

$$\frac{dn_i}{dt} = n_c(N_i - n_i)A_{ni} - n_i s_i \exp\left(\frac{-E_i}{kT}\right) \quad (1)$$

For $(j = 1, \dots, v)$

$$\frac{dmj}{dt} = -A_{mj} m_j n_c \quad (2)$$

The time rate of change of the free electron concentrations may be written as:

$$\frac{dn_c}{dt} = \sum_{i=1}^{u} n_i s_i exp\left(\frac{-E}{kT}\right) - n_c\left(\sum_{j=1}^{v} m_j A_{mj} + \sum_{i=1}^{u}(N_i - n_i)A_{ni}\right) \qquad (3)$$

The TL intensity I is given by the following expression who retained the quasiequilibrium approximation (QE), which means assuming $n_c \ll (n_i + m_j)$ and $\left|\frac{dn_c}{dt}\right| \ll \left|\frac{dn_i}{dt} + \frac{dm_j}{dt}\right|$, [Chen and McKeever, 1997]:

$$I = \sum_{j=1}^{v}\left(\sum_{i=1}^{u} n_i s_i exp\left(\frac{-E_i}{kT}\right)\left(\frac{m_j A_{mj}}{\sum_{j=1}^{v} m_j A_{mj} + \sum_{i=1}^{u}(N_i - n_i)A_{ni}}\right)\right) \qquad (4)$$

This is the analytic form of the TL equation for IMTS model. In the equation (4) assumed that all electron-hole recombination processes are radiative and contribute to the TL signal. Where; n_i represents the concentration of trapped electrons, N_i denotes the corresponding concentration of traps, s_i is the corresponding frequency factor, E_i represents the activation energy of the traps, k is the Boltzmann constant, m_j is the concentration of filled TDT traps in the crystal, $n_c$are the concentration of electrons in the conduction bands, A_{ni} are the probability coefficient of electron retrapping probabilities in the AT traps, A_{mj} is the probability coefficient of electron retrapping in the TDT traps, and T is the temperature in Kelvin. Eq. (4) depends, besides the temperature T, on the following parameters characterizing the physical system, namely: $N_i, n_{i0}, m_{j0}, s_i, E_i, A_{ni}$ andA_{mj}.

In this work, Eq. (4) will be used as the theoretical expression to fit the glow curve by the Levenberg–Marquardt (LM) method, which is frequently used [Dahoe *et al*., 2013; *Press et al*., 1992]. At each iteration of LM algorithm Eqs. (1) - (3) are solved by means of the fourth-order Rosenbrock method in order to obtain $n_i(t), m_j(t)$ and $n_c(t)$. This model, consisting of several active traps, thermally disconnected traps and one recombination center, will be termed as one recombination center-interactive model. The goodness of the fit was evaluated by means of the figure of merit (FOM) given by:

$$FOM = \frac{\sum_{l=1}^{w}\left|I_{fit}(t_l) - I_{exp}(t_l)\right|}{\sum_{l=1}^{w}\left|I_{exp}(t_l)\right|} * 100\% \qquad (5)$$

A set of parameters is acceptable if the FOM is less than 5% [Horowitz and Yossian, 1995].

The Rosenbrock-LM algorithm was programed in Matlab R2013a [Dahoe *et al*., 2013]. In this program, a new method based on the ITMS model using the condition of QE in deriving the solutions was implemented to analyze the TL curves. The program could also use the traditional OTOR models. It can be applied to any TL material for exposures to

different doses and readout profiles. In the case of the OTOR model, an individual peak in the glow curve corresponds to a set of a trap and an RC defined by the corresponding set of parameter. As in the IMTS model the individual traps could interact with each other and thus IMTS is completely different from the OTOR model [Chung *et al*., 2012]. In the IMTS, if one parameter value is changed belonging to a trap or RC, the whole glow curve would be affected. Thus, it is very difficult to introduce intuitively either traps or RCs from the TL glow curve. In addition, there is an ambiguity regarding the numbers of the RCs to be introduced. For instance, a glow curve that exhibit two peaks could be analyzed by a model with two traps and one RC or with one trap and two RCs [Chung *et al*., 2011]. In order to overcome these difficulties in the IMTS modeling, the OTOR model could be introduced in an initial stage of the deconvolution of the glow curves. An important point is that always start the simulations with empty traps and centers. The simulation starts by assuming some initial guess values for the parameters A_{ni} and A_{mj}, which cannot be extracted directly from the experimental TL curve. These guess values were set manually in such a way that the computerized glow curve nearly matched to the experimental one as much as possible. The usefulness of this method had been verified in the numerical analysis for the synthetics glow curves with diversified physical properties.

2.2.-Deconvolution

In Fig. 2 is shown the glow curves of MgF_2(LiF), doped with Ce (2 mol%) and Eu (0.4 mol%), with a sintering process at 1353 K during 30 min and 4hr, respectively. It seems, there are at least five peaks around 400, (442-446), 504, 544 and (596-612) K, respectively. The samples were exposed at 10 Gy gamma dose in a ^{60}Co Gammacell-200 irradiator. The glow curves were recorded in N_2 atmosphere with a constant heating rate of 2 K s^{-1} in a Harshaw model 3500 TL reader. The structure of the experimental glow curves was analyzed using the T_{max}-T_{stop} method [McKeever 1980].

The maximum temperature (T_{max}) along of the glow curves from MgF_2(LiF):Ce and MgF_2(LiF):Eu, was monitored by using T_{stop} temperatures from 80 up to 320°C with steps of 5°C. The behavior of the T_{max}-T_{stop} relation (Fig. 3) for both samples, shows four steps well- defined and confirming that the structure of the glow curves is composed by four peaks. A slight shifted occurs between both T_{max}-T_{stop} curves due to their T_{max} are located at different temperatures in the glow curves as can be seen in Fig. 2.

For the analysis of the main peak, the LM method was employed to fit the experimental data from Eq. (4), it is shown in Fig. 2. In the assumed model for the deconvolution of the glow curves, six traps were considered, one recombination center and one thermally disconnected trap (Fig. 1). In the LM method an initial set of values for the varying parameters, usually termed guess values, must be provided. In order to evaluated and

understand the nature of the traps formed in $MgF_2(LiF)$:Ce or Eu under irradiation, the expressions for general order kinetics (GOK) modified by Rasheedy [Rasheedy, 1993], and the mixed order kinetics (MO) [Kitis and Gomez-Ros, 2000] were used to fit the TL experimental data (Fig.2). The

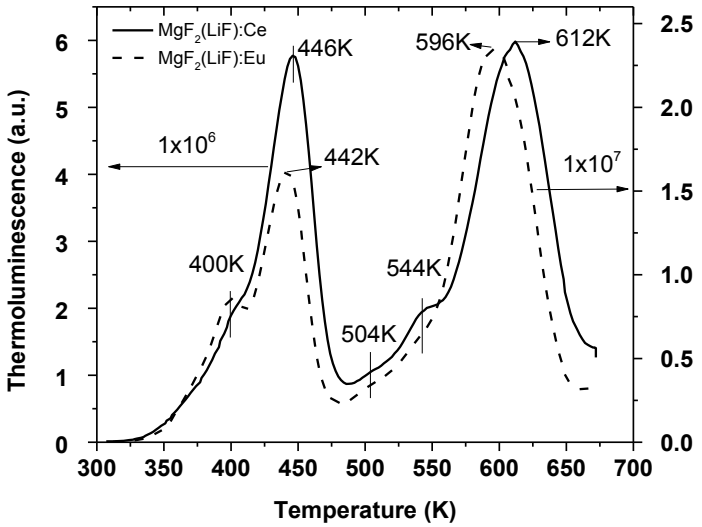

Figure 2: TL glow curves of $MgF_2(LiF)$:Ce (2.0 mol%) and $MgF_2(LiF)$:Eu (0.4 mol%). The samples were irradiated with 10Gy.

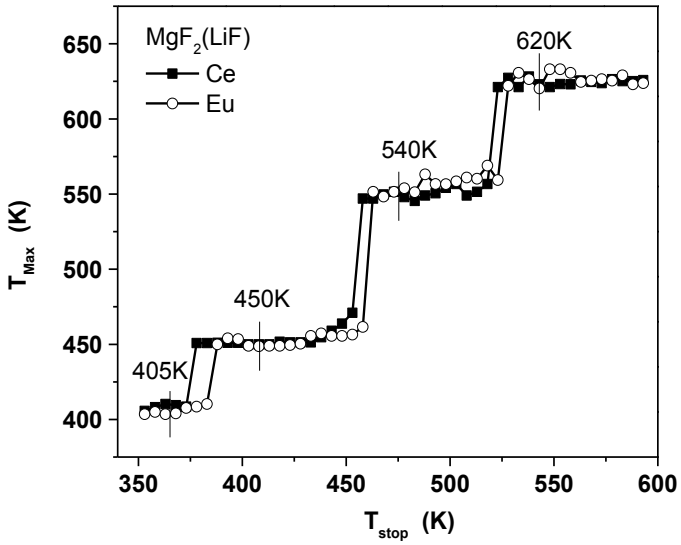

Figure 3: Behavior of T_{max}-T_{stop} curves from $MgF_2(LiF)$:Ce (2.0 mol%) and $MgF_2(LiF)$:Eu (0.4 mol%).

parameters used satisfy the QE conditions [Sunta *et al*., 1999], so that the corresponding analytical expressions as derived above are equally valid for these glow peaks. QE condition is important for the acceptability to applying GOK and MO fits, since the GOK and MO expressions are based on the QE assumption.

The kinetic parameters obtained are presented in table 1, and the computerized glow curves are shown in Fig. 4. It can be seen in Figures 4a1 and 4a2, the fitted peaks presented a change in the order kinetic, which could be attributed to the defects generated by the dopant ion and provokes the change in the shape of the glow peaks. The differences in the *b* vs. α correlation is consistent to the difference of *E* values found in the experimental TL glow peaks using GOK and MO fits (Table 1).

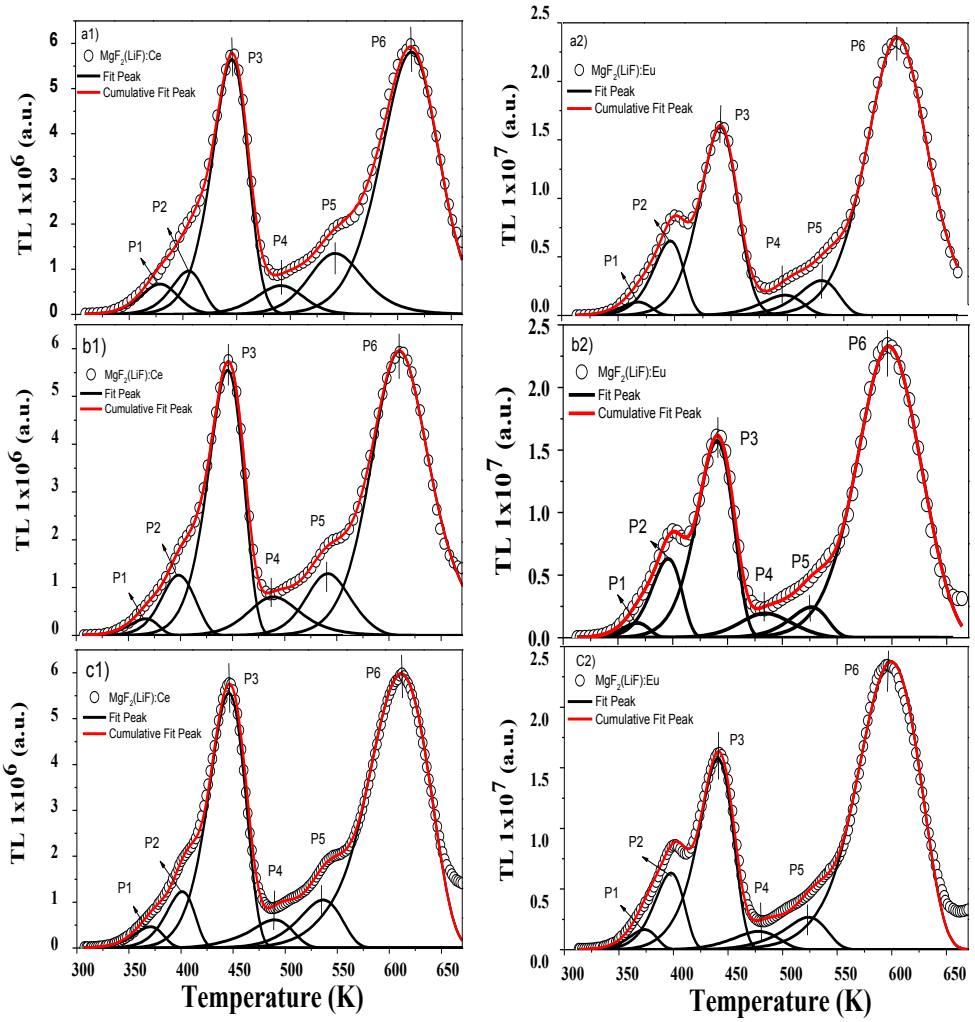

Figure 4: TL glow curve from MgF_2(LiF):Ce or Eu (open circles). a) Fit of glow peak by the GOK expression (continuous lines). b) Fit of glow peak by the MO expression, and c)

Fit of glow peak by the IMTS expression. The best fit parameters are given in Table 1.

The *E* values found from MO fit should be considered more appropriate than those found from GOK fits. The FOM values found also lower in MO fits than those by the GOK fits for the glow curve. In the case of IMTS the FOM value was slightly higher than those obtained by MO and GOK, it can be attributed to the risk involved setting with this IMTS model and including the large number of physical parameters to be consider.

Table 1: Parameters obtained by the GOK, MO and IMTS fits of the TL peaks from the polycrystals samples. In IMTS model A_m=2.1x10^{-21} for MgF_2(LiF):Ce, and A_m=8.989x10^{-22} for MgF_2(LiF):Eu.

Sample	Model	Peak	Parameters								FOM(%)
			n_0 (cm^{-3})	N (cm^{-3})	E (eV)	s (s^{-1})	b	α	T_{max} (K)	A_n (cm^3 s^{-1})	
MgF_2(LiF):Ce	**GOK**	**1**	1.09E5	1.43E8	0.84	6.77E13	1.45	—	—	—	
		2	1.31E5	1.18E5	1.02	1.00E14	1.15	—	—	—	
		3	1.32E5	5.77E5	1.12	9.03E12	1.47	—	—	—	
		4	8.74E5	8.69E4	1.09	2.62E13	1.17	—	—	—	
		5	3.31E5	2.68E5	1.39	1.00E14	2.00	—	—	—	
		6	1.47E6	3.00E8	1.42	6.91E13	1.47	—	—	—	0.99
	MO	**1**	—	—	0.82	2.65E6	—	0.00	366	—	
		2	—	—	1.08	4.46E13	—	0.68	398	—	
		3	—	—	1.12	4.49E11	—	0.34	445	—	
		4	—	—	1.15	1.79E15	—	1.00	494	—	
		5	—	—	1.58	1.82E16	—	0.88	541	—	
		6	—	—	1.61	8.18E15	—	0.99	611	—	0.77
	IMTS	**1**	1.30E8	1.00E10	0.82	1.30E10	—	—	—	7.99E-23	
		2	3.70E8	1.00E10	1.02	6.80E11	—	—	—	2.00E-21	
		3	3.80E9	1.00E10	1.13	3.20E11	—	—	—	2.00E-21	
		4	1.00E9	1.00E10	1.14	2.79E10	—	—	—	1.00E-20	
		5	3.50E9	1.00E10	1.39	5.40E11	—	—	—	8.00E-21	
		6	1.01E11	1.00E10	1.43	1.60E10	—	—	—	2.10E-21	1.49
MgF_2(LiF):Eu	**GOK**	**1**	1.38E5	1.39E5	0.87	1.90E13	1.00	—	—	—	
		2	8.00E5	2.09E6	1.01	9.40E13	1.05	—	—	—	
		3	2.52E6	2.67E6	1.08	4.62E13	1.23	—	—	—	
		4	2.93E5	1.00E6	1.15	7.49E12	1.00	—	—	—	
		5	4.90E5	3.92E6	1.35	9.97E13	1.00	—	—	—	

	6	6.11E6	6.99E6	1.46	2.71E13	1.68	—	—	—	1.11
MO	**1**	—	—	0.94	1.24E8	—	0.00	367	—	
	2	—	—	1.07	3.00E12	—	0.26	395	—	
	3	—	—	1.08	1.61E11	—	0.28	440	—	
	4	—	—	1.15	4.04E12	—	0.85	484	—	
	5	—	—	1.39	2.38E8	—	0.00	526	—	
	6	—	—	1.40	7.74E11	—	0.76	597	—	1.13
IMTS	**1**	2.40E8	1.00E10	0.95	7.14E11	—	—	—	3.09E-23	
	2	1.20E9	1.00E10	1.07	3.31E12	—	—	—	5.01E-21	
	3	5.60E9	1.00E10	1.10	2.81E11	—	—	—	1.03E-21	
	4	1.30E9	1.00E10	1.12	2.89E10	—	—	—	3.00E-20	
	5	4.51E9	1.00E10	1.37	9.26E11	—	—	—	1.00E-20	
	6	1.95E11	1.00E10	1.43	2.95E10	—	—	—	2.40E-21	2.05

It is important to mention about the calculation of E values, the GOK, MO and IMTS models involve some different parameters for fitting. In GOK there are s, b, N and n0. In MO there are s, α and Tm, and for IMTS there are n0, N, s, An and Am. In essence, n0, N, b and s are simply the fitting parameters of the procedure from which the only meaningful parameter obtained is E for GOK. In MO also s and α have a similar meaning. One may, as in GOK case, measure n0 from the area of the glow peak and using this value of n0 and the fitted value of α, which gives the relative concentrations of the filled active traps (AT) and the thermally disconnected trap (TDT). The above interpretations however, exists only in the framework of the models from which GOK and MO expressions are derived. If the glow peak is derived from a different model, these interpretations are no more applicable. For example, when the TL glow curve is derived from IMTS model, the fitted n0 value does not represent the population of the filled AT. It represents that fraction of the filled AT which recombines with recombination center (RC), since a part of the free charge carriers from AT are captured non-radiatively in the vacant TDT [Sunta et al., 1994]. Thus, these fitted parameters are simply the tools of the fitting process to find the value of E parameter.

3.-DISCUSSION AND CONCLUSIONS

The results obtained in the numerical IMTS analysis, based on the Levenberg-Marquardt (LM) with an implicit Rosenbrock method without imposing additional priori assumptions on the original model was less efficient than the analysis using GOK and MO with the approximation of OTOR model. The analysis in IMTS model consume a few hours of computerized calculation due to the large number of possible combinations of the used parameters and it is proved that the method completely well estimates the TL glow curve conditions. However, the time of calculation for a specific material could be reduced using a limited range of variability of parameters. According to the analysis of the TL glow curve of Ce or Eu -doped MgF_2(LiF) by the OTOR and IMTS models, the ordinary IMTS model showed the optimal results. In the case of the OTOR models, the number of traps introduced could be perceived acceptable. However, in the IMTS models it is not possible to speculate the number of different traps of any single glow peak. There are a number of possibilities of CR, AT and TDT could be introduced in order to provide the best glow curve composition. The concentration of the electrons in the traps during irradiation are also governed by the physical parameters of the traps, so it is important to consider this factor to simulation of the glow curves. To get more realistic information about the glow curve composition it is evident that many additional measurements should be performed, for this reason the model IMTS presents a disadvantage regard to GOK and MOK with the approximation of OTOR model. Nevertheless, the main advantage of the IMTS method is that consider parameters more physically acceptable than those in the GOK and MO methods, in which the condition of the maximum temperature is used to simplify the equations of physical model.

REFERENCES

Attix FH. *INTRODUCTION TO RADIOLOGICAL PHYSICS AND RADIATION DOSIMETRY*. John Wiley & Sons, New York. (1986).

Chen R; McKeever S. *THEORY OF THERMOLUMINESCENCE AND RELATED PHENOMENA.* World Scientific. (1997).

Chen R; Pagonis V. *THERMALLY AND OPTICALLY STIMULATED LUMINESCENCE: A SIMULATION APPROACH*. John Wiley & Sons Ltd, West Sussex. (2011).

Chung KS; Choe HS; Lee JI; Kim JL. (2011). *An algorithm for the deconvolution of the optically stimulated luminescence glow curves involving the mutual interactions among the electron traps*. Radiation Measurements **46**: 1598-1601.

Chung KS; Lee JI; Kim JL. (2012). *A computer program for the deconvolution of the thermoluminescence glow curves by employing the interactive trap model*. Radiation Measurements **47**: 766-769.

Chung KS; Park CY; Lee JI; Kim JL. (2015). *An algorithm for the integrated deconvolution of radioluminescence and thermally/optically stimulated luminescence glow curves.* Radiation Measurements **79**: 7-12.

Dahoe AE; Skjold T; Roekaerts DJEM; Pasman HJ; Eckhoff RK; Hanjalic K ; Donze M. (2013). *On the Application of the Levenberg–Marquardt Method in Conjunction with an Explicit Runge–Kutta and an Implicit Rosenbrock Method to Assess Burning Velocities from Confined Deflagrations.* Flow Turbulence Combust **91**: 281–317.

Favalli A; Furetta C; Cruz-Zaragoza E. (2006a). *Variation of the peak temperature at the maximum as a function of dose in thermoluminescent phosphors*. Radiation Effects and Defects in Solids **161**: 279-287.

Favalli A; Furetta C; Cruz-Zaragoza E; Reyes A. (2006b). *Computerized glow curve deconvolution of thermoluminescent emission from polyminerals of Jamaica Mexican flower*. Radiation Effects and Defects in Solids **161**: 591-602.

Furetta C. *HANDBOOK OF THERMOLUMINESCENCE*. World Scientific Publishing, (2003).

Gómez-Ros JM; Furetta C; Cruz-Zaragoza E; Lis M; Torres A; Monsivais G. (2006). *Dose dependence and thermal stability of the thermoluminescence emission in inorganic dust from mint and chamomile*. Nuclear Instruments and Methods in Physics Research A 566: 727-732.

González PR; Furetta C; Cruz-Zaragoza E. (2006). *The thermoluminescent (TL) kinetics parameters of the perovskite –like $KMgF_3$ activated by lutetium impurities*. Nuclear Instruments and Methods in Physics Research B 243: 349-353.

Horowitz YS; Yossian D. (1995). *Computerized glow curve deconvolution: application to thermoluminescence dosimetry*. Radiation Protection Dosimetry **60**: 1-114.

Kadari A; Mostefa R; Marcazzo J; DK. (2015). *Mathematical study of the thermoluminescence process in $K_2YF_5:TB^{3+}$*. Radiation Protection Dosimetry **167**: 437-442.

Kitis G; Cruz-Zaragoza E; Furetta C. (2006). *Critical analysis of the peak-shape methods based on only one temperature value*. Radiation Effects & Defects in Solids **161**: 149-160.

Kitis G; Gomez-Ros JM. (2000). *Thermoluminescence glow-curve deconvolution functions for mixed order of kinetics and continuous trap distribution*. Nuclear Instruments & Methods in Physics Research A **440**: 224-231.

Marcazzó J; Cruz-Zaragoza E; González PR; Santiago M; Caselli E. (2014). *Analysis of the glow curve of $KMgF_3$:Lu compounds without resorting to the quasi-equilibrium approximation*. Radiation Measurements **71**: 262-264.

Marcazzó J; Molina P; Caselli E. (2008). *Analysis of the main thermoluminescent peak of the glow curve of K_2YF_5: Pr^{3+} crystals employing a model of interactive traps*. Radiation Measurements **43**: 208-212.

McKeever SWS. (1980). *On the analysis of complex thermoluminescence. Glow-curves: Resolution into individual peaks*. Physics Status Solid A **62**: 331-340.

McKeever SWS; Moscovich M; Townsend PD. THERMOLUMINESCENT DOSIMETRY MATERIALS: PROPERTIES AND USES. Nuclear Technology Publishing, (1995).

Ogundare FO; Balogun FA; Hussain LA. (2004). *Kinetic characterization of the thermoluminescence of natural fluorite*. Radiation Measurements **38**: 281-286.

Pagonis V; Kitis G; Furetta C. *NUMERICAL AND PRACTICAL EXERCISES IN THERMOLUMINESCENCE.* Springer, (2006).

Press W; Flanery BP; Vetterling WT. *NUMERICAL RECIPIES: THE ART OF SCIENTIFIC COMPUTING.* University Press, (1992).

Rasheedy MS, (1993). *On the general-order kinetics of the thermoluminescence glow peak*. Journal of Physics Condensed Matter **5**: 633-636.

Rasheedy MS, (2005). *A new evaluation technique for analyzing the thermoluminescence glow curve and calculating the trap parameters*. Thermochemica Acta **429**: 143-147.

Sadek AM; Eissa HM; Basha AM; Kitis G. (2014). *Properties of the thermoluminescence glow peaks simulated by the interactive multiple-trap system (IMTS) model.* Physics Status Solidi B **252**: 721-729.

Sakurai T. (2001). *Fatal defect in computerized glow curve deconvolution of thermoluminescence*. Journal of Physics D: Applied Physics **34**: 105-107.

Sunta CM; Yoshimura EM; Okuno E. (1994). *Supralinearity and sensitization factors in thermoluminescence*. Radiation Measurements **23**: 655-666.

Sunta CM; Ayta WEF; Kulkarni RN; Chubaci JFD; Watanabe S. (1999). *The quasi-equilibrium approximation and its validity in the thermoluminescence of inorganic phosphors*. Journal of Physics D: Applied Physics **32**: 717-725.

Yazici AN; Topaksu M. (2003). *The analysis of thermoluminescence glow peaks of unannealed synthetic quartz*. Journal of Physics D: Applied Physics **36**: 620-627

Optimización de la arquitectura de una red neuronal en espectrometría de neutrones para reducer el número de esferas Bonner

Ana Alicia León-Pérez[1-3*], Ma. del Rosario Martínez-Blanco[1-3], Cruz Felipe Hernández-Pérez[1-3], J. Guadalupe Espinoza-García[1-3], Víctor Hugo Castañeda-Miranda[1-3], Luis Octavio Solís-Sánchez[1-3], Rodrigo Castañeda-Miranda[1-3], Hector Rene Vega-Carrillo[4], Roberto Méndez Villafañe[5], Eduardo Gallego[6], Marco Aurelio de Sousa Lacerda[7] y José Manuel Ortiz-Rodríguez [1-3]

Universidad Autónoma de Zacatecas, Av. Ramón López Velarde 801, Col. Centro 98000, Zacatecas, México.
[1] Centro de Investigación e Innovación Tecnológica Industrial (CIITI)
[2] Laboratorio de Innovación y Desarrollo Tecnológico en Inteligencia Artificial (LIDTIA)
[3] Unidad Académica de Ingeniería Eléctrica
[4]Unidad Académica de Estudios Nucleares (UAEN)

[5]Laboratorio de Patrones Neutrónicos del Departamento de Metrología de Radiaciones Ionizantes del Centro de Investigaciones Energéticas, Medioambientales y Tecnológicas (CIEMAT), Avda. Complutense, 22, 28040, Madrid, España

[6]Departamento de Ingeniería Nuclear de la Universidad Politécnica de Madrid (DIN-UPM), ETSI Industriales, C. José Gutiérrez Abascal, 2, 28006, Madrid España

[7]Centro de Investigación de Tecnología Nuclear de la Comisión Nacional de Energía Nuclear (CDTN-CNEN), Av. Presidente Antonio Carlos, 6627, Pampulha, CEP: 31270-901, Belo Horizonte, MG, Brazil

RESUMEN

La espectrometría de neutrones es un proceso experimental para determinar la distribución de energía denominado Espectro. Dentro de los métodos disponibles para la espectrometría de neutrones se puede mencionar el Sistema Espectrométrico de Esferas Bonner como uno de los más utilizados, compuesto por un detector colocado en el centro de un conjunto de esferas de polietileno, cuyos diámetros varían desde 2 hasta 18 pulgadas, sin embargo posee algunas desventajas como son los largos periodos de tiempo para realizar las mediciones,

el peso, y el número de esferas que varían según el sistema. A partir de esto se proponen métodos alternativos como Redes Neuronales Artificiales. Para este proyecto se hizo uso de Redes neuronales de propagación inversa con la Metodología de diseño robusto de redes neuronales artificiales (MDRRNA), con la ayuda de una herramienta computacional que maximiza el rendimiento, haciendo que el tiempo empleado para los entrenamientos de la red sea el menor posible y así obtener los arreglos ortogonales rápidamente para determinar la mejor topología de red. Se usaron las tasas de conteo de un sistema Espectrométrico con 7 esferas, 2 esferas y 1 esfera de 5 y 8 pulgadas. Usando esta metodología se buscó reducir el trabajo empleado como en el sistema Espectrométrico conformado por un número mayor de esferas, ya que al ingresar menos datos en las tasas de conteo para obtener los espectros con 60 niveles de energía se ahorra tiempo y espacio, pues al tener un menor número de esferas su portabilidad es más fácil para desplazarse de un lugar a otro, para esto se realizaron varios experimentos con diferentes errores hasta llegar al error óptimo para que la topología de la red fuera la apropiada y encontrar los mejores parámetros de diseño, también se hizo usó de un software estadístico JMP para obtener las mejores topologías y así volver a entrenar obteniendo sus mejores y peores espectros y de esta manera determinar si es posible la reducción.

Palabras clave: Espectrometría de neutrones; esferas Bonner, redes neuronales artificiales, optimización.

1.- INTRODUCCIÓN

Debido a la ausencia de carga de los neutrones son partículas difíciles de detectar, además de poseer un poder de penetración mayor que las partículas cargadas y la radiación electromagnética, dándole la posibilidad de interactuar con la materia diferente a otras partículas, [Reyes-Haro; Ortiz-Rodríguez & Vega Carrillo, 2012] estas interacciones tienen una baja probabilidad y producen una pequeñísima perdida de energía lo cual significa que se necesitan muchas colisiones en diferentes materiales de gran espesor para que la energía del neutrón disminuya. [Cember 1996]

Desde el descubrimiento del neutrón en 1932 por Chadwick ha sido de gran importancia pues ha brindado las bases para nuevos descubrimientos, dentro de los cuales se puede mencionar la espectrometría de neutrones que es una técnica experimental para determinar por medio de neutrones la intensidad de un campo de radiación con respecto a la energía, a lo cual se le conoce como "espectro" [Del Hoyo-Becerra 2013]

Debido a que los neutrones no son desviados por un campo eléctrico o magnético y también porque producen una ionización apreciable, se deben emplear métodos indirectos para detectarlos y medir su energía [Martínez-Blanco, Ortiz-Rodríguez & Vega-Carrillo, 2006]. La medición y particularmente la determinación de espectros de neutrones no es una tarea fácil, debido a las características que el neutrón presenta, pero para resolver este problema existen detectores e instrumentos que permiten determinar los espectros de los neutrones, uno de los métodos para conocer el espectro de neutrones en los campos de radiación a los que los individuos se ven expuestos es el uso del Sistema Espectrométrico de Esferas Bonner (SEEB). [Ortiz Rodríguez 2005]

1.1 Sistema Espectrométrico de Esferas Bonner (SEEB)

El espectrómetro de neutrones multiesferas también llamado Sistema Espectrométrico de Esferas Bonner fue descrito por primera vez en 1960 por Bramblett, Erwing y Bonner [Bakali 2001] este sistema se basa en el uso de un detector envuelto con esferas de

diferentes diámetros de polietileno, al incidir los neutrones sobre la esfera se convierten en partículas secundarias, estas partículas se transportan e interactúan con los núcleos perdiendo energía y alcanzando al detector, el cual está ubicado en el centro de la esfera. [Reyes-Alfaro 2014] En el detector se produce una reacción nuclear que genera un pulso que es amplificado y acumulado, de acuerdo a su altura, en un analizador multicanal. Al aumentar el diámetro de la esfera aumenta la sensibilidad del sistema hacia las energías altas y de esta manera es posible llevar a cabo la espectrometría de neutrones. [Martínez-Blanco 2006]

Algunas de las desventajas del SEEB son las siguientes:

-El peso del mismo debido al número de esferas y diferentes tamaños que posee.

-Los largos periodos de tiempo empleados para realizar las mediciones.

-La baja resolución del sistema

-La necesidad de un código para la reconstrucción y usuario experimentado para la manipulación del código.

A partir de esto se proponen métodos alternativos como los son las Redes Neuronales Artificiales, para este trabajo se utilizó la Metodología de diseño robusto de redes neuronales artificiales (MDRRNA) para este caso se usó la Red neuronal de propagación inversa [Ortiz-Rodríguez *et al.,* 2005; Ortiz-Rodríguez 2005]

El objetivo de este trabajo es determinar si es posible reducir el número de esferas Bonner por medio de la optimización de la arquitectura de una red neuronal en espectrometría de neutrones, mediante la Metodología de Diseño Robusto de Redes Neuronales Artificiales (MDRRNA), buscando reducir el trabajo empleado como es el caso del sistema Espectrométrico de esferas Bonner conformado por un número mayor de esferas.

2.- MATERIALES Y MÉTODOS

En este trabajo se hizo uso de la metodología de diseño Robusto de Redes Neuronales Artificiales (que se muestra en la figura siguiente) para determinar los valores óptimos de las variables de diseño una red neuronal que sea capaz de reconstruir espectros de neutrones, dicha metodología está basada en la metodología de Taguchi, que está compuesto por varias etapas que son: planeación, experimentación, análisis y confirmación [Unal & Dean, 1991], esto se realizó para cuatro casos los cuales incluyen un diferente número de esferas y tamaños, 7 esferas, 2 esferas, 1 esfera de 8 pulgadas y 1 de 5 pulgadas.

Figura 1.- Metodología de Diseño Robusto de Redes Neuronales Artificiales.

2.1 Planeación

Dentro de la etapa de planeación se hace la búsqueda de variables de diseño, que son las variables controlables que se encuentran dentro de la región de búsqueda, la cual se muestra en la siguiente figura:

Niveles de las variables de diseño			
Var. diseño	Nivel 1	Nivel 2	Nivel 3
A			
B			
C			
D			

Figura 2.- Variables de diseño y sus niveles.

Donde la parte de las variables representadas con A, B, C y D son los parámetros del número de neuronas por capas, tasa de aprendizaje y momento.

Niveles de las variables de ruido		
Vars. ruido	Nivel 1	Nivel 2
U	Conjunto 1	Conjunto 2
V	E:P	E:P
W	Entren1-Prueba1	Entren2-Prueba2

Figura 3.- Variables de ruido y sus niveles

En la figura anterior se muestran las variables de ruido, la variable U representa los conjuntos de inicialización de pesos, en la V la relación tamaño de datos Entrenamientos-prueba y la W la solución del conjunto Entrenamiento-Prueba.

2.2 Experimentación

En esta fase se hace la optimización de la arquitectura de red mediante la herramienta principal de la hoja de Excel siguiendo la metodología de diseño Robusto, en las cuales se hacen las combinaciones correspondientes utilizando las tablas de las variables de diseño y de ruido, para el llenado de los arreglos ortogonales (desempeños) se hizo uso de una herramienta de computo en el entorno de MATLAB, para obtener más rápido los desempeños de las redes entrenadas, reduciendo el tiempo empleado en esta actividad y obteniendo los arreglos ortogonales para cada caso, en esta etapa también se experimentó con la búsqueda del error mínimo con el cual funcionara mejor la red.

R17					G1	G2	G3	G4		
	Neuronas en capa 1	Neuronas en capa 2	Tasa de aprendizaje	Momento	U=1 V=1 W=2	U=1 V=2 W=1	U=2 V=1 W=1	U=2 V=2 W=2	Media de Y	Relación S/R
Exp-1111	1	1	1	1						
Exp-1222	1	2	2	2						
Exp-1333	1	3	3	3						
Exp-2123	2	1	2	3						
Exp-2231	2	2	3	1						
Exp-2312	2	3	1	3						
Exp-3132	3	1	3	2						
Exp-3213	3	2	1	3						
Exp-3321	3	3	2	1						

Figura 4.- Formato para determinación de parámetros

Para el entrenamiento de las Redes se utilizaron los espectros de neutrones publicado por la Agencia Internacional de Energía Atómica, donde se usa una relación de tamaño (entrenamiento-prueba) de datos de entrenamiento prueba, tomando como entrada las tasas de conteo correspondientes a las diferentes esferas con diferentes dimensiones del SEEB y a la salida los 60 niveles de energía.

2.3 Análisis

Después de obtener los arreglos para las diferentes esferas nos pasamos al análisis estadístico se analizan las relaciones señal-ruido por medio de la técnica del análisis de la

varianza, para determinar los efectos significativos, y los niveles óptimos de las variables de diseño mediante el programa JMP y así obtener las posibles mejores topologías.

2.4 Confirmación

Ya que se obtienen las posibles mejores topologías para cada caso de esfera, se vuelven a entrenar con los mismos datos de entrenamiento de prueba que sería con un 80% para el entrenamiento y 20% de prueba, utilizando las mismas columnas de entrenamiento y prueba de cualquiera de los casos.

Se hicieron cuatro experimentos para cada caso (diferente número de esferas), se obtuvieron las gráficas de Chi^2 (χ^2) y correlación (R), a partir de esto se hizo la clasificación de las mejores topologías, de estos resultados se compararon los mejores y peores casos en sus espectros para verificar que funcionan de igual manera para cualquier número de esferas.

3.- RESULTADOS

Utilizando la metodología de diseño robusto de redes neuronales artificiales se aplicaron cada una de sus etapas y se obtuvieron los siguientes resultados:

3.1 Planeación

Dentro de la etapa de planeación se determinaron las variables de diseño y ruido, las cuales se muestran a continuación:

Niveles de las variables de diseño			
Var. diseño	Nivel 1	Nivel 2	Nivel 3
A	6	8	10
B	0	8	10
C	0.001	0.1	0.3
D	0.001	0.05	0.1

Figura 5.- Variables de diseño

Niveles de las variables de ruido		
Vars. ruido	Nivel 1	Nivel 2
U	Conjunto 1	Conjunto 2
V	6:4	8:2
W	Entren1-Prueba1	Entren2-Prueba2

Figura 6.- Variables de ruido

3.2 Experimentación

A continuación se muestra uno de los resultados (para el caso de 7 esferas) un arreglo ortogonal, llevado a cabo en la etapa de experimentación también se encontró que el error más óptimo fue 1e-4 para cada uno de los casos.

R17					G1	G2	G3	G4
	Neuronas en capa 1	Neuronas en capa 2	Tasa de aprendizaje	Momento	U=1 V=1 W=2	U=1 V=2 W=1	U=2 V=1 W=1	U=2 V=2 W=2
Exp-1111	6	0	0.001	0.001	0.000298656	0.000301932	0.000398781	0.000287752
Exp-1222	6	8	0.1	0.05	0.000321691	0.000298608	0.000309831	0.000266297
Exp-1333	6	10	0.3	0.1	0.00035867	0.000275744	0.000326509	0.000296514
Exp-2123	8	0	0.1	0.1	0.000276674	0.000207462	0.000310295	0.000309987
Exp-2231	8	8	0.3	0.001	0.000352625	0.000429237	0.000328881	0.000389557
Exp-2312	8	10	0.001	0.05	0.000341382	0.00015683	0.000325344	0.000302847
Exp-3132	10	0	0.3	0.05	0.000277241	0.000197384	0.000331787	0.000302436
Exp-3213	10	8	0.001	0.1	0.000407251	0.000279461	0.000376102	0.000387481
Exp-3321	10	10	0.1	0.001	0.00030705	0.0004145	0.000380687	0.000257836

Figura 7 Ejemplo de la obtención de parámetros

3.3 Análisis

Después de obtener los arreglos para los distintos números y tamaños de esferas nos pasamos al análisis estadístico JMP donde se obtienen las posibles mejores topologías de red, a continuación se muestra un ejemplo de obtención de una de las topologías, donde se obtienen varios perfiles normal, deseado y maximizado, donde solo se tomaron en cuenta el normal y maximizada pues la normal y deseada son las mismas.

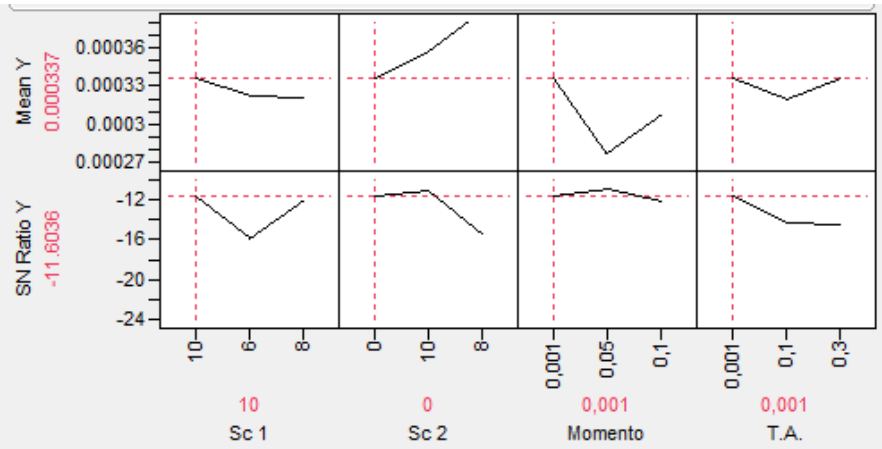

Figura 8.- Ejemplo en obtencion de la mejor topologia para el caso de 7 esferas normal

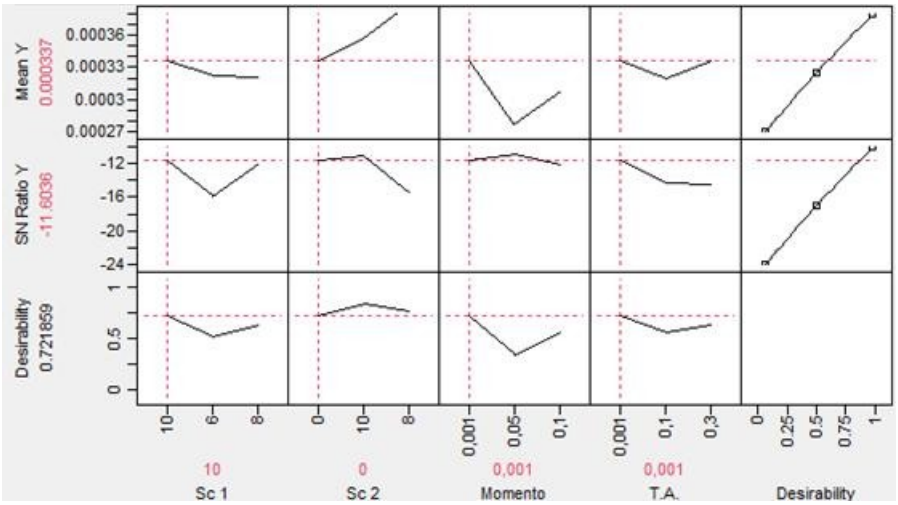

Figura 9.- Ejemplo en obtencion de la mejor topologia para el caso de 7 esferas deseada

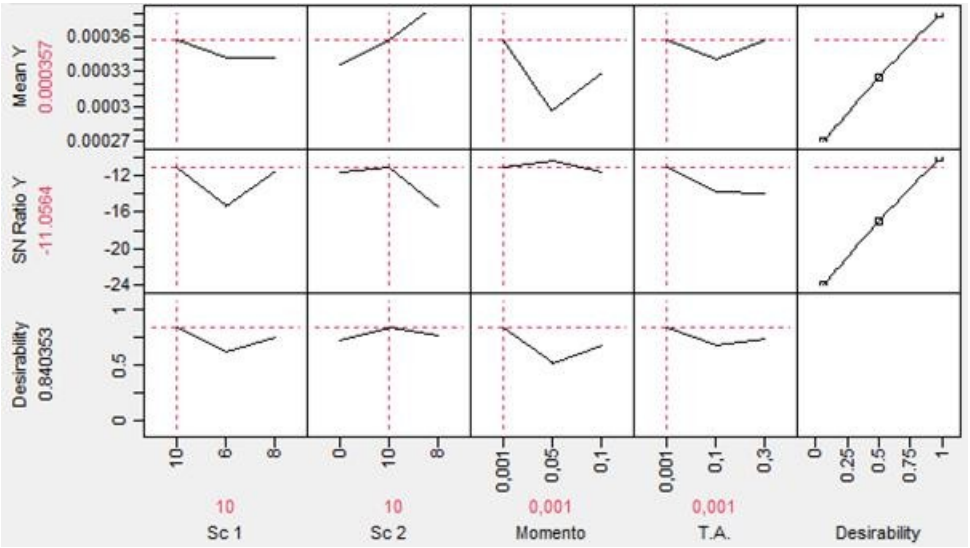

Figura 10.- Ejemplo en obtencion de la mejor topologia para el caso de 7 esferas maximizada

Como se puede observar se obtienen 3 distintas topologias que son normal, deseada y maximizada, que para este caso se tomaran solo las normales y maximizadas ya que las normales y deseadas son las mismas topologias.

3.4 Confirmación

Para esta ultima etapa se hicieron varios pasos para confirmar lo que se realizó anteriormente y asi poder determinar si es posible la reduccion de las esferas.

A partir de los resultados del analisis estadistico JMP se tomaron las mejores topologias obtenidas que son 4 normales y 4 maximizadas (una por cada caso de esfera) estas se volvieron a entrenar 4 veces por cada caso, despues por medio de la obtención de las graficas de χ^2 y R se compararon las topologias y se eligieron las mejores para cada numero de esferas, que para este caso resultaron mejores las normales, que se muestran en la siguiente tabla:

Tabla 1.- Obtención de las mejores Topologías

Gpo	Núm. de esferas	Tamaño de cada esfera (pulgadas)	Neuronas en capa oculta 1	Neuronas en capa oculta 2	Tasa de aprendizaje	Momento	Error
1	**7**	**0, 2, 3,5,8,10 y 12**	**10**	**0**	**0.001**	**0.001**	**2.5E-4**
2	**2**	**8 y 5**	**10**	**0**	**0.001**	**0.001**	**4.5E-4**
3	**1**	**8**	**10**	**0**	**0.001**	**0.001**	**5.0E-4**
4	**1**	**5**	**10**	**0**	**0.001**	**0.001**	**5.2E-4**

Después de obtener las mejores topologías (normales) mostradas anteriormente se compararon de igual manera con χ^2 y R, así como la comparación del mejor y peor espectro obtenido.

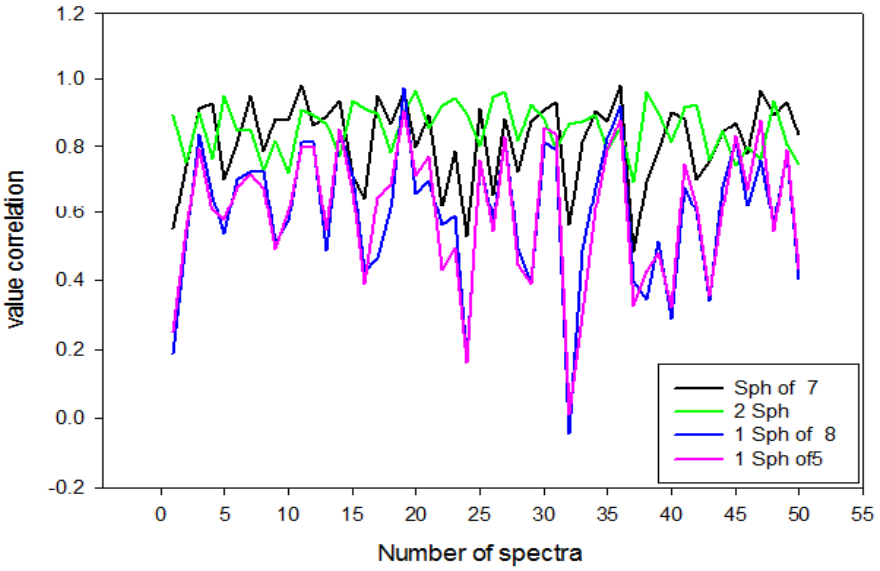

Figura 11.- Comparación de R entre las mejores Topologías

Como se observa en la figura anterior las Topologías con mejor correlación son las de 7 y 2 esferas, las de una esfera para cualquier tamaño también pueden funcionar pero teniendo en

cuenta que tienen más errores, esto se puede observar en la gráfica pues estas tienen unos picos muy abajo y al contrario de estas las de 7 y 2 esferas se mantienen más cerca de 1 que es lo que se espera para cada caso.

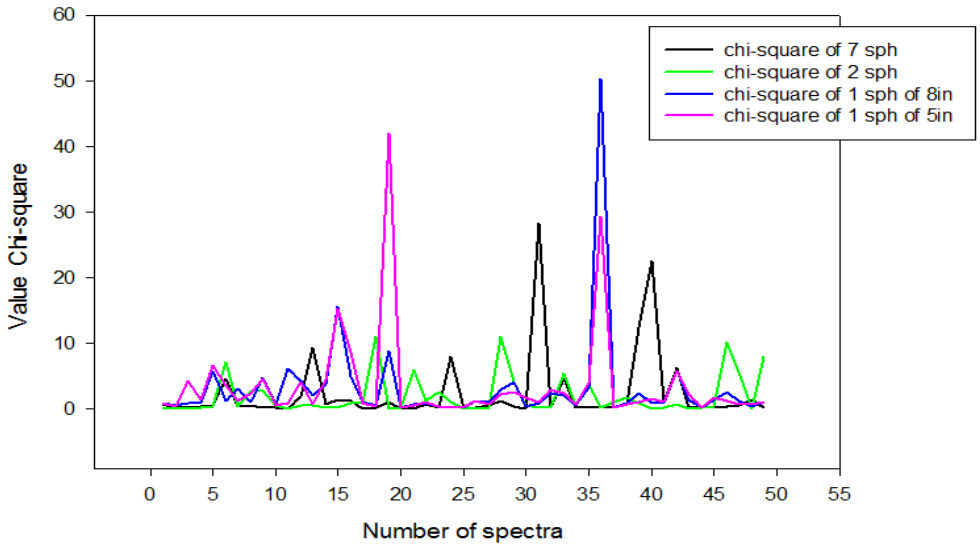

Figura 12.- Comparación de χ^2 entre las mejores Topologías

En el caso de la χ^2 los valores deben estar cercanos a cero, con un rango de 0 a 43.1880, como se puede observar en la figura anterior los valores de las esferas 2 y 7 son mejores pues se mantienen más cerca a cero y dentro del rango, caso contrario al de una esfera que tienen menos estabilidad, pues contienen un mayor número de picos y en algunos casos fuera del rango.

Para el caso de los espectros se tomó solo uno de los ejemplos que fue el de 7 esferas para el mejor y peor caso que a continuación se muestran:

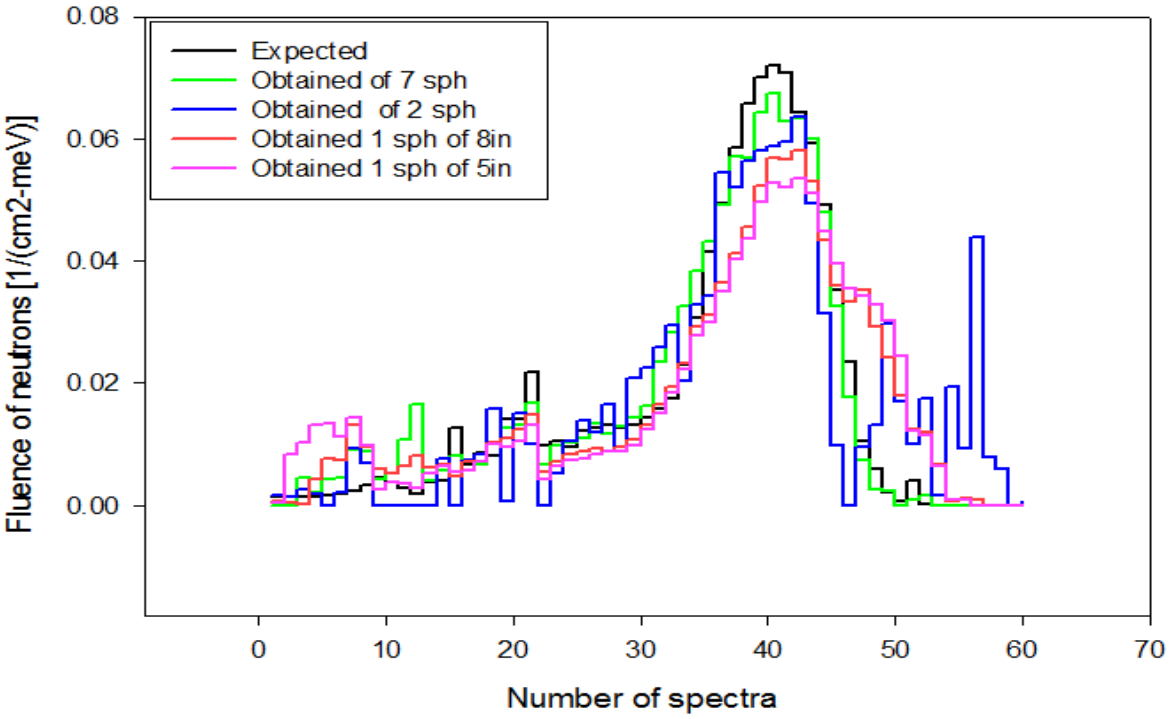

Figura 13.- Mejor espectro obtenido para el caso de 7 esferas comparado con el mismo espectro de las demás esferas (casos)

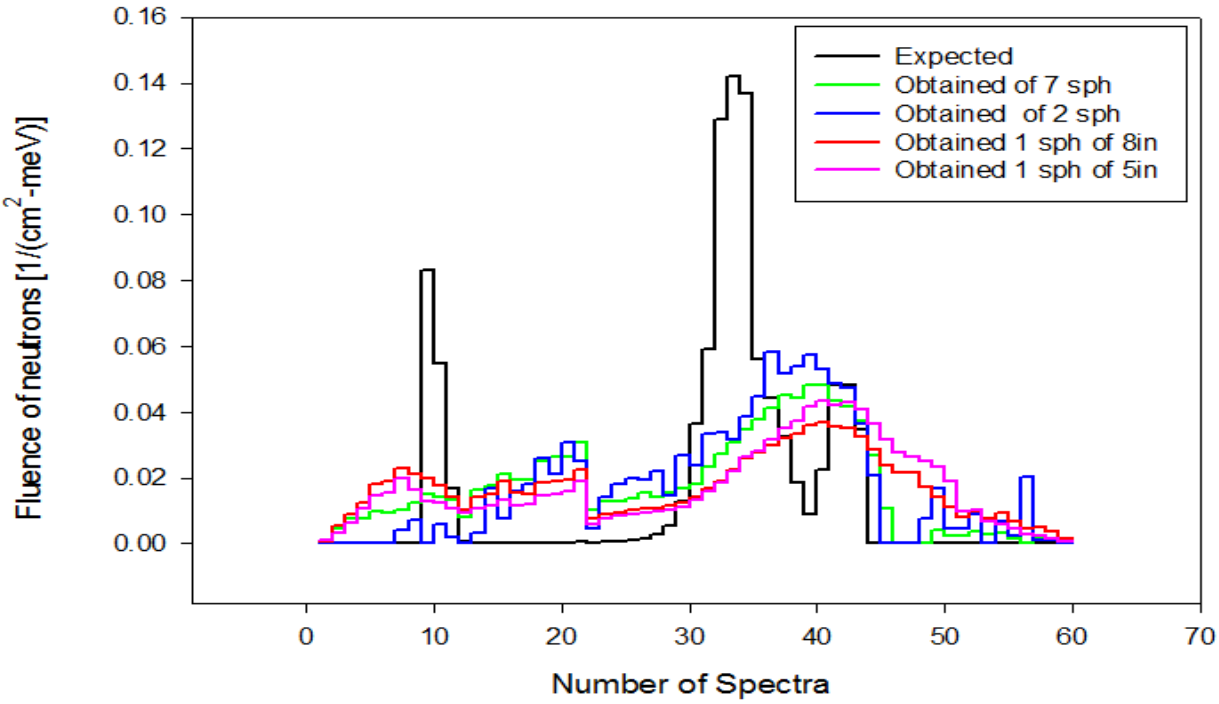

Figura 14.- Peor espectro obtenido para el caso de 7 esferas comparado con el mismo espectro de las demás esferas (casos)

4.- DISCUSIÓN

La metodología de diseño robusto fue de gran importancia para la realización de este proyecto, ya que al aplicar cada una de las etapas que lo conforma, es mucho más fácil su comprensión en la parte de los resultados obtenidos, al entrenar las redes para cada uno de los casos de esferas se obtuvieron los arreglos ortogonales y de allí la mejor Topología mediante el análisis en JMP, después de esto se volvió a entrenar y comparar por medio de R y χ^2 para ver los comportamientos de cada uno de estos, también se hizo comparación con los mejores y peores espectros de cada caso con los demás y de allí determinar si se puede alcanzar el objetivo de disminuir el número de esferas.

5.- CONCLUSIONES

La aplicación de la tecnología de redes neuronales artificiales considerada como una alternativa útil en la espectrometría de neutrones, con ayuda de la estrategia de MDRRNA, ofrecen una forma conveniente de considerar simultáneamente variables de diseño y de ruido, e incorporar el concepto de robustez en el proceso de diseño de las redes, así como la aplicación de varios experimentos usando el sistemas espectrométrico de esferas Bonner, que en el caso de este proyecto se usaron 4 casos que son: para 7 esferas, 2 esferas, 1 esfera de 8 pulgadas y 1 de 5 pulgadas.

Dentro de los resultados obtenidos hasta ahora, se puede mencionar que hay respuestas alentadoras para disminuir el número de esferas, pero aún se encuentra en proceso el análisis de la información, como se vio en los resultados en las gráficas de R y χ^2 cumplen con los parámetros requeridos de una R cerca de 1 y una χ^2 cerca de 0, en la parte de los espectros se observa que son muy parecidos los obtenidos a los esperados como es el caso de las 7 y 2 esferas, pero en el caso de las de una esfera su error es un poco más grande.

Agradecimientos

Este trabajo fue parcialmente financiado por el Fondo de Investigación para la Educación bajo contrato 241771

Este trabajo fue parcialmente financiado por fondos Mixtos SEP-CONACYT bajo contrato ZAC-C03-2015-26357-4.

Este trabajo fue parcialmente financiado por PROSOFT bajo contrato 201513723.

El primero, tercero y cuarto autor agradecen la beca de Licenciatura con número de becario 23241, 23238 y 23240 respectivamente, por Fondo Sectorial de Investigación para la Educación bajo contrato 241771.

El segundo y quinto autor agradecen a la beca de Doctorado con número de becario 23386 y 23385 respectivamente recibido por Fondo Sectorial de Investigación para la Educación bajo contrato 241771.

REFERENCIAS

Bakali M. *Espectrometría neutrónica en las centrales nucleares mediante un sistema de esferas Bonner*. PhD thesis, Universidad Autónoma de Barcelona. (2001)

Cember H. *INTRODUCTION TO HEALTH PHYSICS.* McGraw-Hill, 3rd Edition (1996).

Del Hoyo-Becerra A. *Prueba, validación y documentación del código para espectrometría y dosimetría de neutrones NSDann.,* Tesis de Licenciatura de la Universidad Autónoma de Zacatecas. (2013).

Martínez-Blanco MR. *Espectrometría de neutrones y cálculo simultáneo de dosis equivalentes empleando la metodología de diseño robusto de redes neuronales.* Tesis de Licenciatura de la Universidad Autónoma de Zacatecas. (2016).

Martínez-Blanco MR, Ortiz-Rodríguez JM & Vega-Carrillo HR. (2006) *Neutron spectrometry and dosimetry by means of bonner spheres system and artificial neural networks applying robust design of artificial neural networks*. Memorias del IX International Symposium/XIX National Congress on Solid State Dosimetry: 203-208.

Ortiz-Rodríguez JM, Martínez-Blanco MR, Arteaga-Arteaga T, Vega-Carrillo HR; Hernández-Dávila VM & Manzanares-Acuña E. (2005). *Reconstrucción de espectros de neutrones usando redes neuronales a partir del sistema espectrométrico de esferas de Bonner*. Memorias del VIII International Symposium/XVIII National Congress on Solid State Dosimetry. Pp. 20.

Ortiz-Rodríguez J.M. *Diseño robusto de redes neuronales artificiales aplicadas a la epectrometría de neutrone*s. Tesis de Maestría de la Universidad Autónoma de Zacatecas. (2005).

Reyes-Alfaro A; Ortiz-Rodríguez, JM; Reyes-Haro, A; Castañeda-Miranda R; Solis-Sánchez LO & Vega-Carrillo HR. (2014). *Optimización de redes neuronales artificiales para la reconstrucción del espectro de neutrones y sus dosis equivalentes*. Proccedings of the ISSSD 2014: 475-494.

Reyes-Haro, A., Ortiz-Rodríguez J.M. & Vega-Carrillo. H.R. *Código Iterativo para la Reconstrucción del Espectro de Neutrones usando las Esferas Bonner,* Proccedings of the ISSSD 2012: 44-49.

Unal, R. & Dean EB. (1991). *Taguchi approach to design optimization for quality and cost: An overview*. 1991 Annual Conference of the International Society of Parametric Analysis. Pp. 10.

Entrenamiento de Redes Neuronales de Propagación Inversa Aplicadas a la Dosimetría de Neutrones

Cruz Felipe Hernández-Pérez [1-3], Ma. del Rosario Martínez-Blanco [1-3,], Ana Alicia León-Pérez [1-3*], J. Guadalupe Espinoza-García [1-3], Víctor Hugo Castañeda-Miranda [1-3], Luis Octavio Solís-Sánchez [1-3], Rodrigo Castañeda-Miranda [1-3], Hector Rene Vega-Carrillo [4] , Roberto Méndez Villafañe[5], Eduardo Gallego[6], Marco Aurelio de Sousa Lacerda[7] y José Manuel Ortiz-Rodríguez [1-3]

Universidad Autónoma de Zacatecas, Av. Ramón López Velarde 801, Col. Centro 98000, Zacatecas, México.
[1] Centro de Investigación e Innovación Tecnológica Industrial (CIITI)
[2] Laboratorio de Innovación y Desarrollo Tecnológico en Inteligencia Artificial (LIDTIA)
[3] Unidad Académica de Ingeniería Eléctrica
[4]Unidad Académica de Estudios Nucleares (UAEN)

[5]Laboratorio de Patrones Neutrónicos del Departamento de Metrología de Radiaciones Ionizantes del Centro de Investigaciones Energéticas, Medioambientales y Tecnológicas (CIEMAT), Avda. Complutense, 22, 28040, Madrid, España

[6]Departamento de Ingeniería Nuclear de la Universidad Politécnica de Madrid (DIN-UPM), ETSI Industriales, C. José Gutiérrez Abascal, 2, 28006, Madrid España

[7]Centro de Investigación de Tecnología Nuclear de la Comisión Nacional de Energía Nuclear (CDTN-CNEN), Av. Presidente Antonio Carlos, 6627, Pampulha, CEP: 31270-901, Belo Horizonte, MG, Brazil

RESUMEN

La dosimetría de neutrones es de gran importancia en la protección radiológica ya que tiene como objetivo proporcionar cantidades dosimétricas para valorar la magnitud de los efectos detrimentales en la salud debido a la exposición de radiación de neutrones. Para cuantificar el detrimento a la salud es necesario evaluar la dosis recibida por el personal ocupacionalmente expuesto utilizando diferentes sistemas de detección llamados dosímetros, los cuales poseen respuestas muy dependientes de la distribución de energía de los neutrones. La detección de neutrones es un problema mucho más complejo que la detección de partículas cargadas, ya que no transporta una carga eléctrica, no causan ionización directa, y posee un poder de penetración mayor dándole la posibilidad de interactuar con la materia de manera distinta. Debido a esto se han

desarrollado diversos sistemas de detección de neutrones entre los que destaca el sistema espectrométrico de esferas Bonner debido a las ventajas que posee, tales como un amplio rango de energía, alta sensibilidad y fácil operación. Sin embargo, una vez obtenidas las tasas de conteo, el problema radica en la deconvolución del espectro de neutrones, necesario para el cálculo de las dosis, para lo que se emplean diferentes métodos matemáticos tales como Monte Carlo, máxima entropía, métodos iterativos, entre otros, mismos que presentan diversas dificultades que han motivado el desarrollo de nuevas tecnologías. En la actualidad se están empleando métodos basados en tecnologías de inteligencia artificial para realizar la dosimetría de neutrones, utilizando principalmente la teoría de redes neuronales artificiales. En estos nuevos métodos se puede eliminar la necesidad de reconstrucción del espectro para el cálculo de las dosis. En este trabajo se entrenó una red neuronal artificial de propagación inversa para el cálculo de 15 dosis equivalentes a partir de las tasas de conteo del sistema espectrométrico de esferas Bonner utilizando un conjunto de 7 esferas, uno de 2 esferas y 2 de una sola esfera de diferentes tamaños, probando diferentes valores de error hasta encontrar el más apropiado. La topología de red óptima se obtuvo mediante la metodología de diseño robusto de redes neuronales artificiales donde se seleccionaron los parámetros de la red que produjo los mejores resultados.

Palabras clave: Dosimetría de neutrones; protección radiológica; esferas Bonner; diseño robusto.

1.- INTRODUCCIÓN

1.2.- Dosimetría de neutrones

Debido a la complejidad de las interacciones de los neutrones con el entorno el poder determinar con precisión su energía resulta en una tarea difícil. Al ser partículas que no poseen carga son difíciles de detectar además de tener un poder de penetración mayor que las partículas cargadas y la radiación electromagnética lo que genera un problema para la protección radiológica, que tiene como objetivo el proporcionar un método para valorar la magnitud de los efectos detrimentales en la salud debido a la exposición de radiación de neutrones. Dentro de la protección radiológica la espectrometría y dosimetría de neutrones resultan ser de gran importancia, sin embargo, estas son de las tareas más complejas dentro de esta área. [Thomas 2004; Reyes-Haro *et al.*, 2012, Reyes-Haro *et al.*, 2014]

1.3.- Sistema espectrométrico de esferas Bonner

En espectrometría y dosimetría de neutrones, el sistema espectrométrico de multiesferas, también llamado sistema espectrométrico de esferas Bonner (SEEB), ha sido uno de los métodos más utilizado para la detección de neutrones debido a las ventajas que proporciona, tales como, poseer un extenso rango de energía que va desde los neutrones térmicos hasta los neutrones de alta energía (GeV), funciones de respuesta simple, casi isotrópica, alta sensibilidad y fácil operación. Sin embargo este sistema también cuenta con algunas desventajas como tener una resolución muy baja y requerir largos espacios y periodos de tiempo para la irradiación. [Wang *et al*., 2014; Tripathy *et al*., 2009]

Este sistema está conformado por un detector y diversas esferas de polietileno de diversos tamaños expresados en pulgadas. El detector se coloca en el centro de las esferas las cuales actúan como moderadores reduciendo la incidencia de neutrones de alta energía a menores energías, además, el simple detector desnudo es sensible a la irradiación de neutrones térmicos. Las mediciones de un campo de neutrones particular se realizan tomando esferas

de diferentes tamaños. [Thomas & Alevra 2002; Freeman, Edwards & Bolon, 1999; Bramblett, Ewing & Bonner, 1960]

Casi todos los detectores o espectrómetros se enfrentan al problema de la reconstrucción del espectro, requerido para el cálculo de las cantidades dosimétricas, cuando se utilizan para la caracterización de un campo de neutrones. El SEEB no es la excepción, el espectro de neutrones no es dado directamente como resultado de las mediciones realizadas con el sistema, siendo necesario emplear algún método matemático tal como Monte Carlo, Máxima Entropía, Métodos Iterativos, entre otros [Suman & Sarkar, 2014, Freeman, Edwards & Bolon, 1999]. Sin embargo estos métodos matemáticos también presentan diversas dificultades como la necesidad de un espectro inicial similar al que se desea obtener o el conocer bien el uso de la herramienta diseñada en un entorno no amigable para usuarios no expertos. Esto ha motivado el desarrollo de nuevas tecnologías basadas en inteligencia artificial tales como algoritmos genéticos (AG) y redes neuronales artificiales (RNA). [Vega-Carrillo, Ortiz-Rodriguez & Martinez-Blanco, 2012; Mohammadi, Hakimabad & Motavalli, 2015]

1.4.- Redes neuronales artificiales

Las redes neuronales artificiales se componen de elementos simples que funcionan en paralelo. Estos elementos están inspirados en los sistemas nerviosos biológicos. Como en la naturaleza, la función de red se determina en gran parte por las conexiones entre elementos. Podemos entrenar una red neural para realizar una función particular, mediante el ajuste de los valores de las conexiones (pesos sinápticos) entre los elementos. Una red neuronal tiene tres tipos de capas; de entrada, oculta y de salida. Cada capa tiene varias neuronas que se conectan con otras neuronas a través de pesos y sesgos. Las capas también están conectados entre sí con las funciones de activación. Durante el entrenamiento de la RNA se emplea un conjunto de datos con información de entrada y salida, y los pesos de las neuronas se ajustan hasta que se consigue el patrón entre los datos de entrada y salida. El algoritmo de

aprendizaje de una RNA es el proceso de adaptación que define y modificar los pesos y sesgos. El entrenamiento tiene el propósito de seleccionar los pesos que se adaptan mejor a la red en relación con los datos de entrenamiento. [Mohammadi, Hakimabad & Motavalli, 2015]

El uso de RNA ha resultado ser una gran opción dentro de la dosimetría de neutrones, sin embargo, de los obstáculos principales al emplear RNA de propagación resulta en la búsqueda óptima de los pesos sinápticos de la red, que es altamente dependiente de los pesos iniciales y si éstos están localizados cerca de un mínimo local, el algoritmo podría quedar atrapado, lo que podría ocasionar un pobre desempeño de la red que esté siendo diseñada (Jain, Mao & Mohiuddin, 1996). Otras limitaciones de las RNA son: la determinación de la arquitectura de red, la selección del algoritmo de entrenamiento, el uso de datos de entrenamiento confiables y la relación entre los procesos, todas estas limitaciones han motivado a los investigadores a generar ideas para fusionar las RNA con otros métodos en la búsqueda de un mejor desempeño [Ortiz-Rodríguez, Martinez-Blanco & Vega-Carrillo, 2008].

El objetivo de este trabajo es determinar si es posible reducir el número de esferas utilizadas por el SEEB para la medición de fluencia de neutrones por medio de la optimización de la arquitectura de una red neuronal multicapa de propagación inversa, mediante la Metodología de Diseño Robusto de Redes Neuronales Artificiales (MDRRNA) [Ortiz-Rodríguez 2005; Ortiz-Rodríguez, Martinez-Blanco & Vega-Carrillo, 2006], entrenada para el cálculo de 15 cantidades dosimétricas haciendo uso de las tasas de conteo obtenidas con el SEEB con 4 grupos diferentes de esferas,

2.- MATERIALES Y METODOS

Se utilizaron un compendio de 251 conjuntos de datos compilados por el Organismo internacional de Energía Atómica, que contiene 15 cantidades dosimétricas cada grupo de datos, se utilizaron las tasas de conteo obtenidos de 4 diferentes grupos de esferas del SEEB para el entrenamiento de una red neuronal de propagación hacia adelante con algoritmo de propagación inversa para el cálculo de 15 cantidades dosimétricas, con la finalidad de conocer si es posible reducir el número de esferas empleadas por el SEEB y aun obtener una respuesta satisfactoria. El número de esferas usadas así como sus dimensiones se muestran en la tabla 1.

Tabla 1.- Grupos de esferas utilizados.

Grupo	Numero de esferas	Tamaño de esfera [pulgadas]
1	7	0, 2,3, 5, 8, 10, 12
2	2	8, 5
3	1	8
4	1	5

Se hace uso de la metodología de diseño Robusto de Redes Neuronales Artificiales para la selección de los parámetros óptimos de la arquitectura de una red neuronal artificial aplicada en el ámbito de la dosimetría de neutrones. El método de diseño robusto hace uso de la metodología Taguchi que utiliza una herramienta matemática llamada arreglo ortogonal para estudiar una gran cantidad de variables de decisión con un número pequeño de experimentos. El uso de esto arreglos ortogonales reduce significativamente el número de configuraciones experimentales a ser estudiadas a un punto practico donde aún se es capaz de alcanzar una solución óptima. [Jiju & Frenie Jiju 2001; Unal & Dean 1991]

La metodología de diseño robusto es un método experimental, el cual está compuesto de 4 etapas principales, cada una de las cuales contiene un determinado número de pasos. La figura 1 muestras las etapas la MDRRNA.

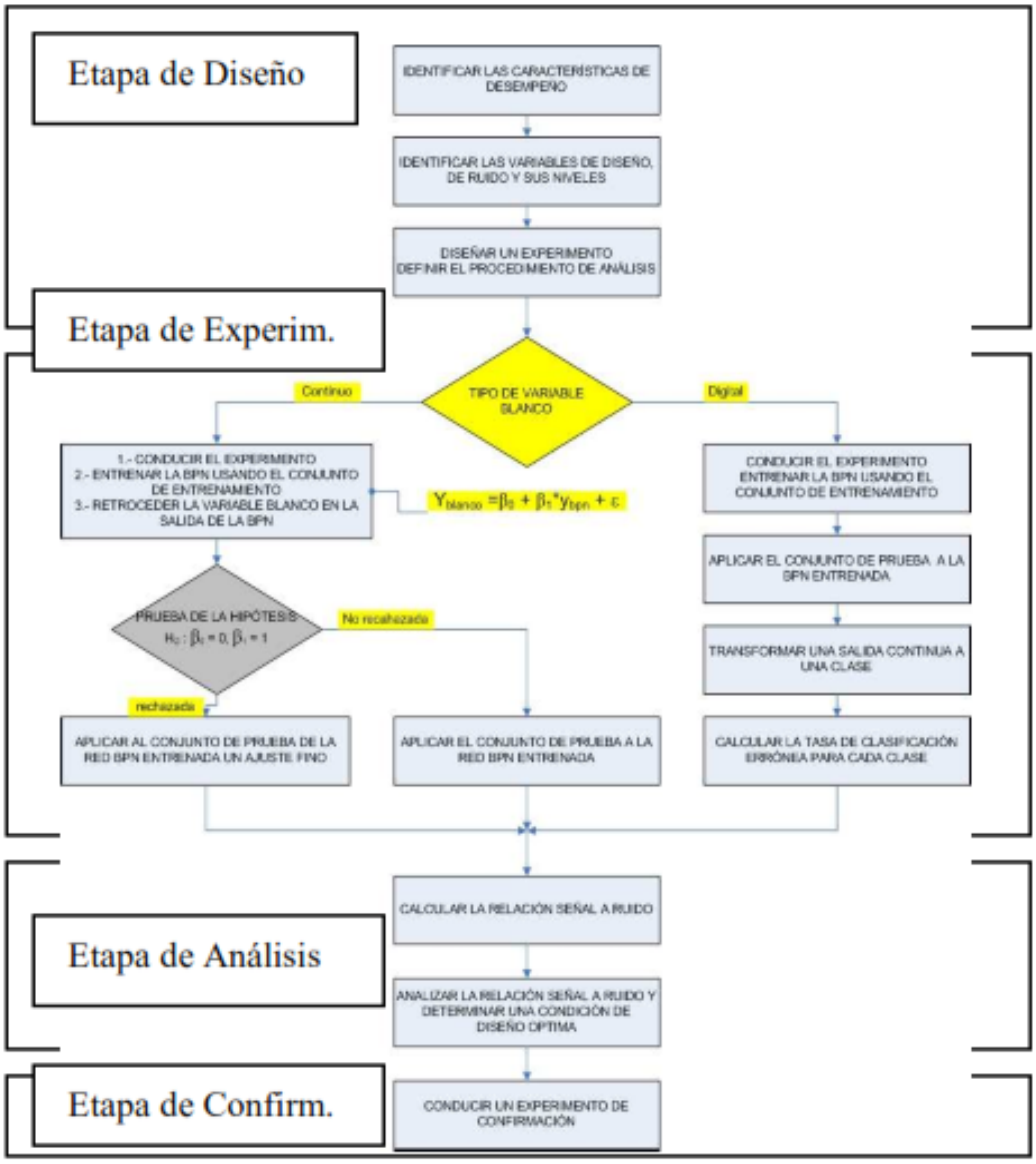

Figura 1.- Etapas de la Metodología de diseño robusto de redes neuronales artificiales.

2.1.- Etapa de planeación

En la etapa de planeación es necesario identificar la función objetivo y la búsqueda de las variables de diseño y de ruido que se encuentran dentro de la región de búsqueda. Las variables de diseño son parámetros que podemos controlar mientras que las variables de

ruido son parámetros que no pueden ser controlados y la función objetivo es la salida del error cuadrático medio (MSE) también conocido como el desempeño de la RNA.

En este trabajo se eligieron 4 variables de diseño, tal como se muestra en la tabla 2 donde se consideraron tres niveles para cada variable de diseño, para el diseño de la topología de la red. Donde A es el número de neuronas de la primera capa oculta, B es el número de neuronas de la segunda capa oculta, C es la taza de aprendizaje y D es el momento, siendo estos los parámetros controlables con mayor influencia sobre la red.

Tabla 2.- Variables de diseño y sus niveles.

Variables de diseño	Nivel 1	Nivel 2	Nivel 3
A			
B			
C			
D			

En la tabla 3 se muestran las variables de ruido seleccionadas, se eligieron 3 variables con 2 niveles cada una. Donde U es el conjunto inicial de pesos sinápticos, V es la relación del tamaño de datos usados para entrenamiento y prueba W es la selección aleatoria de los conjuntos de datos de entrenamiento y prueba, U representa la relación en porcentaje de datos utilizados por W.

Tabla 3.- Variables de ruido y sus niveles.

Variables de ruido	Nivel 1	Nivel 2
U	Conjunto 1	Conjunto 2
V	E:P	E:P
W	Entrenamiento 1-Prueba 1	Entrenamiento 2-Prueba 2

2.2.- Etapa de experimentación

En esta etapa de acuerdo con la MDRRNA, para el diseño de la topología de la red neuronal se seleccionaron las variables de diseño y de ruido conforme con las tablas 1 y 2, como sugiere el

método Taguchi se usó un arreglo ortogonal cruzado L_r (G^c), donde r es el número de renglones, c es el número de columnas y G el número de niveles en cada columna. Se utilizó un arreglo ortogonal con configuración L9 (3^4) y L_4 (2^3), como puede observarse en la tabla 3.

Tabla 4.- Parámetros de optimización de la RNA

					G1	G2	G3	G4		
No. Exp.	A	B	C	D	U=1 V=1 W=2	U=1 V=2 W=1	U=2 V=1 W=1	U=2 V=2 W=2	**Media de Y**	**Relación S/R**
1	1	1	1	1						
2	1	2	2	2						
3	1	3	3	3						
4	2	1	2	3						
6	2	2	3	1						
6	2	3	1	2						
7	3	1	3	2						
8	3	2	1	3						
9	3	3	2	1						

Se realizaron 36 entrenamientos para las diferentes topologías mostradas en el arreglo ortogonal, utilizando una herramienta diseñada en el entorno de programación de MATLAB, para la obtención de los desempeños de las redes, utilizados para el llenado del arreglo ortogonal.

Se utilizaron los datos obtenidos de 4 diferentes grupos de esferas del SEEB y se usó un arreglo ortogonal para cada uno lo que significa que se realizaron 36 entrenamientos diferentes para cada grupo de esferas.

2.3.- Etapa de análisis

Al finalizar con el llenado del arreglo ortogonal y en base a los resultados obtenidos, se calculó la relación señal-ruido por medio de la técnica del análisis de la varianza, con el fin

de determinar los efectos significativos y los niveles óptimos de las variables de diseño de la red y así obtener las mejores posibles topologías que tengan un mejor desempeño. El análisis de la varianza se realizó con la ayuda del programa estadístico JMP. Con los valores obtenidos del análisis de la relación señal-ruido y usando el programa estadístico JMP se calcularon los mejores parámetros de diseño para la RNA, obteniéndose las posibles mejores topologías de red, las cuales se entrenaron nuevamente utilizando la herramienta diseñada en MATLAB con el fin de elegir aquella con un mejor desempeño y capacidad de generalización. Se entrenaron cada topología obtenida un total de 4 veces cada una, utilizando el mismo porcentaje y los mismos datos para la etapa de entrenamiento y prueba, reduciendo así las variables no controlables.

2.4.- Confirmación

Con los resultados obtenidos de los entrenamientos realizados en la etapa de análisis se compararon el comportamiento de las redes de cada grupo de esferas con el fin de elegir la mejor de cada grupo, que contenga los mejores pesos sinápticos, aplicando la prueba de correlación (R) y chi cuadrada (χ^2). Obtenida la mejor red de cada grupo de esferas se compararon ahora entre ellas realizando nuevamente las pruebas de R y χ^2 para conocer el funcionamiento de cada red en comparación con la demás. Finalmente se compararon el mejor y el segundo peor caso de cálculo de dosis de cada red, obtenidos de la etapa de prueba de la red, así como 2 casos aleatorios.

3.- RESULTADOS

Aplicando la MDRRNA y siguiendo cada una de sus etapas se obtuvieron los siguientes resultados para cada grupo de esferas utilizado en este trabajo.

3.1.- Etapa de planeación

De acuerdo a la MDRRNA, para diseñar la estructura de la red neuronal se seleccionaron las variables de diseño y de ruido como se muestra en la tabla 5 y 6.

Tabla 5.- Variables de diseño y sus niveles.

Variables de diseño	Nivel 1	Nivel 2	Nivel 3
A	5	10	15
B	0	10	15
C	0.001	0.1	0.3
D	0.001	0.05	0.1

Tabla 6.- Variables de ruido y sus niveles.

Variables de ruido	Nivel 1	Nivel 2
U	Conjunto 1	Conjunto 2
V	6:4	8:2
W	Entren1-Prueba1	Entren2-Prueba2

3.2.- Etapa de experimentación y análisis

Inicialmente en la etapa de planeación se establecido un error de 1E-04 sin embargo este no resulto ser el mejor error para la red, por lo que se entrenó a prueba y error, utilizando los parámetros de diseño de la red de la etapa de planeación. Se buscó el error mínimo para el cual funciona la red para cada grupo de esferas, quedando como se muestra en la tabla 7.

Tabla 7.- Grupos de esferas utilizados.

Grupo	Numero de esferas	Tamaño de esfera [pulgadas]	MSE
1	7	0, 2, 3, 5, 8, 10, 12	5.5E10-06
2	2	8, 5	4E10-05
3	1	8	1.8E10-05
4	1	5	6.3E10-05

Definido el error para cada grupo de esferas entrena la red y se llena el arreglo ortogonal con los desempeños obtenidos de cada entrenamiento y se realizó el análisis de la relación señal-ruido con el análisis de la varianza con ayuda del programa estadístico JMP, como se muestra en las tablas 8-11.

Tabla 8.- Parámetros de optimización de la RNA para del grupo de 7 esferas.

	G1	G2	G3	G4		
No. Exp.	U=1	U=1	U=2	U=2	Media de Y	Relación S/R
	V=1	V=2	V=1	V=2		
	W=2	W=1	W=1	W=2		
1	8.29E-06	5.57E-06	4.23E-06	5.51E-06	5.90E-06	-11.033566
2	6.87E-06	6.90E-06	1.05E-05	4.90E-06	7.28E-06	-10.249393
3	6.10E-06	6.68E-06	1.73E-05	5.46E-06	8.89E-06	-5.0923811
4	6.22E-06	4.03E-06	5.85E-06	4.34E-06	5.11E-06	-13.575618
6	6.26E-06	5.88E-06	1.00E-05	8.22E-06	7.60E-06	-12.137748
6	5.89E-06	3.89E-06	3.51E-06	6.20E-06	4.87E-06	-11.260633
7	1.23E-05	6.74E-06	8.73E-06	5.99E-06	8.45E-06	-9.8148471
8	4.30E-06	9.33E-06	7.81E-06	4.60E-06	6.51E-06	-8.8890723
9	9.44E-06	6.86E-06	5.12E-06	7.11E-06	7.13E-06	-12.263959

Tabla 9.- Parámetros de optimización de la RNA para del grupo de 2 esferas.

	G1	G2	G3	G4		
No. Exp.	U=1 V=1 W=2	U=1 V=2 W=1	U=2 V=1 W=1	U=2 V=2 W=2	Media de Y	Relación S/R
1	4.13E-05	3.22E-05	4.41E-05	5.566E-05	4.33E-05	-13.195277
2	4.78E-05	5.14E-05	1.21E-04	7.30E-05	7.33E-05	-7.3951548
3	5.43E-05	9.12E-05	5.32E-05	5.17E-05	6.26E-05	-10.602328
4	2.59E-05	3.72E-05	4.80E-05	4.20E-05	3.83E-05	-12.415225
6	5.90E-05	2.47E-05	5.15E-05	3.87E-05	4.35E-05	-9.5866609
6	5.96E-05	5.04E-05	3.46E-05	4.31E-05	4.69E-05	-13.054584
7	5.15E-05	4.68E-05	4.10E-05	3.95E-05	4.47E-05	-18.178096
8	4.14E-05	3.34E-05	3.33E-05	6.06E-05	4.22E-05	-10.598447
9	7.67E-05	2.42E-05	3.78E-05	3.97E-05	4.46E-05	-6.7097919

Tabla 10.- Parámetros de optimización de la RNA para del grupo de 1 esfera de 8 pulgadas.

	G1	G2	G3	G4		
No. Exp.	U=1 V=1 W=2	U=1 V=2 W=1	U=2 V=1 W=1	U=2 V=2 W=2	Media de Y	Relación S/R
1	1.89E-05	1.09E-05	2.13E-05	2.20E-05	1.83E-05	-11.312998
2	2.97E-05	2.79E-05	1.98E-05	2.22E-05	2.49E-05	-14.678531
3	2.22E-05	1.44E-05	1.87E-05	2.60E-05	2.03E-05	-12.440811
4	7.73E-05	2.39E-05	2.34E-05	1.78E-05	3.56E-05	-3.7535232
6	2.85E-05	1.63E-05	1.70E-05	1.63E-05	1.95E-05	-10.555293
6	1.94E-05	1.26E-05	3.36E-05	1.26E-05	1.95E-05	-6.6926055
7	2.26E-05	2.19E-05	4.92E-04	2.19E-05	1.39E-04	-0.4259623
8	1.59E-05	2.58E-05	2.96E-05	2.58E-05	2.43E-05	-12.540991
9	1.62E-05	1.34E-05	2.56E-05	1.34E-05	1.72E-05	-9.7863761

Tabla 11.- Parámetros de optimización de la RNA para del grupo de 1 esfera de 5 pulgadas.

	G1	G2	G3	G4		
No. Exp.	U=1 V=1 W=2	U=1 V=2 W=1	U=2 V=1 W=1	U=2 V=2 W=2	**Media de Y**	**Relación S/R**
1	7.11E-05	6.88E-05	6.97E-05	4.97E-05	6.48E-05	-16.196784
2	6.63E-05	5.05E-05	6.73E-05	7.21E-05	6.41E-05	-16.77257
3	7.33E-05	3.45E-05	6.50E-05	8.14E-05	6.36E-05	-10.169921
4	5.51E-05	7.43E-05	6.10E-05	4.53E-05	5.89E-05	-13.86949
6	6.95E-05	6.11E-05	8.57E-05	6.66E-05	7.07E-05	-16.570144
6	1.01E-04	6.96E-05	6.89E-05	5.57E-05	7.38E-05	-11.930806
7	9.09E-04	5.81E-05	9.72E-05	7.80E-05	2.86E-04	-0.867921
8	6.52E-05	8.12E-05	1.09E-04	5.07E-05	7.67E-05	-10.011406
9	5.64E-04	9.58E-05	8.79E-05	1.31E-04	2.20E-04	-2.2010671

Con la relación señal-ruido obtenida de la etapa de experimentación y el programa JMP se obtuvieron las mejores topologías para cada red, siendo 2 topologías para cada grupo de esferas, estas se entrenaron con una relación entrenamiento-prueba de 80-20 en porcentaje de los datos, posteriormente se compararon lo resultados de cada red para elegir aquella con un mejor desempeño y capacidad de generalización, aplicando las pruebas de R y χ^2. La topología de la mejor red final obtenida para cada grupo de esferas se muestra en la tabla 12.

Tabla 12.- Mejor topología obtenida para cada grupo de esferas.

Grupo	Numero de esferas	Tamaño de esfera [pulgadas]	Arquitectura optimizada				
			Neuronas en capa 1	Neuronas en capa 2	Tasa de aprendizaje	Momento	Error
1	7	0, 2,3, 5, 8, 10, 12	5	15	0.1	0.3	$5.5x10^{-06}$
2	2	8, 5	10	0	0.001	0.001	$4x10^{-05}$
3	1	8	15	0	0.05	0.3	$1.8x10-^{05}$
4	1	5	15	0	0.05	0.3	$6.3x10^{-05}$

3.3.- Etapa de confirmación

Se hizo una comparación de la mejor red obtenida para cada grupo de esferas para conocer si a pesar de utilizar los datos obtenidos con un diferente número de esferas estas logran resolver la tarea del cálculo de dosis. Se compararon realizando las pruebas de la R y X^2 como se observa en las figuras 2 y 3.

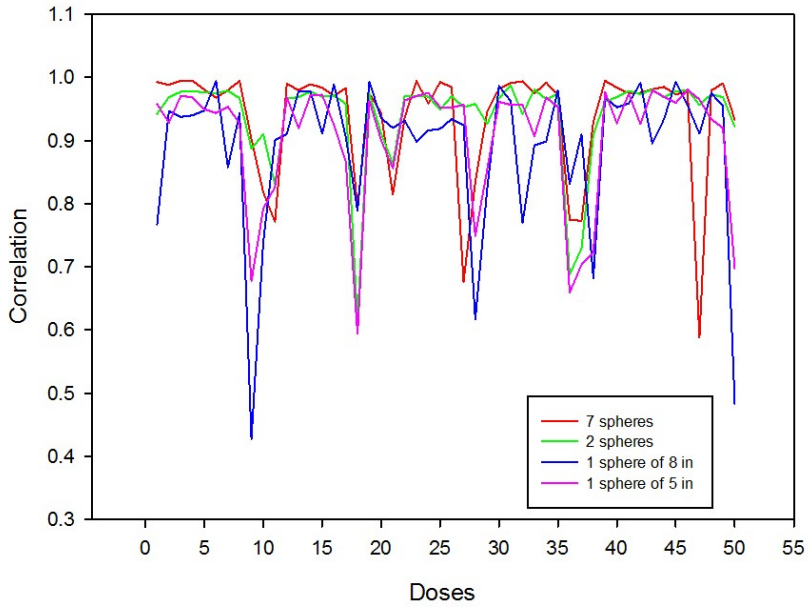

Figura 2.- Prueba de R de los 4 grupos de esferas.

En la figura 2 se puede observar que el conjunto de datos de dosis es capaz de alcanzar el valor óptimo de 1 en la mayoría de los casos, además que los casos en los que la red no es capaz de reconstruir las dosis de manera eficiente son los mismos casos en la red seleccionada para cada grupo de esferas, lo cual nos da a conocer que la red está trabajando de manera similar y es capaz de reconstruir las dosis aun utilizando un número diferente de esferas.

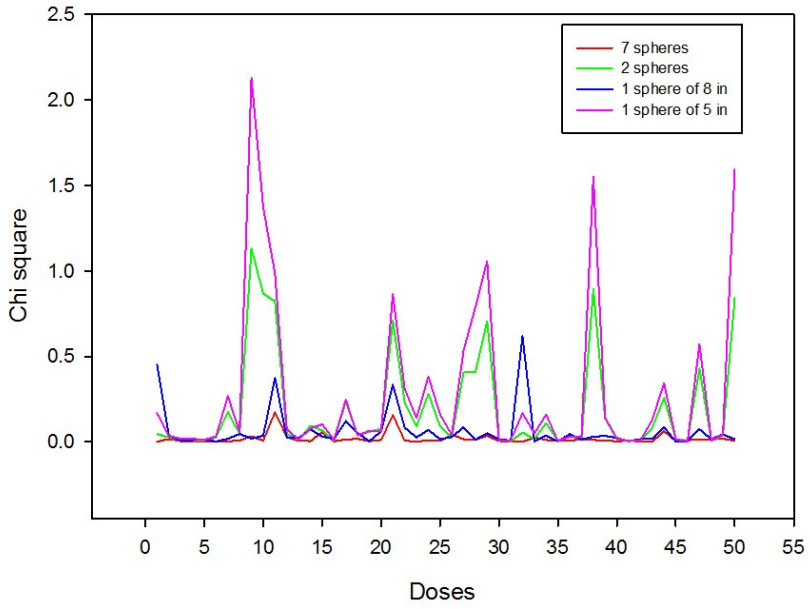

Figura 3.- Prueba de X^2 de los 4 grupos de esferas.

En la figura 3 se observa que en la mayoría de los casos los valores son aproximados a 0 que es lo que se busca, además de que todas se encuentran dentro del valor crítico que es de 6.57, esto nos dice que no existe una gran diferencia entre las dosis calculadas por la red y las dosis deseadas.

Con el fin de confirmar que se comportan de manera similar se compararon el mejor caso para el cual cada red genero una mejor respuesta así como el segundo peor caso de cada red y 2 casos tomados aleatoriamente de los 50 casos de prueba utilizados. La comparación de las dosis calculadas por cada red que emplea cada grupo de esferas y las dosis que se tienen como objetivo se muestran en las figuras 4 a la 12.

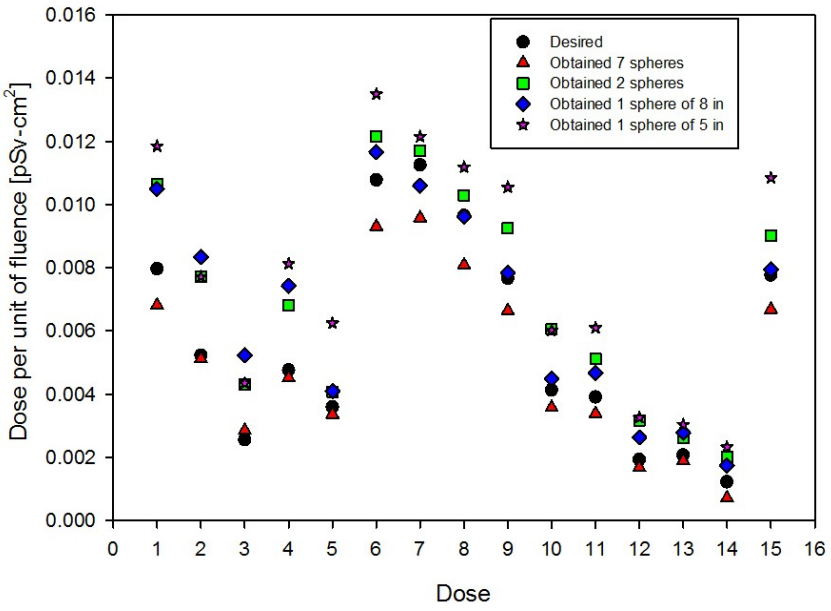

Figura 4.-Comparacion del mejor caso obtenido para 7 esferas (caso 3/50).

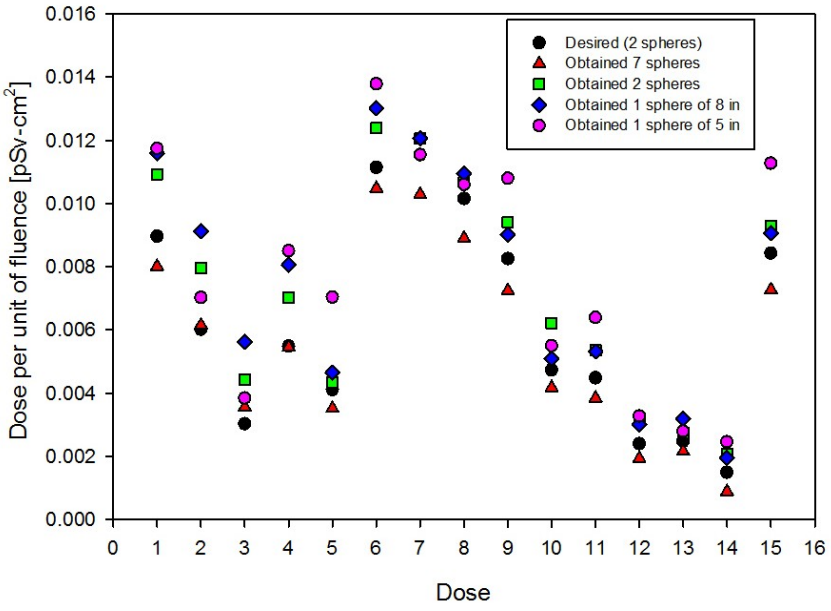

Figura 5.-Comparacion del mejor caso obtenido para 2 esferas (caso 31/50).

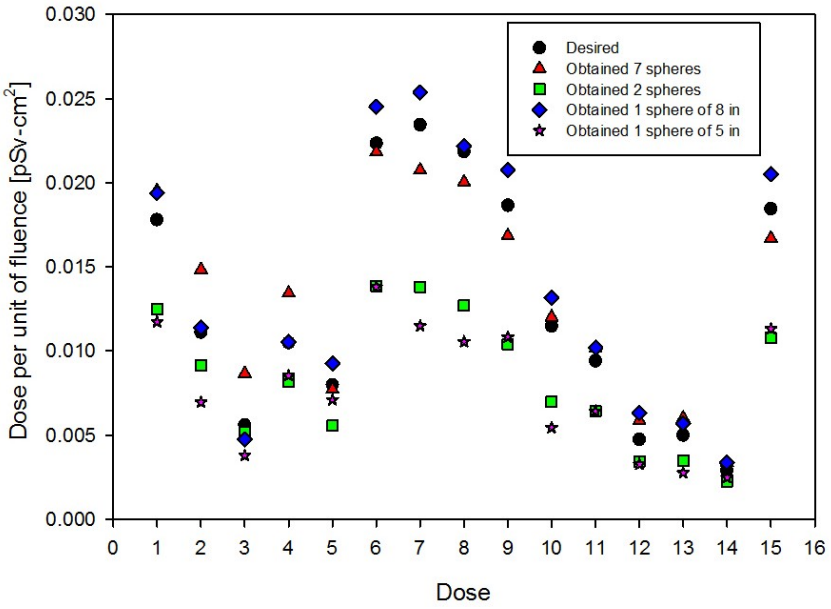

Figura 6.-Comparacion del mejor caso obtenido para 1 esfera de 8 pulgadas (caso 6/50).

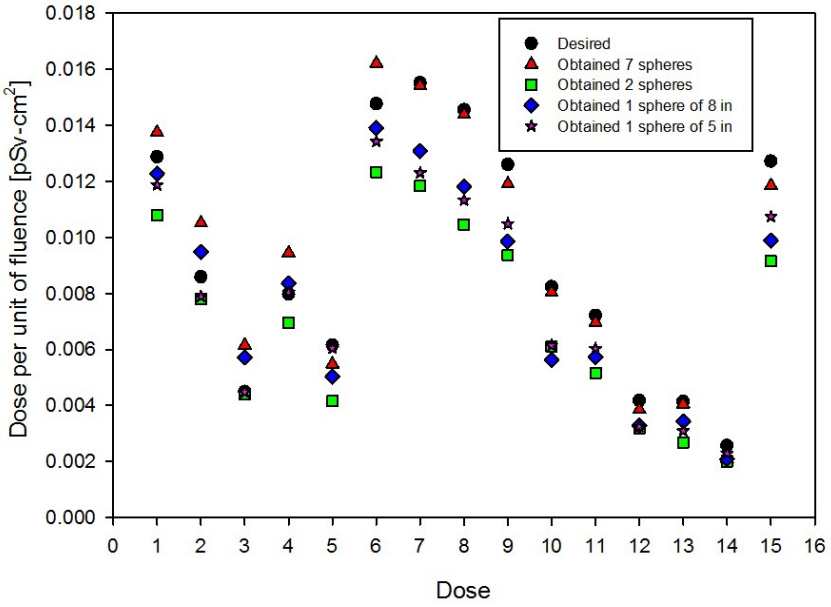

Figura 7.-Comparacion del mejor caso obtenido para 1 esfera de 5 pulgadas (caso 46/50).

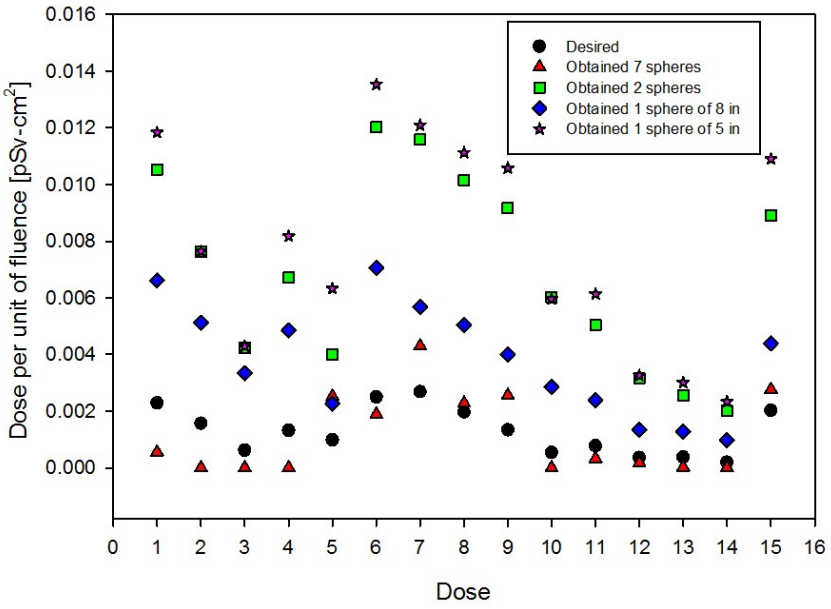

Figura 8.-Comparacion del segundo peor caso obtenido para 7 esferas (caso 27/50).

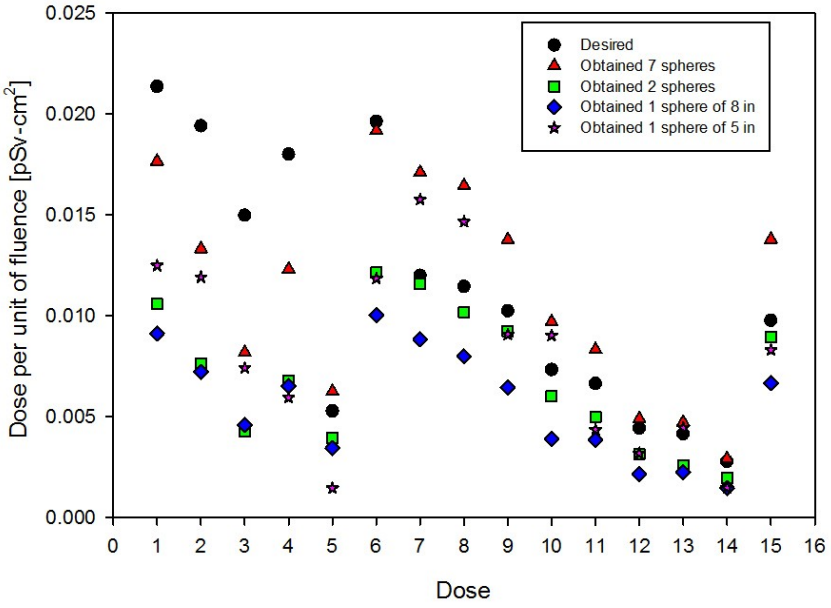

Figura 9.-Comparacion segundo peor caso 2 esferas y 1 esfera de 5 pulgadas (caso 36/50).

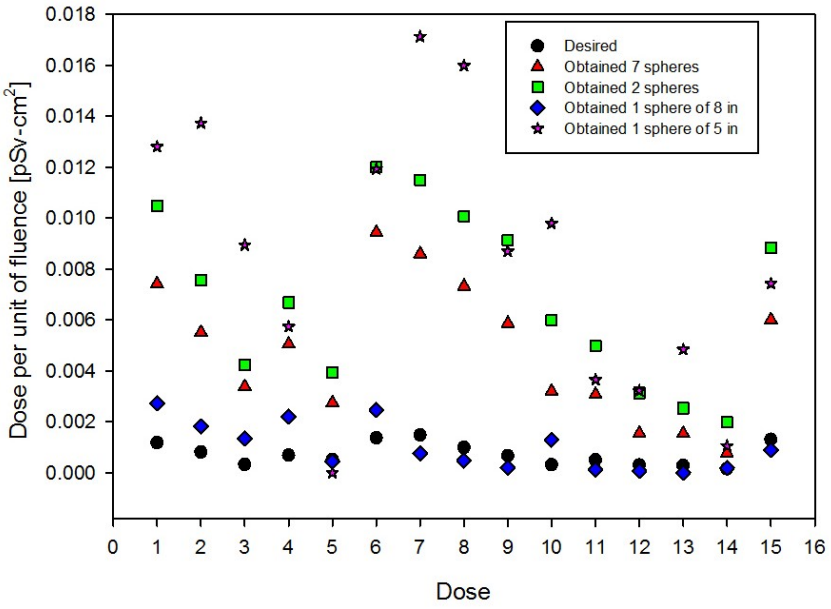

Figura 10.-Comparacion del segundo peor caso para 1 esfera de 8 pulgadas (caso 50/50).

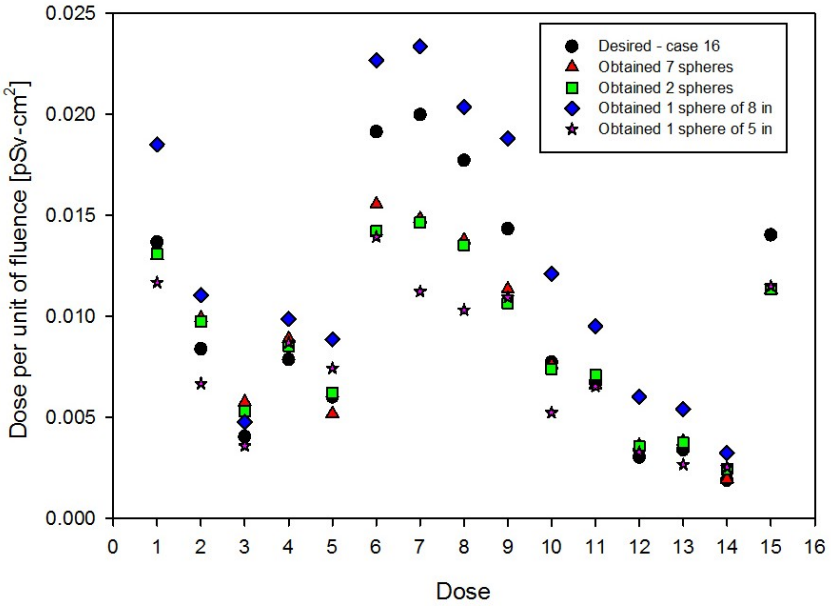

Figura 11.-Comparacion del primer caso aleatorio (caso 16/50).

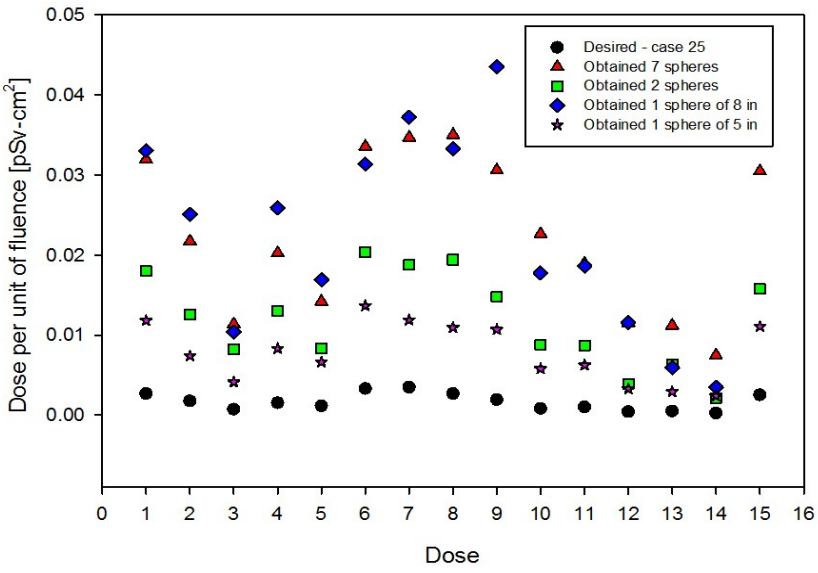

Figura 12.-Comparacion del primer caso aleatorio (caso 25/50).

4.- DISCUSIÓN

La técnica de ensayo y error empleada de forma convencional para obtener la mejor combinación de parámetros de diseño de la RNA ha mostrado ser poco eficiente ya que el diseño obtenido está lejos de ser el más óptimo, produciendo redes de pobre desempeño y baja capacidad de generalización. Además de consumir una gran cantidad de tiempo.

La MDRRNA difiere del método convencional en que adopta una estrategia sistemática experimental, donde se considera la robustez de la red, la cual generalmente no se toma en cuenta en el método convencional. En esta se identifican los parámetros de diseño y de ruido, haciendo uso del diseño robusto de Taguchi para encontrar los mejores parámetros de diseño de las RNA haciendo uso de arreglos ortogonales lo cual significa el reducir el número de experimentos, reduciendo la cantidad de tiempo ocupada en la búsqueda de la obtención de la topología óptima. Esta metodología puede ser empleada, a diferencia de las técnicas convencionales, a cualquier problema sin importar la naturaleza de este, siempre que se utilice una red de propagación hacia adelante entrenada con algoritmo de

propagación inversa, ya que se hace uso de una técnica general para determinar los parámetros óptimos de este tipo de red.

5.- CONCLUSIONES

En este trabajo se aplicó la metodología de diseño robusto de redes neuronales artificiales a la búsqueda de la topología óptima de una red neuronal artificial, aplicada al cálculo de dosis equivalentes de neutrones, esto se realizó para cada uno de los 4 diferentes grupos de esferas descritos, un grupo de 7 esferas de tamaños 0,2,3,5,8,10,y 12 pulgadas, uno de 2 esferas de 5 y 8 pulgadas, un grupo de 1 esfera de 8 pulgadas y 1 grupo de 1 esfera de 5 pulgadas, obteniéndose así 4 diferentes topologías de red que resuelven la misma tarea, esto con el fin de conocer si es posible reducir el número de esferas que pueden ser usadas por el SEEB para la medición de fluencia de neutrones y su posterior cálculo de dosis equivalentes.

El tipo de RNA empleada es de propagación hacia adelante con algoritmo de entrenamiento de propagación inversa, para la cual se entrenó un conjunto de topologías de redes con el objetivo de determinar los parámetros óptimos de cada red que produjera los mejores resultados, es decir, las dosis calculadas con el menor error entre las dosis esperadas y las obtenidas. Los entrenamientos y prueba de las redes se realizaron en una herramienta creada en MATLAB para este fin. Usando el programa estadístico JMP se obtuvieron las mejores topologías las cuales se entrenaron, probaron y compararon sus resultados para la selección de las mejores topologías.

Los resultados obtenidos en el cálculo de las dosis se verificaron aplicando las pruebas de χ^2 y R donde se observa en las figuras 2 y 3 que los resultados de cada red son similares, alcanzando valores cercanos a 1 para la R y valores de 0 para la χ^2, que son los valores que se buscan alcanzar y son capaces de calcular las dosis de forma muy similar a las esperadas tal como se muestra en las figuras 4-12.

Los resultamos obtenidos hasta el momento son alentadores, sin embargo, aún no se puede concluir si es posible reducir el número de esferas ya que los datos aún se encuentran en análisis, siendo necesario la realización de más pruebas estadísticas.

Agradecimientos

Este trabajo fue parcialmente financiado por el Fondo de Investigación para la Educación bajo contrato 241771. Este trabajo fue parcialmente financiado por fondos Mixtos SEP-CONACYT bajo contrato ZAC-C03-2015-26357-4. Este trabajo fue parcialmente financiado por PROSOFT bajo contrato 201513723.

El primero, tercero y cuarto autor agradecen la beca de Licenciatura con número de becario 23238, 23241, y 23240 respectivamente, recibido por Fondo Sectorial de Investigación para la Educación bajo contrato 241771. El segundo y quinto autor agradecen a la beca de Doctorado con número de becario 23386 y 23385 respectivamente, recibido por Fondo Sectorial de Investigación para la Educación bajo contrato 241771.

REFERENCIAS

Bramblett RL, Ewing RI & Bonner TW. (1960) *A new type of neutron spectrometer*, Nuclear Instruments and Methods **9**: 1-12.

Freeman DW, Edwards DR & Bolon AE. (1999) *Genetic algorithms – A new technique for soling the neutron spectra unfolding problem*, Nuclear Instruments and Methods in Physics Research A **425**: 549-576.

Jain AK, Mao J & Mohiuddin KM. (1996). *Artificial neural networks: a tutorial*. IEEE: Computer **29**: 31-44.

Jiju A & Frenie Jiju A. (2001). *Teaching the Taguchi method to Industrial Engineers*. Work Study **50**: 141-149.

Mohammadi N, Hakimabad HM, & Motavalli LR. (2015) *Neuronal network of neutron spectrum measured by gold foil-based Bonner sphere*. Journal of Radioanalytical and Nuclear Chemistry **303**: 1687-1693.

Ortiz-Rodríguez J.M. *Diseño Robusto de Redes Neuronales Artificiales aplicadas a la Espectrometría de Neutrones*. Tesis de Maestría de la Universidad Autónoma de Zacatecas. (2005).

Ortiz-Rodríguez JM, Martínez-Blanco MR & Vega-Carrillo HR. (2008). *Espectrometría y dosimetría de neutrones por medio de redes neuronales evolutivas*. Memorias del XIX Congreso Anual de la Sociedad Nuclear Mexicana: 130-141.

Ortiz-Rodríguez J.M., Martínez Blanco M.R., Vega-Carrillo H.R. (2006). *Diseño robusto de Redes Neuronales Artificiales*. Memoriasl del Encuentro de Investigación en Ingeniería Eléctrica (ENINVIE 2006): 295-300.

Reyes-Haro A, Ortiz-Rodríguez JM & Vega Carrillo HR. (2012). *Código iterativo para la reconstrucción del espectro de neutrones usando las esferas Bonner*. Proccedings of the ISSSD 2012: 44-49.

Reyes-Haro A, Ortiz-Rodríguez JM, Reyes-Alfaro A, Castañeda-Miranda R, Solis-Sanchez LO & Vega-Carrillo HR. (2014). *Prueba y validación del código iterativo para la espectrometría y dosimetría de neutrones: NSDUAZ.* Proccedings of the ISSSD 2014: 296-309.

Suman V & Sarkar PK.(2014). *Neutron spectrum unfolding using genetic algorithm in a Monte Carlo simulation*. Nuclear Instruments and Methods in Physics Research A **737**: 76-86.

Thomas DJ & Alevra AV. (2002). *Bonner sphere spectrometer-a critical review*. Nuclear Instruments and Methods in Physics Research A **476**: 12-20.

Thomas DJ. (2004). *Neutron spectrometry for radiation protection*. Radiation Protection Dosimetry **110**: 141-149.

Tripathy SP, Bakshi AK, Sathian V, Tripathi SM, Vega-Carrillo HR, Nandy M, Sarkar PK & Sharma DN. (2009). *Measurement of ^{241}Am-Be spectra (bare and Pb-covered) using TLD pairs in multi-spheres unfolding by different methods*. Nuclear Instruments and Methods in Physics Research A **598**: 556-560.

Unal R & Dean EB. (1991) *Taguchi Approach to design optimization for quality and cost: An overview*. 1991 Annual Conference of the International Society of Parametric Analysis. Pp.1-10.

Vega-Carrillo HR, Ortiz-Rodriguez JM & Martinez-Blanco MR. (2012). *NSDUAZ unfolding package for neutron spectrometry and dosimetry with Bonner spheres*, Applied Radiation and Isotopes **71**: 87-91.

Wang X, Zhang H, Wu Z. Zebg Z, Li JL, Qiu R & Li CY. (2014). *Development of spectra unfolding code for multi-sphere neutron spectrometer using genetic algorithms,* Nuclear Science and Techniques **25**: S010503.

Breast cancer tumor classification using LASSO method selection approach

José María Celaya Padilla[1-4], Jorge Armando Ortiz Murillo[1-4], María Del Rosario Martínez Blanco[1-4], Luis Octavio Solís Sánchez[1-4], Rodrigo Castañeda Miranda[1-4], Idalia Garza Veloz[1-3], Margarita Martínez Fierro[1-3], José Manuel Ortiz Rodríguez[1-4,*]

Universidad Autónoma de Zacatecas, Av. Ramón López Velarde 801, Col. Centro 98000 Zacatecas, México:

[1] Centro de Investigación e Innovación Tecnológica Industrial (CIITI)

[2] Laboratorio de Innovación y Desarrollo Tecnológico en Inteligencia Artificial, (LIDTIA)

[3] Laboratorio de Bioinformática

[4] Unidad Académica de Ingeniería Eléctrica (UAIE)

[*]Corresponding: morvymm@yahoo.com.mx

Abstract

Breast cancer is one of the leading causes of deaths worldwide among women. Early tumor detection is key in reducing breast cancer deaths and screening mammography is the widest available method for early detection. Mammography is the most common and effective breast cancer screening test. However, the rate of positive findings is very low, making the radiologic interpretation monotonous and biased toward errors. In an attempt to alleviate radiological workload, this work presents a computer-aided diagnosis (CADx) method aimed to automatically classify tumor lesions into malign or benign as a means to a second opinion. The CADx method, extracts image features, and classifies the screening mammogram abnormality into one of two categories: subject at risk of having malignant tumor (malign), and healthy subject (benign). In this study, 143 abnormal segmentations (57 malign and 86 benign) from the Breast Cancer Digital Repository (BCDR) public database were used to train and evaluate the CADx system. Percentile-rank (p-rank) was used to standardize the data. Using the LASSO feature selection methodology, the model achieved a Leave-one-out cross-validation area under the receiver operating characteristic curve (AUC) of 0.950. The proposed method has the potential to rank abnormal lesions with high probability of malignant findings aiding in the detection of potential malign cases as a second opinion to the radiologist.

Keywords: Breast cancer detection, LASSO, malign tumor, data mining.

1.- INTRODUCTION

There is no limit of t Breast cancer is one of the leading causes of woman's death all over the world (Nishikawa, 2007) . In developing countries breast cancer is an important public health issue, where demographic and epidemiological transition is not matched with public screening and treatment programs (Knaul et al.). One of the most effective modality for detecting the early-stage breast cancer is screening mammography, which is an inexpensive tool for classifying abnormalities such as calcifications and masses, as well as subtle signs, like architectural distortion and bilateral asymmetry, and is the most effective method for detection of breast cancer before it becomes clinically palpable(Ng & Muttarak). Screening mammography is a standardized study in which craniocaudal (CC) and mediolateral oblique (MLO)views are acquired from each breast and inspected by a specialized radiologist. However, detection of abnormalities in screening mammography is a repetitive and fatiguing task, which affects the performance of the radiologist over a workday. In a normal screening setting, only 0.3% to 0.4%, of the inspections are cancerous, resulting in radiologists failing to detect 10% - 30% of those (Sampat, Markey, Bovik, & others). In recent years there has been a great effort in research to develop computer-aided detection or diagnosis (CAD) systems that use computer technologies to assist radiologists in their decisions were a high number of studies must be examined. Different approaches have been proposed for detection and characterization of calcifications. (H.-D. Cheng, Cai, Chen, Hu, & Lou) and (Sampat et al.) summarize the different methods used and their performance.

In this work we propose a methodology to detect and classify lesions present in a mammogram for breast cancer that can be used to profile screening mammography patients. The methodology takes the set of mammograms from each patient in a database, using the ROI delimited by the radiologist extracts a set of features from these images. Using a multivariate feature selection algorithm, we were able to identify a set of features with high predictive value. The selected features were then used to distinguish between benign and malign tumors. This procedure can be used as a biomarker as a second opinion to the radiologist, this paper is organized as follows: In Section II we describe the proposed

methodology in detail. Section III contains the obtained results from the methodology. The results are discussed in section IV and V.

2.- MATERIALS AND METHODS

In this research we propose a methodology to aid the radiologist by analyzing the suspicious lesions that may indicate sings of breast cancer. The proposed methodology extracts a series of features to characterize the lesion, then using advanced machine learning techniques, a model to classify said lesions is obtained. The methodology overview is presented in Figure 1, briefly, first a subject's mammogram is presented to the radiologist, the radiologist then adjusts the contrast and other values to better visualize the possible abnormalities, then if any, the Region of Interest (ROI) is segmented. Afterwards, feature extraction is performed in order to characterize the abnormality. Finally, a robust Machine Learning technique (LASSO) is performed in order to find the best subset of features capable of distinguishing malign from benign lesions.

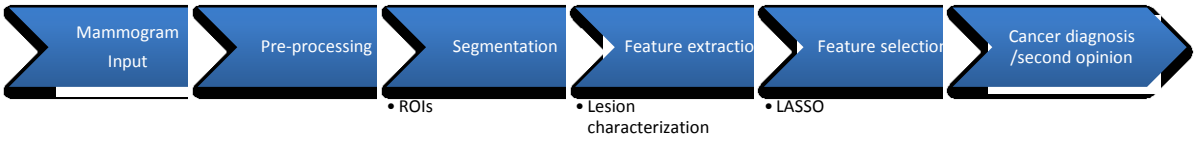

Figure 1.- Methodology overview.

2.1.- Materials

In this research a public available dataset Breast Cancer Digital Repository (BCDR) (López et al., 2012) was used. This dataset is composed by 1734 patients with mammography and ultrasound images, clinical history, lesion segmentation and selected pre-computed image-based descriptors. Patient cases are BIRADS classified and annotated by specialized radiologists. From the above dataset, a subset of 143 abnormal ROI segmentations (57 malign and 86 benign), a total of 28 features were extracted : 8 features were extracted from the intensity descriptors computed directly from the grey-levels of the pixels inside

the lesion's contour identified by the radiologists, 12 texture features were computed from the Grey-level co-occurrence matrix related to the bounding box of lesion's contour, and finally 8 features related to the shape and location descriptors of the lesion, the full description of said features is presented in Table 1 and Table2. The dataset contains two possible outcome classification "Benign" or "Malign" labeled by the specialized radiologist.

Table 1. Texture features.

Feature	Description
Energy (t_energ)	$\sum_{i=1}^{L}\sum_{j=1}^{L} p(i,j)^2$ with L being the number of grey-levels, and p being the grey-level co-occurrence matrix and, thus, $p(i,j)$ is the probability of pixels with grey-level i occur together to pixels with grey-level j.
Contrast (t_contr)	$\sum_{i}\sum_{j}(i-j)^2 p(i,j)$
Correlation (t_corr)	

	$\frac{\sum_i \sum_j (ij)\, p(i,j) - \mu_x \mu_y}{\sigma_x \sigma_y}$ with μ_x, μ_y, σ_x and σ_y being the means and standard deviations of p_x and p_y, the partial probability density functions.
Sum of Squares: Variance (t_sosvh)	$\sum_i \sum_j (i-\mu)^2\, p(i,j)$ with μ being the mean of $p(i,j)$ for all i and j.
Homogeneity (t_homo)	$\sum_i \sum_j \frac{1}{1+(i-j)^2}\, p(i,j)$
Sum Average (t_savgh)	$\sum_{i=2}^{2L} i p_{x+y}(i)$ with $p_{x+y}(i)$ being the probability of the co-occurrence matrix coordinates summing $i = x + y$
Sum Entropy (t_senth)	$se = -\sum_{i=2}^{2L} p_{x+y}(i) \log\left(p_{x+y}(i)\right)$
Sum Variance (t_svarh)	$\sum_{i=2}^{2L} (i-se)^2\, p_{x+y}(i)$
Entropy (t_entro)	$-\sum_{i=1}^{L} \sum_{j=1}^{L} p(i,j) \log\left(p(i,j)\right)$
Difference Variance (t_dvarh)	$\sum_{i=0}^{L-1} i^2\, p_{x-y}(i)$ with $p_{x-y}(i)$ being the probability of the co-occurrence matrix coordinates subtracting $i = \lvert x - y \rvert$
Difference Entropy (t_denth)	$-\sum_{i=0}^{L-1} p_{x-y}(i) \log\left(p_{x-y}(i)\right)$
Information Measure of Correlation 1 (t_inf1h)	$\frac{-\sum_{i=1}^{L} \sum_{j=1}^{L} p(i,j) \log\left(p(i,j)\right) + \sum_{i=1}^{L} \sum_{j=1}^{L} p(i,j) \log\left(p_x(i)\, p_y(j)\right)}{\max\left(\sum_{i=1}^{L} p_x(i) \log\left(p_x(i)\right), \sum_{i=1}^{L} p_y(i) \log\left(p_y(i)\right)\right)}$
Information Measure of Correlation 2 (t_inf2h)	$\sqrt{1 - \exp\left(2\left(\sum_{i=1}^{L} \sum_{j=1}^{L} p_x(i)\, p_y(j) \log\left(p_x(i)\, p_y(j)\right) - \sum_{i=1}^{L} \sum_{j=1}^{L} p(i,j) \log\left(p(i,j)\right)\right)\right)}$

Table 2. Shape and localization features.

Feature	Description
Area (s_area)	$area = \|O\|$ with O being the set of pixels that belong to the segmented lesion
Perimeter (s_perimeter)	$perimeter = length(E)$ with $E \subset O$ being the edge pixels
Center of mass (s_x_center_mass, s_y_center_mass)	Normalized coordinates of the center of mass of O
Circularity (s_circularity)	$4\pi \frac{area}{perimeter^2}$
Elongation (s_elongation)	$elongation = \frac{m}{M}$ with m being the minor axis and M the major axis of the ellipse that has the same normalized second central moments as the region surrounded by the contour
Form (s_form)	$\frac{perimeter \times elongation}{8 \times area}$
Solidity (s_solidity)	$\frac{area}{\|H\|}$ with H being the set of pixels that belong to the convex hull of the segmented region
Extent (s_extent)	$\frac{area}{\|B\|}$ with B being the set of pixels that belong to the bounding box of the segmented region

2.1.- Methods

In order to select the most accurate and compact set of features, a multivariate search strategy was performed using Least Absolute Shrinkage and Selection Operator (LASSO) [38], LASSO is a shrinkage and selection method that minimizes the usual sum of squared errors which penalizes the regression coefficients Equation 1. The multivariate search was performed using a using leave-one-subject-out cross validation (LOOCV) strategy [39], training the models for every split using *N-1* subjects and testing in the left out subject.

$$\hat{\beta}^{lasso} = argmin \sum_{i=1}^{N} \left(y_i - \beta_0 - \sum_{j=1}^{p} x_{ij}\beta_j\right)^2 \; subject\ to: \sum_{j=1}^{p} |\beta| \leq t \qquad (1)$$

3.- RESULTS

A 0.9508 Area Under the Receiver Operation Catachrestic (AUC) was achieved using the final model obtained using the LASSO methodology. On Figure 2 the ROC curve is presented for the final model using the LOOCV.

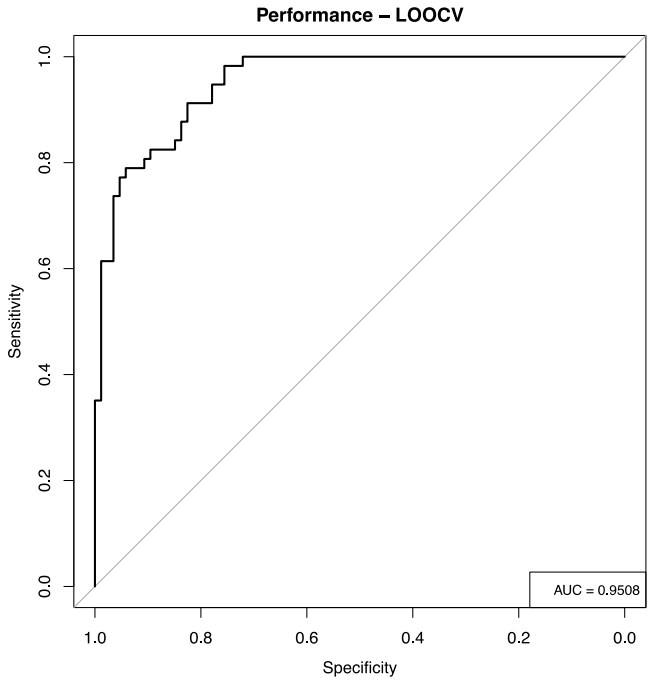

Figure 2.- Model performance using LOOCV, AUC = 0.9508.

From the 28 features pool, the multivariate feature selection methodology LASSO was able to reduce the number of features need down to only nine features. The final model included a combination of features extracted from the intensity descriptors, texture features and features related to the shape and location descriptors of the lesion, summarize the performance achieved by each group of feature. The final model with all the statistic information is shown in Table 3.

Table 3.- Final model.

Feature	Estimate	Std. Error	z value	Pr(>|z|)
(Intercept)	-0.1755	2.6107	-0.067	0.946413
i_skewness	-2.3165	1.6345	-1.417	0.156424
s_perimeter	5.2351	2.3877	2.193	**0.028343***
s_x_center_mass	-3.0137	1.3466	-2.238	**0.025223***
s_elongation	2.8573	1.4871	1.921	**0.054681^**
s_solidity	-6.3953	1.7068	-3.747	**0.000179***
t_energ	-0.9427	1.418	-0.665	0.506176
t_corr	-2.7176	5.5612	-0.489	0.625079
t_sosvh	0.5457	1.3994	0.39	0.696571
t_inf2h	5.0663	4.938	1.026	0.304903

*Statistical significance <0.05, ^marginal statistical significance <0.05

The confusion matrix of the final model is presented in the Figure 3, the model achieved an accuracy of 0.8462 with 95% CI (0.7764, 0.901), and a Mcnemar's Test P-Value of 5.104e-05.

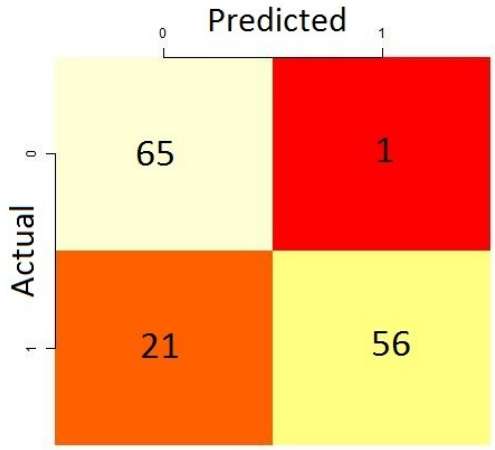

Figure 3.- Confusion matrix.

4.- DISCUSSION

A feature selection strategy was used to find a multivariate model to classify benign from the malignant lesions on the breast images. The methodology demonstrates that image characterization is a good approach to identify patients with lesions that can be cancer-related. The automatically generated Logistic regression classifier included features of different groups, therefore, texture analyses, and signal properties could add discriminant information.

The LASSO model selection strategy yields reproducible models of healthy versus malignant abnormal lesion detection with a LOOCV AUC of 0.9508. Furthermore, the detailed analysis of the ROC curve may give us indications of key triaging points for prioritizing the mammogram reading. Priority triaging may have real practical usage in regions where expert radiological resources are scarce or costly.

The results of the work cannot yet be generalized and the presented findings are limited to a single scanner of the public BCDR dataset. Even having these strong limitations, we believe that the methodology can be replicated with full-field digital mammography and with newer advanced technologies like tomosynthesis.

5.- CONCLUSIONS

This research was able to show that healthy lesions, and subjects with malign lesions can accurately be classified through models generated via accurate mammography feature extraction a feature selection methodology. The methodology demonstrated that abnormal lesions can be automated classified regardless of the size, form and shape. The achieved performance of the system has the potential to be used as a second opinion, and may be used to reduce the unnecessary biopsies.

Future work can include the usage of other image transforms to obtain further information, this methodology is intended to be used to help the radiologist as a second opinion, and to reduce the load of work if the models are used as a screening biomarker that accurately classify which subjects have a malign or benign lesion, therefore, reducing the unnecessary biopsies.

Acknowledgments

This work was partially supported by Fondo Sectorial de Investigación para la Eduación under contract 241771, Fondos Mixtos SEP-CONACYT under contract ZAC-C03-2015-26357-4, and PROSOFT under contract 201513723. The first author wants to thank CONACYT for the post-doctoral scholarship number 24296.

REFERENCES

Bovis, K., & Singh, S. (2000). *Detection of masses in mammograms using texture features.* Paper presented at the Pattern Recognition, 2000. Proceedings. 15th International Conference on.

Cheng, H., Shi, X., Min, R., Hu, L., Cai, X., & Du, H. (2006). Approaches for automated detection and classification of masses in mammograms. *Pattern recognition, 39*(4), 646-668.

Cheng, H.-D., Cai, X., Chen, X., Hu, L., & Lou, X. (2003). Computer-aided detection and classification of microcalcifications in mammograms: a survey. *Pattern recognition, 36*(12), 2967-2991.

Knaul, F. M., Nigenda, G., Lozano, R., Arreola-Ornelas, H., Langer, A., & Frenk, J. (2009). Cancer de mama en Mexico: una prioridad apremiante. *Salud Publica Mex, 51*(s2).

López, M. A. G., de Posada, N. G., Moura, D. C., Pollán, R. R., Valiente, J. M. F., Ortega, C. S., . . . Loureiro10, J. P. (2012). *BCDR: A BREAST CANCER DIGITAL REPOSITORY*. Paper presented at the 15th International Conference on Experimental Mechanics.

Mendez, A. J., Tahoces, P. G., Lado, M. i., a J, Souto, M., & Vidal, J. J. (1998). Computer-aided diagnosis: Automatic detection of malignant masses in digitized mammograms. *Medical Physics, 25*, 957.

Ng, K., & Muttarak, M. (2003). Advances in mammography have improved early detection of breast cancer. *Honk Kong College or radiologist, 6*, 126-131.

Nishikawa, R. M. (2007). Current status and future directions of computer-aided diagnosis in mammography. *Computerized Medical Imaging and Graphics, 31*(4), 224-235.

Sampat, M. P., Markey, M. K., Bovik, A. C., & others. (2005). Computer-aided detection and diagnosis in mammography. *Handbook of image and video processing, 2*(1), 1195-1217.

Yin FF, G. M., Vyborny CJ. (1993). Comparison of bilateral-subtraction and single-image processing techniques in the computerized detection of mammographic masses. *Investigative Radiology, 28*(6), 473-481.

Sociedad Mexicana de Irradiación y Dosimetría

Tuxtla Gutiérrez, Chiapas

México

2016